Characterization of X-Pinches on the MAIZE Linear Transformer Driver

by

George V. Dowhan

A dissertation submitted in partial fulfillment
of the requirements for the degree of
Doctor of Philosophy
(Applied Physics)
in the University of Michigan
2023

Doctoral Committee:

Professor Ryan D. McBride, Chair
Reader Simon N. Bland, Imperial College London
Associate Research Professor Nicholas M. Jordan
Professor Karl M. Krushelnick
Associate Professor Carolyn C. Kuranz

George V. Dowhan

dowhan@umich.edu

ORCID iD: 0000-0001-7963-4361

© George V. Dowhan 2023

ACKNOWLEDGMENTS

I would like to start by thanking Ryan for roping me into this field and advising me over the last few years. I am greatful for all of the freedom and support provided throughout my time in the lab. Following that, a thank you to my present and past fellow grad students of the PPML for the collective support through the many oil spills and MAIZE maintenances, without whom it would have been significantly less enjoyable. Thank you as well to my friends and family who had no idea what I was doing for five years but wholeheartedly supported me nonetheless.

I wish to also give a sincere thanks to everyone I have workied with throughout my studies. Thank you to Dr. Sergei Pikuz, whose expertise was invaluable in properly getting X-pinches running on MAIZE. Thank you to Dr. Simon Bland, for both agreeing to being on my committee and kindly aiding when I hit snags along the way. Thank you to Prof. Jack Hare for the many bits of advice in dealing with interferograms and polarograms. Thank you to Prof. Daniel Klir and Dr. Karel Rezac for their significant support and aid, and without whom the second half of this thesis would not exist. Additionally, thanks to Prof. Hammer and Prof. Kusse, as well as all of the students and staff of the LPS, for the help and openess during my time there.

Lastly, thank you to Prof. Brian Gilchrist for welcoming me to Michigan and being supportive of me following what I wanted to do.

This work was supported by the DOE Early Career Research Program under Grant DE-SC0020239 and by the NNSA SSAP under Cooperative Agreement DE-NA0003764.

TABLE OF CONTENTS

Acknowledgments . . . . . **ii**

List of Figures . . . . . **v**

List of Tables . . . . . **xiii**

List of Appendices . . . . . **xiv**

Abstract . . . . . **xv**

Chapter

1 Introduction and Background **1**

1.1 HEDP and Pulsed Power 1
1.2 X-Pinches and Micro-Pinches 3
1.3 The MAIZE LTD 6
1.3.1 The BLUE LTD 8
1.4 Author's Contribution 8

2 X-Pinch Evolution and Instabilities **9**

2.1 X-pinch Evolution 9
2.2 Instabilities of the Neck Cascade 11
2.3 Radiative Collapse and Micro-Pinch Compression to Small Radius 14
2.4 Recent Work and an Alternative Theory 16

3 X-Pinch Experimental Platforms **17**

3.1 MAIZE X-Pinch Load Hardware 17
3.1.1 Prior Hardware 19
3.2 Diagnostic Platforms 20
3.2.1 Current Measurement 20
3.2.2 Laser Diagnostics and Fast Framing Camera 22
3.2.3 XUV Imaging 23
3.2.4 X-ray Imaging 23
3.2.5 Poly-Crystalline Diamond Detectors 25
3.2.6 COBRA X-ray Crystal Spectrometer 26
3.2.7 Neutron Diagnostics 27
3.3 X-Pinches Driven on MAIZE 27

4 Faraday Rotation Experiments **34**

4.1 Faraday Rotation . . . 35
4.2 Measurement and Modeling of the Faraday Rotation Angle . . . 39
4.3 Faraday Diagnostic Design and Evolution . . . 43
4.3.1 Initial Faraday Design . . . 43
4.3.2 First Implemented Faraday Design . . . 45
4.3.3 Second Implemented Faraday Design . . . 48
4.4 Source of Error from Optical Element Polarization Anisotropy . . . 50
4.5 Results . . . 56
4.5.1 Current Distributions and Magnetic Pressure . . . 66
4.6 Summary . . . 76

5 Deuterated Fiber X-Pinch Experiments . . . 77

5.1 Motivations and Background . . . 77
5.2 Experimental Design . . . 81
5.2.1 Neutron Diagnostics . . . 82
5.2.2 Load Material . . . 88
5.3 Results . . . 90
5.3.1 Neutron Yields . . . 93
5.3.2 Neutron Emission Correlation . . . 96
5.3.3 Neutron Emission Anisotropy . . . 98
5.3.4 Neutron Emission Duration . . . 100
5.4 Summary . . . 103

6 Final Summary and Conclusions . . . 104

6.1 Future Work . . . 105

Appendices . . . 107

Bibliography . . . 154

LIST OF FIGURES

FIGURE

1.1 Illustration of a cylindrically symmetric pulsed-power implosion. (a) Current flows along the surface of conductive vacuum chamber walls (in dark blue) to, and along, a central cylindrical load (yellow and grey). (b) The produced azimuthal magnetic field as the current flows results in a magnetic pressure radially inwards against the cylindrical load. (c) Under sufficient conditions, such as in a thin foil load, the central region will implode. (Adapted with permission from Fig. 1 in Ref [7].) 2

1.2 Illustration of various wire X-pinches. Multiwire X-pinches are conical arrangements of wire arrays twisted to form a central crossing point. Hybrid X-pinches are essentially the limit in the number of wires where the conical section is replaced by a solid electrode and an axial wire spans the gap in place of a crossing point. 5

1.3 Cross-sectional view of the MAIZE LTD showing location of (1) capacitors and switches in oil section, (2) vacuum transmission lines, and (3) vacuum load region. . . 7

2.1 A graphical depiction of X-pinch evolution showing (1–5) initial wire ablation and neck formation, (6–7) initial pinching of the neck plasma, (11–12) the rapid cascading of the neck and the relative order of the cascade, (8) formation of the hot-spot, HS, (9–10) breaking of the plasma neck and production of electron and ion beams. Reprinted from S. A. Pikuz, T. A. Shelkovenko, and D. A. Hammer, "X-pinch. Part I," *Plasma Physics Reports*,vol. 41, pp. 330, Apr. 2015, with permission from Springer Nature. 10

2.2 Simple illustrations showing the current and magnetic field structure of common MHD instabilities. (a) A plasma column in equilibrium with a uniform structure. (b) The $m = 0$ "sausage" instability showing bunching of field lines around the constriction points. (c) The $m = 1$ "kink" instability showing the gradient in the density of field lines across the perturbation. 12

3.1 Pictures of the X-pinch load hardware installed within the MAIZE vacuum chamber. (a) The original design with a 4×35 µm Mo X-pinch loaded into the WCu insets. (b) The modified load hardware for adjustable hybrid X-pinch experiments. A 200 µm Nylon hybrid X-pinch is loaded between the WCu inserts with a 2 mm electrode gap. . 17

3.2 Photograph showing the wear on the electrode surfaces after ∼10s of shots. Metal deposition and roughening of the electrode surfaces are present in roughly equal fashion on both the anode and cathode sides. Also note the central pitting. This is caused by axial plasma jets, which form from ablated wire material (coronal plasma) being swept to the central axis and then jetting axially upward or downward (away) from the central wire-crossing point. 18
3.3 Pictures of the X-pinch radiography hardware for the MAIZE LTD. (a) A 4-wire X-pinch loaded into one of the insert locations with a Rogowski coil to monitor the fraction of current it receives. (b) A view of the MAIZE vacuum chamber where the radiography hardware and return current post extension can be seen. 19
3.4 An example of a typical in-chamber diagnostic setup for an X-pinch experiment. Shown are the locations and distances used for fielding of x-ray diagnostics (PCDs, x-ray cameras), the main anode Rogowski coil, and typical lines of sight for laser and visible imaging through available vacuum port windows. 21
3.5 (a) Image of the X-ray camera housing additionally showing a half-inserted filter holder. The front aperture holder contains the relevant pinhole or slit for the desired diagnostic. (b) The removed back panel of the camera body showing the attached step-wedge filters. These sit between the end of the body cavity and in front of the filter holder groove in the back panel. A graphical view of the filters is provided. Values represent the total thickness of the same-material layers. For example, the far right filter would be read as 76.2 µm Cu + 100 µm Al. 24
3.6 Graph showing the transmitted fraction of x-rays as a function of photon energy through the various filters used for the MAIZE PCDs. 25
3.7 Selected plots showing the various X-pinch and MAIZE parameters as functions of the X-Pinch linear mass and resistance derived from the January 2023 experiments detailed in Table 3.2. The linear fits to the data are given for each data set in the units of the axes. Color corresponds to wire material: Red is silver, Blue is molybdenum, Green is tungsten. 32

4.1 A simplified slice of a cylindrical plasma with an azimuthally symmetric electron density (arbitrarily represented by the color gradient) and magnetic field, $B_\theta(r)$, profiles. The depth of the plasma for a chord of laser propagation through the plasma column changes with its position along the x-axis and is denoted as $L(x)$. 36
4.2 (a,b,c) Simulated Faraday rotation profiles with the entire current (**150 kA**) fully enclosed within the central dense plasma column and (a) constant, (b) linear, and (c) exponential electron density distributions in the surrounding coronal plasma. (d,e,f) Simulated Faraday rotation profiles of a constant electron density distribution in the coronal plasma and (d) 90%, (e) 50%, and (f) 10% of the total drive current contained within the dense neck plasma and the remaining current being linearly distributed in the surrounding coronal plasma. The line out of each simulated rotation profile is plotted in black along with the location of the edges of the central dense neck plasma. All plots were initialized with a coronal plasma density of 2×10^{18} cm^{-3} at the edge of the neck. 41

4.3 (a,b,c) Simulated Faraday rotation profiles with the entire current (**500 kA**) fully enclosed within the central dense plasma column and (a) constant, (b) linear, and (c) exponential electron density distributions in the surrounding coronal plasma. (d,e,f) Simulated Faraday rotation profiles of a constant electron density distribution in the coronal plasma and (d) 90%, (e) 50%, and (f) 10% of the total drive current contained within the dense neck plasma and the remaining current being linearly distributed in the surrounding coronal plasma. The line out of each simulated rotation profile is plotted in black along with the location of the edges of the central dense neck plasma. All plots were initialized with a coronal plasma density of 2×10^{18} cm^{-3} at the edge of the neck. 42
4.4 Diagram of the original design of the imaging Faraday rotation diagnostic for the MAIZE LTD. This design was never fully implemented. Not to scale. 43
4.5 Diagram of the initial imaging Faraday rotation diagnostic fully fielded on the MAIZE LTD. Not to scale. 45
4.6 Diagram of the revised imaging Faraday rotation diagnostic fielded on the MAIZE LTD. Not to scale. 48
4.7 The majority of the optical setup diagrammed in Fig. 4.6. Shown are the portions of the beam path within the laser room undergoing initial expansion and polarization cleaning, as well as the post-MAIZE collection of the beam and splitting into the three diagnostic arms. The pre-MAIZE optical table where the beam is split into the probe and reference beams is not shown. 49
4.8 Diagram illustrating the effect of anisotropies on the reflection and transmission of p- and s-components of a linearly polarized beam passing through a nominally non-polarized beamsplitter. The resulting rotations of the polarization angle, θ_T, θ_R, may be larger or smaller than θ depending on the exact ratios of the transmission and reflection coefficients, $C_{\mathrm{p}}^T/C_{\mathrm{s}}^T$ and $C_{\mathrm{p}}^R/C_{\mathrm{s}}^R$. 51
4.9 (a) While passing through the plasma, the initial laser polarization angle, θ, colored red, is rotated by the Faraday effect by an amount α, colored orange. (b) The rotated laser is passed through a perfectly non-polarizing beamsplitter to split the beam between the two polarization analyzers. The axis of extinction for the polarization analyzers, colored blue, and set to $\theta \pm \beta$. Note that both analyzers see the same value of α. (c) The rotated laser is passed through an imperfect, non-polarizing beamsplitter to split the beam between the two polarization analyzers. From the effect detailed in Fig. 4.8, the polarization analyzers now see different Faraday rotation angles, $\widetilde{\alpha}_{\mathrm{R}}$ and $\widetilde{\alpha}_{\mathrm{T}}$, in the reflected and transmitted beams. 53
4.10 In situ photographs within the MAIZE vacuum chamber of (a) a standard X-pinch load with two 25-μm Ag wires, and (b) a hybrid X-pinch load with a single 50-μm Mo wire. Both photographs show the anode and cathode orientation and the location of the polycrystalline diamond (PCD) detector used to measure the timing of the X-pinch x-ray bursts. The box in red shows the approximate field of view imaged by the Faraday rotation diagnostic. 57
4.11 (a,b,c,d) Images collected for a two-wire, 25-μm-wire-diameter, Ag X-pinch experiment: (a) pre-shot interferogram; (b) interferogram; (c) channel 1 polarogram; and (d) channel 2 polarogram. (e,f,g,h) Images collected for a 50-μm-wire-diameter Mo hybrid X-pinch experiment: (e) pre-shot interferogram; (f) interferogram; (g) channel 1 polarogram; and (h) channel 2 polarogram. 59

4.12 Data from shot 2534, a two-wire, 25-μm-wire-diameter, Ag X-pinch experiment: (a) pre-shot interferogram; (b) shot interferogram; and (c) the areal density image calculated from (a)–(b). Taken 2 ns before x-ray burst. 61
4.13 Data from shot 2241, a two-wire, 25-μm-wire-diameter, Ag X-pinch experiment: (a) pre-shot interferogram; (b) shot interferogram; and (c) the areal density image calculated from (a)–(b). Taken 6 ns before x-ray burst. 61
4.14 Data from shot 2241, a two-wire, 25-μm-wire-diameter, Ag X-pinch experiment: (a) post-shot polarimetry background; (b) smoothed channel 1 polarogram; (c) smoothed channel 2 polarogram; and (d) the Faraday rotation image calculated from (a)–(c). The dashed box in (d) denotes the region used for producing the enclosed current profile and the magnetic pressure profile of Fig. 4.20. The solid lines within the dashed box in (d) denote the edge of the dense core and center axis. Analyzer β was set to 3.5°. . . . 63
4.15 Data from shot 2534, a two-wire, 25-μm-wire-diameter, Ag X-pinch experiment: (a) post-shot polarimetry background; (b) smoothed channel 1 polarogram; (c) smoothed channel 2 polarogram; and (d) the Faraday rotation image calculated from (a)–(c). The dashed box in (d) denotes the region used for producing the enclosed current profiles and the magnetic pressure profiles of Figs. 4.17, 4.18, and 4.19. The solid lines within the dashed box in (d) denote the edge of the dense core and center axis. Analyzer β was set to 3.5°. 64
4.16 Data from shot 2933, a six-wire, 35-μm-wire-diameter, Mo X-pinch experiment: (a) smoothed channel 1 polarogram; (b) smoothed channel 2 polarogram; (c) post-shot polarimetry background; and (d) the Faraday rotation image calculated from (a)–(c). The dashed box in (d) denotes the region used for producing the enclosed current profile and the magnetic pressure profile of Fig. 4.21. The solid lines within the dashed box in (d) denote the edge of the dense core and center axis. Analyzer β was set to 3.0°. 65
4.17 Extracted profiles from shot 2534 using a scale parameter of $L = 700$ μm. (top) Current enclosed as a function of radius from the center of the X-pinch neck. The shaded region bounded by the dotted line gives the calculated errors in the enclosed current measurement. Plotted for reference in red is the 133 kA of load current measured by the anode Rogowski coil on MAIZE at the time of the Faraday rotation imaging. Note that the anode Rogowski coil resides at a radius of 11 cm. (bottom) Magnetic drive pressure as a function of radius from the center of the X-pinch neck with shaded region bounded by the dotted line giving the calculated errors in the drive pressure measurement. The overlaid dashed red line shows a fit with a $1/r^2$ dependence. Note that a $1/r^2$ dependence is expected to occur outside of the radius in which 100% of the total drive current is enclosed (*cf.* Eq. 1.1). 68

4.18 Extracted profiles from shot 2534 using a scale parameter of $L = 2500$ μm. (top) Current enclosed as a function of radius from the center of the X-pinch neck. The shaded region bounded by the dotted line gives the calculated errors in the enclosed current measurement. Plotted for reference in red is the 133 kA of load current measured by the anode Rogowski coil on MAIZE at the time of the Faraday rotation imaging. Note that the anode Rogowski coil resides at a radius of 11 cm. (bottom) Magnetic drive pressure as a function of radius from the center of the X-pinch neck with shaded region bounded by the dotted line giving the calculated errors in the drive pressure measurement. The overlaid dashed red line shows a fit with a $1/r^2$ dependence. Note that a $1/r^2$ dependence is expected to occur outside of the radius in which 100% of the total drive current is enclosed (*cf.* Eq. 1.1). 69

4.19 Abel inverted current enclosed profile as a function of radius from the center of the X-pinch neck from shot 2534. The shaded region bounded by the dotted line gives the calculated errors in the enclosed current measurement. Plotted for reference in red is the 133 kA of load current measured by the anode Rogowski coil on MAIZE at the time of the Faraday rotation imaging. Note that the anode Rogowski coil resides at a radius of 11 cm. Abel inversion causes several artifacts that give low fidelity in portions of the signal highlighted in light blue. Compare features and magnitude to the current enclosed distribution in Fig. 4.18. 70

4.20 Extracted profiles from shot 2241 using a scale parameter of $L = 800$ μm. (top) Current enclosed as a function of radius from the center of the X-pinch neck. The shaded region bounded by the dotted line gives the calculated errors in the enclosed current measurement. Plotted for reference in red is the 135 kA of load current measured by the anode Rogowski coil on MAIZE at the time of the Faraday rotation imaging. Note that the anode Rogowski coil resides at a radius of 11 cm. (bottom) Magnetic drive pressure as a function of radius from the center of the X-pinch neck with shaded region bounded by the dotted line giving the calculated errors in the drive pressure measurement. The overlaid dashed red line shows a fit with a $1/r^2$ dependence. Note that a $1/r^2$ dependence is expected to occur outside of the radius in which 100% of the total drive current is enclosed (*cf.* Eq. 1.1). 72

4.21 Extracted profiles from shot 2933 using a scale parameter of $L = 2000$ μm and recorded 13 ns post first x-ray burst and 2 ns before a second x-ray burst. (top) Current enclosed as a function of radius from the center of the X-pinch neck. The shaded region bounded by the dotted line gives the calculated errors in the enclosed current measurement. Plotted for reference in red is the 388 kA of load current measured by the anode Rogowski coil on MAIZE at the time of the Faraday rotation imaging. Note that the anode Rogowski coil resides at a radius of 11 cm. (bottom) Magnetic drive pressure as a function of radius from the center of the X-pinch neck with shaded region bounded by the dotted line giving the calculated errors in the drive pressure measurement. The overlaid dashed red line shows a fit with a $1/r^2$ dependence. Note that a $1/r^2$ dependence is expected to occur outside of the radius in which 100% of the total drive current is enclosed (*cf.* Eq. 1.1). 73

5.1 MAIZE vacuum chamber during a deuterated polyethylene hybrid X-pinch experiment. Shown are the in-chamber diagnostics and the lines of sights for the external optical diagnostics. Not shown are the neutron diagnostics placed around the vacuum chamber. 81
5.2 (a) An nTOF detector composed of a Hamamatsu H2431-50 PMT assembly and a ⌀15 cm x 2.5 cm EJ-204 scintillator with light cone. (b) The near and far positions of the nTOF detectors for radial lines of sight, roughly 1 and 2.5 m from the source, respectively. (c) The detector placement for near-axial line of sight on the top lid of the vacuum chamber, roughly 0.25 m from the source. 82
5.3 Sample response from one of the nTOF detectors showing the extracted FWHM of the cosmic event response to be ∼12 ns. The signal was recorded with the PMT biased to −1.4 kV. 83
5.4 Bare setup showing the general structure of the PMT electron transit time measurement. Laser light is split between a photodiode and the PMT with known distances to deduce the transit time. Additional ND filters and a light shroud not shown in this figure were added for the actual experiment to prevent over-saturation of the PMT. Resulting fits of the transit time as functions of bias voltage are approximated by the curve: ETT [ns] ≈ $835 \cdot V^{-0.5}$. 84
5.5 (a) Beryllium activation detector in an axial position on the MAIZE vacuum chamber lid. Shown is the relative location of the source and the distance and angle for the center of the active region containing the beryllium rods. (b) An example of a processed beryllium probe signal that has been binned into reasonable time steps and fit to determine the neutron yield. 85
5.6 Example bubble detectors from Bubble Technology Industries of the same type fielded on MAIZE experiments for determination of the total neutron yield. 87
5.7 (a) An image of an uncoated $[CD_2]_n$ fiber imaged through (c) a handheld 50× microscope. (b) The inset of (a) clearly showing the fiber contrasted behind the microscope ruler for measurement of its diameter. (d)–(f) Sample images of $[CD_2]_n$ fibers with each of the three conductive coatings applied: (d) silver, (e) carbon, and (f) nickel. . . 89
5.8 (a) Bright view of the chamber with X-pinch hardware and a loaded fiber X-pinch. (b) Inset of the central X-pinch load of (a) clearly showing the fiber spanning the electrode gap. (c)–(d) Equivalently cropped images to (a)–(b) showing the time-integration in visible emission of an X-pinch experiment. Various emission structures can be seen at varied radii with different emission intensities. 91
5.9 Overview plot of traces for shot 3010, the highest neutron yield shot of the campaign. The shot parameters and neutron yield are presented in the top right corner. The nTOF traces are annotated to mark the HXR pulse and the subsequent neutron pulse. 95
5.10 Overview plot of traces for shot 3012 with shot parameters and neutron yield presented in the top right corner. The nTOF traces show three clear neutron peaks that correlate in time to an initial blip of the PCD signals and two, more traditional, x-ray bursts, implying that while correlated in time, the neutron and x-ray production mechanisms do not necessarily have to both occur simultaneously. 97
5.11 Two subsequent frames captured in XUV emission imaging (large, green) for shot 3012 showing bright plasma structures radially streaming out to high radii. Corresponding frames in visible self-emission (small, grey), sized to similar scaling, do not appear to capture these structures. 99

5.12 MCNP calculations of a similar detector's response 3 m from a point-like 2.5 MeV neutron source, with variation in lead shielding thickness. The detector type in this simulation is a 5×4.5 cm BC-408 scintillator. Figure courtesy of O. Sila, K. Rezac, and D. Klir of the Czech Technical university in Prague. 101

B.1 Diagram of constructed x-ray camera housing showing the location of the primary components including the attachment of a Thorlabs CFH2 filter holder into which a 1" mounted pinhole or slit can be inserted. 111
B.2 Diagram of the front panel of the x-ray camera to which the Thorlabs CFH2 filter holder mounts. 112
B.3 Diagram of the 13 cm x-ray camera body. 113
B.4 Diagram of the 22 cm x-ray camera body. 114
B.5 Diagram of the 26 cm x-ray camera body. 115
B.6 Diagram of the top portion of the back panel. The back panel is in two pieces for easier machining of the film-holder slot. 116
B.7 Diagram of the bottom portion of the back panel. The back panel is in two pieces for easier machining of the film-holder slot. 117
B.8 Diagram of the back piece of the film-holder with film slot. 118
B.9 Diagram of the front film retention piece of the film-holder. 119

C.1 Faraday rotation diagnostic images for Shot 2241. Image intensity scaled for visibility. 121
C.2 Faraday rotation diagnostic images for Shot 2534. Image intensity scaled for visibility. 122
C.3 Faraday rotation diagnostic images for Shot 2933. No additional intensity scaling. . . 123

D.1 Parameters and diagnostic data recorded for Shot 2999. 125
D.2 Parameters and diagnostic data recorded for Shot 3000. 126
D.3 Parameters and diagnostic data recorded for Shot 3001. 127
D.4 Parameters and diagnostic data recorded for Shot 3002. 128
D.5 Parameters and diagnostic data recorded for Shot 3003. 129
D.6 Parameters and diagnostic data recorded for Shot 3004. 130
D.7 Parameters and diagnostic data recorded for Shot 3005. 131
D.8 Parameters and diagnostic data recorded for Shot 3006. 132
D.9 Parameters and diagnostic data recorded for Shot 3007. 133
D.10 Parameters and diagnostic data recorded for Shot 3008. 134
D.11 Parameters and diagnostic data recorded for Shot 3009. 135
D.12 Parameters and diagnostic data recorded for Shot 3010. 136
D.13 Parameters and diagnostic data recorded for Shot 3011. 137
D.14 Parameters and diagnostic data recorded for Shot 3012. 138
D.15 Parameters and diagnostic data recorded for Shot 3013. 139
D.16 Parameters and diagnostic data recorded for Shot 3014. 140
D.17 Parameters and diagnostic data recorded for Shot 3015. 141
D.18 Parameters and diagnostic data recorded for Shot 3016. 142
D.19 Parameters and diagnostic data recorded for Shot 3017. 143
D.20 Parameters and diagnostic data recorded for Shot 3018. 144
D.21 Parameters and diagnostic data recorded for Shot 3019. 145
D.22 Parameters and diagnostic data recorded for Shot 3020. 146

D.23 Parameters and diagnostic data recorded for Shot 3021. 147
D.24 Parameters and diagnostic data recorded for Shot 3022. 148
D.25 Parameters and diagnostic data recorded for Shot 3023. 149
D.26 Parameters and diagnostic data recorded for Shot 3024. 150
D.27 Parameters and diagnostic data recorded for Shot 3025. 151
D.28 Parameters and diagnostic data recorded for Shot 3026. 152
D.29 Parameters and diagnostic data recorded for Shot 3027. 153

LIST OF TABLES

TABLE

3.1 Calibration factors for the MAIZE PCDs when biased to -100 V. PCDs are fielded at a source-to-detector distance of 10 cm, have an area of 3 mm^2, and are 50 Ω terminated. 26

3.2 Summary of the X-pinches fielded on the MAIZE pulsed-power generator. Experiments from October 2020 through February 2022 experienced low current due to MAIZE firing asynchronously and producing peak currents of <250 kA. The January 2023 and April 2023 experiments were driven from MAIZE firing synchronously and delivering peak currents up to 600 kA. 28

3.3 Density and resistivities for the wire and electrode materials used in the MAIZE experiments. 29

4.1 Ideal final intensities, normalized to the initial beam energy, after transmission and reflection of the reference and probe beam through the non-polarizing cube beamsplitters that comprised the Mach-Zehnder interferometer illustrated in Fig 4.5. This accounts for attenuation of the probe beam from port windows (approximately 4% per interface, 8 interfaces) but not additional plasma, lenses, or neutral density filters. 46

4.2 Coefficients of reflection and transmission of the Thorlabs BS032 non-polarizing beamsplitter for s- and p-polarized light. The relevant factor in polarization anisotropy characterization is the ratio $\frac{C_p}{C_s}$ or its inverse. 52

5.1 Parameter space of the deuterated fiber X-pinch experiments detailing scans over anode-cathode gap distance and fiber diameters. 'Good' and 'not-so-good' shots are marked in reference to neutron signal strength recorded by the nTOF detectors. 92

5.2 Tabulated neutron yields recorded from the bubble detector average, the beryllium activation probe, and the average of the two diagnostic methods. The measurement floor of both detectors is approximately 1×10^6 neutrons. Color intensity is proportionally scaled from the minimum to maximum of the average yields. 94

5.3 Minimal measured FWHMs of nTOF detector signals and their deconvoluted neutron emission widths ($FWHM_0$) for shots containing single or well separated peaks. All peaks correlate to singular x-ray peaks except where noted. [a]Neutron peak correlated with two x-ray peaks ∼5 ns apart. [b]Neutron peak correlated with three x-ray peaks spread over ∼10 ns. 102

LIST OF APPENDICES

A Uncertainty Derivations for Extracted Distributions in Faraday Rotation Imaging Experiments **107**

B X-ray Camera Drawings **110**

C Experimental Faraday Rotation Image Sets for Shots 2241, 2534, and 2933 . . . . . **120**

D Diagnostic Data from Deuterated Polyethylene Fiber Experiments **124**

ABSTRACT

An X-pinch, formed by driving an intense current pulse (>100 kA in ∼100 ns) through the crossing of 2 or more wires, can result in the formation of a small radius, runaway compressional micro-pinch. A micro-pinch is characterized by a hot (>1 keV), current-driven (>100 kA), high-density plasma column (near solid density) with a small neck diameter (1–10 μm), a short axial extent (<1 mm), and a short duration ($\lesssim$1 ns). With material pressures often well into the multi-Mbar regime, a micro-pinch plasma often radiates an intense, sub-ns burst of sub-keV to multi-keV x-rays. This dissertation presents two main areas of X-pinch characterization performed on the low-impedance (0.16 Ω), 1-MA, 100-ns MAIZE Linear Transformer Driver (LTD) at the University of Michigan.

The first characterization involved the delivery of electrical current to small pinch radius. A micro-pinch compression to radii on the order of ∼1 μm would lead to pressures on the order of ∼1 Gbar for currents on the order of ∼0.1 MA. However, the fraction of the total current that is driven through the dense micro-pinch plasma at small radii versus the current being shunted through the surrounding coronal plasma at larger radii is not well known. For this study, a Faraday rotation imaging diagnostic (1064 nm) capable of producing simultaneous high-magnification polarimetric and interferometric images was developed for the MAIZE facility. Designed with a variable magnification (1–10×), this diagnostic achieves a spatial resolution of approximately 35 μm, which is sufficient for resolving the ∼100-μm-scale coronal plasma region immediately surrounding the dense core. Analysis of the interferograms shows a coronal density profile that remains low ($\leq 10^{17}$ cm^{-3}) until close to the dense core (≤200 μm) where it quickly increases ($\geq 10^{18}$ cm^{-3}). Extraction of Faraday rotation angles similarly showed low signals with polarization shifts of $|\alpha| \lesssim 3°$. Combined, these profiles provide bounding measurements, up to minimal radii (due to the location of the dense plasma) of ∼100 μm, showing a strong indication that ∼40–60% of the total current delivered by MAIZE is distributed in the coronal plasma region from 100–300 μm, thereby reducing magnetic drive pressures to maxima of ∼100–150 kbar.

The second characterization involved the use of deuterated wires (CD_2) for the X-pinch loads. As the typical configurations of X-pinches produce characteristically small (∼μm), sub-ns x-ray bursts for fast radiographic applications, the conversion of the metallic wire to a deuterated material produces (in addition to an x-ray burst) a burst of 2.45-MeV neutrons from nuclear fusion reactions

occurring between pairs of deuterons. Experiments using a hybrid X-pinch configuration loaded with deuterated polyethylene fiber were performed on the MAIZE LTD to evaluate the main parameters of the neutron emission. The resulting neutron production was found to be highly correlated to x-ray emission peaks within $\lesssim$10 ns, with production duration of typically 15–20 ns. In the limited parameter sweep performed, the average yields were on the order of 10^7 neutrons, while the maximum yield obtained was as high as 1.4×10^8 neutrons. These yields are on par with those obtained using the gas-puff z-pinch system on MAIZE. This is true despite the fact that the X-pinch platform has a region of neutron production that is only a fraction of that in the gas-puff z-pinch platform—i.e., a 1 mm axial extent in the X-pinch platform versus a 10 mm axial extent in the gas-puff z-pinch platform. This highlights the importance of understanding micro-pinch physics.

CHAPTER 1

Introduction and Background

1.1 HEDP and Pulsed Power

High-energy-density (HED) physics (HEDP) comprises the study of matter whose energy density reaches or exceeds 10^{11} J/m^3. Reaching these extreme conditions can be accomplished via pulsed power facilities, which drive and support a multitude of basic science research, ranging in scope from nuclear fusion [1, 2, 3, 4] to laboratory astrophysics [5], as well as stockpile stewardship [6].

In many pulsed-power-driven, high-energy-density physics experiments, implosions are driven via magnetic pressure generated from an axial current in a cylindrical load geometry [7]. Referring to Fig. 1.1(a), the process starts with the application of voltage across the vacuum regions, causing a current to begin flowing along the conductive chamber walls as well as along an axial load. The current rise is inversely proportional to the inductance of the vacuum cavity with the load installed. The axial current that flows in the central load region sets up an azimuthal magnetic field. The combination of this magnetic field and current density, by way of $\mathbf{F} = \mathbf{J}\times\mathbf{B}$, generates a magnetic pressure normal to the conducting surfaces, shown in Fig. 1.1(b). If the central load is, for example, a thin metallic liner, then magnetic pressure can accelerate the liner material to the central axis, as shown in Fig. 1.1(c). This is known as a fast z-pinch implosion.

In this cylindrical configuration, the magnetic drive pressure can be expressed as

$$P_{mag} = \frac{B^2}{2\mu_0} = \frac{\mu_0 I^2}{8\pi^2 r^2}. \tag{1.1}$$

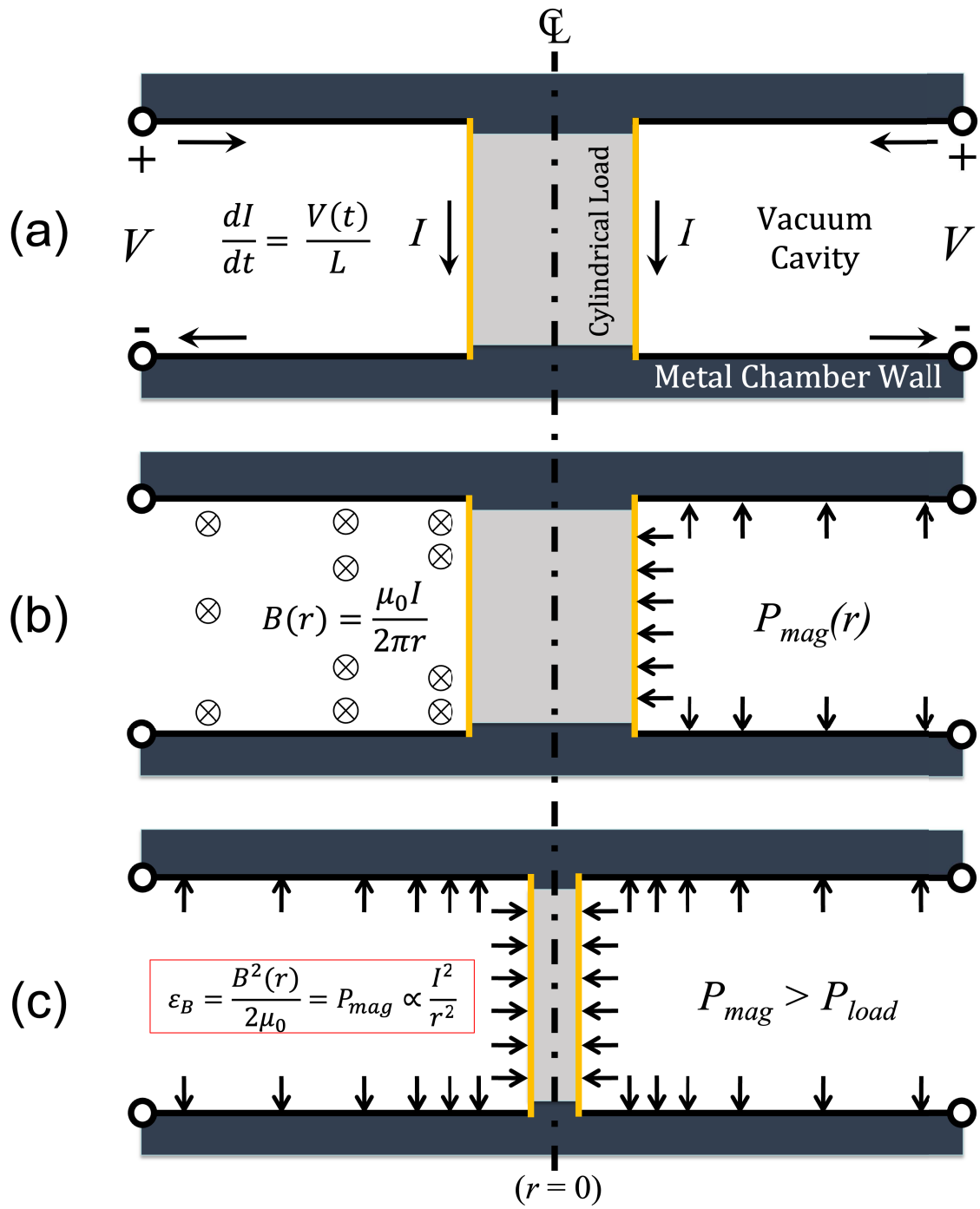

Figure 1.1: Illustration of a cylindrically symmetric pulsed-power implosion. (a) Current flows along the surface of conductive vacuum chamber walls (in dark blue) to, and along, a central cylindrical load (yellow and grey). (b) The produced azimuthal magnetic field as the current flows results in a magnetic pressure radially inwards against the cylindrical load. (c) Under sufficient conditions, such as in a thin foil load, the central region will implode. (Adapted with permission from Fig. 1 in Ref [7].)

Due to the I^2/r^2 dependence, Equation 1.1 shows that very high P_{mag} can be obtained by delivering a large current, I, to a small radius, r. For example, even a modest current of only 400 kA delivered to $r = 5$ μm results in $P_{\text{mag}} = 1$ Gbar. Additionally, the amount of P_{mag} generated can be further enhanced if a radial contraction (or implosion) occurs, since r is further reduced.

The fact that P_{mag} increases as r decreases results in a runaway instability process called the "sausage" instability (or $m = 0$ instability, where m is the azimuthal mode number for the instability structure). This instability has been observed in a number of fast z-pinch configurations [8, 9], including gas-puff z-pinches [10], wire-array z-pinches [11, 12], and dense plasma focuses [13]. In each case, the instability is observed in x-ray self-emission imaging as a series of discrete "bright spots" distributed randomly along the length of the background pinch column (where the background pinch column is usually about 1–2 cm long, and each bright spot has an axial extent of only about 1 mm or less). These bright spots appear in regions where intense pinching has occurred—i.e., where the plasma column has necked down to very small radius (∼microns). These intensely pinched regions are often referred to as "micro-pinches" [14, 15, 16, 17, 18, 19]. It is the behavior and dynamics of these micro-pinches that form the basis of the studies in this dissertation.

1.2 X-Pinches and Micro-Pinches

Micro-pinches compress matter to radii on the order of ∼1 μm, which implies magnetic and material pressures on the order of ∼1 Gbar for very accessible currents of only ∼0.1 MA. The accessibility of such extreme pressures makes micro-pinch plasmas very interesting objects to study for the field of HEDP, particularly in relation to inertial confinement fusion (ICF) efforts. For example, a few Gbar pressure is the same order of magnitude as the stagnated plasma column of a Magnetized Liner Inertial Fusion (MagLIF) experiment on the Z machine [4, 20, 21]. The Z pulsed-power facility at Sandia National Laboratories can provide drive currents upwards of 30 MA [4, 7], which is much larger than the 1–2 MA of a "high-current", university-scale driver. If we now consider the parameters of a micro-pinch on Z, coupling the full 30 MA, the imploded radius to achieve a 1 Gbar pressure is increased significantly from ∼1 μm up to ∼375 μm. Assuming

continued implosion, a micro-pinch on Z could achieve a pressure of 1 Tbar if it compresses to a radius of $\sim$10 μm! Such an HED plasma would be of significant interest towards efforts of ignition within a z-pinch plasma. Of course, there is a caveat: it remains unknown what fraction of the total current supplied by the driver is delivered to the dense micro-pinch plasma at small radii versus that being shunted through the surrounding coronal plasma at larger radii. This dissertation seeks to better understand the current distribution surrounding the dense micro-pinch core and to inform the limits on magnetic pressure.

The study of micro-pinch plasmas is challenging because micro-pinch plasmas are physically small ($\sim$microns), last for very short periods of time ($\sim$ns), and appear at random locations along the length of the background pinch column. To better enable detailed studies of micro-pinch plasmas, an X-pinch configuration can be used [22, 23]. In a typical X-pinch configuration, two or more fine metal wires are crossed in the shape of an 'X'. This forces the micro-pinch to form where the wires cross—i.e., where the system radius is smallest and thus the current density and magnetic pressure is highest, in a predetermined location in space and, to a lesser extent, time. Figure 1.2 illustrates the basic structure of X-pinches and their variations. Additional configurations (not shown) can consist of multiple nested n-wire arrays, where the wires of inner or outer arrays can have diameters chosen to achieve a desired mass density profile at the crossing point [22, 24]. As more wires are added, the conical regions increasingly approximate a full shell, particularly as the wires are pulsed with electrical current, which causes them to ablate and expand with surrounding coronal plasma. A hybrid X-pinch essentially reduces the wire complexity by substituting the conical crossed-wires section with solid conical electrodes, which can either directly connect by a carefully machined cross-point [22, 25] or via a single wire strung between the millimeter-length electrode gap [22, 26, 27].

The X-pinch platform in general has been used previously to characterize micro-pinch plasma parameters via x-ray spectroscopy [22, 23]. Studies on the 450-kA XP pulser at Cornell University have confirmed that micro-pinch plasmas are indeed in the HED regime, with electron temperatures of about 1–3 keV, ion temperatures on the order of 10 keV, and electron number densities on the

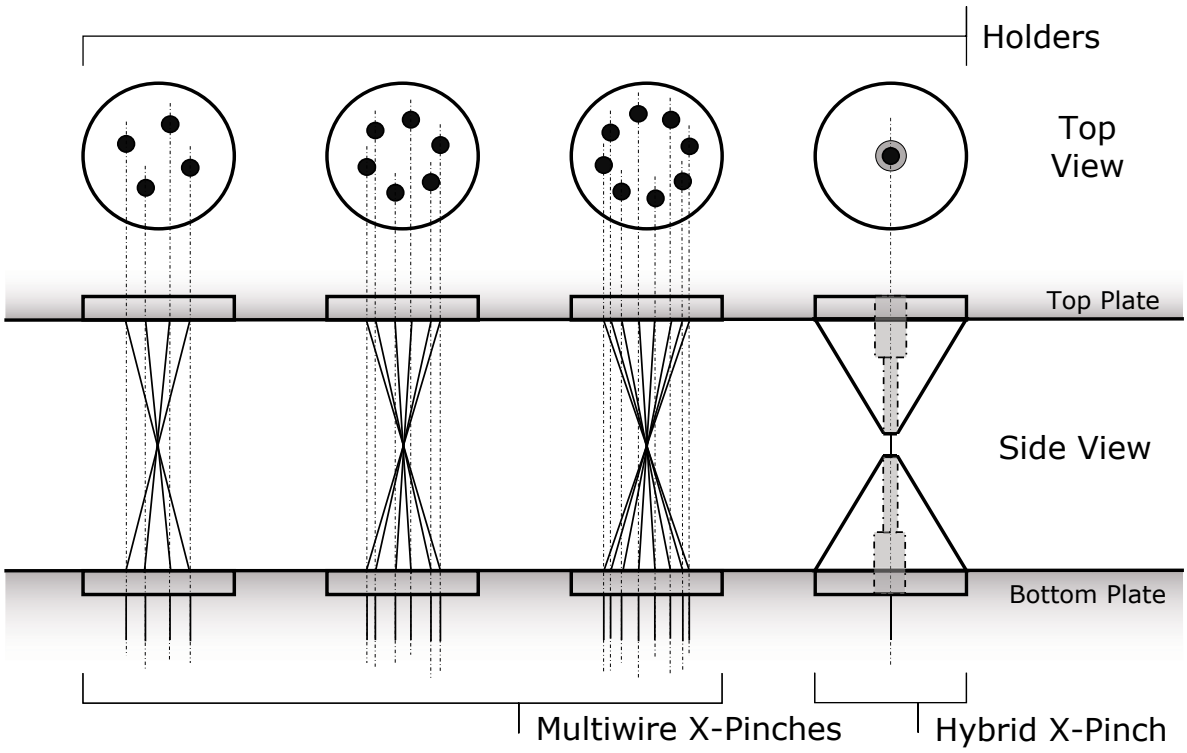

Figure 1.2: Illustration of various wire X-pinches. Multiwire X-pinches are conical arrangements of wire arrays twisted to form a central crossing point. Hybrid X-pinches are essentially the limit in the number of wires where the conical section is replaced by a solid electrode and an axial wire spans the gap in place of a crossing point.

order of 10^{22} cm^{-3} to 10^{23} cm^{-3}, depending on the wire material used [22, 23]. This is equivalent to material pressures ranging from 10 Mbar to >1 Gbar. Furthermore, using x-pinch-based x-ray radiography techniques, the dense cores within the micro-pinch neck-down regions have been imaged with radii as small as a few microns [22, 23]. With all 450 kA delivered to the dense core at $r = 3$ μm, the magnetic pressure would be $P_{\text{mag}} > 3$ Gbar. However, it is possible that some of the load current flows in low-density coronal plasma at radii larger than that of the dense core [28, 29, 30]. This would reduce the magnetic drive pressure applied directly to the core. Thus, it is desirable to measure the load current's radial distribution directly. This motivates the experiments detailed in Chapter 4. By knowing the total current enclosed as a function of radius, $I(r)$, the radial profiles $B(r)$ and $P_{\text{mag}}(r)$ are known via Eq. 1.1.

1.3 The MAIZE LTD

The Plasma, Pulsed Power, and Microwave Laboratory (PPML) at the University of Michigan houses the Michigan Accelerator for Inductive Z-pinch Experiments (MAIZE), a single cavity, low impedance (0.16 Ω) Linear Transformer Driver (LTD) [7, 31, 32]. The MAIZE LTD stores energy in a ring of 40 "bricks" connected electrically in parallel. Each brick consists of two bipolar-charged capacitors separated by a spark-gap switch. At full bipolar charge of the capacitors to ±100 kV, MAIZE stores 16 kJ of energy and is capable of supplying a current pulse of up to 1 MA peak current with a 100 ns rise time when discharged into a matched load. MAIZE is usually run at more moderate charge voltages, ∼ ±60–70 kV, producing currents on the order of 300–600 kA and rise times on the order of 100-200 ns depending on load parameters. Figure 1.3 shows a cross-sectional view of the MAIZE LTD providing a look at the various internal regions. The capacitors (red blocks) and switches (white cylinders) are housed within the highest radius section of MAIZE [Section (1) in Fig. 1.3], which is filled with transformer oil to mitigate electrical breakdowns. The capacitors are discharged, sending current along metal transmission lines within the MAIZE vacuum chamber. The current is diverted into a conical feed region (to raise the target for diagnostic access) where it meets the installed load hardware (e.g., a cylindrical foil or X-pinch load). The various X-pinch

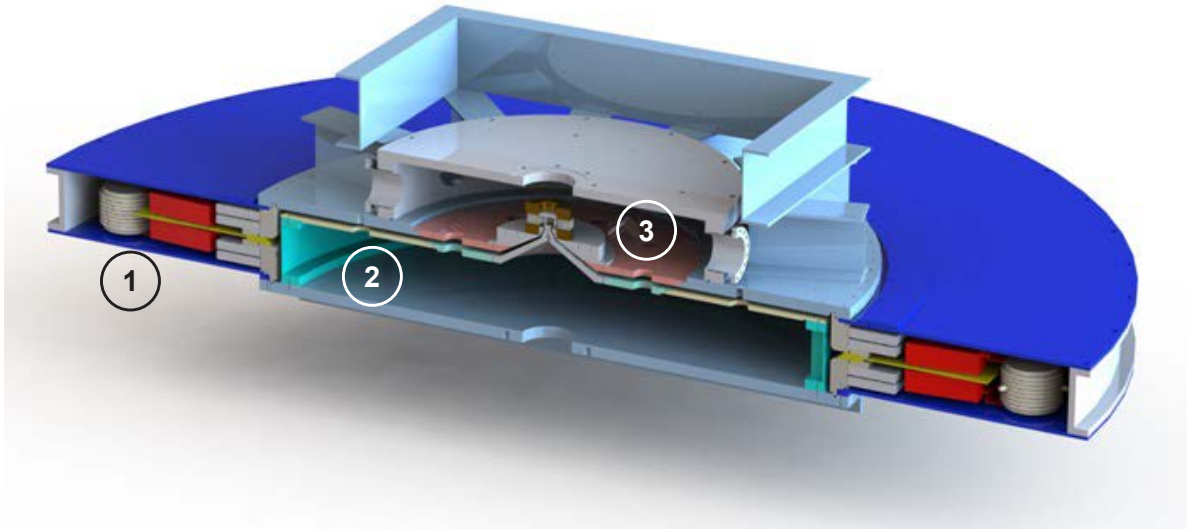

Figure 1.3: Cross-sectional view of the MAIZE LTD showing location of (1) capacitors and switches in oil section, (2) vacuum transmission lines, and (3) vacuum load region.

load hardware are described in Section 3.1.

Comparing MAIZE to other university-based pulsed power drivers further highlights its relative uniqueness in terms of having a low driver impedance. Generators based on Marx-bank architectures typically have innately high impedances, ranging from ∼0.5–2.0 Ω [7]. Of the few university drivers that are also LTD based, the impedances vary. For example, the GenASIS driver at UCSD has an impedance of 0.3 Ω [33], the BLUE LTD at the University of Michigan (described below) has a variable impedance from 0.5–2.0 Ω, and the MACH facility at Imperial College London has an unspecified impedance, but it is likely comparable to that of MAIZE based on the parameters provided in the literature [7, 34]. It is clear that these low-impedance university-based LTDs are relevant to the driver impedance found on the much larger scale Z facility, which has a driver impedance of only 0.18 Ω, despite being a Marx-based system. (Note that the Z facility obtains such a low overall driver impedance by connecting 36 Marx-generator/pulse-forming-line modules in parallel [7].) As such, experiments performed on MAIZE have the ability to inform how such platforms may behave when scaled to the Z facility.

1.3.1 The BLUE LTD

While not presently utilized for X-pinch experiments, the PPML also houses a second LTD facility known as BLUE [7, 35]. BLUE, the Bestowed LTD from the Ursa-minor Experiment, is a four-cavity LTD capable of a 200 kA peak current in a 100 ns rise time. BLUE can be run with any number of its cavities in use (1 to 4), which allows the open-circuit driver voltage to be varied from approximately 100 kV to 800 kV.

This modular stacking could enable investigations into effects of driver voltage and driver impedance on the performance of various z-pinch loads, including X-pinches. This is discussed further in the future work section of Chapter 6.

1.4 Author's Contribution

The bulk of experimental design, execution, calibrations, and analyses were completed by the author. Contributions to machine maintenance and experimental aid, performed by various members of the PPML, were indispensable to the completion of this work. Several collaborations were additionally invaluable to the design and implementation of the presented experiments. The Faraday rotation imaging diagnostic presented in Chapter 4, based on the diagnostic fielded on the MAGPIE generator by Dr. George Swadling [36], was designed and adapted to MAIZE by the author with discussion and advice from Prof. Sergey Lebedev, Prof. Roland Smith, Dr. Simon Bland, and Dr. Lee Suttle of Imperial College London. Sourcing of the deuterated polyethylene fiber for the experiments detailed in Chapter 5 was through Prof. Daniel Klir of Czech Technical University in Prague. Members of his group, Dr. Karel Rezac and Jan Novotny, provided aid in the fielding and troubleshooting of neutron diagnostics during the experimental collaboration.

CHAPTER 2

X-Pinch Evolution and Instabilities

2.1 X-pinch Evolution

The overall dynamics of an X-pinch during an experiment is illustrated by Fig. 2.1. As current is delivered to the wires, they begin to ablate plasma around the remaining cold, dense wire core. With sufficient ablation and magnetic pressure, the crossing point of the wire begins to form a plasma "neck" region that mimics a miniaturized z-pinch, as illustrated in Fig. 2.1(5). Jets of plasma also begin to form along the cylindrical axis just above and below the central wire crossing point. These jets propagate axially upwards and downwards (away) from the central wire-crossing point. Eventually, the plasma neck goes unstable and results in a cascade of necks with increasing order (increasingly smaller spatial scales), as shown in Fig. 2.1(11). This cascade continues until a few ($\sim$1–3) micro-pinches are formed from the highest order necks. These micro-pinches form what are generally referred to as "hot spots", in reference to the bright sub-ns burst of thermal x-rays generated from them. After the formation of the hot spot (Fig. 2.1(8)), the neck cascade breaks and forms a diode region (Fig. 2.1(9)), causing the formation of electron and ion beams (Fig. 2.1(10)), which generate harder bremsstrahlung radiation. Figure 2.1 depicts a two-wire X-pinch for clarity. By contrast, in a hybrid X-pinch, the single wire begins in an axisymmetric geometry. This wire then ablates and begins to fill the gap between the electrode cone tips with low-density wire material (vapor and plasma). Both multiwire and hybrid X-pinches were studied for this dissertation. dissertation. Note that the time scale indicated in Fig. 2.1 is depended on the driver characteristics and the linear mass of the wire loads. For the experiments of this dissertation,

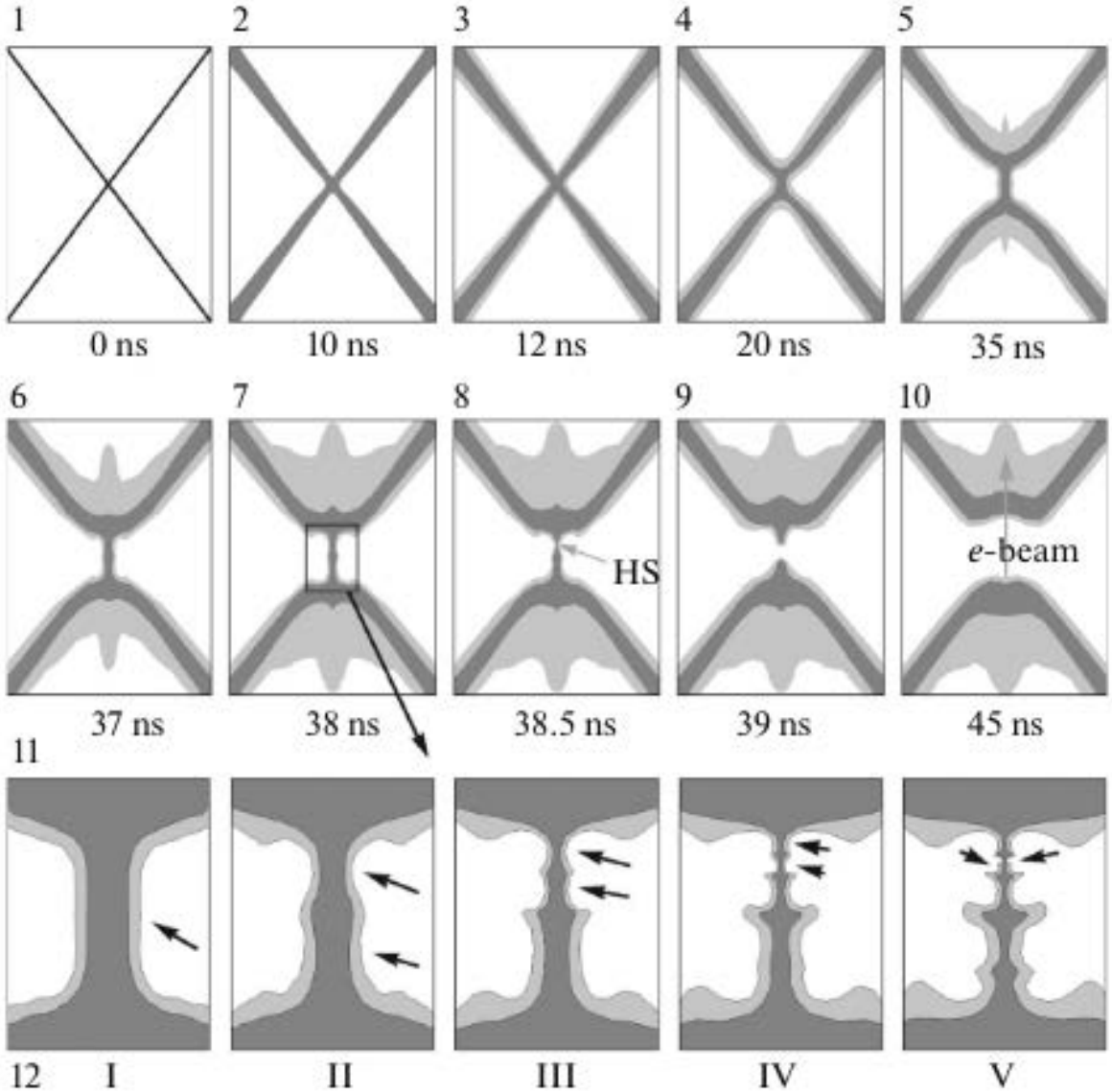

Figure 2.1: A graphical depiction of X-pinch evolution showing (1–5) initial wire ablation and neck formation, (6–7) initial pinching of the neck plasma, (11–12) the rapid cascading of the neck and the relative order of the cascade, (8) formation of the hot-spot, HS, (9–10) breaking of the plasma neck and production of electron and ion beams. Reprinted from S. A. Pikuz, T. A. Shelkovenko, and D. A. Hammer, "X-pinch. Part I," *Plasma Physics Reports*,vol. 41, pp. 330, Apr. 2015, with permission from Springer Nature.

which were conducted on MAIZE, the temporal duration was about 2–3$\times$ that shown in Fig. 2.1.

2.2 Instabilities of the Neck Cascade

The instability of the neck and runaway cascading is caused by a combination of multiple instabilities, of which the $m = 0$ magnetohydrodynamic (MHD) instability mode is dominant. Figure 2.2(a) shows a z-pinch column in equilibrium. In this case, the outward force resulting from the plasma pressure within the column is in balance with the inward force generated by the external magnetic pressure. If we assume that the plasma is isothermal, with a pressure of $P(r) = n(r)k_{\mathrm{B}}T$, then this geometry is also known as a Bennett Pinch, and the steady state is given by the equation:

$$N_{\mathrm{i}}(1 + Z_{\mathrm{eff}})k_{\mathrm{B}}T = \frac{\mu_0 I^2}{8\pi}, \tag{2.1}$$

where N_{i} is the ion number per unit length, Z_{eff} is the effective atomic number, T is the plasma temperature (assumed $T = T_{\mathrm{e}} = T_{\mathrm{i}}$), and I is the total current [37, 38]. Let us also assume that the plasma column has an equilibrium radius, R. This equilibrium is unstable.

Figure 2.2(b) shows the $m = 0$ mode, also called the "sausage" instability, where $m = 0$ indicates that the structure is azimuthally symmetric. Here we have some azimuthally symmetric perturbation of the plasma column, such as a slight drop in density along a section of the column. This causes a pressure imbalance in that region, and the magnetic pressure can begin to bite into the column. For an incompressible plasma, material is displaced from the compressed regions into the adjacent bulging regions. The region perturbed to smaller than the equilibrium radius ($r < R$) sees an increased magnetic pressure (*cf.* Eq. 1.1). This only adds to the force imbalance and increases the perturbation. Conversely, the bulge at larger than the equilibrium radius ($r > R$) sees a decreased magnetic pressure, allowing the material pressure to overcome the magnetic pressure and allow the bulge to increase its amplitude outward. As stated, it is this instability mode that is dominant within the destabilization of the X-pinch neck and has been observed extensively.

The higher order $m = 1$ helical mode, called the kink instability [37], has also been observed

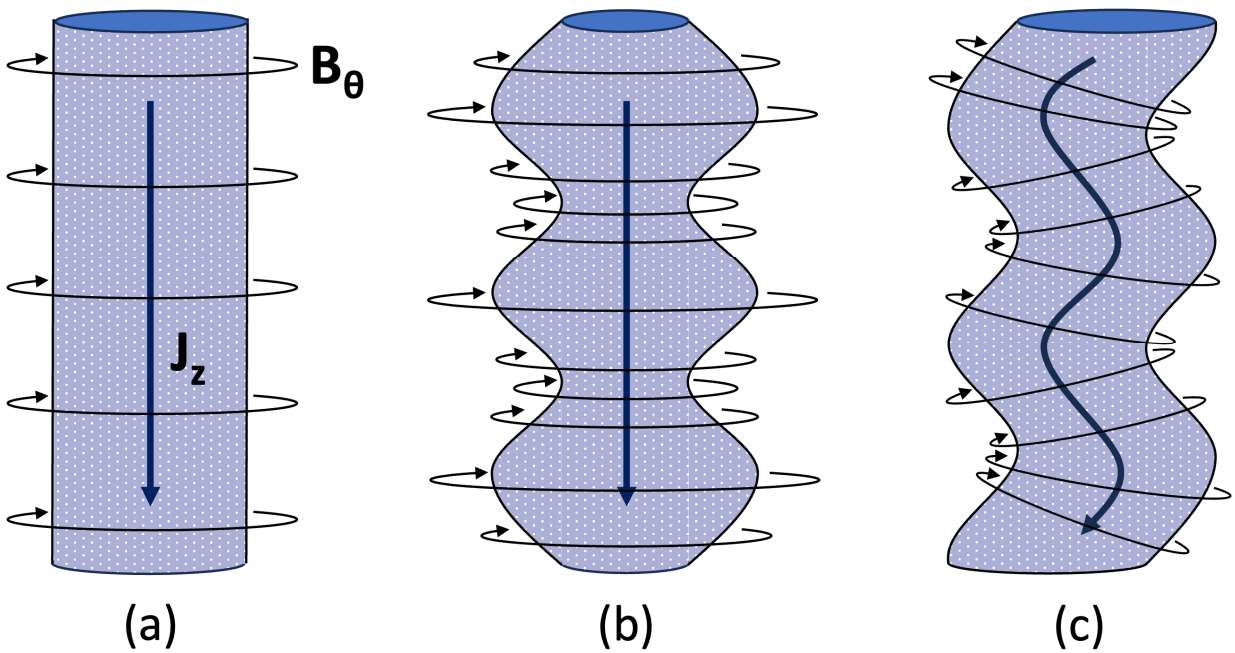

Figure 2.2: Simple illustrations showing the current and magnetic field structure of common MHD instabilities. (a) A plasma column in equilibrium with a uniform structure. (b) The $m = 0$ "sausage" instability showing bunching of field lines around the constriction points. (c) The $m = 1$ "kink" instability showing the gradient in the density of field lines across the perturbation.

in X-pinch necks, though it does not contribute to the cascade to smaller radii directly. Here we have the plasma being translated off-axis from the main column creating a "kink." In Fig. 2.2(c) we can see that the kinking creates a magnetic pressure gradient across the plasma. On the inner concave side of the kink there is a bunching of magnetic field lines, indicating an enhanced field strength from equilibrium. On the opposite bulge, there is conversely a spreading of the field lines and a lower magnetic field strength. This difference translates to a pressure gradient in the direction of the bulge, meaning that the perturbation will grow. This in turn increases the pressure gradient across the kink and continues in a positive feedback loop. While Fig. 2.2(c) appears as a rather planar, wavy structure, in three dimensions this creates a helical perturbation which can be seen, for example, in many of the radiographs of X-pinch necks presented in Ref. [22].

Lastly, while likely not a significant source of the instability growth within an X-pinch, the Magneto-Rayleigh-Taylor (MRT) instability likely occurs concurrently with the $m = 0$ mode, amplifying the instability growth in the formation of the micro-pinch. At its core, MRT is an analogue of the Rayleigh-Taylor (RT) fluid instability [37, 39, 40]. Here, the instability occurs when a denser fluid is balanced in an unstable equilibrium on top of a lighter fluid under an external acceleration, such as gravity, g. More generally, a pressure gradient is opposing a density gradient for an RT unstable system. This is translatable to the MHD case where the lighter fluid can also be replaced by magnetic pressure, as in the case of an imploding liner [15, 37, 41]. When the equilibrium interface is perturbed, similar to the $m = 0$ mode, "spikes" of plasma and "troughs" of vacuum form along the interface. As the net potential energy of the perturbed state is lower than the equilibrium state, the spikes and troughs continue to grow. For the case where the wavevector, $\mathbf{k}$, is perpendicular to the magnetic field, and thus $\mathbf{k} \cdot \mathbf{B} = 0$, the MRT growth rate is well known to be $\gamma_{\mathrm{MRT}} = \sqrt{kg}$ [37, 41], which is the case for an X-pinch with an axial perturbation and an azimuthal magnetic field. However, the MRT instability plays a larger role in systems that implode with larger overall convergence ratios—e.g., gas-puff z-pinch implosions. Nevertheless, the MRT bubble and spike-like structures that form during a large convergence ratio implosion can still influence the micro-pinch process by seeding the axial locations and initial conditions of the micro-pinches. For

example, in a typical gas-puff z-pinch, micro-pinches form along the pinch axis where the MRT bubbles stagnate on axis. This occurs because these axial locations are the first locations to have current transferred to the axis.

In an X-pinch, the seeding of these instabilities can arise from the X-pinch geometry itself. In a multiwire configuration, the crossing point is inherently azimuthally nonuniform due to its construction out of finite wires. The wires themselves are subject to the tolerances of their manufacturing, likely having slight variations in radius and material composition along their length. In a hybrid configuration, the initial state of the single wire allows for the control of greater symmetry, but it is still subject to inherent inhomogeneity within the wire. All of these factors will lead to variations in ablation and in the structure of the plasma column before it implodes.

2.3 Radiative Collapse and Micro-Pinch Compression to Small Radius

The mechanism that allows for the formation of such a small ($\sim$microns) and hot ($>$1 keV) micro-pinch plasma is still debated; however, a longstanding theory is that the implosion to minimum radius is driven by radiative collapse [38, 42, 43]. The process of radiative collapse occurs when the thermal pressure is decreased through radiation losses in a dense plasma such that it can no longer withstand the compressive forces of the the magnetic field. These radiation losses are primarily due to bremsstrahlung (free-free) and, for high-Z plasma, line radiation. The following derivation outlines a simplified version of the that given in Ref. [38].

We start with a plasma in equilibrium as defined by Eq. 2.1. We also assume that Joule heating is balanced by radiation losses. Furthermore, within the plasma column, we assume a constant current density given by

$$J(r) = \frac{I}{\pi R^2}, \tag{2.2}$$

and a Spitzer conductivity given by

$$\sigma = \frac{\sigma_0 T^{3/2}}{Z_{\text{eff}} \ln \Lambda}, \tag{2.3}$$

where $\ln \Lambda$ is the Coulomb logarithm and T is in units of eV. The Joule heating rate per unit length

is then given by

$$P_{\text{Joule}} = 2\pi \int_0^R \frac{J^2}{\sigma} r\mathrm{d}r = 3.3 \times 10^9 \frac{Z_{\text{eff}} \ln \Lambda}{T^{3/2}} \frac{I^2}{R^2} \left[\frac{\text{W}}{\text{cm}}\right], \tag{2.4}$$

where T is in eV, I is in MA, and R is in cm.

For radiation losses we will consider only bremsstrahlung in an optically thin plasma, but this is primarily only valid for a hydrogen plasma, as a higher Z plasma would require the inclusion of line radiation. The radiative power density for bremsstrahlung is defined as

$$D_{\text{ff}} = X_{\text{ff}} n_{\text{e}} n_{\text{i}} \left[\frac{\text{W}}{\text{cm}^3}\right], \tag{2.5}$$

where

$$X_{\text{ff}} = 1.4 \times 10^{-32} Z_{\text{eff}}^2 T^{1/2} \left[\text{W cm}^3\right]. \tag{2.6}$$

Combining with Eq. 2.1 provides an expression for the bremsstrahlung radiation loss per unit length:

$$P_{\text{ff}} = 2\pi \int_0^R X_{\text{ff}} n_{\text{e}} n_{\text{i}} r\mathrm{d}r = 4.3 \times 10^{10} \frac{Z_{\text{eff}}}{T^{3/2}} \frac{I^4}{R^2} \left[\frac{\text{W}}{\text{cm}}\right], \tag{2.7}$$

for $Z_{\text{eff}} \gg 1$ (such that $(1 + Z_{\text{eff}}) \approx Z_{\text{eff}}$ in Eq. 2.1).

Equating these gives the formula for the Pease-Braginskii current,

$$I_{\text{PB}} = 0.27 \left(\ln \Lambda\right)^{1/2} \left[\text{MA}\right], \tag{2.8}$$

at which a higher current without temperature increase will cause the magnetic pressure to dominate. For a Coulomb logarithm of $\ln \Lambda \sim 10$, the critical current is $I_{\text{PB}} \sim 1$ MA. When the critical current is surpassed, and the magnetic pressure overcomes the thermal pressure, the plasma column decreases in radius, thereby increasing the density. As we saw in Eq. 2.5, bremsstrahlung is dependent on the square of the density and only increases as the column continues to contract. Eventually, this runaway process is overcome at some minimal radius due to the combination of increased opacity and radiation transport effects, as well as electron degeneracy pressure [38, 43]. As this was a

simplified derivation, this estimate of the Pease-Braginskii current really only gives an estimate of the current scale. For example, the inclusion of line radiation to better match high-Z plasma, where power loss from line emission can exceed bremsstrahlung losses, would lower the threshold [38]. Additionally, this assumed an equilibrium plasma state, uniform current density, and Spitzer conductivity, all of which likely break down—or were never accurate—as the plasma approaches high density and minimal radius.

2.4 Recent Work and an Alternative Theory

Simulation work by Chittenden *et al.* have modeled the formation of micro-pinches within an X-pinch plasma [44] using the GORGON MHD code [45] giving good agreement of the evolution to experiment. More recent simulations using GORGON, with improvements such as improved radiative loss models and mesh refinement to capture the fine scale of the cross-point, have been conducted providing further support to a radiative-collapse-driven micro-pinch [46, 47].

Recent experimental work at Cornell University, however, has begun to prompt a re-examination of whether radiative collapse is the likely process [48, 49]. This is due to the lack of K- or L-shell emission immediately prior to the formation of the micro-pinch hot-spot, implying that the plasma neck remains too cold to strongly radiate until very close ($<$100 ps) to micro-pinch formation. Simulations were performed using PERSEUS, an extended MHD code [50], to support the experimental observations [49]. What the simulations showed was that the hot spot is not formed from the radiative collapse of the dense neck. Instead, the dense, cold ($<$100 eV) core is ejected axially as the neck is compressed, allowing for the cascading $m = 0$ instabilities to compress a low-density coronal plasma on axis, forming the micro-pinch which rapidly increases to keV temperatures. These simulations also predict that only a very small portion of the total current ($\sim$120 kA) is delivered into the micro-pinch at minimal radius ($\sim$3 μm). If correct, this would have significant implications on the maximal pressures achievable by an X-pinch platform.

CHAPTER 3

X-Pinch Experimental Platforms

3.1 MAIZE X-Pinch Load Hardware

Design considerations for the X-pinch load hardware on the MAIZE LTD included: (1) ease of load installation, (2) diagnostic access, and (3) the ability to modify or install new hardware without the redesign of bulk elements. The resulting design, pictured in Fig. 3.1(a), utilized changeable inserts and return posts to allow for easy exchange between different configurations. Varying the length of the return current posts allows for tailoring of the A-K gap spacing and the wire-crossing angle. Initial inserts to field 4-, 6-, and 8-wire, as well as hybrid X-pinches, were designed and fabricated with 3 mm diameter wire feedthroughs (to allow for clearance of attached weights)

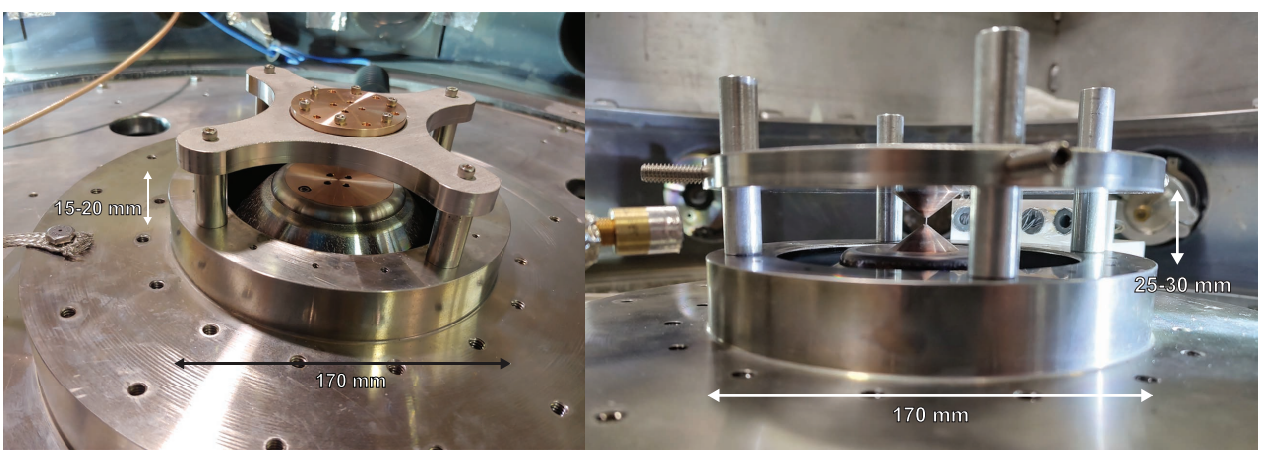

(a) (b)

Figure 3.1: Pictures of the X-pinch load hardware installed within the MAIZE vacuum chamber. (a) The original design with a 4 × 35 µm Mo X-pinch loaded into the WCu insets. (b) The modified load hardware for adjustable hybrid X-pinch experiments. A 200 µm Nylon hybrid X-pinch is loaded between the WCu inserts with a 2 mm electrode gap.

positioned at $r \approx 6$ mm. The anode post heights were selected to obtain A-K gaps of 10, 13, 15, or 21 mm. The hybrid insert was initially designed using the 21 mm posts to leave a fixed $\sim$2 mm gap between the cone tips for the wire load; however, this was later modified to a variable gap structure as pictured in Fig. 3.1(b). This modification of the anode plate is similarly compatible for any type of X-pinch. Overall, the inserts have been robust in allowing a variety of X-pinches throughout this dissertation work, and they can easily be expanded upon in the future, with such designs as a double X-pinch insert for reciprocal radiography.

The inserts themselves are made of a 70:30 W:Cu alloy due to its high electrical conductivity and resistance to ablation under arc discharges. This is primarily useful in the fielding of hybrid X-pinches, in which the conical tips are severely stressed and would ablate rapidly with weaker materials. Two sets of hybrid inserts were fabricated and have been fielded for 40 experiments in total, roughly 20 each, and are still intact. Similarly, one copy of each multi-wire insert type was made and, besides mild surface pitting and ablation by axial jets seen in Fig. 3.2, have seen minimal ablation around the wire contacts. The only clearly noticeable ablation at the wire contacts is on the 4-wire inserts, which have been fielded on over 90 X-pinch experiments.

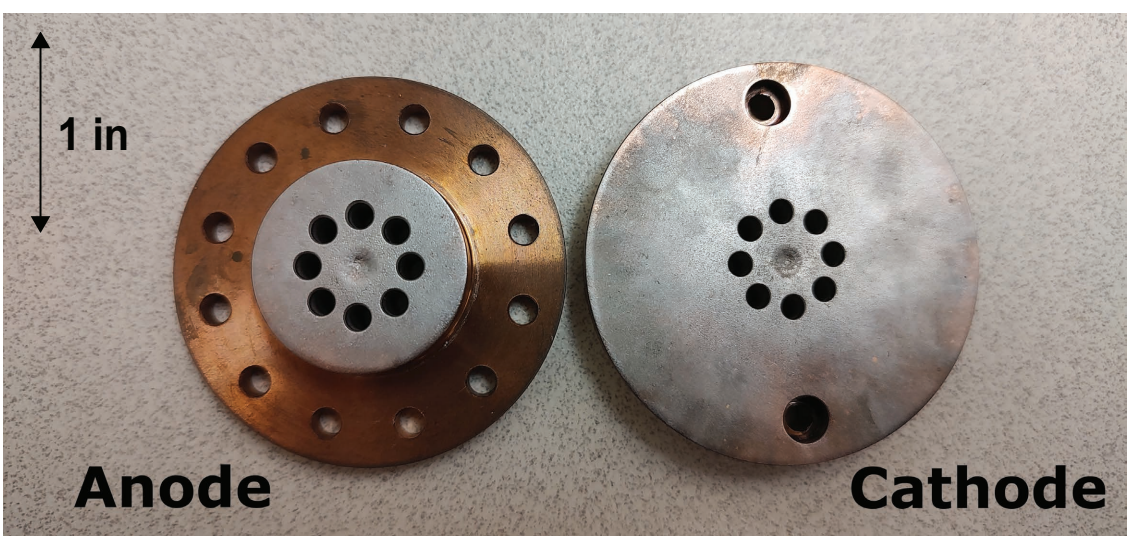

Figure 3.2: Photograph showing the wear on the electrode surfaces after $\sim$10s of shots. Metal deposition and roughening of the electrode surfaces are present in roughly equal fashion on both the anode and cathode sides. Also note the central pitting. This is caused by axial plasma jets, which form from ablated wire material (coronal plasma) being swept to the central axis and then jetting axially upward or downward (away) from the central wire-crossing point.

3.1.1 Prior Hardware

A brief mention should be made of prior versions of X-pinch hardware that have been fielded on MAIZE, which informed decisions for the experiments detailed by this dissertation. The first hardware was the original main load X-pinch hardware for a variation of the MAIZE transmission lines that terminated in a vertically planar geometry [51, 52, 53]. It was designed as a test for later use of X-pinches as radiographic back-lighters for foil loads and ran Mo and Al hybrid X-pinches. The present location of this hardware or further results of the experiments are unknown.

The second X-pinch hardware is the radiographic hardware. This hardware fields return-current X-pinches for the purpose of multi-X-pinch main-load radiography. Figure 3.3 shows the second iteration of the hardware. As can be seen, the hardware is comprised of two circular steel sheets with 30 cm diameters where six circular cutouts are symmetrically located around the central load region. These are to hold inserts that allow for switching between X-pinch types similar to the same capability on the main load hardware. The first iteration of the hardware was near identical, save for having eight circular cutouts for inserts on the top plate, and eight sets of four holes on the bottom plate, presetting the X-pinch geometry. The center portion of the hardware in both iterations was

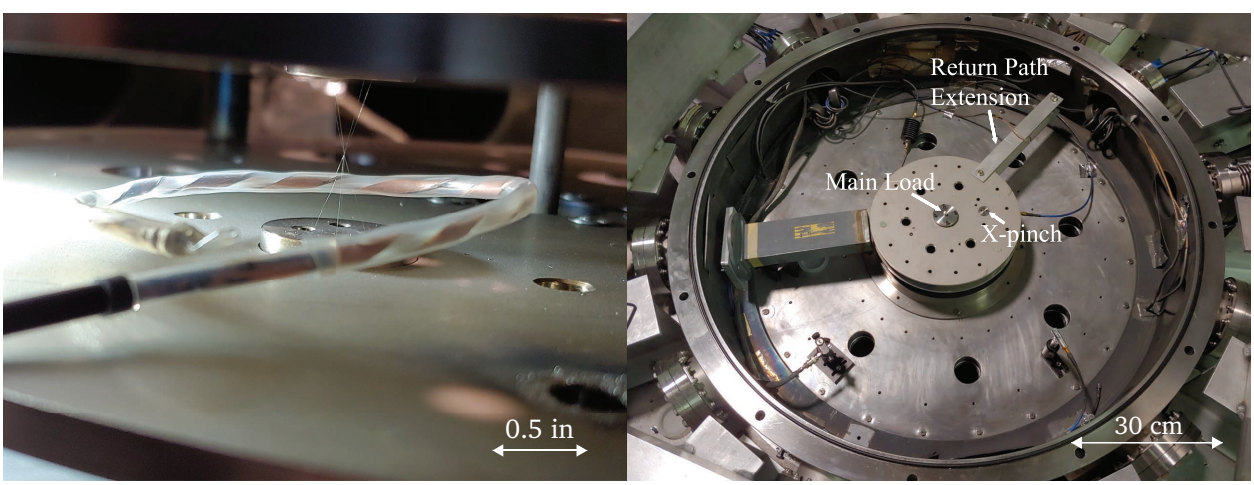

(a) (b)

Figure 3.3: Pictures of the X-pinch radiography hardware for the MAIZE LTD. (a) A 4-wire X-pinch loaded into one of the insert locations with a Rogowski coil to monitor the fraction of current it receives. (b) A view of the MAIZE vacuum chamber where the radiography hardware and return current post extension can be seen.

designed to hold a cylindrical foil load for radiography via the return path X-pinch(es).

Unfortunately, the radiographic hardware was unable to drive X-pinches as designed. Figure 3.3(b) shows the return current post extension that we attached to move the solid return post (only one was installed, the remainder were replaced with dielectric supports) to nearly the edge of the MAIZE vacuum chamber. This was due to current preferentially choosing the solid return current posts, even at their locations at larger radii than the X-pinch, due to the path's lower inductance. Reducing the return path to a single post, Rogowski coils were used to determine that the current distribution was roughly 2:1 between the return post and the X-pinch. Due to a low drive current from a poorly operating MAIZE at this time, this current split was delivering an insufficient fraction of current to the X-pinch. Moving the single return post to larger radius via an extension nearly to the edge of the vacuum chamber ($\sim$45 cm) increased the inductance sufficiently to redistribute the current to another ratio of 2:1, but in favor of the X-pinch over the return post. This configuration produced the first successful pinching on the hardware as confirmed by XUV imaging. However, due to the extreme modification necessary to achieve this goal with a singular X-pinch, the hardware was determined nonviable without significant redesign. Even with nominal MAIZE operation, better care in accounting for the inductive and resistive differences between the two paths is necessary before the fielding of multiple X-pinches would be viable.

3.2 Diagnostic Platforms

This section looks to outline the main diagnostic capabilities of MAIZE relevant to fielded X-pinch experiments. Figure 3.4 gives an example arrangement of diagnostics present on MAIZE surrounding the main load X-pinch hardware (additionally, see Fig. 5.1 for visualization of additional diagnostics).

3.2.1 Current Measurement

Current measurements on MAIZE are primarily performed via Rogowski coils. The main coil on MAIZE is 69 cm long with 34 turns and is embedded within a grove at the base of the conical

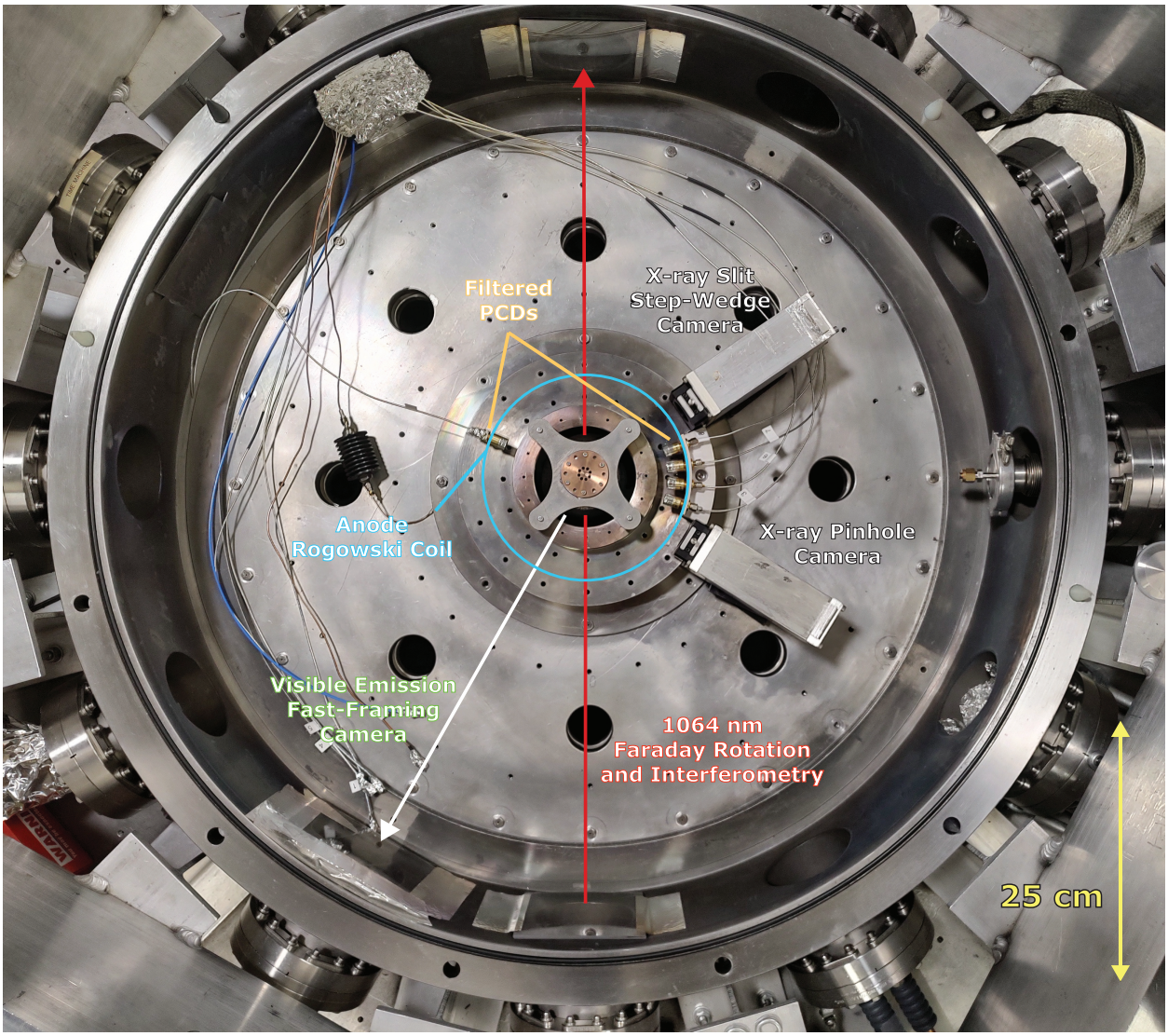

Figure 3.4: An example of a typical in-chamber diagnostic setup for an X-pinch experiment. Shown are the locations and distances used for fielding of x-ray diagnostics (PCDs, x-ray cameras), the main anode Rogowski coil, and typical lines of sight for laser and visible imaging through available vacuum port windows.

section of the anode transmission line [54]. As this still has some transmission line left between the coil and the load, the Rogowski coil measurement is really only an estimate of the load current in the assumption that there is no arcing after the coil and before the load. The current measurements from the anode Rogowski coil are almost always reliable past current peak, but it may fail or indicate a crowbar effect upon current fall.

3.2.2 Laser Diagnostics and Fast Framing Camera

PPML's diagnostic laser source is an Ekspla NL122 Nd:YAG laser with a fundamental 1064-nm output of up to 300 mJ, a frequency-doubled 532-nm beam (125 mJ), and a frequency-tripled 355-nm beam (80 mJ). The single-pulse output has a duration of 2 ns with a jitter of 0.5 ns. Due to instability and failure of laser system components, the output energies currently are typically limited to maxima of $\sim$35 mJ in 1064-nm and 200 μJ in 532 nm. The output pulses of the Nd:YAG laser are used for a number of diagnostics.

The second harmonic is used for laser Schlieren, shadowgraphy, and interferometric imaging. Multi-frame Schlieren and shadowgraphy imaging are achieved by sending the 2 ns pulse through a 15 ns optical relay that shaves off 5% of the beam energy per cycle [54]. The resulting pulses are then sent through the target and are recorded by an Invisible Vision Ultra UHSi 12-frame fast framing camera. A single-frame interferometry image can be taken using either the entirety of the laser pulse or the discarded energy of the optical relay ($\sim$90% of the total beam energy). The first harmonic is primarily used for the Faraday rotation imaging diagnostic. Details of the diagnostic are given extensively in Chapter 4. The third harmonic of the laser remains unused for the work presented in this dissertation.

Additionally, the fast framing camera can be utilized without coupling to laser pulses for recording visible self-emission sequences of the X-pinch implosion. The Invisible Vision Ultra UHSi 12-frame fast framing camera is capable of up to 200,000,000 frames per second and minimal exposure lengths down to 5 ns. This allows for both focused imaging of the main neck development or a broad record of the X-pinch plasma throughout the duration of the MAIZE current pulse.

3.2.3 XUV Imaging

Imaging into the ultraviolet is available through an extreme ultraviolet (XUV), time-gated, four-frame, micro-channel-plate (MCP) pinhole camera [54]. The light is imaged via 100 μm pinholes onto the 4-way-split MCP, where each section is individually biased. The XUV camera's four frames are set for 15 ns inter-frame spacing and can be set for 5, 10, or 15 ns exposures, here run with a 5 ns exposure. The electrons from the MCP frames are then incident on a visible phosphor screen which is then imaged by a Canon Rebel XTi DSLR. The object-to-pinhole, p, and pinhole-to-image, q, distances used were p = 54.5 cm and q = 20.0 cm. This results in a minimal geometric resolution of 370 $\pm$ 20 μm for photon energies above $\sim$22 eV.

3.2.4 X-ray Imaging

To allow for x-ray imaging, a new x-ray camera was designed that allows for modular fielding in terms of pinhole size and shape, magnification, and filtering. Appendix B provides the schematic details of the diagnostic. Essentially, the design is a rectangular body that on one end has a slot to insert a film with 1" $\times$ 2" exposable area within a holder, and on the other mounts a Thorlabs CFH2 filter holder for 1" mounted optics. The holder allows for easy installment of various sized pinholes and slits for different imaging purposes. Here, the x-ray cameras generally took two configurations. The first was an x-ray pinhole camera with a 50 μm pinhole for direct x-ray imaging of the X-pinch, and the second was a slit step-wedge using a 50 μm $\times$ 10 mm slit for single axis spatial resolution and spectral resolution through filtering. For both, the object-to-aperture distance was p = 139 $\pm$ 1 mm. The pinhole-to-image distance for the pinhole camera was q = 148.5 $\pm$ 0.5 mm, and the slit-to-image distance for the slit step-wedge camera was slightly longer at q = 149.7 $\pm$0.5 mm to account for the added filter packet. Figure 3.5 shows the assembled housing with both aperture and film holders, as well as an image and graphical layout of the filters used for the step-wedge. The slit step-wedge works by placing the slit perpendicular to the X-pinch (or other load's) primary axis—i.e., the slit is horizontal in the case of an X-pinch on MAIZE, with the filter variation similarly in the horizontal direction. This results in images with spatial resolution in the

vertical (axial) direction and spectral information in the horizontal direction. For an X-pinch, this means time-integrated measurements of the x-ray spectrum can be resolved along the X-pinch neck. The geometric resolution for the parameters provided is $L_{\text{geo}} = 96.4 \pm 5.8$ µm. The resolution of the pinhole camera is equivalent within 0.5 µm.

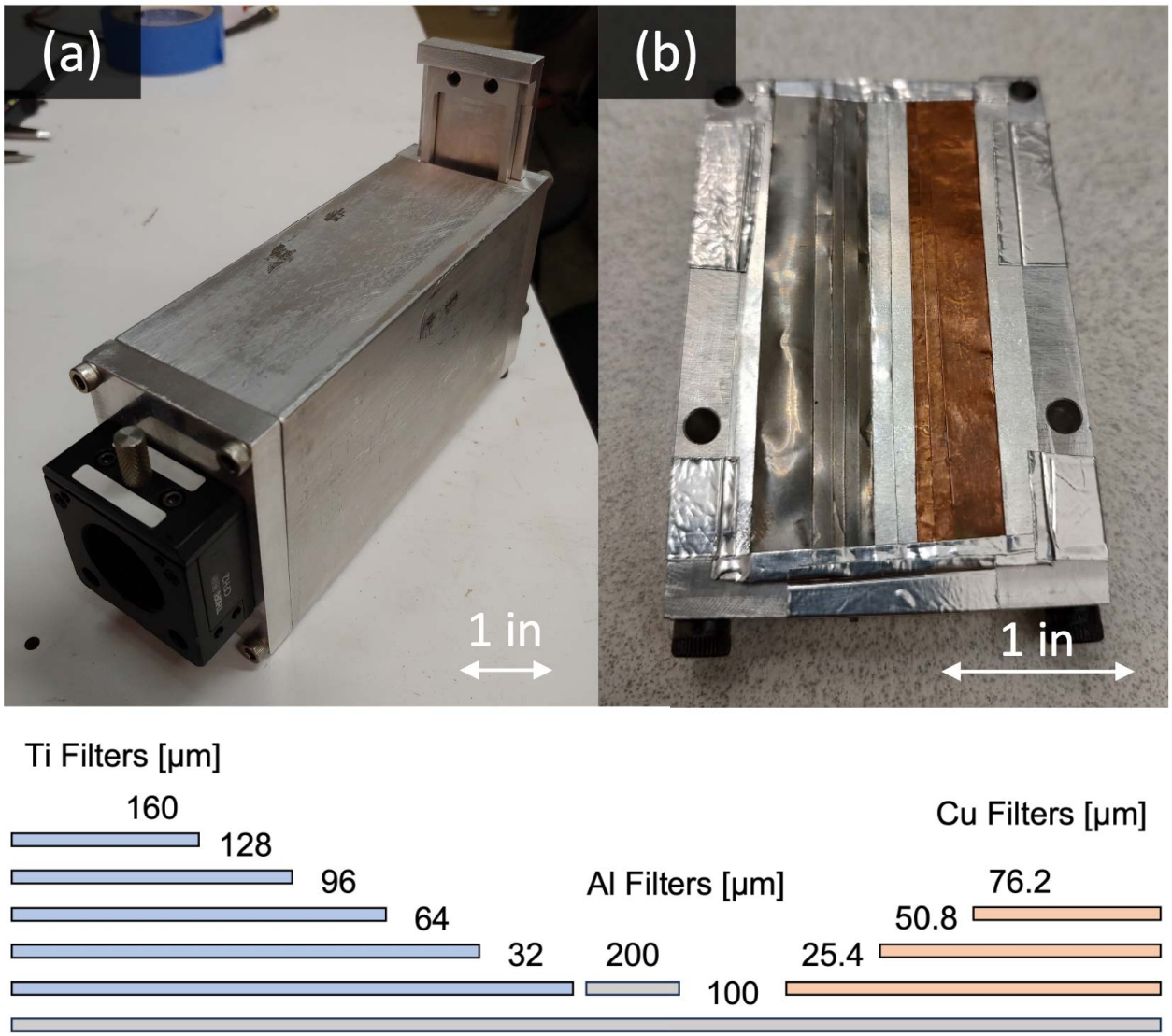

Figure 3.5: (a) Image of the X-ray camera housing additionally showing a half-inserted filter holder. The front aperture holder contains the relevant pinhole or slit for the desired diagnostic. (b) The removed back panel of the camera body showing the attached step-wedge filters. These sit between the end of the body cavity and in front of the filter holder groove in the back panel. A graphical view of the filters is provided. Values represent the total thickness of the same-material layers. For example, the far right filter would be read as 76.2 µm Cu + 100 µm Al.

3.2.5 Poly-Crystalline Diamond Detectors

Timing diagnostics are essential for X-pinch experiments to measure when the bright x-ray burst occurs. MAIZE utilizes a suite of five poly-crystalline diamond (PCD) detectors for use in time-resolved measurements. These consist of a 1 mm $\times$ 3 mm $\times$ 0.5 mm diamond held between two electrodes that, when exposed to x-ray emission, becomes conductive creating a response signal. For simple timing measurements, a single PCD, filtered with 20 µm Kapton film, is fielded at a known source-to-detector distance and provides an accurate fiducial for the time of maximal compression. This is then used to inform the timing of laser diagnostics. Additionally, a set of filtered PCDs can be fielded to investigate the temporal emission of harder x-rays. These can simultaneously be constructed to act as Ross filter pairs for basic energy binning [55, 56]. The typical filters used and their transmissions are shown in Fig. 3.6. Since the copper filter is quite fragile, it is often omitted in experiments where its associated energy binning is not needed.

Additionally, the MAIZE PCDs were previously uncalibrated. To allow for evaluation of the emission yields, the calibration factors for the MAIZE PCDs were found by comparison to a known

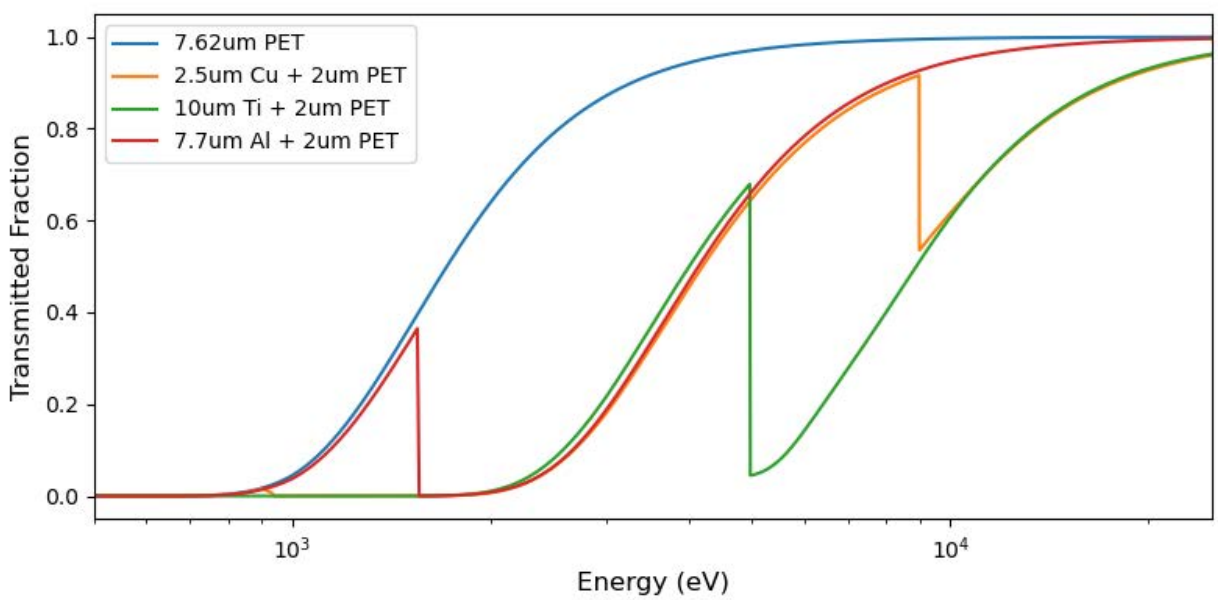

Figure 3.6: Graph showing the transmitted fraction of x-rays as a function of photon energy through the various filters used for the MAIZE PCDs.

calibrated PCD (fielded on COBRA at Cornell University [57]) through a series of co-fielded experiments. The results are tabulated in Table 3.1 and are valid for a bias voltage of -100 V.

PCD	**Calibration Factor [$\frac{\mathbf{mA}}{\mathbf{W}}$]**
A	1.1 ± 0.1
B	0.9 ± 0.1
C	2.0 ± 0.1
D	1.4 ± 0.1
E	1.3 ± 0.1

Table 3.1: Calibration factors for the MAIZE PCDs when biased to -100 V. PCDs are fielded at a source-to-detector distance of 10 cm, have an area of 3 mm^2, and are 50 Ω terminated.

3.2.6 COBRA X-ray Crystal Spectrometer

Due to constraints on the fabrication of an x-ray crystal spectrometer for the MAIZE facility, the choice was made to borrow one from Cornell University, though it did create vacuum issues when coupled to the MAIZE chamber. The original intention of fielding this diagnostic was to provide an estimate of the density and temperature (and therefore material pressure) to compare with the magnetic drive pressures determined from Faraday rotation imaging. Measurements were made using a 50 mm $\times$ 15 mm Quartz 10-11 crystal with a radius of curvature of 180 mm. The crystal was chosen as it allows for imaging of multiple lines of both silver and molybdenum. Unfortunately, the silver spectra had very low signal, which was partially expected, though one or two were potentially usable. The molybdenum had a much stronger signal, though only two were recorded before the diagnostic was removed. A significant background signal, potentially strong bremsstrahlung emission, was present despite the use of a 12-μm aluminized Mylar filter. Currently, full results of these spectra have not been processed, but the diagnostic is mentioned here for completeness and as

an indication of possible future directions.

3.2.7 Neutron Diagnostics

Over the past year, neutron diagnostic capabilities have been built up for the MAIZE LTD, but capabilities remain limited. The present state of neutron diagnostics are further discussed separately within Section 5.2.1.

3.3 X-Pinches Driven on MAIZE

The behavior of X-pinches on MAIZE was not well understood at the beginning of this work. Continued issues with low MAIZE current (100–200 kA) following its rebuild in 2018–2019 made it increasingly difficult to characterize the response of MAIZE to an X-pinch. Early experiments to find reliable X-pinch configurations that were well suited for coupling with laser probing were consequently starting within an entirely different parameter space. The standard X-pinch configuration initially chosen was one with two 25-µm-diameter Ag, Mo, or W wires, with a wire crossing angle of 70° (slightly taller than wide). This configuration gave the greatest repeatability of a clear neck region and a sharp x-ray burst (implying nominal pinching to minimal radius) for MAIZE currents with maximal peaks of under 200 kA. Though not ideal for a well-functioning MAIZE, they were sufficient for the sake of undertaking laser coupled experiments to probe into the neck region. This then became the main configuration through many campaigns until the MAIZE performance issue was solved. Table 3.2 tabulates all main-load X-pinch experimental parameters fielded over the course of the work contained in this dissertation. Similarly, the relevant material properties are provided in Table 3.3. As can be seen, from 2020 through 2022, primarily 2-wire Ag X-pinches were fielded until MAIZE performance was improved in late 2022.

In January 2023, additional experiments on a fully operational MAIZE were performed to again investigate the behavior of X-pinches driven on the low-impedance MAIZE LTD. As can be seen from Table 3.2, the improved operation expanded the parameter space of drivable X-pinches on MAIZE. It was also realized with these experiments that a two wire X-pinch is a poor configuration

Date		Wire Material	Wire No.	Wire Diameter [µm]	Electrode Gap [mm]	Linear Density [mg/cm]	Static Resistance [mΩ]	Static Inductance [nH]	No. Tests
Oct	2020	Mo	4	35	21	0.39	0.33	24.0	7
		Mo	4	25	21	0.20	0.65	24.4	1
Mar	2021	Mo	4	35	10	0.39	0.19	15.9	2
		Mo	2	35	10	0.20	0.39	23.8	1
		Mo	2	35	13	0.20	0.46	26.0	1
		Mo	2	25	13	0.10	0.90	26.7	5
		Mo	1	50	∼2	0.20	0.04	9.5	3
		W	2	25	13	0.19	0.90	26.7	1
		Ag	2	25	13	0.10	0.26	26.7	6
Jun	2021	Ag	2	25	13	0.10	0.26	26.7	6
Jul	2021	Ag	2	25	13	0.10	0.26	26.7	5
Aug	2021	Ag	2	25	13	0.10	0.26	26.7	13
Oct	2021	Ag	2	25	13	0.10	0.26	26.7	16
Feb	2022	Ag	2	25	13	0.10	0.26	26.7	13
		W	2	25	13	0.19	0.90	26.7	4
		Mo	2	25	13	0.10	0.90	26.7	8
		Mo	1	50	∼2	0.20	0.04	9.53	6
Jan	2023	Ag	4	25	13	0.21	0.13	18.5	4
		Ag	6	25	13	0.31	0.09	15.8	3
		Ag	8	25	13	0.41	0.06	14.4	4
		Ag	10	25	13	0.51	0.05	13.6	1
		Mo	4	25	13	0.20	0.45	18.5	1
		Mo	6	25	13	0.30	0.30	15.8	1
		Mo	8	25	13	0.40	0.22	14.4	1
		Mo	4	35	13	0.39	0.23	18.1	2
		Mo	6	35	13	0.59	0.15	15.5	1
		Mo	8	35	13	0.79	0.11	14.2	1
		W	2	25	13	0.19	0.90	26.7	1
		W	4	25	13	0.38	0.45	18.5	3
		W	6	25	13	0.57	0.30	15.8	2
		W	8	25	13	0.75	0.23	14.4	2
		Nylon	1	∼200	1.0	0.27	10^{19}	6.8	1
		Nylon	1	∼200	2.2	0.27	10^{19}	9.1	1
Apr	2023	$\{CD_2\}_n$	1	60-200	1.6-3.4	0.026-0.29	10^{23}	7.7-12.8	29

Table 3.2: Summary of the X-pinches fielded on the MAIZE pulsed-power generator. Experiments from October 2020 through February 2022 experienced low current due to MAIZE firing asynchronously and producing peak currents of <250 kA. The January 2023 and April 2023 experiments were driven from MAIZE firing synchronously and delivering peak currents up to 600 kA.

Material	Density [g/cm^3]	Resistivity [Ω·m]
Mo	10.22	5.59×10^{-8}
W	19.3	5.6×10^{-8}
Ag	10.49	1.59×10^{-8}
Nylon	1.14	14×10^{13}
Polyethylene	0.93	17×10^{13}
WCu (70%:30%)	13.8	4.1×10^{-8}

Table 3.3: Density and resistivities for the wire and electrode materials used in the MAIZE experiments.

due to the high resistance and inductance values which, due to the low impedance of MAIZE as a driver, consequently lowers the peak drive current. Simultaneously, the amount of linear mass needs to be balanced such that the drive current is able to implode the crossing point and form a micro-pinch. Thus, it becomes a balance of finding the right resistance and linear mass, which under these constraints are essentially dictated by the same group of parameters: material density, resistance, and wire geometry. The equations for both are related as:

$$\bar{m} = n\rho_m A = n\rho_m \cdot \frac{\pi d_w^2}{4} \tag{3.1}$$

$$R = \frac{\rho_w L}{nA} = \frac{\rho_w \rho_m L}{\bar{m}}, \tag{3.2}$$

where $\bar{m}$ is the linear mass of the X-pinch, R is the X-pinch's initial static resistance, n is the number of wires, A is the area of one wire, d_w is the wire diameter, ρ_w is the material resistivity, and ρ_m is the material density. This seems to imply that there would be an "ideal" X-pinch for MAIZE starting from matching a resistance of $\sim$0.16 Ω (though this is already flawed as it will have dynamic resistance when ablated, but this should still scale similarly). The issue is that there is presently no

way of determining the correct combination of linear mass and material properties except by trial and error. A reasonable estimate would be to start with what has already been proven to work in the literature and scale to MAIZE.

Z-pinches have a well defined self-similar-scaling parameter, termed the Π parameter derived by modeling a z-pinch as the implosion of a thin annular shell with the simple equation $F/A = -P_{\text{mag}}$. Non-dimensionalizing this equation gives the dimensionless scaling parameter as

$$\Pi = \frac{\mu_0 I^2 \tau^2}{4\pi \bar{m} r_0^2}, \tag{3.3}$$

where I is the peak driver current, τ is the time of peak current, $\bar{m}$ is the linear mass of the initial load, and r_0 is the initial radius of the load [9]. Using the Π parameter as a basis to scale the linear mass of X-pinch experiments ($\bar{m} \sim I^2$) gives values larger than those empirically determined in previous experiments [58, 59, 60] and from this parameter sweep on MAIZE. This is due to the key difference in the geometry. The mass of an X-pinch is initially located within the crossing point, essentially a solid cylinder, and not distributed as a cylindrical imploding shell. To adjust for this, there are two modified versions of the Π parameter for an X-pinch, both of which are based in noting that the linear mass density of the X-pinch is given by $\bar{m} = \rho \pi r_0^2$. Here r denotes the effective radius of the crossing point and ρ the initial material density. The first of the two parameters recognizes some symmetry of the denominator and condenses it into a $\bar{m}^2$ term, giving

$$X_1 = \frac{I^2 t^2 \rho}{\bar{m}^2}. \tag{3.4}$$

Here, $\bar{m}$ is as defined above, I is now the current at the time, t, of x-ray emission, and ρ is the density of the crossing point at instance of x-ray emission [23]. As the density at the time of pinching is unknown, this parameter is not directly calculable and is usable only to translate the conditions of one driver to another. Though this does make the assumption that the density at the time of x-ray emission is a constant, even between drivers. If inspected, there is also some ambiguity in the implicit ρ^2 within $\bar{m}^2$ which remains defined by the initial density (else scaling is not possible)

and the explicit ρ which is seemingly to allow for the simplification to $\bar{m}^2$. The second scaling factor goes in the opposite direction and directly substitutes for $\bar{m}$ in the original Π parameter [25, 58, 61, 62]:

$$X_2 = \frac{\mu_0 I^2 \tau^2}{4\pi^2 \rho r_0^4}. \tag{3.5}$$

All variables are defined the same as in the Π parameter with the addition of the initial material density, ρ. Ignoring exact definitions of the variables, similar to Eq. 3.4, Eq. 3.5 scales as r_0^4, but differs by scaling with ρ instead of ρ^2. In practice, these result in very similar values when scaling either linear mass or array radius.

Unfortunately, while Eqs. 3.4 and 3.5 scale reasonably on high-impedance drivers, the derived linear masses for MAIZE were 4-6$\times$ larger than what was found to perform best in terms of clear implosion dynamics and x-ray signal. In response, an attempt was made to find a generalized scaling parameter extendable to a low-impedance driver, but one was not found. Figure 3.7 presents a small example of the parameter scalings derived from the January 2023 experiments. It additionally highlights the inverse nature of the linear mass and the resistance. Of all the parameters tested, the strongest correlations involved the time of peak x-ray emission and the value of the drive current at peak x-ray emission. From Table 3.3, the three materials were chosen due to having overlapping material parameters, such as the similar densities of molybdenum and silver and the similar resistivities of molybdenum and tungsten. From these plots it is clear that the resistivity, likely due to its importance for impedance matching with MAIZE, is an important factor in many of these scalings due to the similarity in slopes for molybdenum and tungsten as compared to silver.

As such, empirical equations can easily be generated to correlate specific parameters, but they fail if used generally. A data set that encompasses a multitude of X-pinches across a variety of drivers is likely necessary, if such a scaling parameter is derivable. It is likely that the nature of MAIZE as a low-impedance driver skews the scaling of the MAIZE data, as X-pinch performance is highly dependent on the material properties. Further, since X-pinch bursts typically occur during current rise, and on such a fast time scales, the relevant values to use for scaling are left ambiguous. For example, the Π parameter uses the peak current for scaling, but by that time in an X-pinch, the

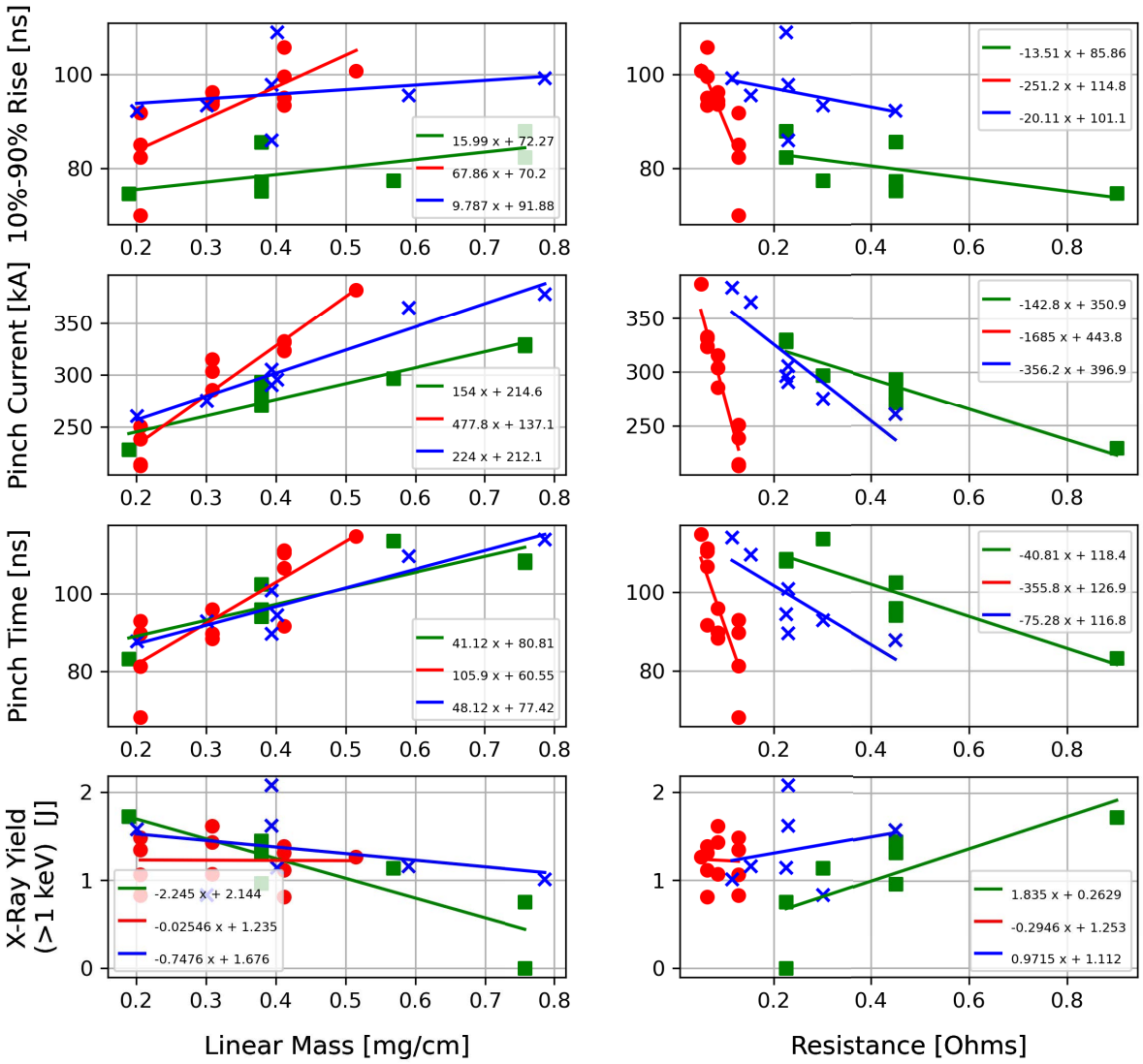

Figure 3.7: Selected plots showing the various X-pinch and MAIZE parameters as functions of the X-Pinch linear mass and resistance derived from the January 2023 experiments detailed in Table 3.2. The linear fits to the data are given for each data set in the units of the axes. Color corresponds to wire material: Red is silver, Blue is molybdenum, Green is tungsten.

hot spot has already formed and disrupted. With the low impedance of MAIZE, the inductive spike has presumably changed the relevant current dynamics, obfuscating the relationship. Compounding multiple variables over three materials and across different charging voltages, this generates an increasingly complex parameter space.

CHAPTER 4

Faraday Rotation Experiments

To measure the load current distribution immediately surrounding a dense micro-pinch core, we developed a Faraday rotation imaging and interferometry system. Faraday rotation diagnostics have been fielded on multiple platforms in a variety of forms [36, 63, 64, 65, 66]. In general, the rotation angle is given by

$$\Delta\phi = V \int_L \mathbf{B} \cdot d\mathbf{l}, \tag{4.1}$$

where V is the Verdet constant, which is material and wavelength dependent. In some Faraday rotation systems, a piece of material with a large, known Verdet constant is placed at the probing location to obtain measurable rotation angles. Such systems have been successful in measuring current delivery at relatively large, cm-scale radii [67, 68, 69]. However, due to the small size of the micro-pinch neck, it is not possible to use such a bulk material. Fortunately, though, due to the very high magnetic fields in micro-pinch necks, measurable rotation angles can be obtained using only the low-density plasma as the rotation medium [70, 71].

This chapter presents the design and demonstration of a high-magnification Faraday rotation imaging and interferometry diagnostic on the 1-MA, 100–250-ns MAIZE facility at the University of Michigan [31, 54, 72]. This system has been developed specifically to measure the load current's radial distribution in the low-density plasma surrounding the dense core of the X-pinch micro-pinch. The original goal of this diagnostic was to achieve a spatial resolution on the order of 10 μm. However, upon designing the system for practical implementation on MAIZE, the theoretical limit was estimated to be approximately 20 μm. Upon implementation, as described in Sec. 4.3, the

experimental resolution turned out to be 25–35 μm. Though higher resolution is always desirable, the resolution achieved on MAIZE was found to be useful for resolving the spatial distributions of interest in the ∼100-μm-scale coronal plasma region immediately surrounding the dense micro-pinch core.

4.1 Faraday Rotation

The Faraday effect is the rotation of polarized light while passing through a medium in the presence of a magnetic field. In a plasma, the rotation is usually well described by the quasi-longitudinal approximation [63, 73]

$$\begin{aligned} \alpha &= \frac{e^3\lambda^2}{8\pi^2\varepsilon_0 m_e^2 c^3}\int_L n_e \mathbf{B}\cdot d\mathbf{l} \\ &= \gamma\lambda^2 \int_L n_e \mathbf{B}\cdot d\mathbf{l} \end{aligned} \tag{4.2}$$

where $d\mathbf{l}$ is in the direction of laser propagation. That is, the magnitude of rotation of the polarization axis experienced by the probe laser is proportional to the integrated product of the electron density and the magnetic field component parallel to the the laser propagation vector. This approximation is valid as long as the electron plasma frequency and electron cyclotron frequency remain small compared to the laser frequency. For a 1064-nm laser, this approximation may start to break down below a radius of 15 μm for $I = 250$ kA (note that this threshold radius will increase with increasing current). Fig. 4.1 provides a simple diagram for orientation of the axes for the equations presented in the remainder of this section.

If the magnetic field and electron density profiles are azimuthally symmetric, and if the areal electron density $N_e = \int_L n_e\, dl$ can be measured independently of the magnetic field (e.g., from simultaneous 2D imaging interferometry), then Abel inversion allows for the extraction of the full radial magnetic field profile, $B(r)$. (Note that Abel inversion converts spatial information from the transverse projection axis, x, to the radial dimension, r.) The Abel inversion of Eq. 4.2 takes the

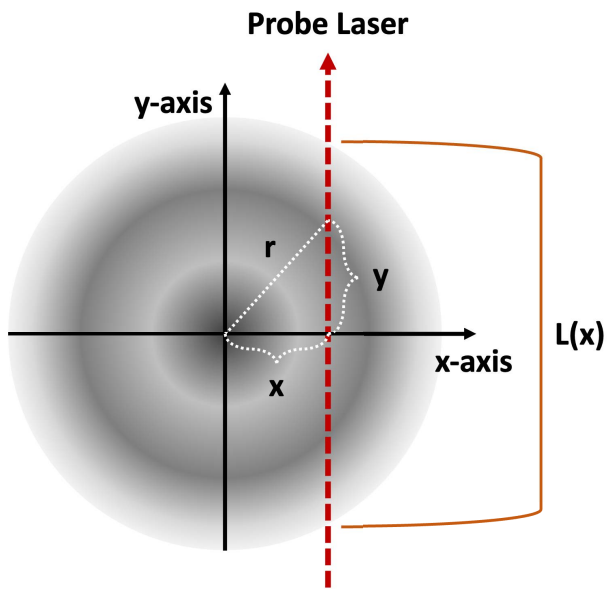

Figure 4.1: A simplified slice of a cylindrical plasma with an azimuthally symmetric electron density (arbitrarily represented by the color gradient) and magnetic field, $B_\theta(r)$, profiles. The depth of the plasma for a chord of laser propagation through the plasma column changes with its position along the x-axis and is denoted as $L(x)$.

form

$$n_e(r)B(r) = -\frac{1}{\pi}\int_r^\infty \frac{d}{dx}\left(\frac{\alpha}{\gamma\lambda^2}\right)\frac{dx}{\sqrt{x^2-r^2}}, \tag{4.3}$$

where the density, n_e, is itself the Abel inversion of the areal electron density profile

$$n_e(r) = -\frac{1}{\pi}\int_r^\infty \frac{d}{dx}\left(2n_c\lambda N_e\right)\frac{dx}{\sqrt{x^2-r^2}}, \tag{4.4}$$

where n_c is the critical plasma density. However, if the plasma geometry deviates sufficiently from azimuthal symmetry, or if the data are particularly noisy, then Abel inversion algorithms may return nonphysical profiles. Therefore, as an alternative to Abel inversion, Eq. 4.2 can be approximated using [36]

$$\alpha \approx \frac{e^3\lambda^2}{8\pi^2\varepsilon_0 m_e^2 c^3} N_e \bar{B}_{||}, \tag{4.5}$$

where $\bar{B}_{||} = \int_L \mathbf{B}\cdot d\mathbf{l}/L$ is the average magnetic field along (and parallel to) a ray of laser light

propagating through the plasma. Inverting Equation 4.5 provides the equation [36, 73]

$$\begin{aligned}\bar{B}_{||} &= \frac{8\pi^2\varepsilon_0 m_e^2 c^3}{e^3\lambda^2}\frac{\alpha(x,y)}{\int n_e(x,y,z)dz} \\ &= \frac{3.82\times 10^{12}}{\lambda^2}\frac{\alpha(x,y)}{\int n_e(x,y,z)dz}\end{aligned} \tag{4.6}$$

It would seem reasonable to suggest that using this in place of $B(r)$ may provide a reasonable estimate of the enclosed current via:

$$I_{\text{encl}}(r) = \frac{2\pi r}{\mu_0}B(r) \approx \frac{2\pi x}{\mu_0}\bar{B}_{||}(x)\Big|_{x=r} \tag{4.7}$$

However, using this provides measurements roughly half to one order of magnitude smaller than expected. This is reasonably expected when noting that (the non-averaged) $B_{||}(x,y)$ will always be $\leq B(r)$ at any point along the chord of integration. Translating the projection axis to the radial axis will primarily undershooting the total field for any (mostly, on average) monotonically decreasing projected profile. An improved approximation can be found by geometrically comparing $B_{||}$ to $B(r)$ and noting that the trigonometric functions collapse to the simpler form of

$$B_{||}(x,y) = \frac{x}{\sqrt{x^2+y^2}}\,B(x,y) \tag{4.8}$$

where x is the radial projection axis and y is the axis of laser propagation. Therefore we can make an additional corrective approximation by integrating Eq. 4.8 for the average of this quantity along

the propagation direction

$$
\begin{aligned}
\bar{B}_{||} &= \frac{1}{L}\int_{-L/2}^{L/2} B_{||} dy \\
&= \frac{1}{L}\int_{-L/2}^{L/2} B \frac{x}{\sqrt{x^2+y^2}} dy \\
&= \frac{1}{L}\int_{-L/2}^{L/2} \frac{\mu_0 I_{\text{encl}}}{2\pi} \frac{x}{x^2+y^2} dy \\
&= \frac{\mu_0 \bar{I}_{\text{encl}}}{\pi L} \arctan\left(\frac{L}{2x}\right),
\end{aligned}
\tag{4.9}
$$

where L is the chord length for the integrated region. For a cylindrically symmetric plasma, illustrated in Fig. 4.1, the length of each chord is clearly a function of x. If we note the diameter of the cylindrical plasma as L_0, then the expression for the integration chord length at each point along the projection axis, x, is $L(x) = \sqrt{L_0^2 - 4x^2}$. Now, these equations have technically made an assumption that we are restricted to positive x only, which is valid if we note symmetry and are careful about the direction of the magnetic field. Otherwise the final relation of Eq. 4.9 should be multiplied by an extra factor of $\text{sgn}(x)$ to compensate. Inverting Eq. 4.9, carefully noting that $\lim_{L\to 0} \frac{L}{\arctan(L/2x)} = 2x$ and substituting for $L(x)$, provides the final approximate form of

$$
\bar{I}_{\text{encl}} = \begin{cases} \frac{\pi \bar{B}_{||}}{\mu_0} \frac{\sqrt{L_0^2 - 4x^2}}{\arctan\left(\sqrt{(L_0/2x)^2 - 1}\right)} & \text{for } x < \frac{L_0}{2} \\ \frac{2\pi x}{\mu_0} \bar{B}_{||} & \text{for } x \geq \frac{L_0}{2} \end{cases}
\tag{4.10}
$$

This form of approximation is strongly dependent on the choice of L_0; however it is accurate to $<1\%$ when chosen to match the true diameter of the plasma column. The scaling is monotonic with the growth of L_0, though nonlinear. If we assume an error in the choice of L_0 up to $\pm 100\%$, the corresponding error in the current is +50% for a +50% error in L_0 and a -40% for a -50% error in L_0. How the value of L_0 was chosen is described in Sec. 4.5.

4.2 Measurement and Modeling of the Faraday Rotation Angle

To measure both the densities and Faraday rotation angles necessary to extract the magnetic field profile, the 1064-nm output of the Nd:YAG laser described in Sec. 3.2.2 was chosen over the 532-nm second harmonic to take advantage of the λ^2 scaling of the rotation. This will simultaneously have the effect of lowering the critical density by a factor of four ($n_c \sim 10^{21}$ cm^{-3}), however the expected density of the coronal plasma is at or below $\sim 10^{19}$ cm^{-3} and well below the critical density of $\sim 10^{21}$ cm^{-3} [74].

The optical diagnostic itself consists of a 3-channel polaro-interferometer that branches the diagnostic beam into a single, Mach-Zehnder interferometry line for simultaneous density and two polarimetry lines to extract the rotation angle [36]. The two polarimetry lines contain polarization analyzers to selectively attenuate the rotated laser light, and are counter-rotated to each-other so as to reduce the noise from self-emission. Following Ref. [36], the rotation angles are calculated from the captured polarograms via

$$\alpha(x,y) = \frac{1}{2}\arcsin\left[\frac{E_B(x,y)}{E_S(x,y)}\left\{\frac{I_{S+}(x,y)}{I_{B+}(x,y)} - \frac{I_{S-}(x,y)}{I_{B-}(x,y)}\right\}\frac{\tan(\beta)}{2}\right], \tag{4.11}$$

where the subscripts "S" and "B" refer to the shot and background values of the laser energy (or image intensity), and the subscripts "$+$" and "$-$" refer to the polarimetry channels with their analyzers rotated by $\pm$ the selected angle β. It is this selection of β in relation to the expected maximal rotation α_{max} that gives the highest sensitivity to the measured rotations. While initially designing the diagnostic, the current and density distributions surrounding the micro-pinch cores were unknown, and thus the relative magnitudes of the expected rotations were initially unknown. To provide estimates for the polarizer setting, a simple model to simulate Faraday rotation images was necessary to test the effects of various current and density distributions and to estimate the likely rotation angles.

While the overall magnetic and density profiles of X-pinches are complicated and vary between experiments, a basic approximation can be made by assuming that the neck region, or any subsection

of the neck region, can be described by a cylindrically symmetric region composed of a critically dense neck that sharply transitions to coronal plasma. The magnitude of the rotation angles that might be observed can then be calculated by imposing varied density and current profiles within this geometry.

Figures 4.2 and 4.3 show a selection of simulated rotation profiles for total currents characteristic of MAIZE in a poor operational state (150 kA, Fig. 4.2) versus during nominal operation (500 kA, Fig. 4.3). In both Figs. 4.2 and 4.3, parts (a)–(c) show the effects of constant, linear, and exponential electron density profiles with the full drive current contained within the dense neck plasma. Figures 4.2(d)–4.2(f) and 4.3(d)–4.3(f) show the effects of a constant electron density in the coronal plasma and the current now being partitioned between the dense neck and the coronal plasma with 90%, 50%, and 10% of the drive current within the neck plasma and the remaining current being linearly distributed in the surrounding coronal plasma. Each plot is normalized to a coronal electron density of 2×10^{18} cm^{-3} at the edge of the neck. This value is roughly the average value of what initial interferometry results had indicated. From Figs. 4.2 and 4.3 it can be seen that regardless of the exact variants of the density and current distributions considered when initialized with the same maximal parameters, the simulations produced similar maximal rotation values. This provided an initial value for the analyzing polarizers of $< 10^\circ$ for expected densities of 10^{17}–10^{19} cm^{-3} and a current of 200–500 kA. For the experiments reported herein, analyzer offset angles of 5° or less were found to provide the highest sensitivities, which is roughly in line with the simulated estimates. Note that the rotation angle is linear with current. Therefore, having greater current improves the signal strength and thus the signal-to-noise ratio for a given density profile.

In addition to providing the initial estimates for proper diagnostic design and operation, the model also doubles as a way to estimate the likely parameters of the measured rotations. The maximal current that can be delivered is known from MAIZE's anode Rogowski coil and the density distribution is known from the collected interferogram. Therefore, fits to the rotation assuming various distributions of the current can be generated to produce an additional bound to the measured current distribution.

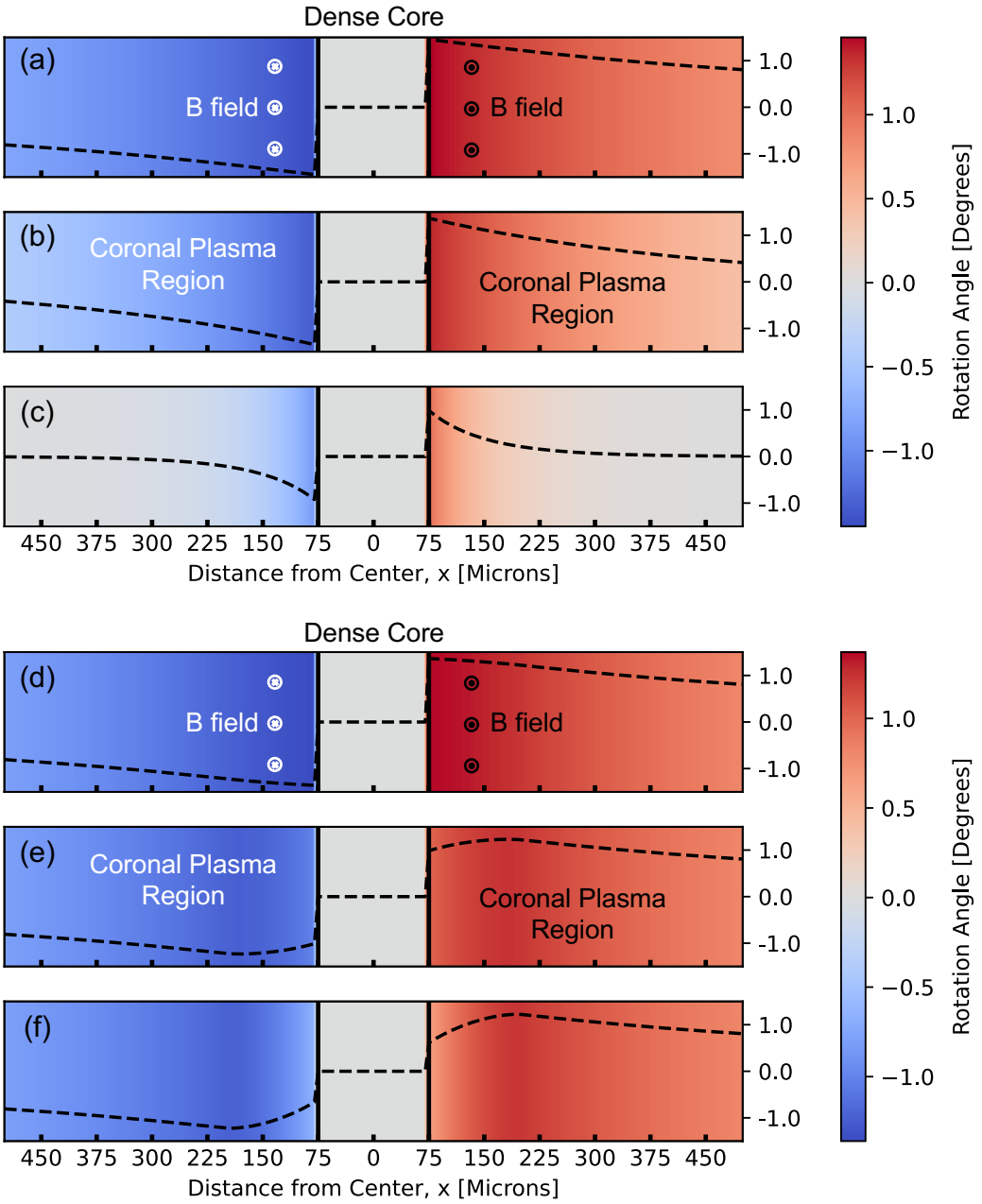

Figure 4.2: (a,b,c) Simulated Faraday rotation profiles with the entire current (**150 kA**) fully enclosed within the central dense plasma column and (a) constant, (b) linear, and (c) exponential electron density distributions in the surrounding coronal plasma. (d,e,f) Simulated Faraday rotation profiles of a constant electron density distribution in the coronal plasma and (d) 90%, (e) 50%, and (f) 10% of the total drive current contained within the dense neck plasma and the remaining current being linearly distributed in the surrounding coronal plasma. The line out of each simulated rotation profile is plotted in black along with the location of the edges of the central dense neck plasma. All plots were initialized with a coronal plasma density of 2×10^{18} cm^{-3} at the edge of the neck.

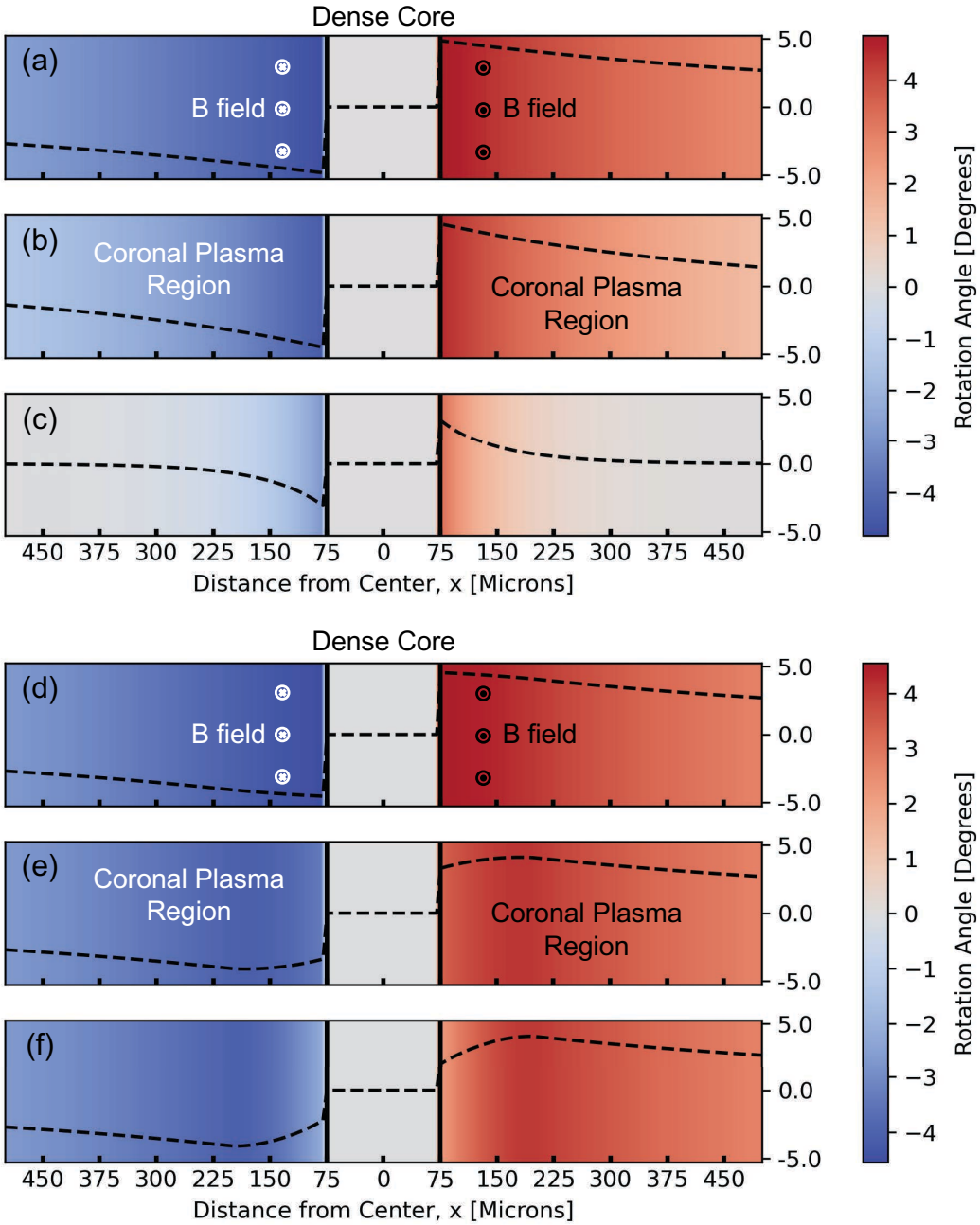

Figure 4.3: (a,b,c) Simulated Faraday rotation profiles with the entire current (**500 kA**) fully enclosed within the central dense plasma column and (a) constant, (b) linear, and (c) exponential electron density distributions in the surrounding coronal plasma. (d,e,f) Simulated Faraday rotation profiles of a constant electron density distribution in the coronal plasma and (d) 90%, (e) 50%, and (f) 10% of the total drive current contained within the dense neck plasma and the remaining current being linearly distributed in the surrounding coronal plasma. The line out of each simulated rotation profile is plotted in black along with the location of the edges of the central dense neck plasma. All plots were initialized with a coronal plasma density of 2×10^{18} cm^{-3} at the edge of the neck.

4.3 Faraday Diagnostic Design and Evolution

This section presents the evolution of the imaging Faraday diagnostic design from its initial inception to its present iteration and the main difficulties and improvements with each.

4.3.1 Initial Faraday Design

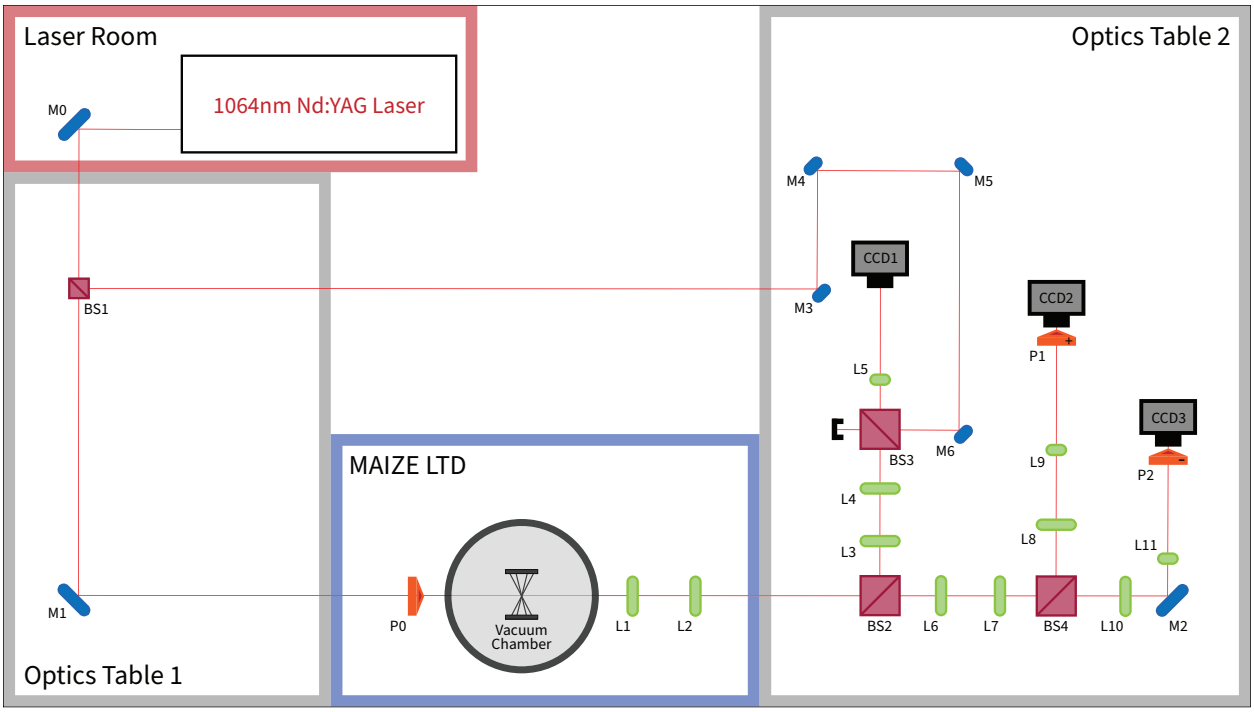

Figure 4.4: Diagram of the original design of the imaging Faraday rotation diagnostic for the MAIZE LTD. This design was never fully implemented. Not to scale.

The initial design was produced with guidance from collaborators at Imperial College London, drawing from the Faraday rotation system fielded on the 1.4-MA, 240-ns MAGPIE generator at Imperial College London, which consists of two polarimetry channels and a simultaneous interferometry channel [36, 75]. The probing laser source was the Ekspla NL122 Nd:YAG laser described in Sec. 3.2.2. The fundamental 1064-nm output was chosen for the Faraday rotation probe because of the higher energy available and to exploit the greater polarization rotation that can be expected, since Eq. 4.2 scales as λ^2. The diagnostic parameters were additionally constrained by the spatial dimensions of the X-pinch, namely a <5 mm region of interest with neck diameters

potentially down to <50 μm. While challenging, these magnifications and resolutions were not impossible in theory.

The greatest challenge and constraint for the design was the dimensions of MAIZE. The vacuum chamber of MAIZE is 1 m in diameter and the outer diameter of the MAIZE cavity is 3 m. This means that there is a significant distance between the object and the initial collection optic, for a collection optic placed outside of the MAIZE vacuum chamber. This also means that there is a significant distance to relay the image while maintaining desirable magnifications. Figure 4.4 illustrates the first solution using a series of relay lens pairs to properly maintain both magnification and a high collection angle ($\sim$2.4°). Here, the initial collection optic ($\varnothing$50.8 mm, f=75 mm, d=$\sim$600 mm) was placed at the first viable location outside of the vacuum chamber port window. The decision to not increase the collection angle by moving the collection optic within the vacuum chamber was justifiable as sharp density gradients were expected to exist only in a very thin transition layer from the dense core plasma to the surrounding coronal plasma. Thus, any loss of light from this transition region would only minorly perturb our measurement. Furthermore, a significant portion of the transition densities are likely above the laser's critical density and therefore could not be probed regardless of the acceptance angle. While collection angle can be significantly improved by moving the first lens within the vacuum chamber, it is practically less viable. Without any method of easily adjusting the optic, any shifts in the laser line (e.g., A-K gap shift while under vacuum, machine settling post shot, etc.) would be time consuming to correct. The optic would also require shielding to mitigate damage from the experimental environment. Lastly, it would greatly complicate the relay design from the vacuum chamber to the optics table.

Ultimately, the design shown in Fig. 4.4 was never fielded in full due to significant aberration in image quality and difficulty in alignment due to the large number of lenses. Additionally, the relay lenses were only included within the probe beam leaving the interferometric reference uncompensated, producing non-ideal fringes. Cannibalizing the design, a working alternative was produced.

4.3.2 First Implemented Faraday Design

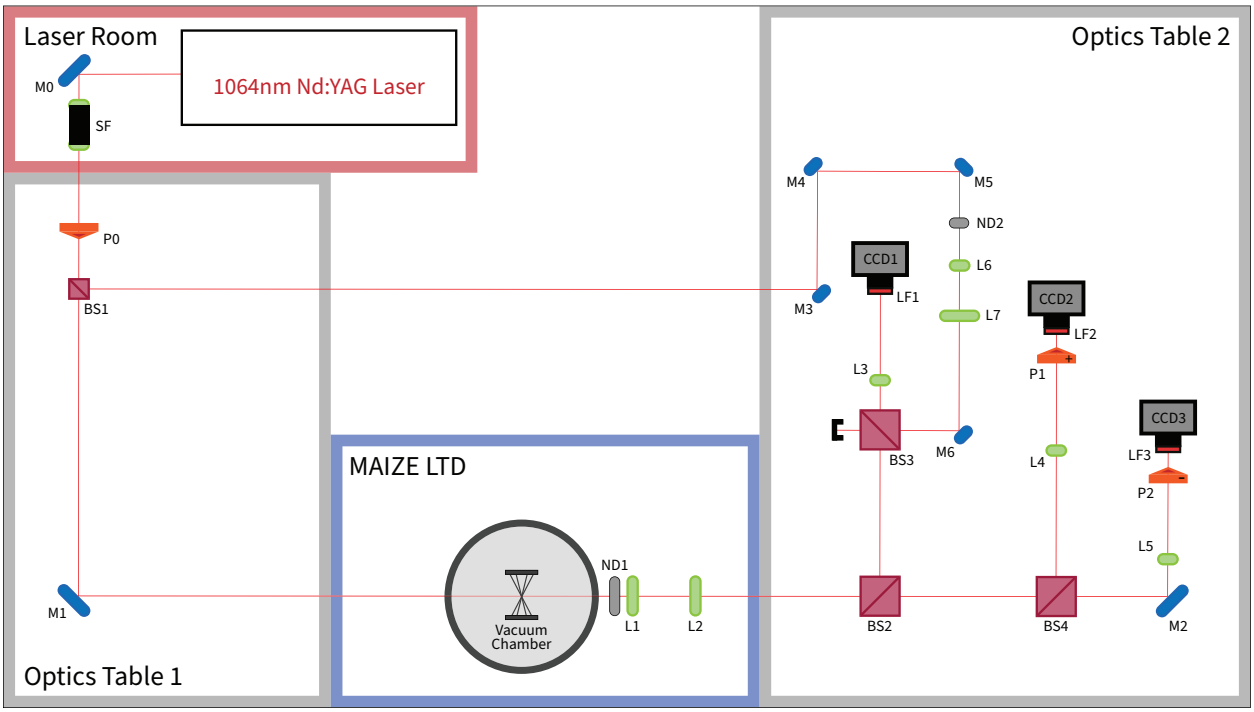

Figure 4.5: Diagram of the initial imaging Faraday rotation diagnostic fully fielded on the MAIZE LTD. Not to scale.

Figure 4.5 shows the redesigned version of the polaro-interferometer that was fielded with only minor revisions from June–October 2021 over several experimental campaigns. Notably, it reduced the setup to a single relay lens pair and one imaging lens per optical leg to achieve high magnification.

To maintain the energy densities reasonably below damage thresholds of the optical components (primarily that of the polarization analyzers), the output energy of the laser was maintained at 10 mJ $\pm 5\%$, with an average pulse-to-pulse energy jitter of approximately $\pm 1\%$. All laser energies were measured using a Coherent energy meter (J-50MB-LE) calibrated to within $\pm 2\%$ energy uncertainty. The initial beam was relayed to the first optics table from the laser room after passing through an expanding spatial filter to clean the beam profile and increase the beam size from the initial 6 mm diameter to $\approx$12 mm in diameter. This spatial filter had several revisions of the lens pair and pinhole size; however, all were nearly equivalent. The primary difference being the trend towards longer

focal length lens pairs to prevent ionization of the air at the focal point. A vacuum spatial filter was attempted but was not compatible with the focal length lenses presently used due to window reflection occurring close to $f/2$ and causing damage to lenses.

As the beam reached the first optical table, it was "cleaned" to have purely p-polarization. It was then split into a reference beam (10% of the incident energy) and probe beam (90% of the incident energy) by a 10:90 (R:T), non-polarizing beam splitter (Thorlabs BS044, denoted as BS1 in Fig 4.5). This 10:90 split is used to ensure that the probe beam has sufficient energy to be split into the Faraday and interferometry channels after passing through the vacuum chamber and the X-pinch plasma. Ratios of the probe-reference beam energies after passing through each beamsplitter are provided in Table 4.1. Final matching was done by the addition of neutral density filters. The probe beam then passed through the vacuum chamber before being collected by the same initial lens as specified in Sec. 4.3.1. The vacuum chamber port windows are made of an unknown material, either fused silica or Kodial glass. These windows were found to not measurably disrupt the linear polarization of the laser light. As X-pinches tend to deposit material in the chamber, an additional, exchangeable/sacrificial layer of commercial borosilicate glass panes were used to cover/protect the port glass. Commercial borosilicate glass was necessary instead of the typical Lexan panes used in other experiments, as Lexan panes were found to severely and non-uniformly disrupt the laser polarization after irregular or non-existent rotation patterns were seen from the first experimental

	BS_1	**BS_2**	**Chamber**	**BS_3**	**Total**
Probe Line	85%	45%	72%	45%	12.4%
Reference Line	10%	–	–	45%	4.5%

Table 4.1: Ideal final intensities, normalized to the initial beam energy, after transmission and reflection of the reference and probe beam through the non-polarizing cube beamsplitters that comprised the Mach-Zehnder interferometer illustrated in Fig 4.5. This accounts for attenuation of the probe beam from port windows (approximately 4% per interface, 8 interfaces) but not additional plasma, lenses, or neutral density filters.

campaign.

The spacing of the second lens of the relay was adjusted in this configuration to form an image plane at an additional distance of $\approx$1.1 m. After exiting the vacuum chamber, the beam is split into three channels via 50:50 (R:T), non-polarizing beamsplitters (Thorlabs BS032). Referring to Fig. 4.5, BS2 splits the probe beam equally between the interference and polarimetry legs, BS4 splits the polarimetry leg into the two polarimetry channels, and BS3 recombines the interferometry leg of the probe beam with the reference beam. As can be seen in Fig. 4.5, a magnifying lens pair was added to the reference beam to better match the size of the probe beam and give a usable interference pattern. Due to not being a perfect compensation, the fringe pattern was mildly unstable from shot to shot.

After being split into the three legs, the final magnifications of each are variable through the positioning of the final imaging lenses (L3, L4, L5 in Fig. 4.5). Typical magnifications used were between 1–10$\times$. Assuming a typical camera with detectors on the scale of 10–20 mm, these magnifications will roughly enlarge the $\sim$1–2 mm region of interest to cover a majority of the sensor.

For the interferometry line, the signal is recombined and collected by a 12-bit CCD camera (Canon Rebel XS with all internal filters removed). The unused portion of the recombined signal during this version was dumped. Each leg of the polarimetry line contains a polarization analyzer (Thorlabs LPNIR100-MP2). The polarization analyzers have a high extinction ratio ($>10^7$) and a high acceptance angle ($\pm 20^\circ$). The analyzers are counter rotated to each other by $\pm\beta$ from the extinction angle. The extinction angle is determined in situ each time the diagnostic is assembled by mapping the full transmission profile in 1° increments. This is done to account for any background rotation introduced within the optical path. Having the two counter-rotated polarimetry channels has the benefits of: (1) reducing the effects of pinch self-emission; and (2) removing the double valued nature of measured rotations above β (but still less than $\frac{\pi}{2}$) which is seen in systems with a paired polarimetry and shadowgraphy channel. This does come at the expense of being unable to clearly identify shadowgraphy effects. Both signals are finally collected by 14-bit CCD cameras (Canon

Rebel XSi with all internal filters removed). The CCDs of both the Faraday and interferometry channels were additionally filtered with 1064-nm line filters (Edmund Optics #39-364, denoted LF1, LF2, LF3 in Fig. 4.5) to reduce image contamination from broadband self-emission.

4.3.3 Second Implemented Faraday Design

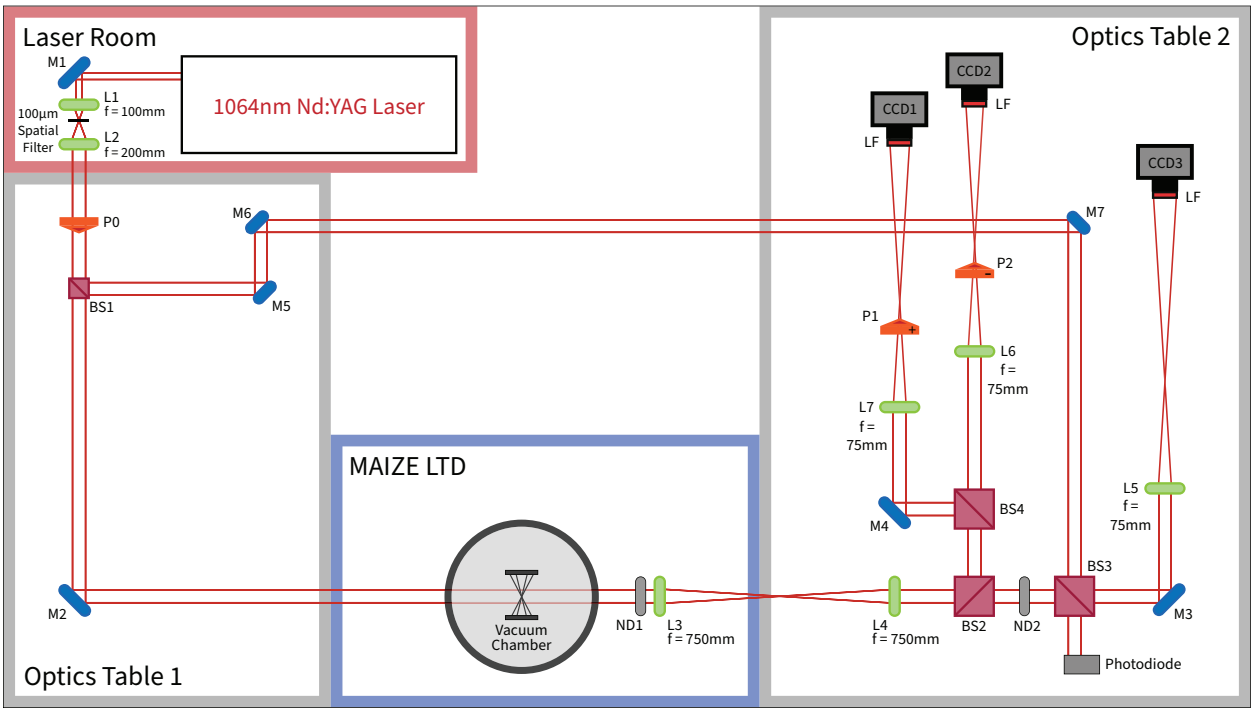

Figure 4.6: Diagram of the revised imaging Faraday rotation diagnostic fielded on the MAIZE LTD. Not to scale.

Figures 4.6 and 4.7 show the diagram and in situ images of the second revised form of the diagnostic fielded for the final two campaigns. The primary improvement in this version is the implementation of a proper collimating lens relay that removes the need for compensation lenses in the reference beam. By this iteration, a 200-µm pinhole was standard within the initial 2× magnifying lens pair. Presumably due to maintenance performed on the laser, the laser output in the fundamental was now primarily s-polarized. The expanded beam was then passed through the initial polarizer, denoted by P0 in Fig. 4.6, removing the p-polarized components and passing an almost fully s-polarized beam.

The beam is then split by a 10:90 (R:T), non-polarizing beamsplitter (denoted as BS1 in

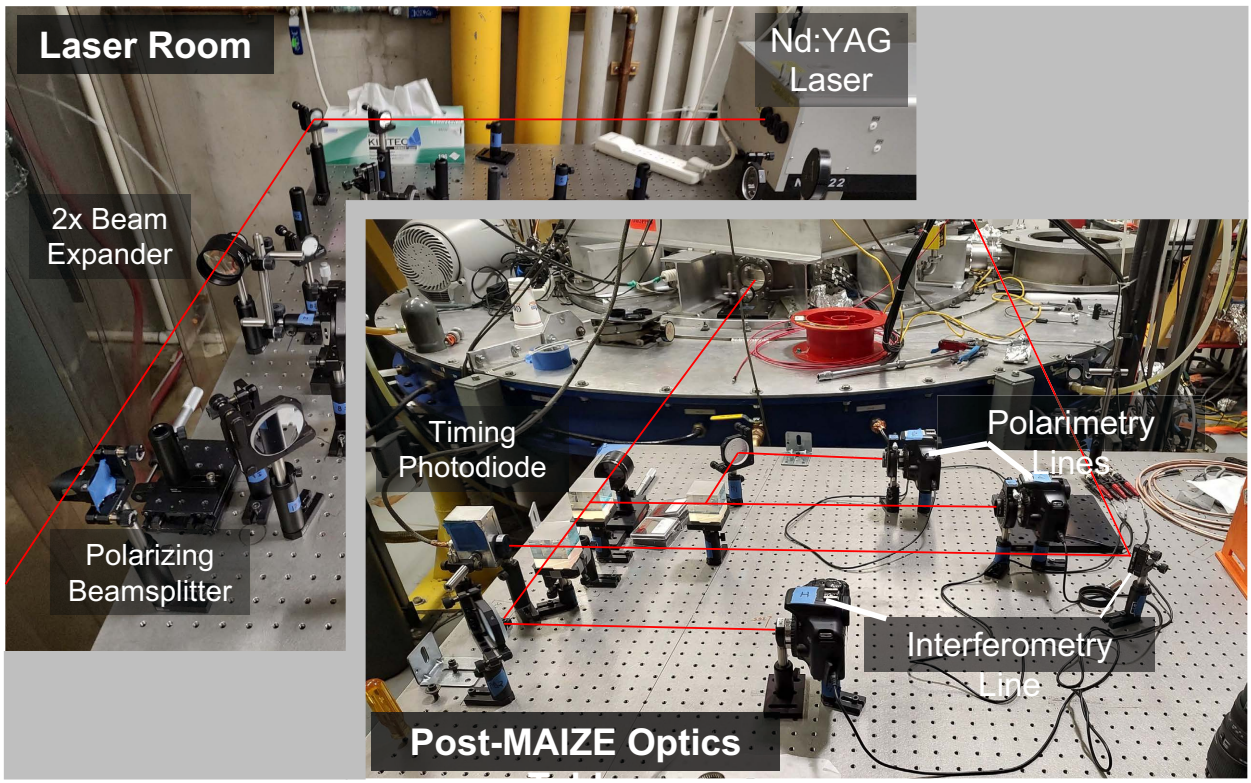

Figure 4.7: The majority of the optical setup diagrammed in Fig. 4.6. Shown are the portions of the beam path within the laser room undergoing initial expansion and polarization cleaning, as well as the post-MAIZE collection of the beam and splitting into the three diagnostic arms. The pre-MAIZE optical table where the beam is split into the probe and reference beams is not shown.

Fig. 4.6) into a probe and reference beam. Upon exiting the vacuum chamber, the probe beam (and scattered light) are collected by the aforementioned image relay of $1\times$ magnification (f=750 mm). Due to having a necessarily longer object-lens distance, this reduced the acceptance angle of the primary collection optic to 1.75°. The resulting numerical aperture of the system is calculated to be approximately 0.03, corresponding to a minimum spatial resolution of approximately 20 µm. Tests conducted with a USAF resolution target showed that features were clearly resolvable down to 35 µm, marginally resolvable down to 25 µm, and unresolvable below 25 µm due to diffraction effects.

After being relayed, the probe beam is again split three times via 50:50 (R:T) non-polarizing beamsplitters (denoted as BS2, BS3, and BS4 in Fig. 4.6). The primary difference here is that the

reflected portion of BS2 now constitutes the polarimetry leg of the diagnostic while the transmitted portion constitutes the interferometry leg. This was done to better ensure proper path length matching for interference upon recombination. The line filtered CCD cameras remained the same as in the prior diagnostic version. The non-imaged portion of the recombined interferometry signal was now used as the timing fiducial via a fast photodiode. (Previously, the timing fiducial used a portion of the simultaneous 532 nm output.)

Though designed for use with X-pinch micro-pinches at high magnification, the system shown in Fig. 4.6 can be easily converted to a low magnification operation by removing the magnification lenses (denoted as L5, L6, and L7) and moving the CCD cameras to the image plane of the relay lenses. However, even running at $1\times$ magnification, the diagnostic is limited in probing size to a maximum of 20 mm in diameter, due to the size of the probe-reference beamsplitter. For the final fielding of the diagnostic, a Galilean beam expander was installed to remove the focal point and allow for beam energies of up to 30 mJ (which remained within the optical damage threshold). Relocation of the on-hand neutral density filters was necessary to properly balance the higher intensities. The diagnostic was also run in its $1\times$ configuration with the magnification lenses removed and the CCDs placed at the image plane of the relay pair. Operation was otherwise the same with equivalent resolution.

4.4 Source of Error from Optical Element Polarization Anisotropy

A section is interjected here to make note of a source of error relating to the imperfection in optical components, namely the "non-polarizing" beamsplitters. While comparatively they are non-polarizing, any real optical component is likely to have small differences in their interactions between the polarization components [76, 77]. In the case of the beamsplitters, the reflected and transmitted coefficients for the s- and p-polarized portions of the beam differ. As such, the rotation angle of the beam may become affected while passing through the polarizer as illustrated in Fig. 4.8. For the Thorlabs beamsplitters used in this work, the coefficients of reflection and transmission for each component of the BS032 beamsplitter are listed in Table 4.2. The BS044 beamsplitter prior to

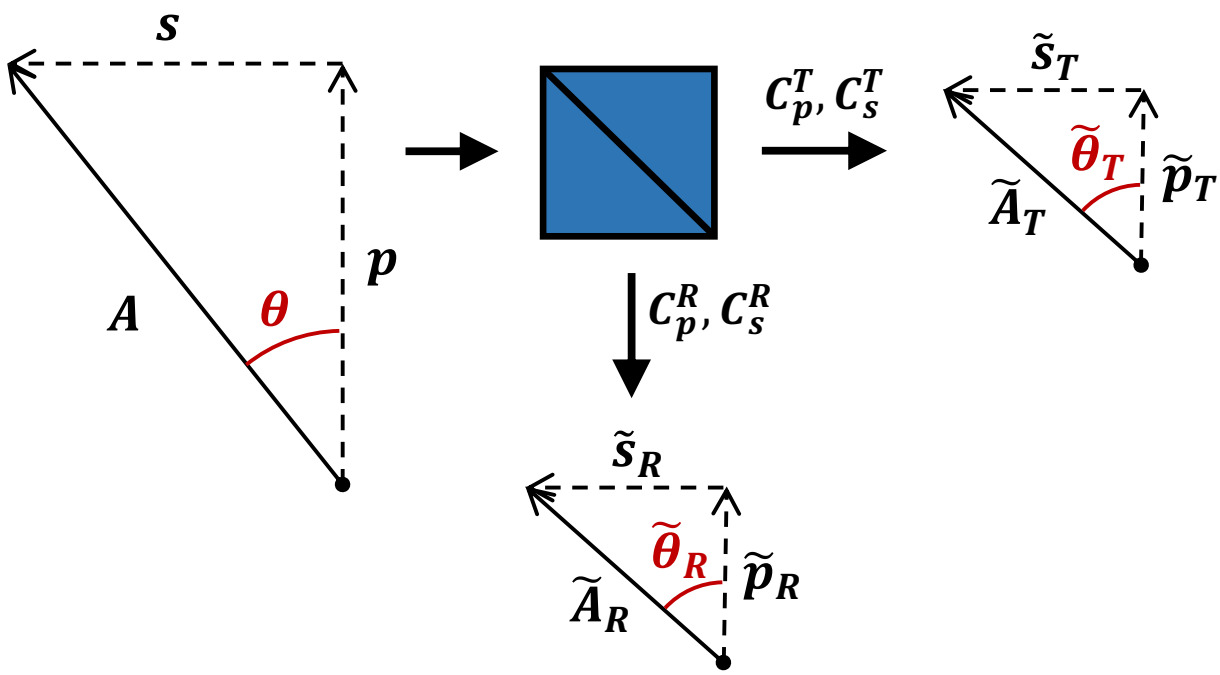

Figure 4.8: Diagram illustrating the effect of anisotropies on the reflection and transmission of p- and s-components of a linearly polarized beam passing through a nominally non-polarized beamsplitter. The resulting rotations of the polarization angle, θ_T, θ_R, may be larger or smaller than θ depending on the exact ratios of the transmission and reflection coefficients, $C_{\mathrm{p}}^T/C_{\mathrm{s}}^T$ and $C_{\mathrm{p}}^R/C_{\mathrm{s}}^R$.

the plasma does not affect the measurement. During these experiments the laser path was through two beamsplitters, adding an extra factor of reflection or transmission to both. This makes little difference to the underlying equations and, for simplicity of the following math, the total ratios will be simply denoted as $R_\pm$ to indicate an arbitrary coefficient corresponding to each polarimetry channel with analyzer angles $\pm\beta$.

To walk through what occurs, we begin with Fig. 4.9(a). Here we have an initial beam polarization angle, θ, which experiences the Faraday effect when passing through a plasma (and magnetic field) producing a new beam polarization of $\theta + \alpha$. For the two channel polarimetry scheme, this beam is then necessarily split via a beamsplitter into the two channels housing the oppositely-rotated polarization analyzers. If the beamsplitter is a perfectly non-polarizing beamsplitter, as in Fig. 4.9(b), then there is no change to the input states. If no plasma is present, θ remains θ in both the reflected and transmitted beams. The polarization analyzers have their extinction axes both set to θ and then offset by either $+\beta$ or $-\beta$ to give background intensities of $I_\pm \propto \sin^2(\beta)$.

BS032	C_s	C_p
Transmission	0.445	0.433
Reflection	0.459	0.503

Table 4.2: Coefficients of reflection and transmission of the Thorlabs BS032 non-polarizing beamsplitter for s- and p-polarized light. The relevant factor in polarization anisotropy characterization is the ratio $\frac{C_p}{C_s}$ or its inverse.

When plasma is present, both channels see a Faraday-rotated polarization of $\theta + \alpha$. As such, the intensities through both analyzers are now $I_\pm \propto \sin^2(\alpha \pm \beta)$, and Eq. 4.11 from Ref. [36] can be produced.

The deviation, as said, then comes if we consider an imperfect beamsplitter. This is presented as Fig. 4.9(c), though note that in the figure the reflected channel, denoted with subscript R, is the $+\beta$ channel, and the transmitted channel, subscript T, is the $-\beta$ channel. Now, as the beam passes through the beamsplitter, the s- and p-polarization components are unequally affected producing an effective rotation. Without any plasma, the initial polarization θ is rotated by the beamsplitter to angles $\widetilde{\theta}_\pm$ in the different analyzer channels. If we again inspect Fig. 4.8, noting that $\tilde{s} = C_s s$ and $\tilde{p} = C_p p$, then the initial and rotated polarization angles are related trigonometrically:

$$\begin{aligned} \widetilde{\theta}_\pm &= \arctan((C_s/C_p)_\pm \tan(\theta)) = \arctan(R_\pm \tan(\theta)) \\ \theta &= \arctan((C_p/C_s)_\pm \tan(\widetilde{\theta}_\pm)) = \arctan(R_\pm^{-1} \tan(\widetilde{\theta}_\pm)), \end{aligned} \tag{4.12}$$

where, again, θ is the initial beam polarization angle and $\widetilde{\theta}_\pm$ are the angles of polarization in the $\pm\beta$ analyzer channels. Unlike the perfect case, the polarization analyzers now have their extinction axes set to $\pm\beta$ from the different angles $\widetilde{\theta}_+$ and $\widetilde{\theta}_-$; however, this still results in intensities of $I_\pm \propto \sin^2(\beta)$ due to the equivalent magnitude of the offset.

When rotation of the plasma is added, the angles after passing through the beamsplitter can be decomposed into the original rotated polarization (known from measurement without plasma

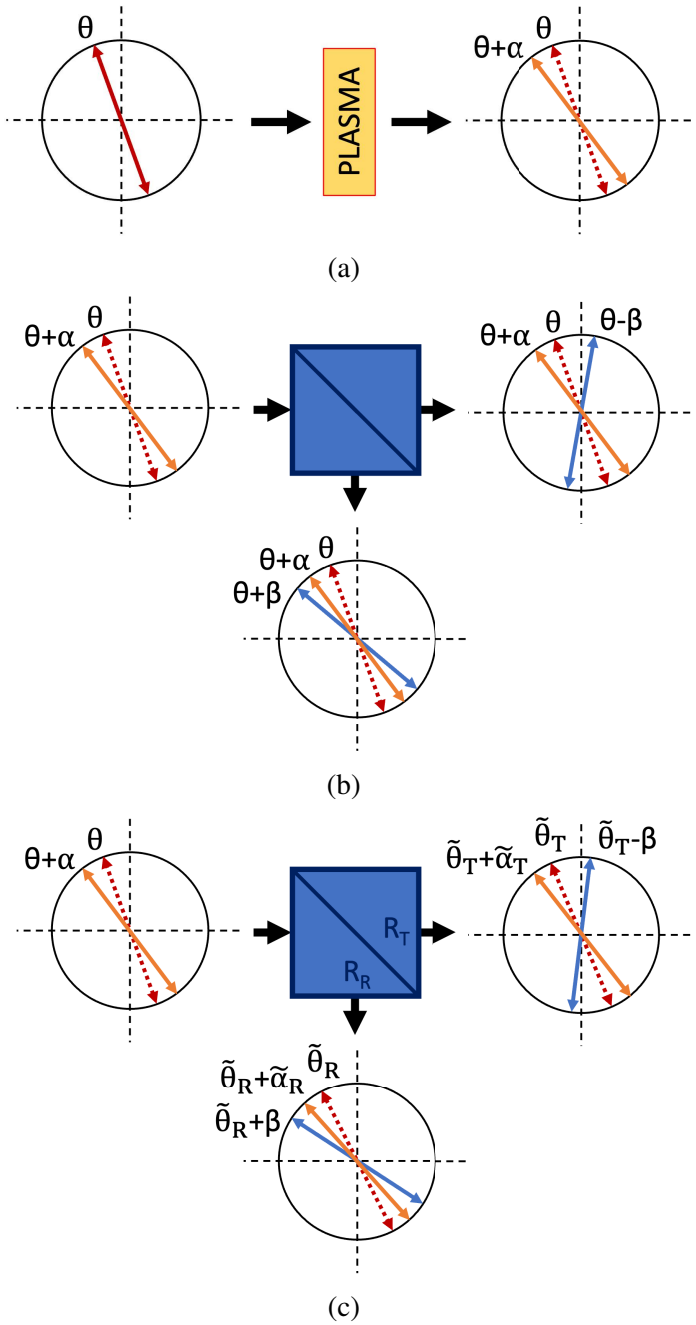

Figure 4.9: (a) While passing through the plasma, the initial laser polarization angle, θ, colored red, is rotated by the Faraday effect by an amount α, colored orange. (b) The rotated laser is passed through a perfectly non-polarizing beamsplitter to split the beam between the two polarization analyzers. The axis of extinction for the polarization analyzers, colored blue, and set to $\theta \pm \beta$. Note that both analyzers see the same value of α. (c) The rotated laser is passed through an imperfect, non-polarizing beamsplitter to split the beam between the two polarization analyzers. From the effect detailed in Fig. 4.8, the polarization analyzers now see different Faraday rotation angles, $\tilde{\alpha}_R$ and $\tilde{\alpha}_T$, in the reflected and transmitted beams.

present) and the apparent rotation within the channel. This is written as $\widetilde{\theta}_{\pm} + \widetilde{\alpha}_{\pm}$. Similar to Eq. 4.12, the relationship to the initial state can be similarly written:

$$\begin{aligned} \widetilde{\theta}_{\pm} + \widetilde{\alpha}_{\pm} &= \arctan(R_{\pm} \tan(\theta + \alpha)) \\ \theta + \alpha &= \arctan(R_{\pm}^{-1} \tan(\widetilde{\theta}_{\pm} + \widetilde{\alpha}_{\pm}). \end{aligned} \tag{4.13}$$

In the ideal case of $R_{\pm}$=1, that is, equal transmission or reflection of the s- and p-polarized components, we see that Eqs. 4.12 and 4.13 reduce simply to: $\widetilde{\theta}_{\pm} = \theta$ and $\widetilde{\theta}_{\pm} + \widetilde{\alpha}_{\pm} = \theta + \alpha$, or, more simply, $\widetilde{\alpha}_{\pm} = \alpha$. That last equivalence is the crux of this error. In practice, $\widetilde{\theta}_{\pm}$ are the in situ measured extinction angles for each channel. As they differ between the channels, the apparent rotation magnitudes, $\widetilde{\alpha}_{\pm}$, also differ between the channels. Therefore the intensities transmitted through the analyzers are $I_{\pm} \propto \sin^2(\widetilde{\alpha}_{\pm} \pm \beta)$.

The angle θ remains unknown, but derivable, via Eq. 4.12, and $\widetilde{\alpha}_{\pm}$ is measurable through the respective captured polarogram. Starting from Eq. 4.13, we can give an expression that can then extract α from either measured $\widetilde{\alpha}$:

$$\alpha = \arctan\left(R_{\pm}^{-1} \tan(\widetilde{\theta}_{\pm} + \widetilde{\alpha}_{\pm})\right) - \theta. \tag{4.14}$$

Substituting the relation for the unknown θ in terms of the known $\widetilde{\theta}_{\pm}$ from Eq. 4.12 and condensing the two terms via trigonometric identities gives

$$\begin{aligned} \alpha &= \arctan\left(R_{\pm}^{-1} \tan(\widetilde{\theta}_{\pm} + \widetilde{\alpha}_{\pm})\right) - \arctan\left(R_{\pm}^{-1} \tan(\widetilde{\theta}_{\pm})\right) \\ &= \arctan\left(\frac{R_{\pm}^{-1}(\tan(\widetilde{\theta}_{\pm} + \widetilde{\alpha}_{\pm}) - \tan(\widetilde{\theta}_{\pm}))}{1 + (R_{\pm}^{-1})^2 \tan(\widetilde{\theta} + \widetilde{\alpha}_{\pm}) \tan(\widetilde{\theta}_{\pm})}\right). \end{aligned} \tag{4.15}$$

Notably, this equation is only valid for a single channel when α_{+} or α_{-} are known, which can be done by processing each polarogram individually. However, this reintroduces the issues of self-emission and double-valued rotations and is rather counter to the purpose of having a dual-polarimetry diagnostic. Referring back to the method of Ref. [36], Eq. 4.11 is derived from inverting

the equation for the difference in intensities between the normalized polarograms for the two channels. The result can be rewritten using a few trigonometric identities into the form

$$D = \left\{ \frac{I_{S+}(x,y)}{I_{B+}(x,y)} - \frac{I_{S-}(x,y)}{I_{B-}(x,y)} \right\} = \frac{I_S}{I_B} \left[\frac{\sin(2\alpha)\sin(2\beta)}{\sin^2(\beta)} \right], \tag{4.16}$$

where, again, the subscripts "S" and "B" refer to shot and background values of the laser intensity, and the subscripts "$+$" and "$-$" refer to the counter-rotated polarimetry channels with analyzers at $\pm$ the selected angle β. If we wish to rederive this formula in the presence of anisotropy, it follows that the modified intensity equations become:

$$\begin{aligned} I_{B\pm} &= s_{\pm} I_B \sin^2(\beta) \\ I_{S\pm} &= s_{\pm} \left[I_S \sin^2(\widetilde{\alpha}_{\pm} \pm \beta) + \frac{I_{SE}}{2} \right] \end{aligned} \tag{4.17}$$

Now, these are nearly the same equations as those for the ideal beamsplitter; however, the key difference is that the intensities of the polarograms between the two channels differ in their perceived values of $\widetilde{\alpha}$. When the difference is taken, the result is similar to that of Eq. 4.16, but with the two values of $\widetilde{\alpha}$ included:

$$D = \frac{I_S}{I_B} \left[\frac{\sin(\widetilde{\alpha}_+ + \widetilde{\alpha}_-)\sin(\widetilde{\alpha}_+ - \widetilde{\alpha}_- + 2\beta)}{\sin^2(\beta)} \right]. \tag{4.18}$$

This equation does not seem to have a simple closed form solution for combining with Eqs. 4.12 and 4.13 and inverting for α. Thankfully, the error between Eq. 4.16 and Eq. 4.18 can be modeled to give an upper bound. In the case of the experiments described within this chapter, this is conservatively $\leq$15% for the rotation angles observed. Unfortunately, the behavior of the error curve appears very chaotic due to its dependence on essentially five variables (the (+)-analyzer extinction angle, the (-)-analyzer extinction angle, the (+)-channel anisotropy ratio, (-)-channel anisotropy ratio, and the analyzer offset angle) and is again difficult to generalize. Future experiments should take care in characterizing this source of error when selecting optical components, namely beamsplitters, along

with initial polarization of the beam and selection of β.

4.5 Results

To extract any magnetic field, enclosed current, or magnetic pressure trace, the collected data needs to have both measurable rotation signal over a measurable length scale *and* there needs to be measurable fringe shifts over this same region. This already presents a difficult constraint, on top of which the combined timing jitter between the laser and the MAIZE switch triggering ($\sim$20 ns), the chance of catching a highly cascaded neck (diameter $\leq$200 μm) was even further diminished. Experimental data appears to support the original assumption that capturing neck diameters of $\leq$100 μm may be impossible due to the motional blurring and temporal integration of the $\sim$1 ns object with a 2 ns laser pulse. In all, the Faraday diagnostic was fielded for 101 experiments. The first 24 shots diagnosed the depolarization properties of the Lexan sacrificial panes and would not have had the ability to produce functional rotation data. This leaves the remainder of 77 shots split across three campaigns. The first two of these campaigns (16 shots and 31 shots, respectively) produced one shot that met each of the above criteria. The final fielding, in its most updated version, had the remaining 30 shots, of which four were potential candidates. This does show an improvement in the percentage of usable shots during a given campaign from $\sim$5 % to $\sim$13 %. Regardless, the data that was collected was enough to process and extract desired information about the current distribution, and three of the six shots (2241, 2534, and 2933) are presented. The target designs used throughout these experiments, and described in Sec. 3.1, are presented in Fig. 4.10. Both a standard X-pinch design [78] [Fig. 4.10(a)] and a hybrid X-pinch design [26] [Fig. 4.10(b)] were fielded [22, 23]. Also shown within Fig. 4.10 are the small regions imaged by the Faraday rotation diagnostic.

For each Faraday rotation experiment, nine images are produced by the diagnostic: a pre-shot image, a 'shot' image taken during the experiment, and a post-shot image for each of the polarimetry channels and the single interferometry channel. Refer to Appendix C for the full collection of images used to construct the data within this chapter. Figure 4.11 shows example

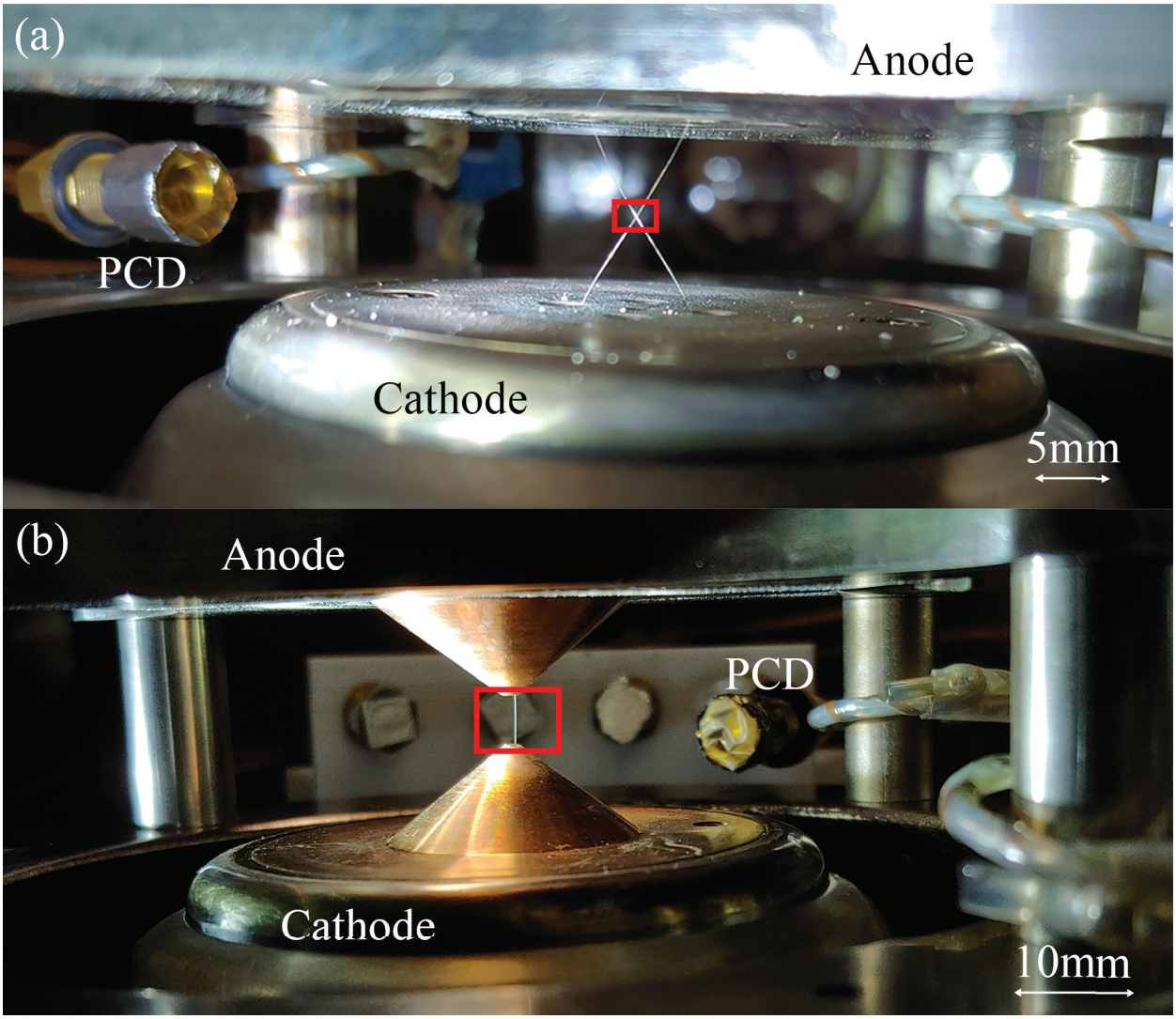

Figure 4.10: In situ photographs within the MAIZE vacuum chamber of (a) a standard X-pinch load with two 25-µm Ag wires, and (b) a hybrid X-pinch load with a single 50-µm Mo wire. Both photographs show the anode and cathode orientation and the location of the polycrystalline diamond (PCD) detector used to measure the timing of the X-pinch x-ray bursts. The box in red shows the approximate field of view imaged by the Faraday rotation diagnostic.

images collected for a two-wire X-pinch experiment and a hybrid X-pinch experiment. For both sets of images, the analyzer angles were set to $\pm 3.5°$. In the experimental run that produced the images of Fig. 4.11, magnifications were about 7.5–8$\times$ for two-wire X-pinches, corresponding to approximately 0.66 microns per CCD pixel, and 4.5–4.75$\times$ for hybrid X-pinches, corresponding to approximately 1.1 microns per CCD pixel. Note that these pixel resolutions are higher than the achievable optical resolution, but they are still desirable for reducing what would be an extraneous field of view on the sensor and for easing image registration and alignment when processing the images.

There are several noticeable differences seen between the two X-pinch types. Areas of rotation in the two-wire X-pinch [Fig. 4.11(c) and 4.11(d)] are generally small and difficult to visually discern without added contrast or brightening. From the paired interferogram of Fig. 4.11(b), it is seen that fringe shifts remain small until very close to the neck, implying that much of the neck region is devoid of sufficient plasma density for measurable rotation angles, except where either plumes of density exist or the magnetic field strength becomes large enough to utilize the minimal density at small radius.

Conversely, hybrid X-pinches consistently produced sharper areas of rotation with higher contrast even at larger radii, as seen in the clear bright and dark areas in Figs. 4.11(g) and 4.11(h), though they tend to produce far more complicated structures. For example, compare and contrast Figs. 4.11(f)–4.11(h), where regions of more complicated and increased fringe shifts correspond to regions with larger rotations. It is likely that the density is high enough in some regions of the hybrid pinches that the rotation angle is exceeding that of the analyzer angle and is becoming double valued. This would correspond to areas of rotations that appear to be bright in both polarograms, which can be observed in multiple areas of Figs. 4.11(g) and 4.11(h). The consistent matching of the areas of fringe shifts and areas of visible rotation strongly suggests that the limiting factor in measuring Faraday rotation around an X-pinch is the coronal plasma density.

Note that in Fig. 4.11, the images appear slightly defocused. This could be due to a slight optical misalignment, motional blurring due to time-integration over the 2-ns laser pulse, or a shallow

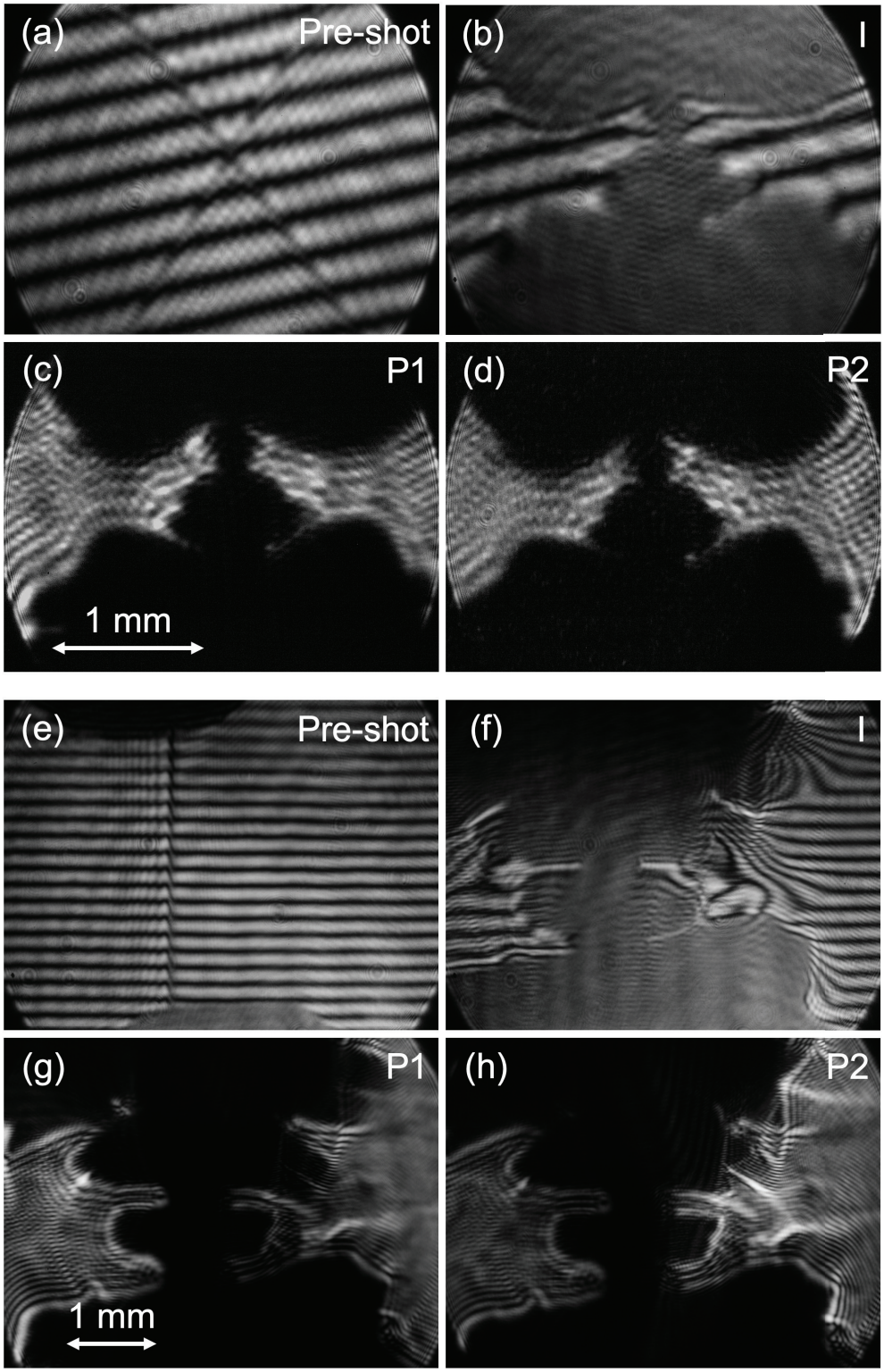

Figure 4.11: (a,b,c,d) Images collected for a two-wire, 25-μm-wire-diameter, Ag X-pinch experiment: (a) pre-shot interferogram; (b) interferogram; (c) channel 1 polarogram; and (d) channel 2 polarogram. (e,f,g,h) Images collected for a 50-μm-wire-diameter Mo hybrid X-pinch experiment: (e) pre-shot interferogram; (f) interferogram; (g) channel 1 polarogram; and (h) channel 2 polarogram.

depth-of-field. Reducing the time-integration would require a new laser, while the depth-of-field could be extended in future experiments by reducing the aperture of the collection lens. Also apparent in the images of Fig. 4.11 is edge diffraction. While this form of noise should oscillate around a mean value, the ratio of oscillation amplitude to the mean value becomes sufficiently high to lose the signal in areas of low rotation angle. This, combined with large unusable portions of the image (due to the X-pinch plasma scattering or attenuating the probe beam) and the low fringe density in the regions of interest, made most basic computational methods for interpreting the interferogram excessively challenging. Higher fringe density would have improved the results of the computationally determined areal density; however, the trade off between spatial resolution and sensitivity would have reduced the sensitivity of the interferogram below the noise threshold.

Processing the collected images occurs in three parts. The first step is to process the interferograms to extract the areal density profile. The second step is to process the polarograms to extract the rotation angle profile. The third step is to align the two profiles and extract the magnetic field profile. Figures 4.12 and 4.13 show two similar pinches, though they differ in fringe density. To extract the areal density profiles from Figs. 4.12(b) and 4.13(b), there are a few methods. One option is to simply measure the fringe shifts by hand. While this is a valid method, and was done in whole for one set of experimental interferograms, it is hard to match spatial location of the measured point locations to their respective rotation values. Doing so carefully can result in extractable field profiles; however, they can be low resolution and miss potential structure, effectively smoothing the data. This method is best when only one or two viable fringes exist in the region of interest and require a manual fitting of the profile. This method also provides a nice sanity check when using more sophisticated, automated processing methods.

A processing method based on the Fourier transform was attempted. However, the the large amounts of the image blocked by the expanded wire plasma, coupled with very low fringe numbers in the regions of interest, did not prove conducive to its implementation. Automated processing of interferograms with sufficient fringes for interpolation made use of the Magic2 code developed at Imperial College London from the original MAGIC code [79, 80]. Essentially this required

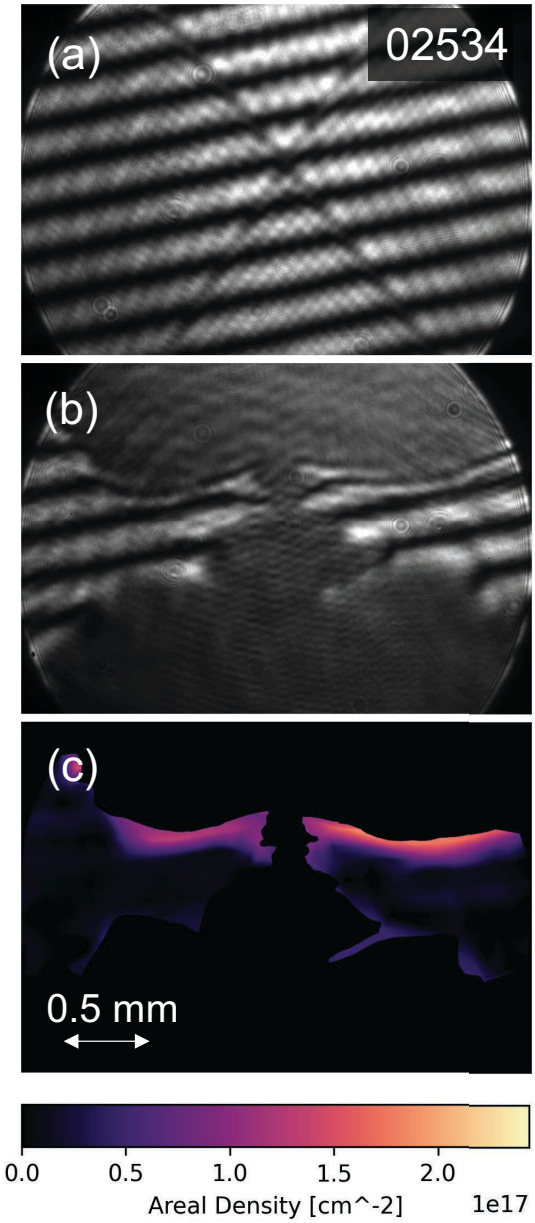

Figure 4.12: Data from shot 2534, a two-wire, 25-µm-wire-diameter, Ag X-pinch experiment: (a) pre-shot interferogram; (b) shot interferogram; and (c) the areal density image calculated from (a)–(b). Taken 2 ns before x-ray burst.

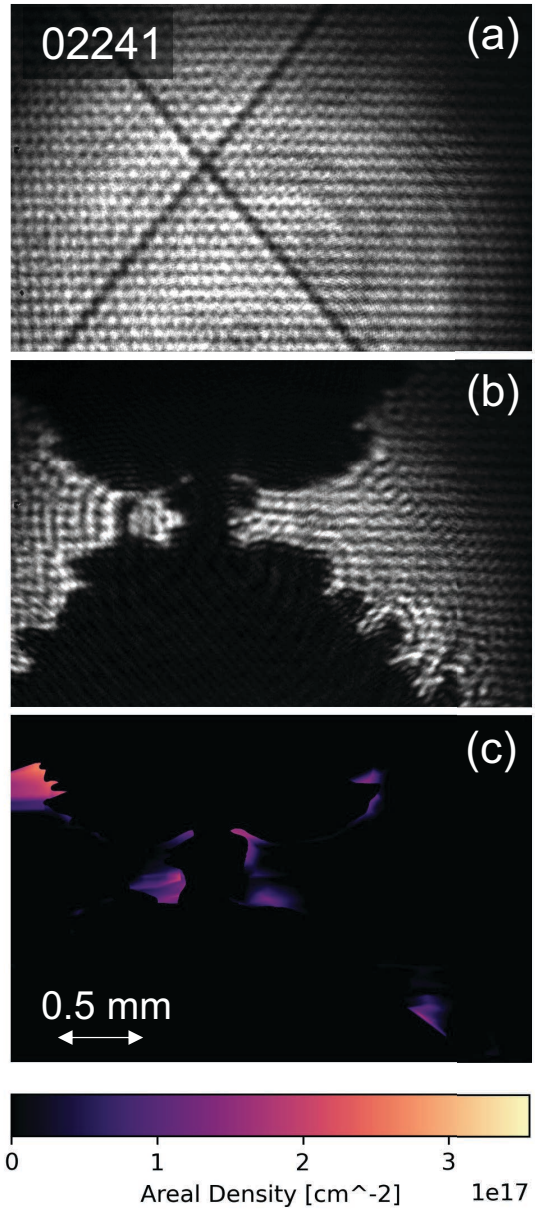

Figure 4.13: Data from shot 2241, a two-wire, 25-µm-wire-diameter, Ag X-pinch experiment: (a) pre-shot interferogram; (b) shot interferogram; and (c) the areal density image calculated from (a)–(b). Taken 6 ns before x-ray burst.

pre-processing of a background interferogram and an experimental interferogram with single-pixel, black fringe traces on a white background. Any unused portions of the image, such as regions blocked by dense plasma, are masked in grey. These pre-processed interferograms are then taken by the code and the user is asked to label the fringes on both interferograms, which are then interpolated by Magic2, which then returns the resulting fringe shift map. Refer to the appendix of Ref. [81] for further information on the Magic2 code and its method. In some cases, likely due to user error in labeling the fringes, the fringe shift will have an arbitrary offset (almost always a $2n\pi$ shift in phase space) that requires correction from comparison with a known zero fringe region. The resulting corrected phase shift maps are then converted to areal density via

$$N_e = 2\lambda n_{cr} N_f = 2.1 \times 10^{21} \cdot N_f \quad [\mathrm{SI}], \tag{4.19}$$

where N_f is the initial fringe shift, n_{cr} is the critical density of the plasma, and λ is the laser wavelength, which for our experiments was 1.064×10^{-6} m. Examples of the resulting areal density profiles are presented in Figs. 4.12(c) and 4.13(c) showing the typical distribution of higher density regions on the order of 10^{17} cm^{-2} very close to the edge of the dense plasma neck and around additional portions of the expanded wire regions. This plasma quickly falls off by an order of magnitude to 10^{16} cm^{-2} and below the sensitivity of the interferometer ($\lesssim 10^{16}$ cm^{-2}). This further reiterates the difficulties in achieving high rotation signals with such low density media. Even so, as was seen in Fig. 4.11, the characteristic bright and dark regions characteristic of Faraday rotation were still sufficient for measurement.

Following Ref. [36], the rotation angles were calculated from the polarograms via Eq. 4.11. Figures 4.14(d), 4.15(d), and 4.16(d) present plots of the rotation angle calculated from the box-filtered polarograms of Figs. 4.14(b), 4.15(b), 4.16(b) and 4.14(c), 4.15(c), 4.16(c), respectively. They are normalized to their post-shot background polarograms, and one example of each is presented in Figs. 4.14(a), 4.15(a), and 4.16(a). It can be seen that in most regions, the rotation stays well below the value of the analyzer rotation (for these shots β was either 3.5° or 3.0°) and

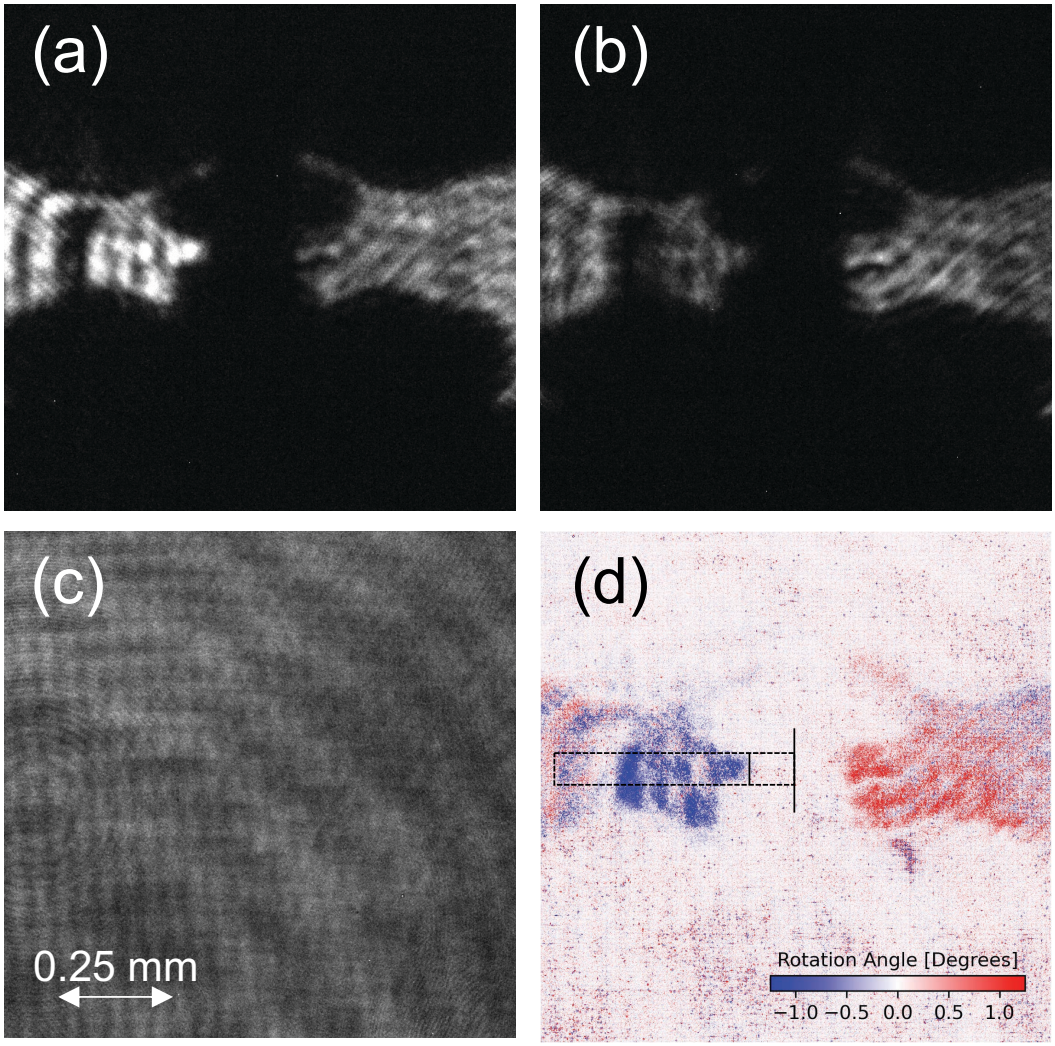

Figure 4.14: Data from shot 2241, a two-wire, 25-μm-wire-diameter, Ag X-pinch experiment: (a) post-shot polarimetry background; (b) smoothed channel 1 polarogram; (c) smoothed channel 2 polarogram; and (d) the Faraday rotation image calculated from (a)–(c). The dashed box in (d) denotes the region used for producing the enclosed current profile and the magnetic pressure profile of Fig. 4.20. The solid lines within the dashed box in (d) denote the edge of the dense core and center axis. Analyzer β was set to 3.5°.

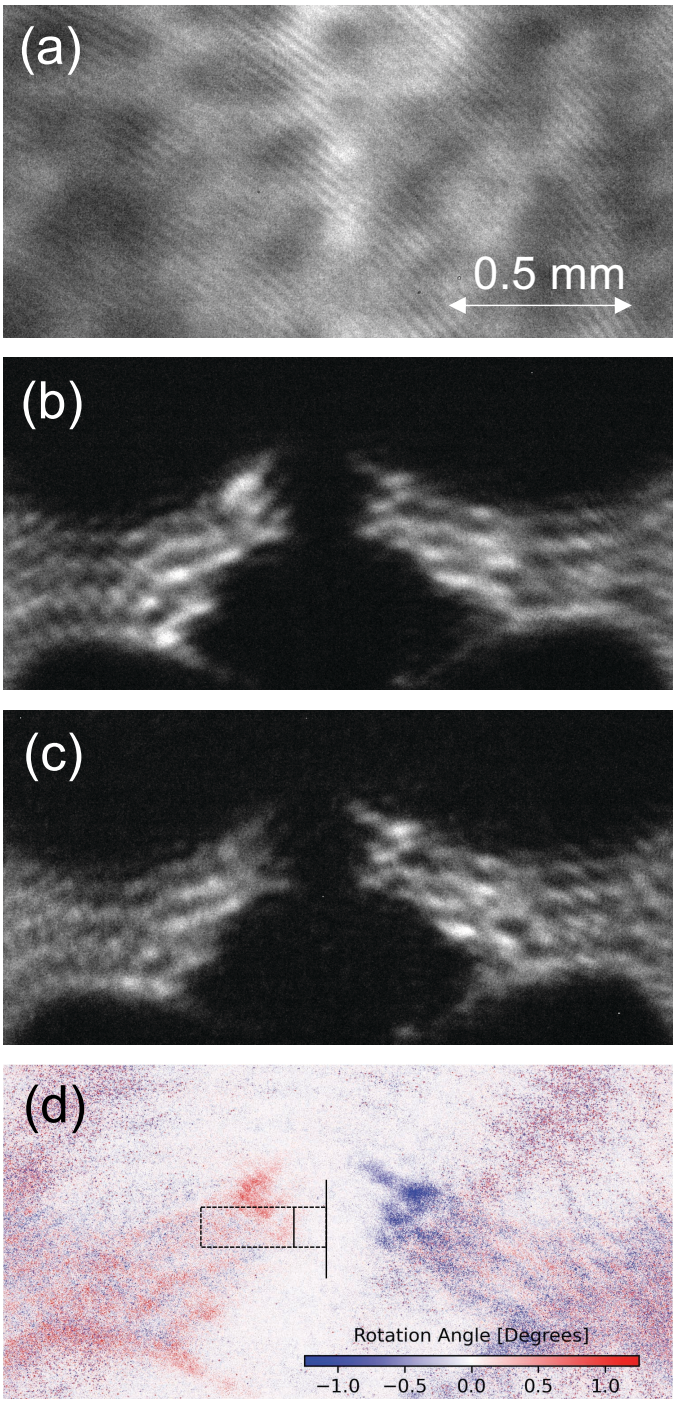

Figure 4.15: Data from shot 2534, a two-wire, 25-µm-wire-diameter, Ag X-pinch experiment: (a) post-shot polarimetry background; (b) smoothed channel 1 polarogram; (c) smoothed channel 2 polarogram; and (d) the Faraday rotation image calculated from (a)–(c). The dashed box in (d) denotes the region used for producing the enclosed current profiles and the magnetic pressure profiles of Figs. 4.17, 4.18, and 4.19. The solid lines within the dashed box in (d) denote the edge of the dense core and center axis. Analyzer β was set to 3.5°.

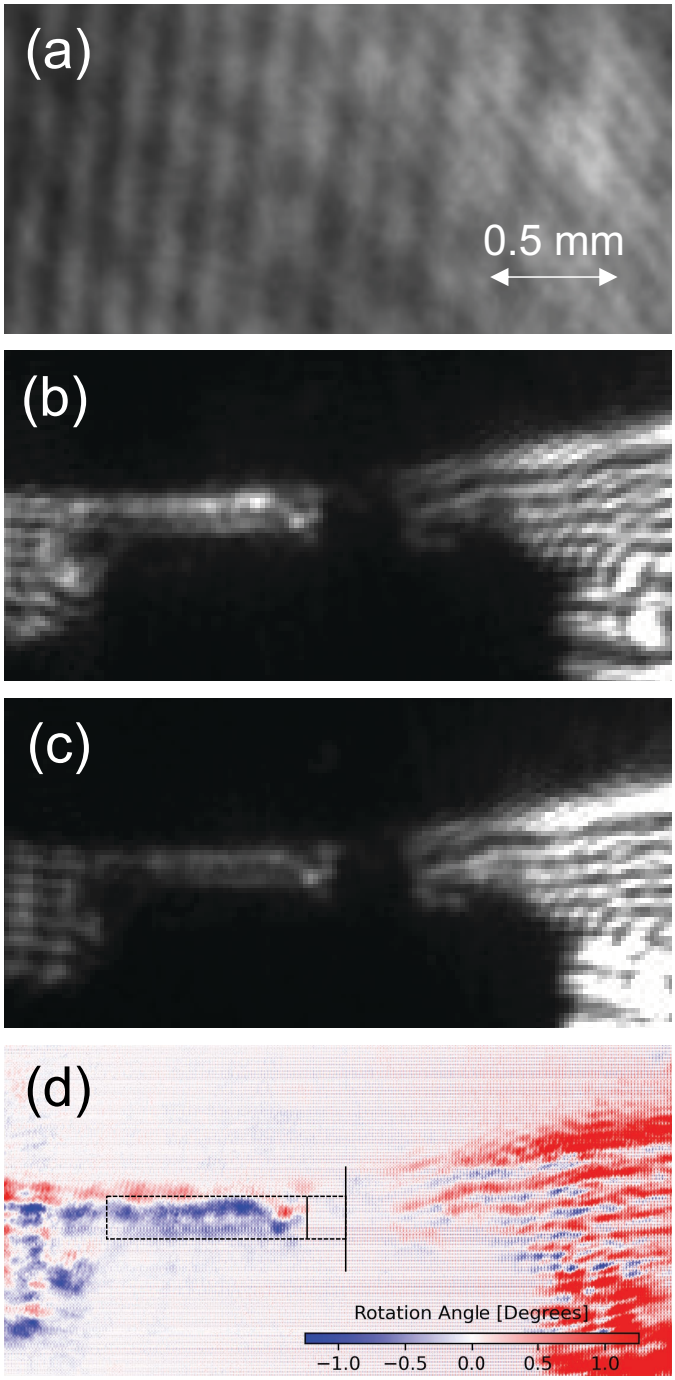

Figure 4.16: Data from shot 2933, a six-wire, 35-μm-wire-diameter, Mo X-pinch experiment: (a) smoothed channel 1 polarogram; (b) smoothed channel 2 polarogram; (c) post-shot polarimetry background; and (d) the Faraday rotation image calculated from (a)–(c). The dashed box in (d) denotes the region used for producing the enclosed current profile and the magnetic pressure profile of Fig. 4.21. The solid lines within the dashed box in (d) denote the edge of the dense core and center axis. Analyzer β was set to 3.0°.

were consistently around $\lesssim 1^\circ$, save for a few regions speculated to be areas of increased density (due to loss of interference fringes in these regions). Dashed boxes mark the the regions used in extracting radial current profiles with the center axis and edge marked in solid black. A single radial line-out is produced in each case from averaging over the height of the boxed region. A line-out of the density is similarly taken from the areal density distributions in Figs. 4.12(c) and 4.13(c) over the same regions for the corresponding shot. Due to a thin neck-down region in shot 2933, apparent in Fig. 4.16 though the interferogram is not shown, only one fringe was traceable in to the dense plasma edge. The corresponding density line-out within the region was manually approximated with a piece-wise linear fit.

With both the areal density and rotation profiles extracted, they can either be Abel inverted and combined to produce the radial magnetic field profile following Eqs. 4.3 and 4.4, or they can be directly combined into the average parallel magnetic field profile via Eq. 4.6. Abel inversion was attempted on multiple occasions, but the low sampling density of the fringe shifts and the edge diffraction within the rotation angle profile tended to introduce sources of noise that result in nonphysical inverted profiles. It does have the use of at least showing where certain shifts in the profiles occur, as these shifts typically correspond to regions where the inversion fails to handle the large change (e.g. regions where the signal levels spike or where negative density values are present). In a few cases, with sufficient signal quality and sufficient smoothing of the extracted line-outs, the Abel inversions resulted in reasonable (though noisy) magnetic field profiles. However, for the most part, because of the noise, the Abel inversions were used primarily for the purpose of corroborating the field profiles (particularly the peak values) obtained from the approximate methods described by Eqs. 3.6 and 3.10.

4.5.1 Current Distributions and Magnetic Pressure

Referring back to Sec. 4.1 and Eqs. 4.9 and 4.10, there is the free length scale parameter, L_0, that must be chosen to provide the proper signal magnitude if Abel inversion is not used. There are two "bounding" interpretations for L_0 based on known parameters. The first is that there will

be a maximal L_0 for which the extracted current trace will match the amplitude captured by the anode Rogowski coil, as it would not be possible to have greater current to the load. By normalizing the maximum current enclosed to the amplitude captured by the Rogowski coil, we are assuming that there is no shunt current loss at radial locations between the outer edge of the Faraday rotation imager field of view (at r=X mm) and the major radius of the Rogowski coil (at r=11 mm). The second is that for any fully enclosed current surrounded by a region devoid of further current density, the magnetic pressure profile should decay as $1/r^2$, and the current enclosed profile should be constant with r, even in vacuum. However, Faraday rotation imaging is not possible for probed regions containing only vacuum (or sufficiently low plasma density). The radius above which the plasma density becomes too low for a Faraday rotation signal to be obtained will result in nonphysical and nonsensical magnetic pressure and current enclosed values, often appearing as regions of large amplitude noise at large radius. The transition from expected radial dependence to regions of large amplitude noise often occurs abruptly at a particular radial location. Thus, we may use this transition point to set the plasma length scale, L_0. Here, L_0 is twice the radius of where this transition occurs, since in our approximation, L_0 is defined as the diameter of the plasma column, rather than the radius of the plasma column. If no transition point is visible within the radial field of view, then an assumption can be made from either a reasonable point of decay in the magnetic pressure curve or from the length scale of measurable density variation. Beyond such points, the amount of integrated rotation is likely negligible.

The first dataset to have an enclosed current profile properly extracted was shot 2534. Figures 4.17 and 4.18 show the resulting average current enclosed as a function of distance from the center of the plasma neck for the X-pinch images shown in Fig. 4.12 and Fig. 4.15. The difference between them is that Fig. 4.17 assumes L_0 from the $1/r^2$ deviation radius, $r_{\mathrm{dev}} \approx 325$ μm (alternate side of the neck has a deviation at r = ∼375 μm), so $L \approx 2r_{\mathrm{dev}} \approx 700$ μm, while Fig. 4.18 assumes $L = 2500$ μm so that the current enclosed profile levels off at a maximum value that matches the Rogowski coil measurement of 133 kA. Interestingly, this value of 2500 μm is roughly the extent of the entire implosion region—i.e., the radial span of the region between the remaining lobes of the

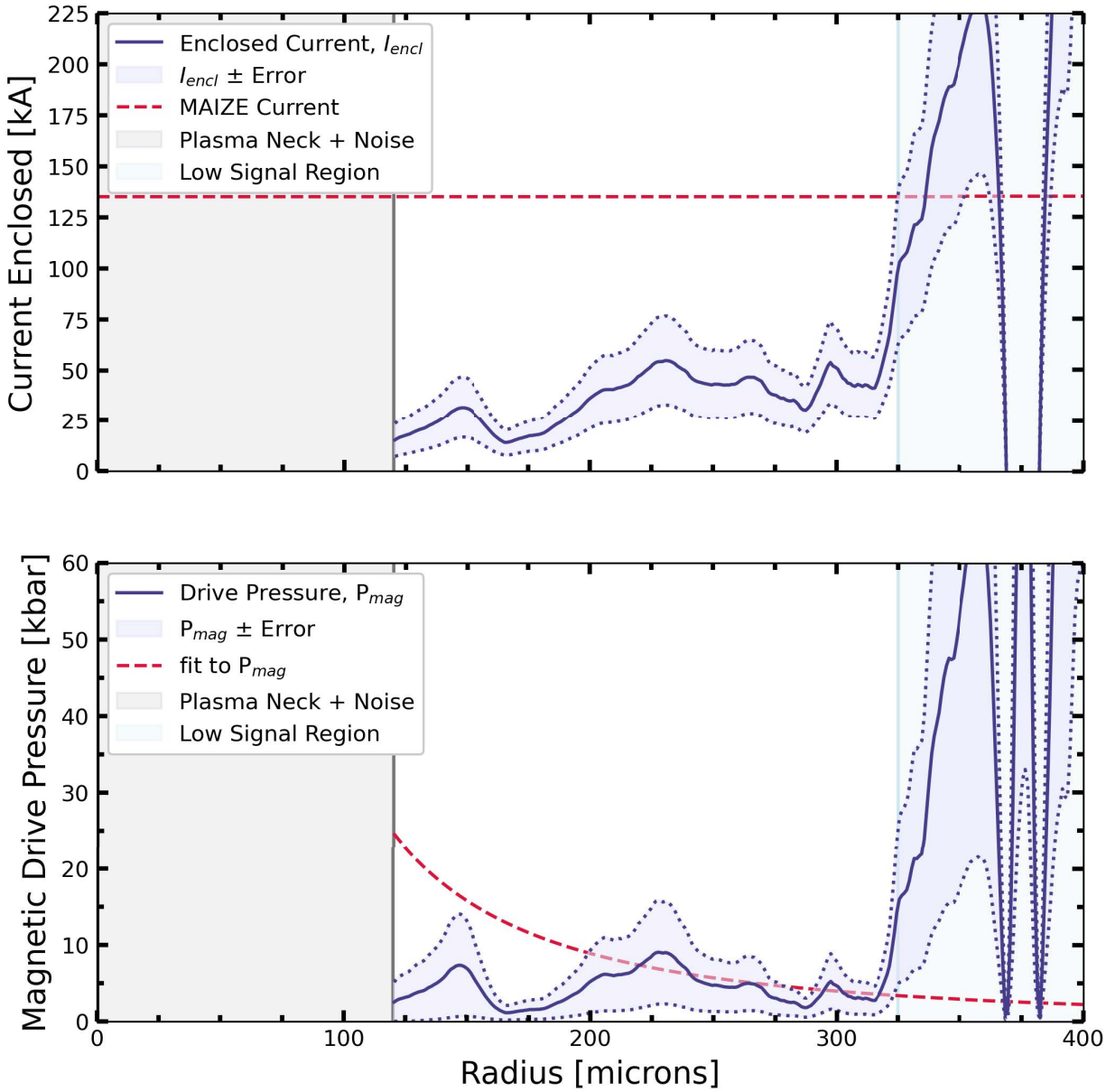

Figure 4.17: Extracted profiles from shot 2534 using a scale parameter of $L = 700$ µm. (top) Current enclosed as a function of radius from the center of the X-pinch neck. The shaded region bounded by the dotted line gives the calculated errors in the enclosed current measurement. Plotted for reference in red is the 133 kA of load current measured by the anode Rogowski coil on MAIZE at the time of the Faraday rotation imaging. Note that the anode Rogowski coil resides at a radius of 11 cm. (bottom) Magnetic drive pressure as a function of radius from the center of the X-pinch neck with shaded region bounded by the dotted line giving the calculated errors in the drive pressure measurement. The overlaid dashed red line shows a fit with a $1/r^2$ dependence. Note that a $1/r^2$ dependence is expected to occur outside of the radius in which 100% of the total drive current is enclosed (*cf.* Eq. 1.1).

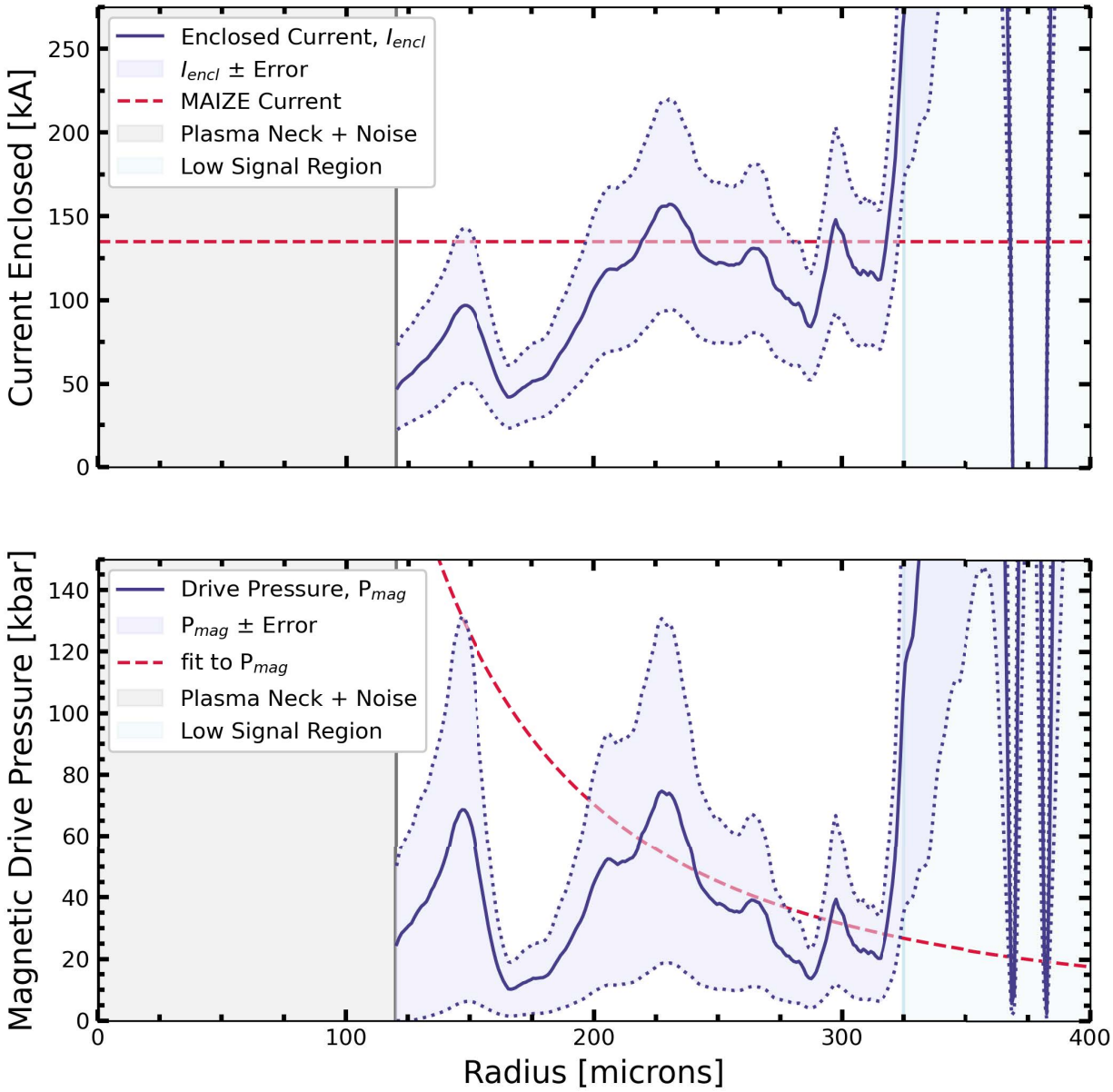

Figure 4.18: Extracted profiles from shot 2534 using a scale parameter of $L = 2500$ µm. (top) Current enclosed as a function of radius from the center of the X-pinch neck. The shaded region bounded by the dotted line gives the calculated errors in the enclosed current measurement. Plotted for reference in red is the 133 kA of load current measured by the anode Rogowski coil on MAIZE at the time of the Faraday rotation imaging. Note that the anode Rogowski coil resides at a radius of 11 cm. (bottom) Magnetic drive pressure as a function of radius from the center of the X-pinch neck with shaded region bounded by the dotted line giving the calculated errors in the drive pressure measurement. The overlaid dashed red line shows a fit with a $1/r^2$ dependence. Note that a $1/r^2$ dependence is expected to occur outside of the radius in which 100% of the total drive current is enclosed (*cf.* Eq. 1.1).

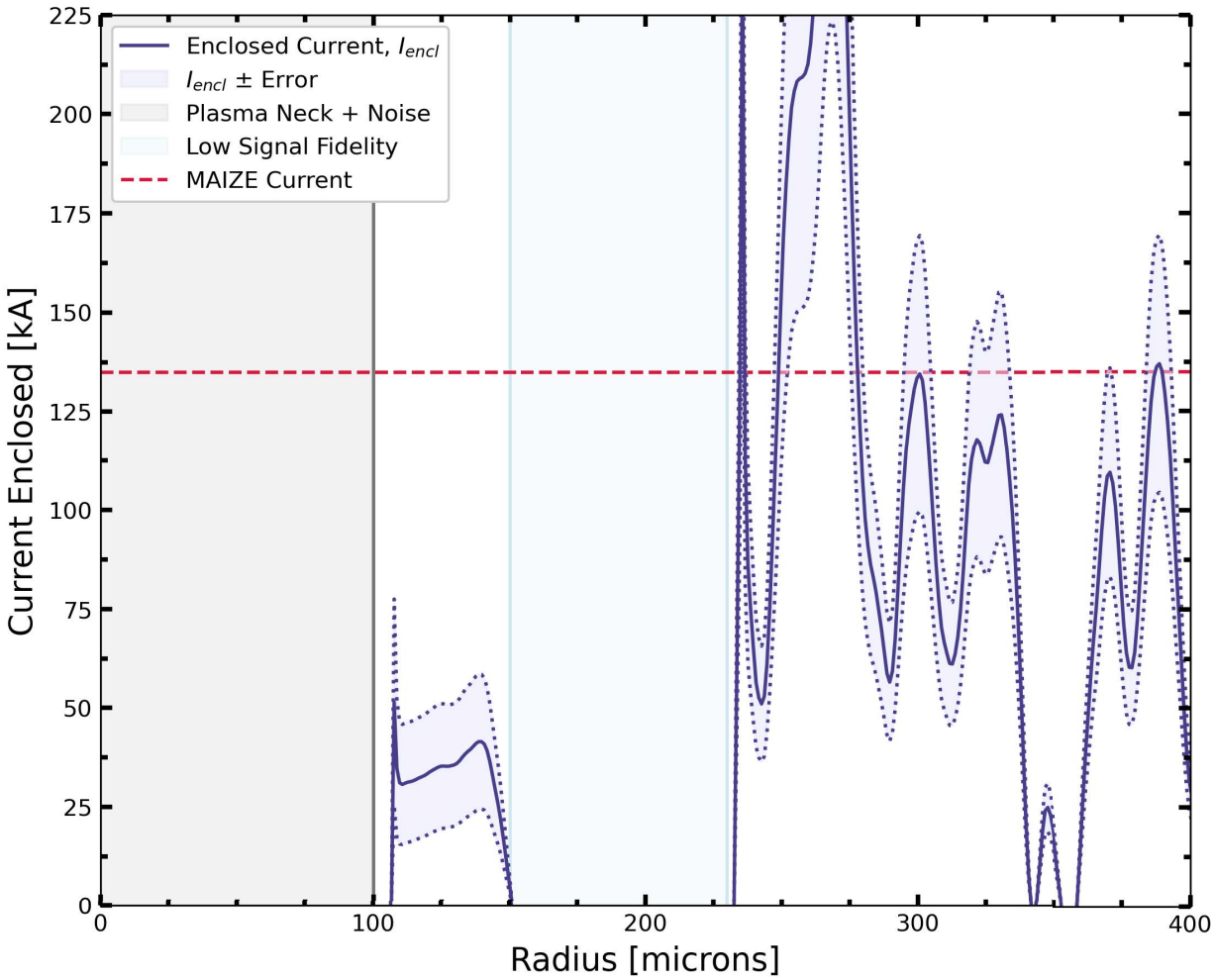

Figure 4.19: Abel inverted current enclosed profile as a function of radius from the center of the X-pinch neck from shot 2534. The shaded region bounded by the dotted line gives the calculated errors in the enclosed current measurement. Plotted for reference in red is the 133 kA of load current measured by the anode Rogowski coil on MAIZE at the time of the Faraday rotation imaging. Note that the anode Rogowski coil resides at a radius of 11 cm. Abel inversion causes several artifacts that give low fidelity in portions of the signal highlighted in light blue. Compare features and magnitude to the current enclosed distribution in Fig. 4.18.

ablated wires above and below the neck. While matching the $1/r^2$ deviation radius, the choice of $L = 700$ μm in Fig. 4.17 results in the current enclosed profile going directly from 40% of the total current measured by the Rogowski coil to an infeasible 200% of the total current measured by the Rogowski coil near the boundary of signal loss. Despite the poor matching, Fig. 4.17 provides a lower bound for the magnitude of the current enclosed. By definition, the trace of Fig. 4.18 is the upper bound for the magnitude of the current enclosed.

To provide some insight into which trace is closer to the true magnitude, the Abel inverted trace was calculated and is presented in Fig. 4.19. Notably, the noise already present in the trace before inversion is amplified, particularly in the region of low signal strength, which is now distorted to a nonphysical value. Overall, the radial features of the distribution still match reasonably well with Figs. 4.17 and 4.18. In terms of magnitude, the region of $r \geq 300$ μm the current enclosed matches reasonably well with the Rogowski coil, implying that the trace of Fig. 4.18 is closer to correct and that current is not being shunted within the A-K gap at radii beyond the Faraday rotation imager's field of view. This comparison also shows that the approximated traces are reasonably valid substitutes for the full Abel inverted profiles specifically in preserving the main features of the distributions and presenting them with less noise. The drawback of uncertainty in the choice of L_0 is still present, but as shown, the choice in L_0 can be constrained by the Abel inverted results.

The nature of why the discrepancy in the choice of L_0 exists is uncertain and seemingly unique to shot 2534. For the two remaining shots processed and presented in this chapter, shots 2241 and 2933 (Figs. 4.20 and 4.21, respectively), setting $L = 2r_{\text{dev}}$ resulted in reasonable matches to the total load current measured by the Rogowski coil. Also note that shots 2534 and 2241 were intended to be nominally equivalent shots. Both were 2×25 μm Ag X-pinches producing singular x-ray bursts with peak currents of about 150 kA and rise times of about 100 ns, further confusing why the necessary L_0 parameters are dissimilar. Such a discrepancy in L_0 would be a minimum requirement for spotting when current is shunted in the A-K gap before reaching the X-pinch, particularly if the Abel inverted magnitude additionally shows a total enclosed current below that measured by the Rogowski coil. This does beg the question that if the Abel inverted trace is needed, why not solely

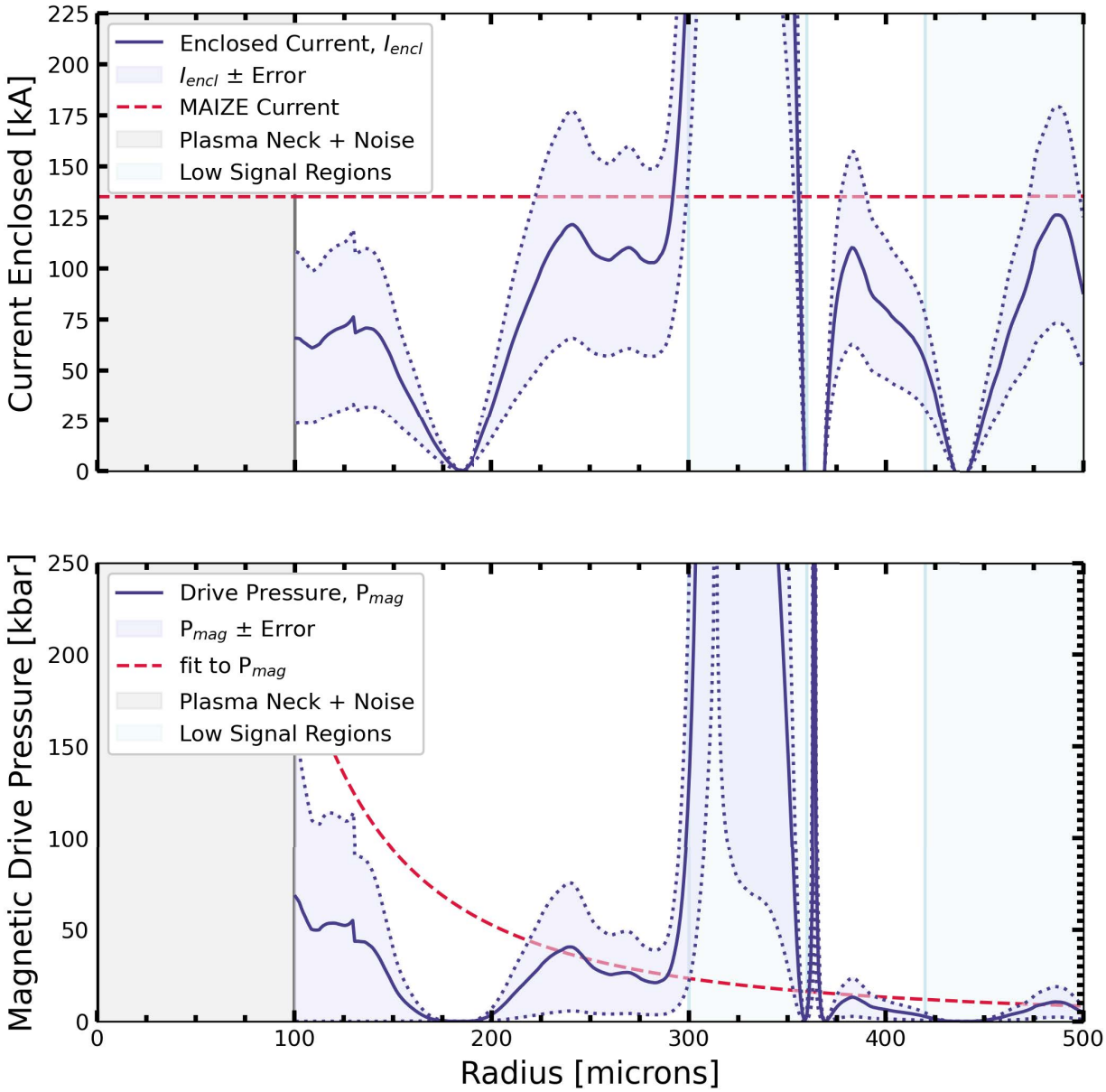

Figure 4.20: Extracted profiles from shot 2241 using a scale parameter of $L = 800$ µm. (top) Current enclosed as a function of radius from the center of the X-pinch neck. The shaded region bounded by the dotted line gives the calculated errors in the enclosed current measurement. Plotted for reference in red is the 135 kA of load current measured by the anode Rogowski coil on MAIZE at the time of the Faraday rotation imaging. Note that the anode Rogowski coil resides at a radius of 11 cm. (bottom) Magnetic drive pressure as a function of radius from the center of the X-pinch neck with shaded region bounded by the dotted line giving the calculated errors in the drive pressure measurement. The overlaid dashed red line shows a fit with a $1/r^2$ dependence. Note that a $1/r^2$ dependence is expected to occur outside of the radius in which 100% of the total drive current is enclosed (*cf.* Eq. 1.1).

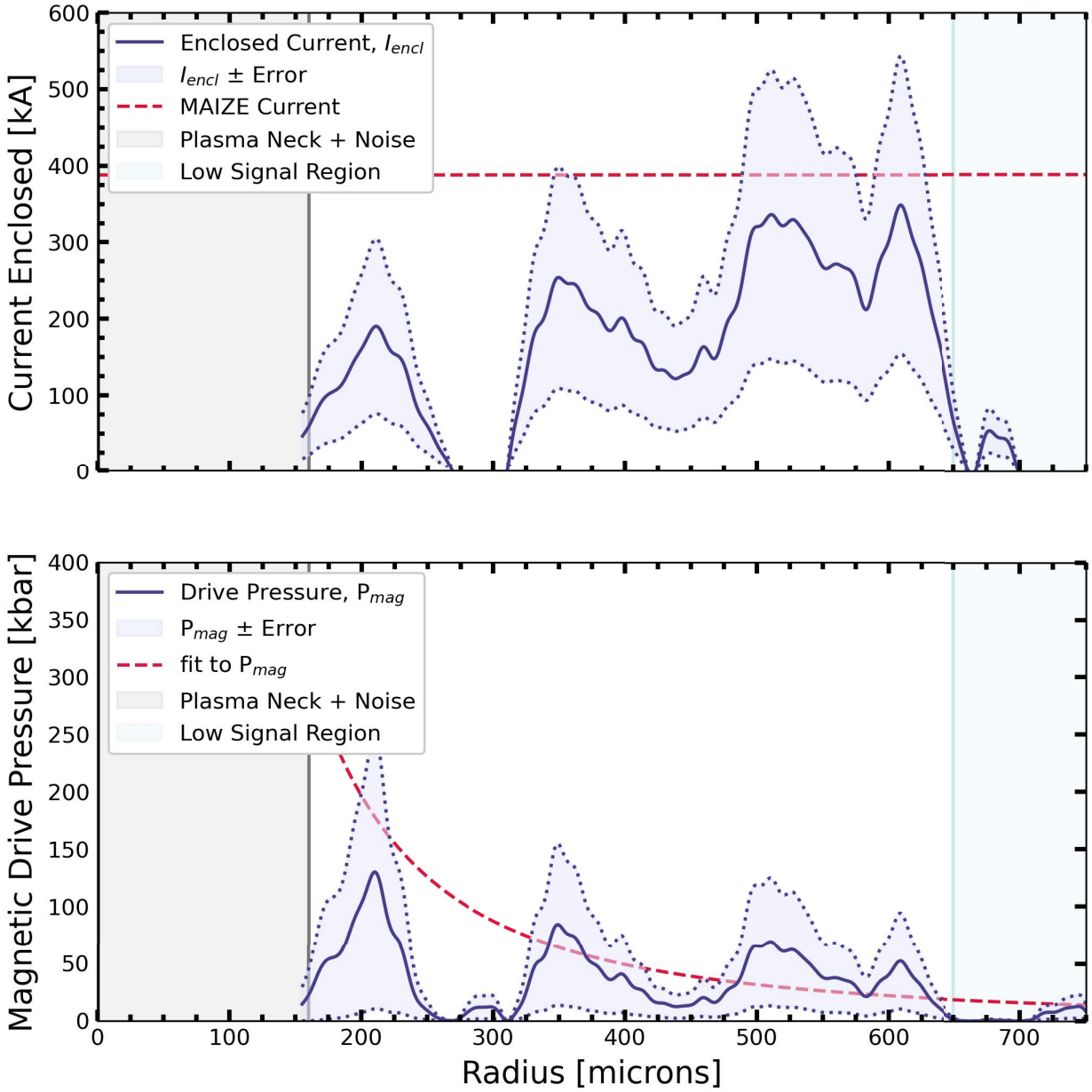

Figure 4.21: Extracted profiles from shot 2933 using a scale parameter of $L = 2000$ µm and recorded 13 ns post first x-ray burst and 2 ns before a second x-ray burst. (top) Current enclosed as a function of radius from the center of the X-pinch neck. The shaded region bounded by the dotted line gives the calculated errors in the enclosed current measurement. Plotted for reference in red is the 388 kA of load current measured by the anode Rogowski coil on MAIZE at the time of the Faraday rotation imaging. Note that the anode Rogowski coil resides at a radius of 11 cm. (bottom) Magnetic drive pressure as a function of radius from the center of the X-pinch neck with shaded region bounded by the dotted line giving the calculated errors in the drive pressure measurement. The overlaid dashed red line shows a fit with a $1/r^2$ dependence. Note that a $1/r^2$ dependence is expected to occur outside of the radius in which 100% of the total drive current is enclosed (*cf.* Eq. 1.1).

use it? The answer is that majority of the Abel inversion attempts have resulted in far too much noise and oscillation to be useful.

With that said, we can revisit what the processed traces actually say. This will be done considering all three shots simultaneously and proceeding from the location of the neck edge to larger radii. All three shots had plasma neck diameters of $\sim$200–300 μm corresponding to radii of $\sim$100–150 μm. While other regions of the same plasma necks may have had a slightly smaller diameter (but were otherwise not conducive to extraction of a profile), the dearth of data collected with diameters of $\leq$100 μm indicates that these are the likely the minimal radii that can be measured by the present instantiation of the diagnostic.

Advancing outward in radius in the line-outs for all three shots, there seems to be a pattern of a fractional current enclosed ($\sim$40–60% of the total), be it a loss of signal or low signal dip, followed by a recovery to full or close to full current. Best seen in Fig. 4.14(d), where a clear high-low-high pattern of rotation intensity is seen radially outward from the dense neck edge, this seems to be a consistent feature resulting from the noise pattern off of the neck. The dip occurs at $\sim$175–200 μm for shots 2534 and 2241 and at $\sim$250–300 μm for shot 2933. It is speculated that the motional blurring from the laser pulse length being longer than the development time of the neck cascade at small radii might produce notable image artifacts, as dense plasma imploding inwards allows later portions of the 2-ns laser pulse to pass and reach the detectors. This may present an alternate explanation to the reduced signals at radii immediately outside of the neck region. Instead of reduced rotation due to distributed current, there is simply a reduction in signal due to the plasma dynamics. A counterargument to this theory is that even with the reduction in intensity due to motional blurring, the intensity should still ramp to full intensity at large radius, where the laser probe is not obstructed by the imploding plasma dynamics at small radius. Therefore, the current enclosed profile should also ramp up to the full current measured by the Rogowski coil, provided there is no shunt current losses occurring between the radial locations of the Rogowski coil and the Faraday rotation imager's field of view. While the signal dips make it difficult to interpret, the current enclosed at the minimal measurable edges are non-zero and do not appear to trend in a way

consistent with a monotonically imploding edge, implying that at least an additional method would be needed to explain the profile.

Both shots 2534 and 2241 were 2-wire Ag X-pinches with a measured anode current at the time of data collection of about 135 kA while shot 2933 was a 6-wire Mo X-pinch with a measured anode current at the time of data collection of about 388 kA, nearly 3× higher. Considering the similarity of the enclosed current traces between shots 2534 and 2241, but dissimilarity to shot 2933, this points to potential material or current magnitude dependencies. With such a low sample size, this can alternatively be explained by the differences in starting conditions, particularly the difference in wire number and resultant initial linear mass in the neck region being on the order of 3× greater in the case of six wires versus two. For the sake of brevity throughout the remainder of the chapter, shots 2534 and 2441 may be referred together, where appropriate, as the "Ag X-pinches."

For all three profiles in the top plots of Figs. 4.18, 4.20, and 4.21, the enclosed current beyond the radius of the signal dip decently matches the Rogowski coil measurement. Shot 2933 potentially has two plateaus, the first spanning from ∼300–500 μm with ∼75% of the total current before increasing to ∼95–100% at ∼500 μm. This could also be a single plateau or a gradual increase over the entire region. For the two Ag X-pinches, the enclosed current matches 100% over the valid signal region before loss of signal fidelity. At larger distances from the neck (r >350–400 μm for the Ag X-pinches and $r > 650$ μm for shot 2933), the signal degrades to the point where it is nearly indistinguishable from noise on a local scale, denoted by the shaded region labeled "Low Signal Region" in the respective plots.

Similar trends are seen in the magnetic pressure profiles given in the bottom plots of Figs. 4.18, 4.20, and 4.21. In the regions corresponding to the constant enclosed currents, the magnetic pressure profile is fitted to a curve following a $1/r^2$ dependence that matches the data reasonably well. This is encouraging because a $1/r^2$ dependence is expected to occur outside of the radius in which 100% of the total drive current is enclosed (*cf.* Eq. 1.1). At smaller radii, in the region of reduced enclosed current, the magnetic pressure falls below the fitted $1/r^2$ curve because the current density is distributed in this region—i.e., the current is not full contained within the dense neck region. For

the low current Ag X-pinch shots, this means maximal drive pressures of $\sim$80–100 kbar at radii of $\sim$125–150 μm. For the high current Mo X-pinch shot, the maximal drive pressure measured was only minimally higher at $\sim$150 kbar but at the larger radius of $\sim$200 μm. Making a final quick calculation, assuming the current remains distributed such that $\sim$40–60% of the current is contained within the dense neck as it collapses to minimal radii, then the maximal pressures at radii of $\sim$3 μm only reach pressures on the order of 100s of Mbar.

4.6 Summary

This chapter presented the math, design, and results for the Faraday rotation imaging diagnostic fielded on the MAIZE LTD facility. Despite non-ideal conditions around the dense neck of an X-pinch, with low coronal areal density ($\sim 10^{17}$ cm^{-2}) and small rotation angles (averaging $\leq 1^{\circ}$), the diagnostic had sufficient sensitivity to produce viable interferometric and polarimetric data. These data were used to extract the magnetic field, enclosed current, and magnetic pressure profiles as functions of radius around the X-pinch neck. The resulting profiles strongly point to a distribution of the drive current within the surrounding coronal plasma on the order or 50%. The full current density delivered to the load is enclosed within a radius of $\sim$200–300 μm, and it does not appear to have portions distributed beyond the overall structure of the implosion region at very large radii. Consequently, low drive pressures are recorded at measured maxima of $\sim$100–150 kbar with extrapolated maxima only reaching 100s of Mbar. The distribution of current density and the limits of magnetic drive pressure at highly compressed radii ($<$100 μm) remains an open question immeasurable with the current diagnostic.

CHAPTER 5

Deuterated Fiber X-Pinch Experiments

5.1 Motivations and Background

Neutron production and characterization is actively studied over many pulsed-power load configurations, namely z-pinches, gas-puff z-pinches, and dense plasma focuses [82, 83, 84, 85, 86, 87, 88, 89, 90]. X-pinches have been a slower exception. Similar to using the standard configurations of an X-pinch to produce temporally and spatially small x-ray sources, there have been a lesser number of various explorations into whether an X-pinch could be similarly used for neutrons. These experiments have made use of cryogenic D_2 fibers, CD_2 fibers, or D_2 loaded Pd wires [91, 92, 93]. The most relevant of these experiments were those conducted on the former 1.5-MV, 4.5-Ω LION accelerator at Cornell University [94]. This set of experiments similarly investigated CD_2 fiber X-pinches, but in a multi-wire configuration using two CD_2 fibers. By contrast, this dissertation investigates hybrid X-pinches using a single CD2 fiber on the low-impedance MAIZE facility.

The basis of neutron production in these experiments is deuterium-deuterium (D-D) fusion reactions taking place in the X-pinch plasma. In general, the basis of these reactions are two light nuclei managing to interact and fuse into a product nucleus while emitting a neutron or other additional products. To achieve this, the interacting nuclei require sufficient energy to overcome the coulomb repulsion between the protons in the separate nuclei. In a z-pinch plasma, there are two main ways that this occurs. The first is simply thermonuclear fusion. Thermonuclear fusion overcomes the coulomb barrier through heating a plasma to temperatures sufficient for overcoming the repulsion, which requires temperatures on the order of 10s of millions of degrees kelvin. In

actuality, the effect of quantum tunneling allows for nuclei with lower energies to still react, though this will occur at a much lower rate. Furthermore, sufficient density is required to increase the probability of interaction between the fusion nuclei. In z-pinches, the temperatures and densities required to efficiently catalyze these reactions are typically achievable only within the stagnated z-pinch column after implosion, and only with sufficiently high drive currents. Thermonuclear fusion yield scales as I^4 and achieves only a significant fraction of the total fusion yield on high current drivers like SATURN or Z [95, 96].

The fusion mechanism in lower-current z-pinches, and in X-pinches, is through a beam-target mechanism [95, 97]. Here, ions are accelerated to the kinetic energies necessary to overcome the coulomb barrier and directed into a stationary target. As the target is an unionized solid, a significant portion of the beam energy gets dissipated through ionization of the material or bremsstrahlung radiation [98]. In thermonuclear fusion, assuming that there is no net velocity of the plasma, the produced neutrons are emitted isotropically. For net motion of the plasma, and in the case of an accelerated deuteron beam, the emission remains isotropic when viewed in the center-of-mass frame. Shifting to the laboratory frame translates then to an anisotropic emission, and is therefore a strong indication of beam-target interactions.

For z-pinches, deuterons are accelerated due to the induced electric fields formed via instability modes. For X-pinches in particular, this occurs primarily in the minidiode formed after the break of the plasma-neck and secondarily within the smaller $m = 0$ sausage modes during the neck cascade [95, 97]. As the neck breaks, there is a rapid change in the inductance and resistance of the X-pinch, charge builds within the plasma on both sides of the break, and a strong electric field is generated across the minidiode. As the full description of the voltage drop is $V = L\frac{dI}{dt} + I\frac{dL}{dt} + IR$, the exact values of the changing inductance and resistance of the diode make it difficult to produce a clear value. If we want to make a very rough, back-of-the-envelope calculation of the induced electric fields from the inductance change, then we can assume $E = {}^{V}/_{d}$, $V \approx \frac{d}{dt}(LI)$, $\Delta L \sim$15 nH, $\Delta I \sim$10 kA, $\Delta t \sim$1-5 ns, and $d \sim$0.2–1 mm. This gives values on the order of 1–10 MV/mm. Of course, this value ignores scattering and is an average of the time and distance scales of the cascade

and minidiode formation. Nonetheless, even if we assume the average deuteron is accelerated to a fraction of the maximum possible kinetic energy, these energies are still well into the multi-keV range to allow for beam-target fusion to occur.

Written out, the deuterium-deuterium fusion reactions are as follows [99]:

$$ {}^{2}_{1}\mathrm{D} \;+\; {}^{2}_{1}\mathrm{D} \;\longrightarrow\; {}^{3}_{2}\mathrm{He}\;\;(0.82\,\mathrm{MeV}) \;+\; {}^{1}_{0}\mathrm{n}\;\;(2.45\,\mathrm{MeV})\;\;(50\,\%) \tag{5.1} $$

$$ {}^{2}_{1}\mathrm{D} \;+\; {}^{2}_{1}\mathrm{D} \;\longrightarrow\; {}^{3}_{1}\mathrm{T}\;\;(1.01\,\mathrm{MeV}) \;+\; {}^{1}_{1}\mathrm{p}\;\;(3.02\,\mathrm{MeV})\;\;(50\,\%) \tag{5.2} $$

Equations 5.1 and 5.2 are branches of the D-D reaction, with effectively a 50%-50% branching ratio, termed the "neutron branch" and the "proton branch" from their production of either a neutron and a proton, respectively. Additionally, secondary reactions can occur, where the primary deuterons interact with the products of the primary D-D reactions:

$$ {}^{2}_{1}\mathrm{D} \;+\; {}^{3}_{1}\mathrm{T} \;\longrightarrow\; {}^{4}_{2}\mathrm{He}\;\;(3.52\,\mathrm{MeV}) \;+\; {}^{1}_{0}\mathrm{n}\;\;(14.06\,\mathrm{MeV}) \tag{5.3} $$

$$ {}^{2}_{1}\mathrm{D} \;+\; {}^{3}_{2}\mathrm{He} \;\longrightarrow\; {}^{4}_{2}\mathrm{He}\;\;(3.6\,\mathrm{MeV}) \;+\; {}^{1}_{1}\mathrm{p}\;\;(14.7\,\mathrm{MeV}) \tag{5.4} $$

For the majority of experiments, the main focus is on the measurement of the 2.45 MeV neutrons produced from the neutron branch. Typically these measurements cover the neutron yield, production time and duration, anisotropy, and energy spectrum.

At present, all measurements made of deuterated X-pinches have been conducted on high-impedance or high-voltage drivers. It was still an open question of if or how the behavior of a deuterated X-pinch would change when driven by a low-impedance, low-drive-voltage LTD, and the comparative characteristics of the neutron emission. Running the deuterated X-pinches on MAIZE was only the second neutron producing load for the facility. Deuterium gas-puff z-pinches had previously been fielded on MAIZE, producing average neutron yields on the order of 10^7 and a peak yield of 1.3×10^8 neutrons [89]. The gas-puff z-pinch experiments were done in a 2022 experimental campaign in collaboration with Prof. Daniel Klir's team from the Czech Technical

University in Prague (CTU).

The original concept for a deuterated X-pinch experiment on MAIZE was to utilize loaded palladium wires in a multi-wire geometry matching the prior X-pinches driven on the facility. Without a true avenue to properly adding and characterizing the deuterium gas within the wires from creation up to implosion, the experiment plan was never significantly investigated. During the gas-puff collaboration, the use of deuterated polyethylene ($[CD_2]_n$) fibers in a hybrid X-pinch configuration was suggested by Prof. Daniel Klir. These experiments were similarly performed in collaboration with Prof. Klir's group at CTU, with the two groups having different points of focus. Instead of monitoring the products of the neutron branch, the Klir group had interest in fielding proton diagnostics to measure the 3 MeV protons produced from the proton branch of the D-D reaction. Their diagnostics are not discussed in detail apart from mentioning their purpose and fielding for completeness.

The main goals for the CD_2 fiber X-pinch experiments on the MAIZE LTD, listed in relative order of ability to measure, were the following:

1. Determine the ability of MAIZE to drive non-metallic X-pinches.
2. Measure the neutron yields achievable in a deuterated hybrid X-pinch on a low-impedance driver.
3. Measure the time of neutron emission.
4. Measure the correlation between neutron emission and x-ray emission from the pinch.
5. Measure the neutron production duration.
6. If possible:
   - Estimate production anisotropy.
   - Estimate energy spectrum from nTOF pair.

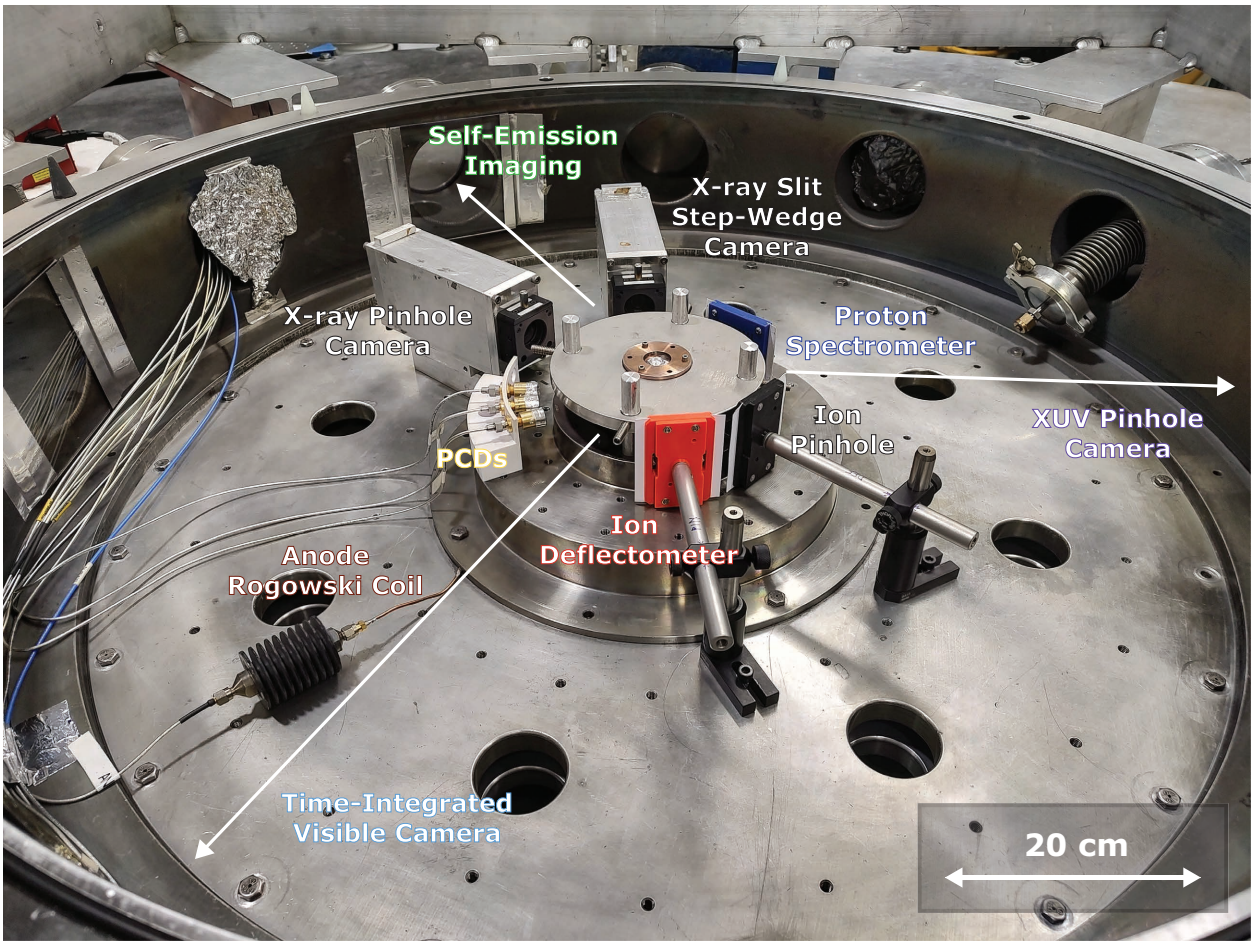

Figure 5.1: MAIZE vacuum chamber during a deuterated polyethylene hybrid X-pinch experiment. Shown are the in-chamber diagnostics and the lines of sights for the external optical diagnostics. Not shown are the neutron diagnostics placed around the vacuum chamber.

5.2 Experimental Design

The X-pinch hardware required only the modification of the anode plate and return posts as detailed in Sec. 3.1 to allow for finer ability to adjust the conical electrode spacing (and consequently the length of CD_2 fiber between them). An image of the hardware with the full diagnostic suite is provided in Fig. 5.1.

The printed housings surrounding the main hardware are the proton spectrometer, ion pinhole detector, and ion deflectometer diagnostics fielded by the CTU collaborators aiming to measure the proton and ion energy and distributions produced from the deuterated X-pinch. The remaining diagnostics span the full range of those fielded on prior metallic X-pinch experiments. All four types

of available imaging diagnostics were fielded: the fast-framing camera for visible self-emission imaging, the quad-frame XUV pinhole camera, the x-ray pinhole camera, and a time-integrated visible camera. While significant signal levels were not expected, the x-ray slit step-wedge camera was included in the event that sufficiently hard and bright x-ray bursts were achieved. Similarly, PCDs with filter pairs were also fielded to discriminate between the hardness of various signals. Not pictured here are the various neutron diagnostics discussed below.

5.2.1 Neutron Diagnostics

The components for two neutron time-of-flight (nTOF) detectors were supplied from the University of Michigan's Center for Ultrafast Optical Science (CUOS). These consisted of two $\varnothing$15 cm $\times$ 2.5 cm EJ-204 scintillators with coupled light cones and two Hamamatsu R2083 photomultiplier tubes (PMTs) in an H2431-50 assembly. The scintillator was optically coupled

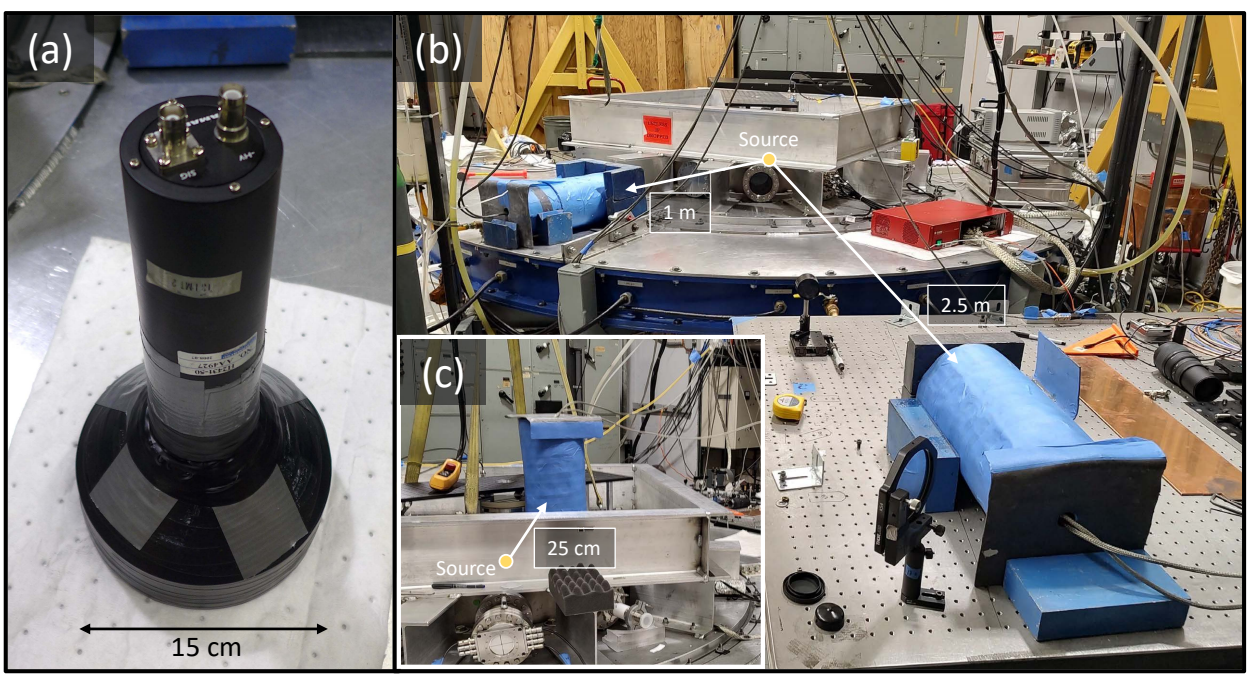

Figure 5.2: (a) An nTOF detector composed of a Hamamatsu H2431-50 PMT assembly and a $\varnothing$15 cm x 2.5 cm EJ-204 scintillator with light cone. (b) The near and far positions of the nTOF detectors for radial lines of sight, roughly 1 and 2.5 m from the source, respectively. (c) The detector placement for near-axial line of sight on the top lid of the vacuum chamber, roughly 0.25 m from the source.

to the PMT without the use of optical grease as it was unavailable at the time of the experiments. Figure 5.2(a) shows the pair of coupled components as the final nTOF assembly. Figures 5.2(b)–(c) show the radial and axial line-of-sight positions that the two detectors were variously fielded in. The H2431-50 PMTs have a maximum bias voltage rating of −3.5 kV, though they were biased between −(1.2–1.6) kV depending on the detector, distance, and expected response. The detector signals were recorded with a Tektronix TDS3054 (0.5 GHz) oscilloscope, well within the resolution of the detector response.

The basic response time of the detectors were determined from simple measurement of the cosmic response. An example trace is provided by Fig. 5.3. As can be seen, the response is rather broad with a full-width at half-max (FWHM) of ∼12 ns. This is slightly strange as the PMT has a sub-ns rise time, while the scintillator has a pulse width of 2.2 ns, so the detector response was expected to be much faster, perhaps ∼5 ns. This is possibly due to a combination of scintillator geometry and coupling. While the large scintillator volume is great for increased signal, it also

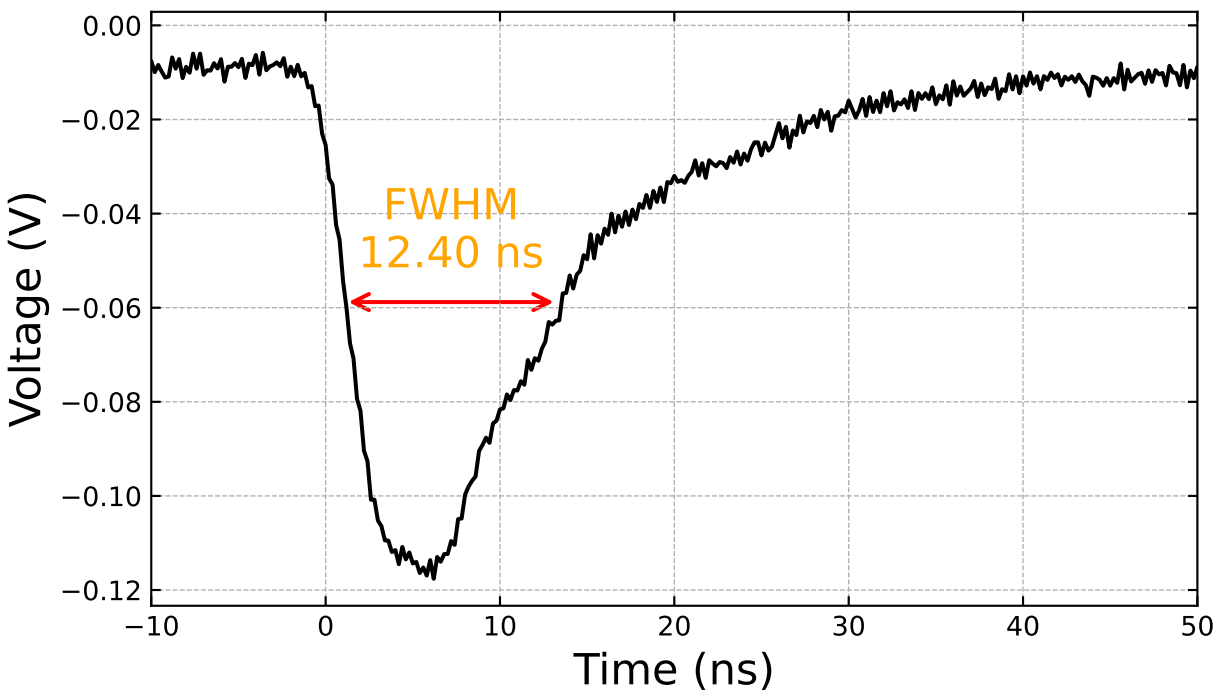

Figure 5.3: Sample response from one of the nTOF detectors showing the extracted FWHM of the cosmic event response to be ∼12 ns. The signal was recorded with the PMT biased to −1.4 kV.

allows for increased scattering within the volume. Additionally the scintillating material and light cone are both coated white for additional containment of signal, likely increasing the scattering. Lastly, without optical grease, reflections are sure to occur at the light cone–PMT interface.

While proper response and calibration of the detectors using a known neutron source was unavailable, the characterization of the PMTs was possible and performed. Both the electron transit time (ETT) and the relative sensitivities as functions of the bias voltage were determined. The partial setup is shown in Fig. 5.4, where the diagnostic Nd:YAG laser was used to provide a 2 ns, ∼30 μJ pulse in 532 nm. This was the lowest energy sufficient to give a measurable pulse in the PMT and a reference photodiode without saturating the PMT at the highest bias voltage. The beam was split by a 50:50 R:T beamsplitter between the PMT and the photodiode. The energy in the PMT leg was further reduced by diverging the beam with an f=30 mm lens and a stack of ND filters to an estimate of 1–10 nJ. A light shroud covered the entire setup to prevent errant light from

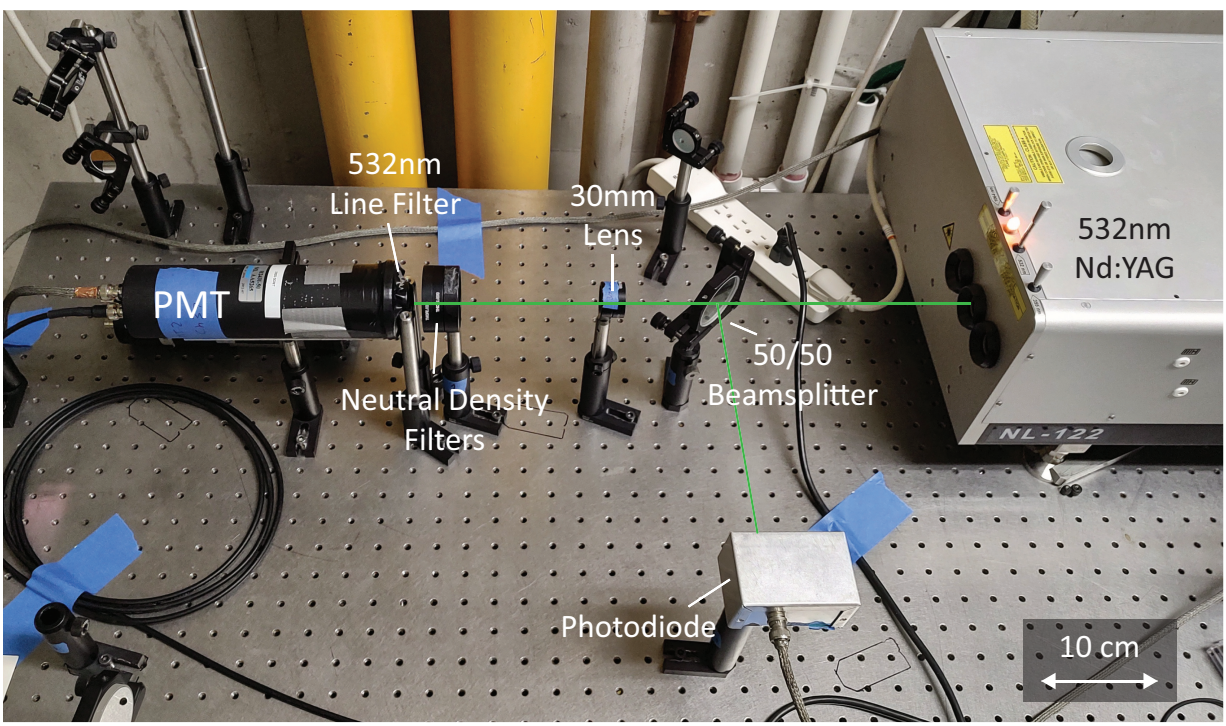

Figure 5.4: Bare setup showing the general structure of the PMT electron transit time measurement. Laser light is split between a photodiode and the PMT with known distances to deduce the transit time. Additional ND filters and a light shroud not shown in this figure were added for the actual experiment to prevent over-saturation of the PMT. Resulting fits of the transit time as functions of bias voltage are approximated by the curve: ETT [ns] $\approx 835 \cdot \mathrm{V}^{-0.5}$.

contaminating the measurement or over-saturating the PMT. Signals for both PMTs were recorded over a range of bias voltages from slightly below to slightly above the range utilized during the experiments. The relative sensitivities were determined from the relative pulse heights between the PMTs. The ETT function was found by carefully measuring the difference in laser path length between the PMT and photodiode legs and determining the additional signal delay of the PMT at each bias voltage. The resulting collected curves are presented in Fig. 5.4, where both curves can be generalized to the equation of ETT [ns] $\approx 835 \cdot \mathrm{V}^{-0.5}$. Unlike the relative responses, which had little application for the data collected, the ETT measurement was vital for correct correction of the neutron production time.

A beryllium activation detector measures neutron yields via the $^{9}\mathrm{Be}(n,\alpha)^{6}\mathrm{He}$ reaction. The unstable $^{6}\mathrm{He}$ nucleus quickly undergoes beta decay ($^{6}\mathrm{He} \rightarrow {}^{6}\mathrm{Li} + \mathrm{e}^{-} + \bar{\nu}$) with a half-life of 807 ms. The detector fielded is composed of beryllium rods encased in scintillation material. The scintillation material is excited through the interaction with the beta radiation and emits a pulse of light. This light pulse is then digitized via a discriminator into a binary interaction count [100]. Figure 5.5(a) shows the beryllium probe fielded on top of the MAIZE vacuum chamber lid. Prior to

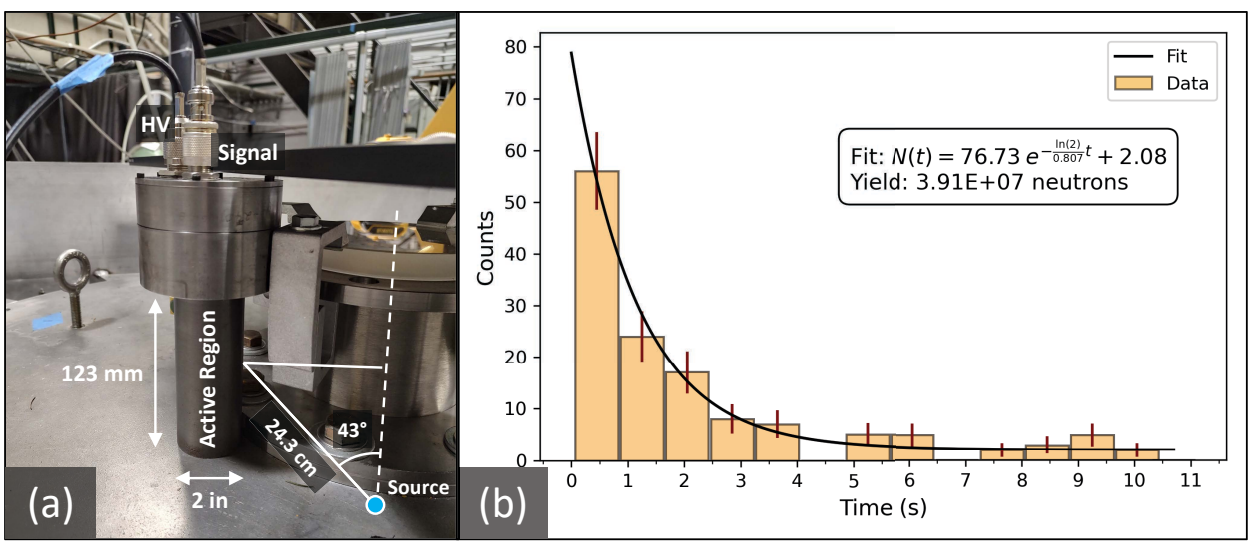

Figure 5.5: (a) Beryllium activation detector in an axial position on the MAIZE vacuum chamber lid. Shown is the relative location of the source and the distance and angle for the center of the active region containing the beryllium rods. (b) An example of a processed beryllium probe signal that has been binned into reasonable time steps and fit to determine the neutron yield.

fielding, the calibration factor of the probe, in terms of its neutron response and the effects of the MAIZE geometry and environment, were unknown. It was hoped that cross-calibration from the other detectors would allow for a working calibration to be extracted; indeed, this cross-calibration was later successfully performed. Figure 5.5(b) shows an example data set. This data set has been cleaned and binned and shows the relevant signal decay. The decay is fit with an exponential with the characteristic half-life of ^{6}He. The constant term is included due to some amount of random signal background being present. This background is usually on the order of about 0–2 counts. The fit is then extrapolated back to t_0, which is inferred from a prompt signal generated from a combination of x-ray emission and electromagnetic noise within the discriminator, and the peak count value (minus the constant background fit) is used to calculate the yield via:

$$Y = \frac{4\pi A_0 d^2}{\lambda F}, \tag{5.5}$$

where A_0 is the corrected peak count value, d is the distance from the source, λ is the ^{6}He decay constant (ln(2) / 807 ms), and F is the calibration factor. for our experiments, F was typically in the range of 0.03–0.04 [counts cm^2 / neutron].

The last kind of neutron detectors fielded for these experiments were Bubble Detector-Personal Neutron Dosimeters (BD-PNDs) produced by Bubble Technology Industries. Bubble detectors utilize super-heated droplets dispersed within a polymer medium (here about 12 cm^3 active volume). When a neutron interacts with the medium and deposits energy in the medium, the medium undergoes a phase transition into a gas creating a measurable bubble [101, 102]. These commercially available detectors, shown in Fig. 5.6, are used as personal dosimeters and come in three sensitivity ranges: low ($\sim$5 bubbles/mrem), medium ($\sim$15 bubbles/mrem), and high ($\sim$33 bubbles/mrem). Assuming that these are essentially mono-energetic (2.45 MeV), D-D neutrons, the fluence per equivalent dose is known to be 29×10^6 n cm^{-2} rem^{-1}. Therefore, combined with the source-to-detector distance and the number of bubbles in the detector, the total neutron yield can be determined. For the bubble detector yields reported in this dissertation, the neutron emission was assumed to be

Figure 5.6: Example bubble detectors from Bubble Technology Industries of the same type fielded on MAIZE experiments for determination of the total neutron yield.

isotropic. This was done because the yields measured on and off axis were insufficient to make an accurate determination of the anisotropy.

Three bubble detectors were fielded on each experiment. All three were of the medium sensitivity type ($\sim$15 bubbles/mrem); however, they were a year into their three month calibration certification window. Two were fielded axially and one radially. It was originally planned for four detectors to be fielded, two of medium sensitivity and two of high sensitivity, and to have one of each in the axial and radial directions. Unfortunately, the shipping of these detectors was delayed and did not arrive until after the experiments. Thus, the uncertified detectors had to be used. Fortunately, a DD neutron generator located in the University of Michigan's Neutron Science Laboratory became available to cross-calibrate the uncertified bubble detectors at a later date. The generator has a neutron fluence into 4π steradians of $\sim 2\times 10^6$ n/s. Both the uncertified BDs and the newly arrived BDs were placed together in the plane of the generator at a distance of 23 $\pm$ 1 cm. To get a reasonable amount of bubbles to reduce error in the calibration, a dose of $\sim$3 mrem was targeted, corresponding to an irradiation time of 5 minutes at 23 cm. All bubbles were counted and confirmed the original calibrations of the detectors to within $\sim$1 bubble/mrem, validating the initial yield measurements.

5.2.2 Load Material

The material used for these experiments was a $[CD_2]_n$ or deuterated polyethylene fiber. The original material is in a powder form that is then melted and drawn into fibers. As a result, the fibers do not have a uniform diameter along their length; their diameters varied over a range of about 50–200 μm. Additionally, some portions of the fibers deviate from a round cross-section to ovular or even near flat in profile. For each experiment, a length of about 3 cm of fiber was cut, and a weight was added to one end to allow for loading between the cones. Figures 5.7(a)–5.7(b) shows the characterization of the fiber diameter via a hand-held microscope (shown in Fig. 5.7(c)). The fibers chosen for these experiments ranged from 60–200 μm in diameter. The ranges of CD_2 fiber load parameters are included in portions within Tables 3.2, 3.3, and 5.1. As polyethylene is a plastic, its resistivity as an X-pinch load is difficult to quantify, as it will quickly flash over the surface of the fiber and ablate into a plasma. Figures 5.7(d)–5.7(f) show three conductive coatings procured in the event that breakdown of the fibers was not spontaneous and to explore whether the addition of the coatings would have any affect on the resulting neutron production. Three coatings available were: silver, carbon, and nickel. From Figs. 5.7(d)–5.7(f) one can see that the coatings vary significantly in grain size. The carbon coating is most uniform, followed by the silver coating, with micron-scale grains and high uniformity along the fiber length. The increase in diameter due to these two coatings was unmeasurable, in part due to the irregularity of the base fiber diameter, and so it was estimated conservatively to add $\leq$10 μm to the diameter. The nickel coating, however, has significantly irregular grains of up to $\geq$50 μm and a highly irregular coating along the length. Each coating was tested on two shots for general comparison and for indication of future experimental paths.

It should be noted that the material used for these fibers was originally fully deuterated; however, it is now >40 years old. The exchange rate of protium and deuterium within polyethylene post-deuteration does not seem well characterized. However, due to typical deuteration exchanges requiring a catalyst under temperatures and pressures well above normal standards, the process is slow and would likely take years, which have also elapsed [103]. All of this is to say that the true

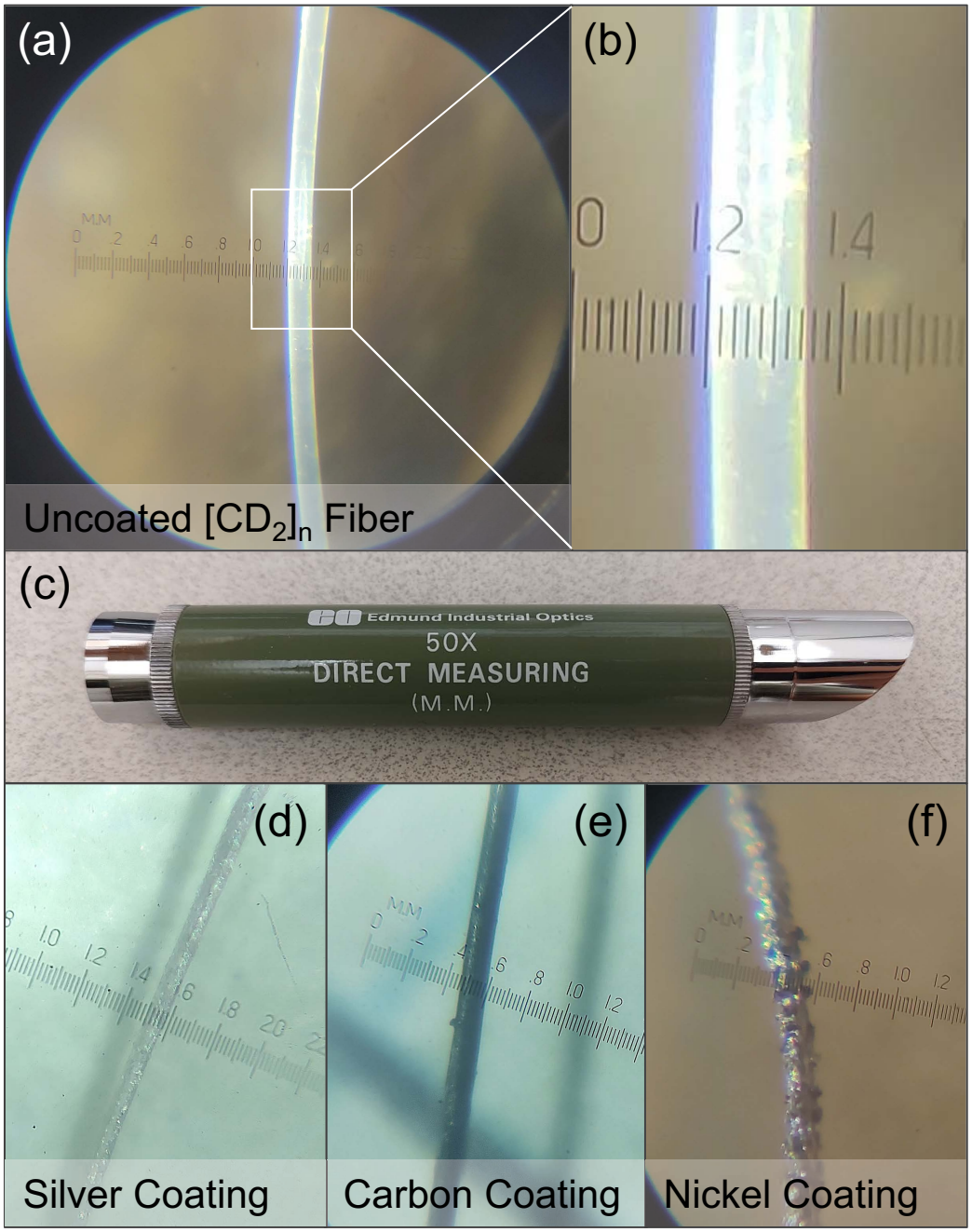

Figure 5.7: (a) An image of an uncoated $[CD_2]_n$ fiber imaged through (c) a handheld 50× microscope. (b) The inset of (a) clearly showing the fiber contrasted behind the microscope ruler for measurement of its diameter. (d)–(f) Sample images of $[CD_2]_n$ fibers with each of the three conductive coatings applied: (d) silver, (e) carbon, and (f) nickel.

D:H fraction within the 40-year-old fibers is unknown. We were unable to find a lab capable of measuring the D:H fraction of the fibers. Due to polyethylene being a polymer, normal methods such as nuclear magnetic resonance (NMR) or laser induced breakdown spectroscopy (LIBS) are typically not well suited, and more specialized measurements such as a combination of size exclusion chromatography (SEC) and infrared spectroscopy (IR) are required [104].

5.3 Results

Figure 5.8 shows an example image of a deuterated X-pinch loaded within the MAIZE vacuum chamber and the subsequent time-integrated image taken during the experiment. The brightest visible emission appears to be from the initial surface flash-over of the fiber followed by the dense expanding ablated plasma. There is plasma seen at the edge of the cathode structure and creeping slightly farther out along the anode; however, the plasma seems to remain contained within the region. Due to the time integration, it is hard to say when the relative structures occur relative to the main shot dynamics. Despite this, the image does portray well the main areas where energy is coupled to the load.

For these experiments, there were three controllable parameters: charging voltage, fiber diameter, and A-K gap spacing. Table 5.1 shows the parameter space covered as well as the large regions unexplored. Due to both material and time constraints, a focus on incremental improvement was chosen over broader characterization for the campaign. The shots are also classified as 'good' or 'not-so-good' based on the nTOF signal response; here, 'good' would indicate a decent signal amplitude above noise with one peak or clear peak separation. The specific load parameters and collected data for each deuterated X-pinch shot are included in Appendix D.

As MAIZE had previously been running metallic X-pinches with peak currents of ∼300–400 kA, the diagnostics fielded by our CTU collaborators assumed parameters consistent with these currents. It was a surprise to find that MAIZE, with a deuterated fiber load, was generating peak currents consistently between ∼400–600 kA, which could threaten the measurements of the ion diagnostics by deflecting them out of measurement range due to the higher fields. This was mitigated due to

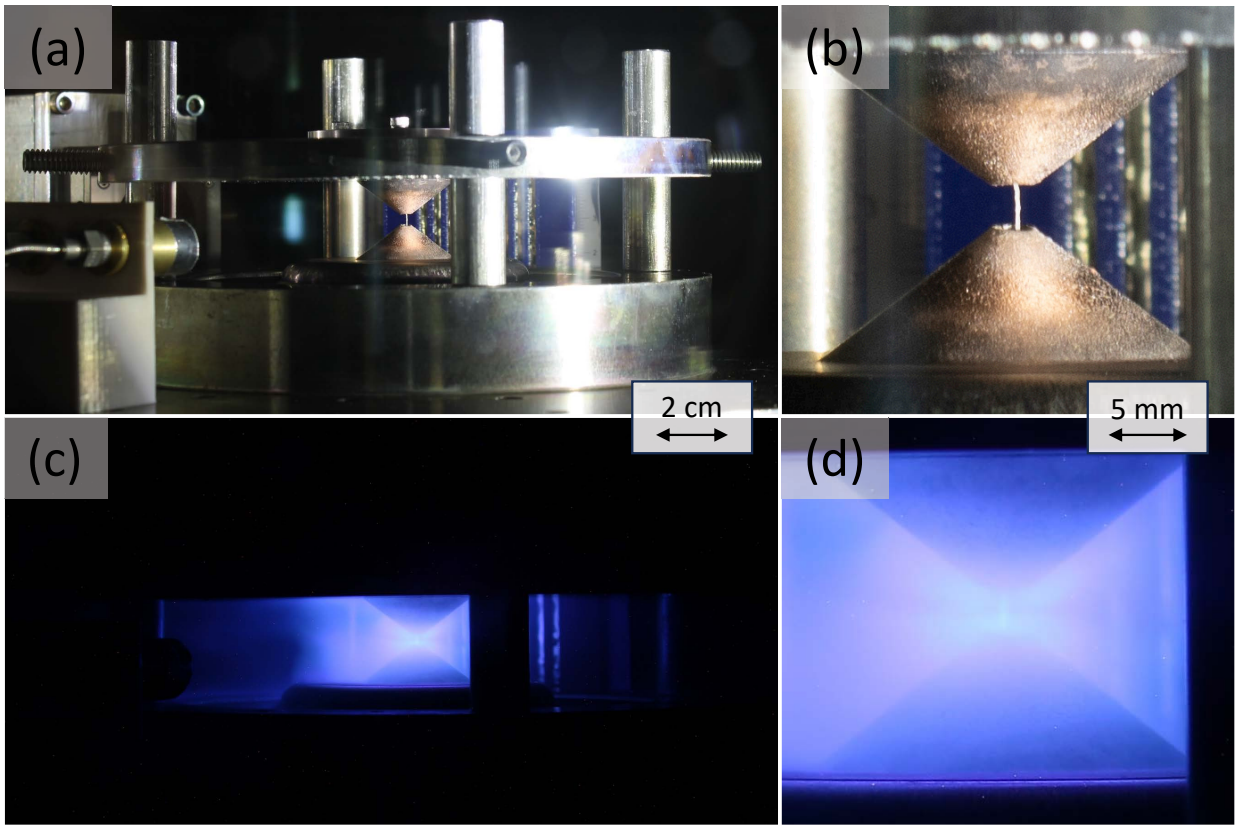

Figure 5.8: (a) Bright view of the chamber with X-pinch hardware and a loaded fiber X-pinch. (b) Inset of the central X-pinch load of (a) clearly showing the fiber spanning the electrode gap. (c)–(d) Equivalently cropped images to (a)–(b) showing the time-integration in visible emission of an X-pinch experiment. Various emission structures can be seen at varied radii with different emission intensities.

A-K gap (mm)	CD_2 diameter (um)					
60 kV	**50-70**	**70-90**	**90-110**	**110-130**	**130-160**	**160-200**
1.6						
		1			1	
2.2						
2.5-2.6	1	1	1	1		
		1			1	
2.8						
3.4						

A-K gap (mm)	CD_2 diameter (um)					
70 kV	**50-70**	**70-90**	**90-110**	**110-130**	**130-160**	**160-200**
1.6						
2.2					1	
			2		1	
2.5-2.6		1				
2.8		2	1	2	4	
			1	1	1	2
3.4				1		
					1	

Total shots:	**29**

Number of good and not-so-good shots.

Table 5.1: Parameter space of the deuterated fiber X-pinch experiments detailing scans over anode-cathode gap distance and fiber diameters. 'Good' and 'not-so-good' shots are marked in reference to neutron signal strength recorded by the nTOF detectors.

the current at the time of the pinch being around the originally planned ∼300–400 kA. Due to the higher currents potentially limiting the diagnostics, the charge voltage of MAIZE was restricted to ±70 kV max.

5.3.1 Neutron Yields

The neutron yields produced during the campaign is provided in Table 5.2. The highest yield shot, shot 3010, was completely unexpected in intensity. The collected scope traces given in Fig. 5.9 show that the nTOF signals clipped well off the oscilloscope and had a sufficient hard x-ray (HXR) signal to be measured by the detector through the 5.4 mm lead shielding. Thankfully, the lower sensitivity channel of the nTOF at further distance was able to record the dip showing that there were at least two peaks. Comparing the shifts with the time-of-flights for photons and 2.45 MeV neutrons reveals that the second peak is a neutron peak that aligns in production time to the second x-ray burst. The first peak similarly has a delay between the two nTOF signals, corresponding to photons from the first x-ray burst. As the signals are clipped, it is difficult to say whether two prompt photon signals or an initial neutron signal are also convolved under the first clipped peak. Additional to the signals clipping, the beryllium activation probe failed to communicate with the recording software properly and produced no data. This left the only measurement to the bubble detectors, which recorded an averaged yield of 1.44×10^8 neutrons. Surprisingly, this is equivalent to the highest recorded gas-puff z-pinch yield on MAIZE.

Unfortunately, even with 17 additional experiments, the same level of yield was unable to be achieved, though several shots produced yields that were notably higher then the rest, such as shots 3024 and 3025. Interestingly, these two shots had the carbon conductive coating, suggesting that improvements in current initiation may improve the overall yield. Shots 3022 and 3024 had the silver conductive coating and shots 3026 and 3027 had the nickel conductive coating. While not as impressive, the coatings as a whole certainly present more consistent yields, and the addition of the metallic species do not seem to hinder the neutron production, at least in the still unoptimized configuration. Overall, the average neutron yield was $\sim1.6\times10^7$ neutrons, again comparable to the

Shot	V_{charge}	Bubble Detector Yield	Be Probe Yield	Average Yield
2999	±60 kV	3.31E+06	Not Fielded	3.31E+06
3000	±60 kV	4.96E+06	Not Fielded	4.96E+06
3001	±60 kV	1.65E+06	Not Fielded	1.65E+06
3003	±60 kV	1.65E+06	Below Floor	1.65E+06
3004	±60 kV	4.96E+06	No HV	4.96E+06
3006	±60 kV	1.65E+06	Below Floor	1.65E+06
3007	±60 kV	0.00E+00	5.35E+06	2.68E+06
3008	±70 kV	2.12E+07	7.84E+06	1.45E+07
3009	±70 kV	0.00E+00	6.33E+06	3.17E+06
3010	±70 kV	**1.44E+08**	**Failed**	**1.44E+08**
3011	±70 kV	1.65E+06	Below Floor	1.65E+06
3012	±70 kV	2.95E+07	2.64E+07	2.80E+07
3015	±70 kV	1.65E+06	1.65E+07	9.08E+06
3016	±70 kV	6.61E+06	1.49E+07	1.08E+07
3018	±70 kV	1.65E+06	2.83E+06	2.24E+06
3019	±70 kV	0.00E+00	1.14E+06	5.70E+05
3020	±70 kV	1.65E+06	Below Floor	1.65E+06
3021	±70 kV	8.27E+06	2.05E+07	1.44E+07
3022	±70 kV	2.62E+07	1.55E+07	2.09E+07
3023	±70 kV	4.96E+06	1.27E+07	8.83E+06
3024	±70 kV	2.81E+07	3.91E+07	3.36E+07
3025	±70 kV	3.44E+07	4.34E+07	3.89E+07
3026	±70 kV	0.00E+00	1.49E+07	7.45E+06
3027	±70 kV	2.78E+07	1.33E+07	2.06E+07
Average:		1.48E+07	1.60E+07	**1.59E+07**
Min:		1.65E+06	1.14E+06	**5.70E+05**
Max:		1.44E+08	4.34E+07	**1.44E+08**

Table 5.2: Tabulated neutron yields recorded from the bubble detector average, the beryllium activation probe, and the average of the two diagnostic methods. The measurement floor of both detectors is approximately 1×10^6 neutrons. Color intensity is proportionally scaled from the minimum to maximum of the average yields.

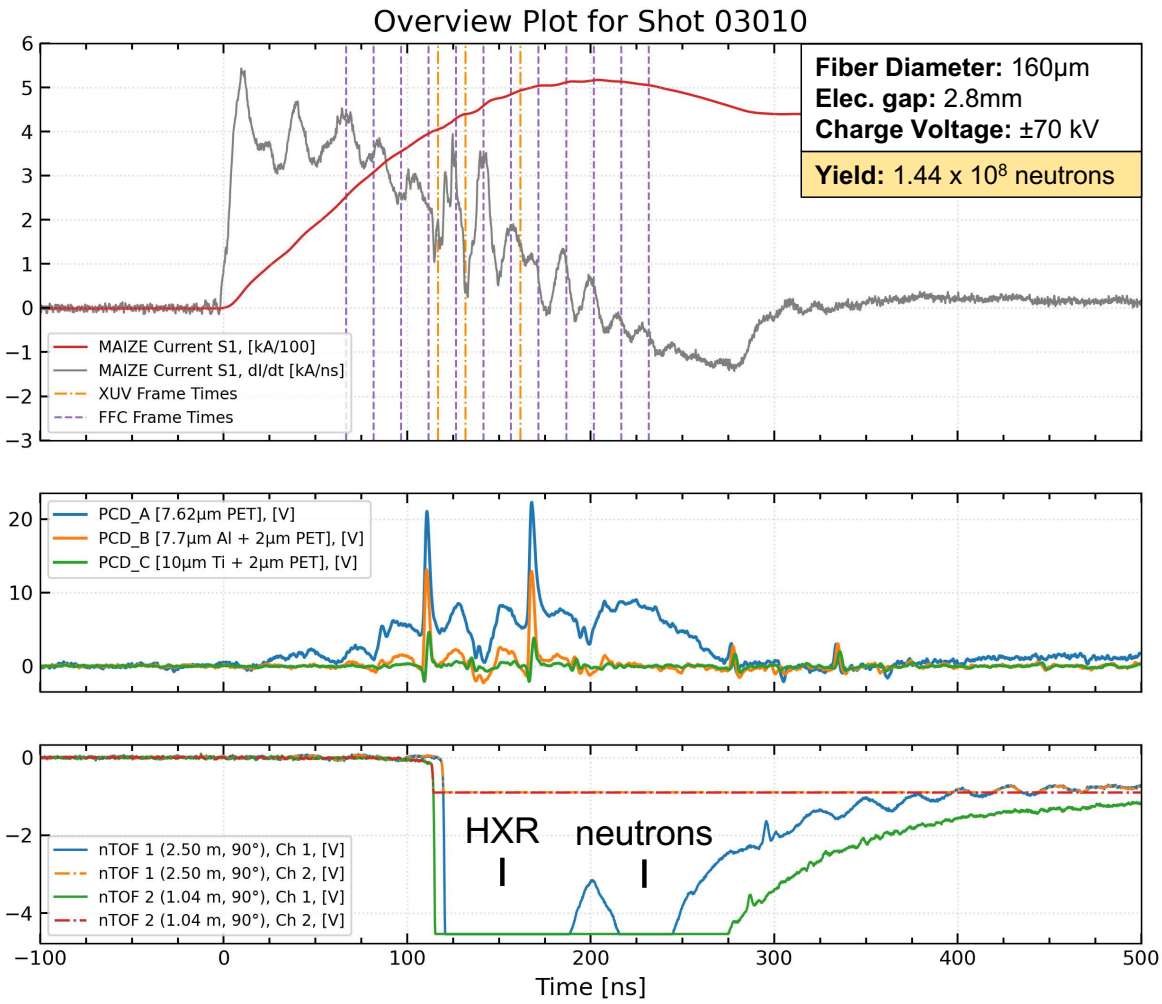

Figure 5.9: Overview plot of traces for shot 3010, the highest neutron yield shot of the campaign. The shot parameters and neutron yield are presented in the top right corner. The nTOF traces are annotated to mark the HXR pulse and the subsequent neutron pulse.

average yield of MAIZE's gas-puff platform. Note that while no ±60 kV shot reached 10^7 neutrons, the electrode cone tip spacing was never optimized at the lower charge voltage. Optimization would likely have brought the yield closer if not above that threshold. Similarly, it is uncertain how experiments run at ±80 kV would have affected the yield, though presumably it would have been higher, as z-pinch yields generally scale with the stored energy and the delivered load current—e.g., gas-puff z-pinches and dense plasma focuses scale as I^4, where I is the delivered load current. Notably, previous experiments have primarily been done on high-impedance machines, where the drive current is relatively unaffected by changes in the load parameters [29, 92]. On MAIZE, due to

its low impedance, even small changes in the X-pinch geometry can significantly affect parameters such as pinch time, peak current, etc. Regardless, the yields recorded on MAIZE and LION for similar currents ($\sim$400 kA) were of directly comparable orders. Comparison of the neutron yields on MAIZE, using average values of $I \sim$500 kA, $Y \sim 10^7$, to the results on MAGPIE [83] or S-300 (3.5 MA, 100 ns, 0.15Ω) [88, 91], $I \sim$1 MA, $Y \sim 10^9$, seems to reasonably agree with an upper yield scaling along the lines of I^5. It is interesting that this holds as an average between drivers when there is no indicated scaling over the $\pm$100 kA variance on MAIZE alone, though the higher yields with increased charging voltage does hint towards a likely similar kind of scaling.

5.3.2 Neutron Emission Correlation

For the question of neutron production time, correcting the traces for their times-of-flight revealed that neutron production began within 10 ns of the x-ray burst (compared primarily against the Al filtered PCD with a lower transmission energy of $\sim$2 keV). For almost all shots where the x-ray peaks were separated sufficiently in time, the number of neutron peaks was in a 1:1 ratio. with the x-ray peaks The major exceptions to these observations were the shots where: (1) where the x-ray bursts were not sufficiently separated and the neutron peaks were merged; (2) where neutron signals were not recorded for an x-ray burst (PCD peaks $>$ nTOF peaks); and (3) one particular shot (3012) that had a clear extra neutron peak corresponding to little or no x-ray emission recorded by the PCDs (nTOF peaks $>$ PCD peaks). The traces from shot 3012 are given in Fig. 5.10, showing three distinct neutron signals. Subtracting the time-of-flight, the latter two neutron peaks were emitted at the same time as the two clear x-ray peaks. The first neutron peak was emitted at around 95 ns, corresponding to the little blip of x-rays that are barely visible through the 1 keV cutoff filter and essentially nonexistent in the harder filters.

It was assumed that subsequent pinching could cause significant mixing, especially if portions of ablated plasma from the metallic electrodes were swept in and included in the mix, and that this mixing could quench neutron production, due to higher radiative loss rates. This was commonly seen for shots with late time x-ray emission peaks and low/negligible nTOF response. Shot 3012

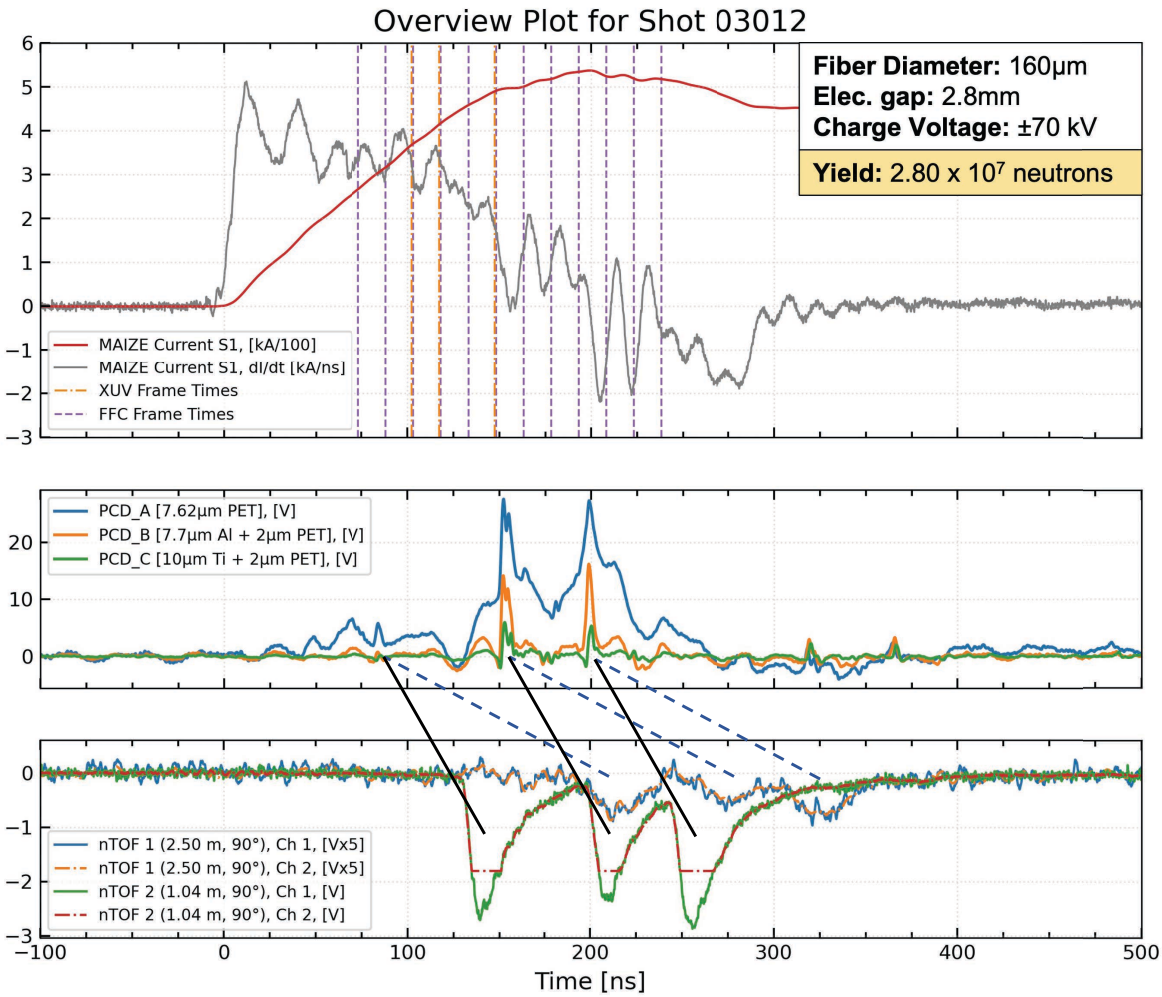

Figure 5.10: Overview plot of traces for shot 3012 with shot parameters and neutron yield presented in the top right corner. The nTOF traces show three clear neutron peaks that correlate in time to an initial blip of the PCD signals and two, more traditional, x-ray bursts, implying that while correlated in time, the neutron and x-ray production mechanisms do not necessarily have to both occur simultaneously.

presents evidence that while the mechanisms that drive x-ray and neutron production within the pinches are developing simultaneously, there are ways that the x-ray burst can be suppressed while leaving the neutron production unaffected. From observations of the fiber implosions via visible self emission, the solid electrode cones of the hybrid X-pinch configuration cause a retention of the ablated fiber material that would have otherwise been ejected axially away from the crossing point in a multi-wire X-pinch configuration. This excess plasma floods the neck region with additional plasma. It is possible that this mechanism could, in the right circumstances, extinguish or dampen the x-ray burst, or potentially, if at a lower temperature, absorb emission, leaving only a reduced signal.

5.3.3 Neutron Emission Anisotropy

Due to having only two nTOF detectors, and with the primarily goal of measuring the temporal characteristics of the neutron emission, anisotropies could only be estimated from the shots where one detector was fielded axially and one detector was fielded radially. Noting that while the exact calibrations of the detectors were not performed, as a sufficient source was unavailable to characterize the absolute response and scattering at the time, the relative radiant sensitivities of the two PMTs were characterized. Assuming the scintillator materials had nominally equal responses, this should be sufficient to extract a very rough estimate of the anisotropy. Similarly, since the bubble detectors were always fielded with one detector along the radial axis, a second anisotropy measurement can be estimated.

The resulting calculated axial/radial anisotropy from the nTOF measurements is unexpectedly bizarre at a value of 0.21. As these are likely beam-target fusion products, it was expected that there would be an enhanced axial yield with a measured anisotropy value >1. For comparison, the CD_2 fiber z-pinches fielded on MAGPIE had anisotropies ranging from 1–1.7 [83] and the CD_2 multi-wire X-pinches on LION were stated as <1.07 [92]. Initially, the assumption was that the PMT characterization was not enough to reasonably calculate the anisotropy; however the BD anisotropy value then agreed at a value of 0.19. In light of the agreement between the

two diagnostics, it does appear that there is a real effect producing the measured anisotropy. At present, there is not enough data to say whether this is an external effect (e.g., due to the scattering environment) or a true emission anisotropy.

There are, however, some additionally observed features to note that are potentially related. For shot 3010, Prof. Klir's group recorded signatures of a highly-anisotropic, 3-MeV deuteron beam with their radially fielded ion diagnostics (D. Klir, personal communication, July 10, 2023). This beam energy interestingly agrees with the estimate in Sec. 5.1 of the induced electric fields within the X-pinch neck. As the imaged deuteron beam was highly non-uniform, and since this phenomenon was only captured on this one shot, this likely indicates that the acceleration mechanism or surrounding plasma environments were also similarly non-uniform. This is reasonably supported by the images recorded by the XUV pinhole camera. Figure 5.11 shows large, non-uniform, radial jets of plasma with recorded intensities that are similar to the main plasma neck. For visible self-emission imaging taken at nearly the same time, bunching of expelled plasma near the electrodes is clear, but only hints of the larger scale jetting in the radial direction appear, even with high contrast enhancement. As there was no interferometry fielded on these experiments, it is tentatively assumed that it may look similar to Fig. 4.11(f), which would further indicate that these are particularly low-density jets. It is possible that the presence of these large and dynamic radial structures indicates

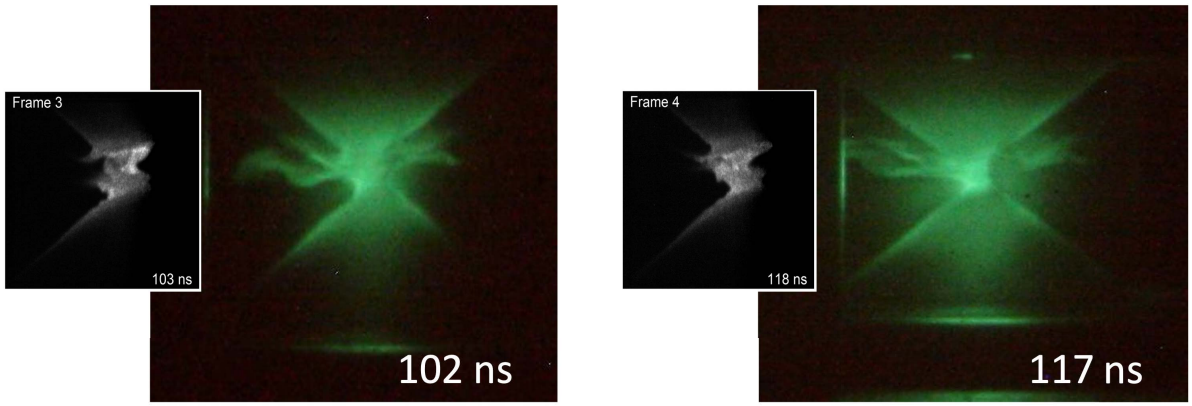

Figure 5.11: Two subsequent frames captured in XUV emission imaging (large, green) for shot 3012 showing bright plasma structures radially streaming out to high radii. Corresponding frames in visible self-emission (small, grey), sized to similar scaling, do not appear to capture these structures.

that the hybrid X-pinch geometry is somehow significantly conducive to radial acceleration.

5.3.4 Neutron Emission Duration

Looking at the nTOF signals for singular neutron peaks, there were differences in the FWHMs between the two nTOFs, usually between 3–5 ns. The time spread cannot be fully attributed to the neutron velocity spread, as the differences were always greater in one specific detector, implying that it had a response time of at least 1–3 ns longer than the other, though the initial determination of detector responses via cosmic events did not seem to support this. Theoretically, if higher energy neutrons are emitted first, the signal could compress, muddying the results here, but a significantly more defined and sensitive setup would be needed to properly say something more precise about the neutron energy spectrum. Especially since the two nTOF detectors were fielded in varied locations and were not separated by significant differences, this inability to measure peak spread is unsurprising and unlikely, even if the exact response profiles of the detectors were known.

This did not, however, impact the ability to measure the duration of neutron emission. The measured signal width is primarily a convolution of the emission duration with the detector response and scattering within the lead shielding, though there are certainly other unaccounted for scattering parameters. To a first order approximation, the measured FWHM is given by

$$\mathrm{FWHM}_{\mathrm{Meas}} = \sqrt{\mathrm{FWHM}_0^2 + \mathrm{FWHM}_{\mathrm{Det}}^2 + \mathrm{FWHM}_{\mathrm{Pb}}^2} \tag{5.6}$$

where ‘0’ refers to the neutron emission duration, ‘Det’ refers to signal spread by the detector, and ‘Pb’ refers to the signal spread by the lead shielding. Table 5.3 details the measured FWHMs for each shot that had a single, clear neutron peak. The table presents the convolved width of the detector response with the broadening due to the lead thickness, as well as the resulting deconvolved width of the detector response and the lead thickness of the given shot, and the resulting deconvoluted width of the neutron emission. The value used for the signal spread due to shielding would have ideally been modeled via MCNP for the MAIZE LTD and detector configuration. Creating the

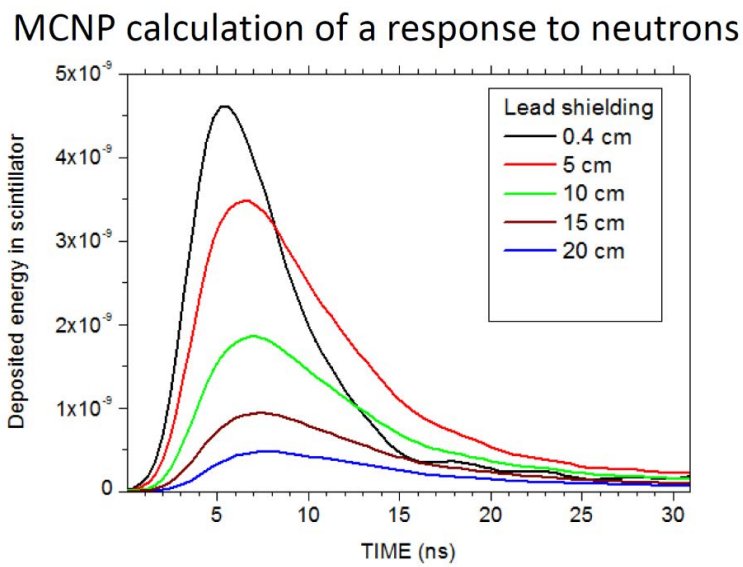

Figure 5.12: MCNP calculations of a similar detector's response 3 m from a point-like 2.5 MeV neutron source, with variation in lead shielding thickness. The detector type in this simulation is a 5×4.5 cm BC-408 scintillator. Figure courtesy of O. Sila, K. Rezac, and D. Klir of the Czech Technical university in Prague.

model would have been temporally inefficient in light of the lack of proper detector characterization and the temporary use of the detectors. Therefore, the temporal spread as a function of different shielding thicknesses was approximated from the modeled spread for a roughly similar detector (see) Fig. 5.12). The result is that for most of the production events that correlated to a single x-ray burst, the duration was on the order of 15–25 ns, though some fell above and below this range. This range is consistent with the duration proposed in Ref. [92] for the probable neutron emission duration on LION. Those that were correlated to multiple bursts had longer emission times of $\gtrsim$30 ns; however, as can be somewhat inferred from the two examples given in Table 5.3, the resulting lengthening of the neutron emission time did not strongly follow the x-ray burst separation time. If we also speculate slightly on these times and remember that the detector responses are exceptionally broadened compared to the expected responses from the constituent parts, the deconvolution of this possible component would mean that the minimal emission times are actually slightly shorter, on the order of 10–20 ns. Further investigation with fully characterized detectors would be of particular interest.

Shot	$FWHM_{Meas}$ [ns]			$FWHM_{Det+Pb}$ [ns]	$FWHM_0$ [ns]		
	Peak 1	Peak 2	Peak 3		Peak 1	Peak 2	Peak 3
3003	20.4			14.5	14.5		
3005	24.4			15.4	18.9		
3006	24.8			15.4	19.4		
3007	27.0	23.0		15.4	22.2	17.1	
3012	22.0	22.2	26.0	15.4	15.7	15.6	21.0
3016	25.8			15.4	21.0		
3018	21.8	23.0		15.4	15.4	17.1	
3020	28.6			15.4	24.1		
3021	23.8			15.4	18.1		
3022	37.2[a]	25.4		15.4	33.8	20.2	
3023	24.8			15.4	19.4		
3026	30.0[b]			15.4	25.7		

Table 5.3: Minimal measured FWHMs of nTOF detector signals and their deconvoluted neutron emission widths ($FWHM_0$) for shots containing single or well separated peaks. All peaks correlate to singular x-ray peaks except where noted. [a]Neutron peak correlated with two x-ray peaks $\sim$5 ns apart. [b]Neutron peak correlated with three x-ray peaks spread over $\sim$10 ns.

5.4 Summary

This chapter covered the experiments characterizing the first deuterated polyethylene fiber X-pinches run on MAIZE, and more generally, on a low-impedance LTD. The experiments, performed in collaboration with Czech Technical University in Prague, looked to determine the neutron emission time, duration, and total yield. The result was that deuterated X-pinches on an LTD were found to be a viable neutron generator with average yields of 1.6×10^{7} neutrons, and a maximum yield of 1.4×10^{8} neutrons. Additionally, the application of thin conductive coatings to the fibers appears to have resulted in more consistent results, and in the case of the carbon based coating, an improvement in yield compared to the baseline. Neutron emission was found to be correlated with x-ray bursts to within 10 ns and with emission times of 15–20 ns FWHM. The reason behind an anisotropy of $\sim$0.2 (axial/radial) remains an open question. Future work should include more sensitive measurements for the determination of the neutron energy spread, and greater exploration of the parameter space to probe if higher yields can be achieved.

CHAPTER 6

Final Summary and Conclusions

This dissertation documents the results of two studies involving various X-pinch configurations on the 1-MA, 100-ns MAIZE LTD. The first set of experiments characterized the electrical current distribution in the coronal plasma surrounding the dense X-pinch core. For this study, a Faraday rotation imaging diagnostic was developed for MAIZE. Such measurements were found to be extremely challenging due to the very small spatial and temporal scales involved with micro-pinches. It was found that the limiting factor in making such measurements was the coronal plasma density, which fell from 10^{18} cm^{-3} near the dense neck to 10^{17} cm^{-3} (or less) within only 100 μm. Additional challenges included low drive currents for most of the experiments and temporal and radial resolution limits imposed by the long laser pulse duration. These challenges prevented the direct imaging (and resolving) of regions of space and time with simultaneously high plasma density and high magnetic field strength. Ultimately, these difficulties resulted in measured rotation angles of only 1° or less. Despite the challenges, the diagnostic is capable of spatial resolutions of $\leq$35 μm, with variable magnifications of 1–10$\times$, and it provided the first quantitative experimental measurements of the current distribution surrounding the dense plasma neck of an X-pinch. Measurements taken with the diagnostic indicate that current density is being distributed to radii larger than that of the dense neck, with 40–60% of the total current supplied by MAIZE being distributed in the coronal plasma region from 100–300 μm. This split of the current between the dense neck and the coronal plasma then significantly limits the maximal magnetic drive pressures, with maximal values reaching only 100–150 kbar.

The second set of experiments investigated the neutron radiation characteristics of hybrid X-

pinches made with CD_2 fibers. Deuterated polyethylene fiber was available as a load material due to a collaboration with Prof. Daniel Klir's group at the Czech Technical University in Prague. To minimize the material use per shot, and thereby maximize the number of experiments, a hybrid x-pinch geometry was chosen. An array of various neutron diagnostics were assembled to provide measurements of neutron yield, neutron emission start time, and neutron emission duration. Additionally, multiple measurements were taken to calibrate the bubble detectors, the beryllium activation probe, and the nTOF PMT detectors. The calibrations then allowed the neutron emission data to be corrected. Surprisingly, it was found that even with the limited, unoptimized parameter sweep, both the average and maximal neutron yields were comparable to those produced by the MAIZE gas-puff z-pinch platform. This is true despite the fact that the X-pinch platform has a region of neutron production that is only a fraction of that in the gas-puff z-pinch platform (i.e., a $\sim$1 mm axial extent in the X-pinch platform versus a $\sim$10 mm axial extent in the gas-puff z-pinch platform). Similarly, these yields are comparable to the multi-wire experiments on the LION accelerator at Cornell University despite the significant disparity in driver impedance ($\sim$0.16 Ω versus 4.5 Ω). Emission times were found to be roughly 15–20 ns FWHM in agreement with the proposed neutron emission duration on LION. Additionally, the theory that neutron emission occurs at roughly the same time (within $\leq$10 ns) as the typical x-ray burst was supported; however, results indicate that the x-ray and neutron producing mechanisms have a degree of independence, as it is possible to produce a strong neutron signal without a strong x-ray signal.

6.1 Future Work

Additional measurements looking to improve the sensitivity and resolution of the imaging Faraday rotation diagnostic should focus on further improvements to the optical relays. Relocating the image relay optics within the MAIZE vacuum chamber would increase the numerical aperture and thus improve the minimal resolution of the diagnostic. This would also aid in decreasing diffraction effects and increase the collection angle for light refracted from steep density gradients. A shadowgraphy line may also be included to (1) identify spurious signal arising from density

gradients and (2) allowing for single channel polarimetry measurements for which anisotropy effects can be corrected. As the primary neck cascade (implosion) occurs in $\lesssim$2 ns, the acquisition of a new sub-ns laser source would improve the minimum radius that can be measured, since the present 2-ns laser limits the minimum radius that can be measured to $\sim$100 μm due to motional blurring.

Dedicated modeling and simulation of X-pinches are of significant interest. Doing so is challenging, however, because of the small spatial and temporal scales. Nonetheless, the implementation of codes with mesh refinement are allowing for progress to be made [46]. In particular, simulating the distribution of current in the coronal plasma surrounding the dense core would be especially useful. Other micro-pinch phenomena of interest include the study of radiative collapse and how such a collapse might be characterized in experiments.

The work conducted on X-pinch produced neutron sources for this dissertation presents a small fraction of possible initial conditions and leaves much future work to be completed. Immediately, repeating the experiments presented in this dissertation while using fibers of greater uniformity, both in circular cross-section and along the fiber length, would likely improve reproducibility. Furthermore, acquiring a fully calibrated array of nTOF detectors would properly allow for time-of-flight reconstruction of neutron energy spectra and the ability to properly measure anisotropy in the neutron production. The anisotropy is particularly intriguing. A measured anisotropy of $\sim$0.2 (axial/radial), even while corroborated by two entirely separate detectors, seems to strongly imply that some detail is being overlooked. Lastly, while unlikely on MAIZE with the present neutron yields, determination of neutron emission source size within an X-pinch would be novel. If a configuration can be found to reliably increase the average neutron yield, then penumbral imaging could potentially be applied [105]. Furthermore, it may be possible to determine the neutron emission location by imaging a lead grid in a neutron radiograph.

APPENDIX A

Uncertainty Derivations for Extracted Distributions in Faraday Rotation Imaging Experiments

The error bounds presented in Figs. 4.17, 4.18, 4.20, and 4.21 were derived following normal error propagation in quadrature assuming fully independent error sources. From Eq. 4.10, the error in the enclosed current is dependent on the the error in the average parallel magnetic field, $\bar{B}_{||}(x)$, and the error in the radial projection axis, x. The error in the projection axis is mildly convoluted in the approximation for the radial axis, r, and is separated into two terms dependent on the projected axis and the length scale parameter, L_0. The error in the enclosed current is then calculated as

$$\sigma^2_{\tilde{I}_{\text{encl}}} = \left(\frac{\partial \tilde{I}_{\text{encl}}}{\partial \bar{B}_{||}}\right)^2 \sigma^2_{\bar{B}_{||}} + \left(\frac{\partial \tilde{I}_{\text{encl}}}{\partial L_0}\right)^2 \sigma^2_{L_0} + \left(\frac{\partial \tilde{I}_{\text{encl}}}{\partial x}\right)^2 \sigma^2_{x}, \tag{A.1}$$

which can be simplified to the form

$$\frac{\sigma_{\tilde{I}_{\text{encl}}}}{\tilde{I}_{\text{encl}}} = \begin{cases} \sqrt{\left(\frac{\sigma_{\bar{B}_{||}}}{\bar{B}_{||}}\right)^2 + C_1\left(\frac{\sigma_{L_0}}{L_0}\right)^2 + C_2\left(\frac{\sigma_x}{x}\right)^2} & \text{for } x < \frac{L_0}{2} \\ \sqrt{\left(\frac{\sigma_{\bar{B}_{||}}}{\bar{B}_{||}}\right)^2 + \left(\frac{\sigma_x}{x}\right)^2} & \text{for } x \geq \frac{L_0}{2} \end{cases}, \tag{A.2}$$

where the coefficients are defined as

$$C_1 = \left(\frac{L_0^2}{L^2} - \frac{2x}{L \arctan\left(L/2x\right)} \right)^2 \tag{A.3}$$

$$C_2 = \left(\frac{2x}{L \arctan\left(L/2x\right)} - \frac{4x^2}{L^2} \right)^2 \tag{A.4}$$

and $L = \sqrt{L_0^2 - 4x^2}$. From Eq. 1.1, the error in the magnetic pressure is dependent on both I_{encl} and r, when calculated from the derived current. The error in the magnetic pressure is then given by

$$\frac{\sigma_{P_{\text{mag}}}}{P_{\text{mag}}} = \sqrt{2\left(\frac{\sigma_{\tilde{I}_{\text{encl}}}}{\tilde{I}_{\text{encl}}}\right)^2 + 2\left(\frac{\sigma_r}{r}\right)^2}. \tag{A.5}$$

For the error bounds presented on the Abel inverted profile of Fig. 4.19, the error equation for the enclosed current is no longer approximated with the scale length, L, and is simply dependent on the radial distance, r, again approximated with the error in the projected length, x. Thus, the error equation for the radial enclosed current profile is:

$$\frac{\sigma_{I_{\text{encl}}}}{I_{\text{encl}}} = \sqrt{\left(\frac{\sigma_{\bar{B}_{||}}}{\bar{B}_{||}}\right)^2 + \left(\frac{\sigma_x}{x}\right)^2}. \tag{A.6}$$

The error in the radial projection axis, x, is found directly from the average of the spatial scale errors found for each image; it is a constant relative error. From Eq. 4.5, $\bar{B}_{||}(x)$ is dependent on the areal density, N_{e}, and on the Faraday rotation angle, α. Thus, the error equation for $\bar{B}_{||}(x)$ is:

$$\frac{\sigma_{\bar{B}_{||}}}{\bar{B}_{||}} = \sqrt{\left(\frac{\sigma_\alpha}{\alpha}\right)^2 + \left(\frac{\sigma_{N_{\text{e}}}}{N_{\text{e}}}\right)^2}. \tag{A.7}$$

The error in the areal density is calculated from the uncertainties in the measurements of the fringe shifts and the fringe periods. From Eq. 4.11, the error in the Faraday rotation angle is a function of the laser energy ratio between the background and shot images, the error in the analyzer angle, and the error in the pixel overlap between the two polarimetry channels. The overlap error was

estimated by calculating the average standard deviation from shifting the channels relative to each other in the x, y, xy, and $-xy$ directions by a set number of pixels. Note that due to their complexity and non-uniformity, there is likely unaccounted error inherent from the intensity aberrations seen in the polarograms and interferograms that was not captured by σ_α and σ_{N_e}.

APPENDIX B

X-ray Camera Drawings

Drawing measurements are in inches unless otherwise specified. Parts were designed for manufacture from Aluminum 6061.

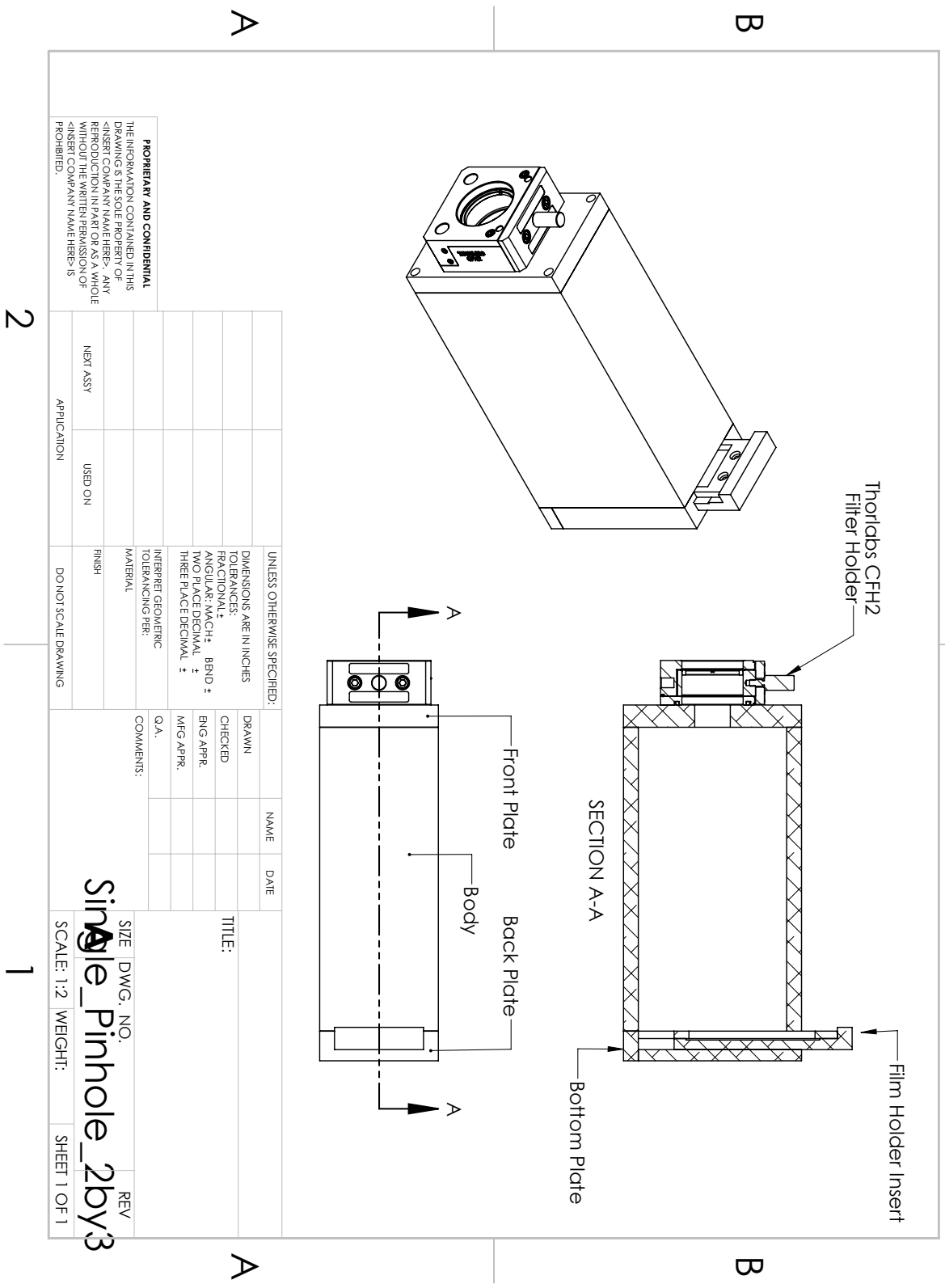

Figure B.1: Diagram of constructed x-ray camera housing showing the location of the primary components including the attachment of a Thorlabs CFH2 filter holder into which a 1” mounted pinhole or slit can be inserted.

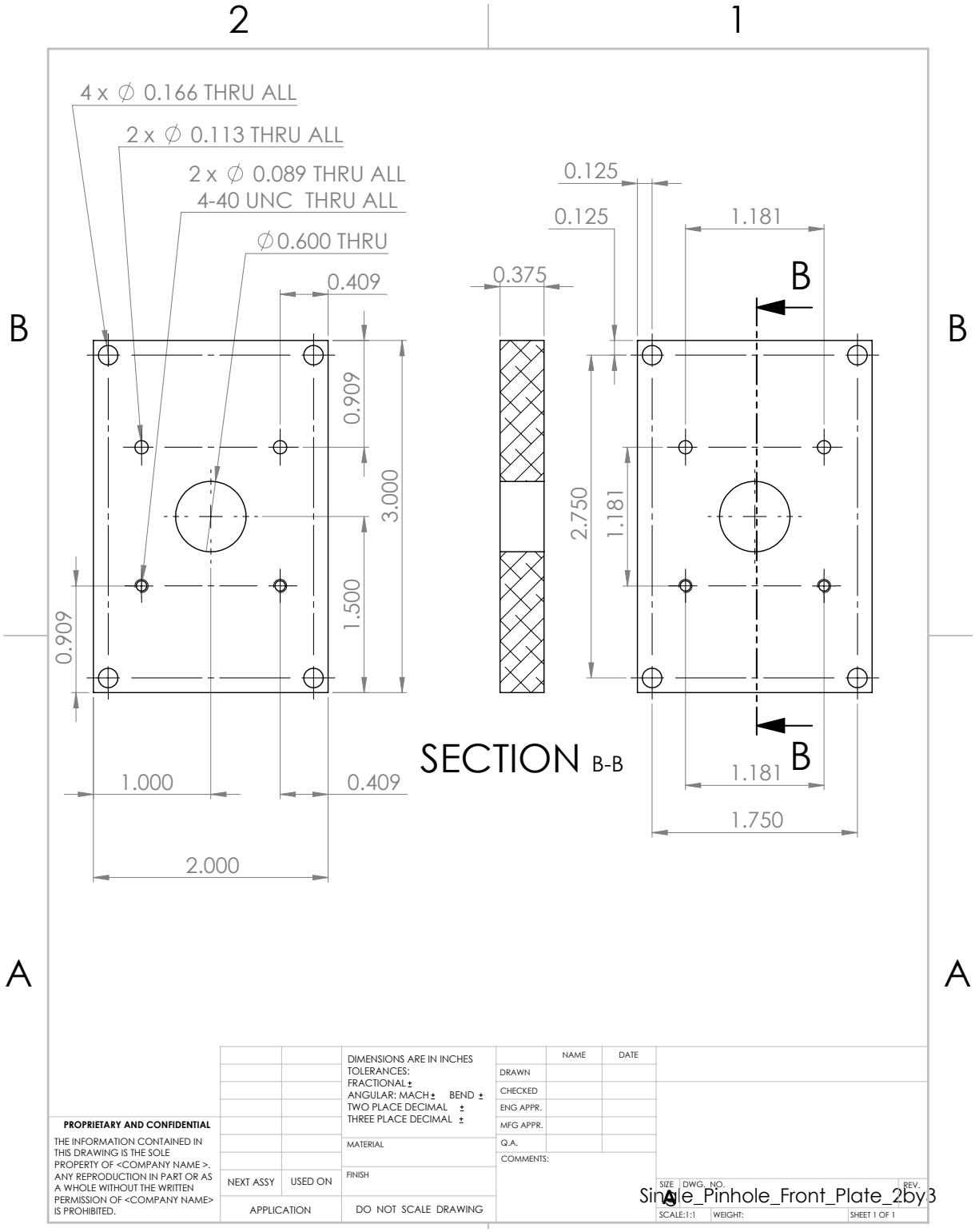

Figure B.2: Diagram of the front panel of the x-ray camera to which the Thorlabs CFH2 filter holder mounts.

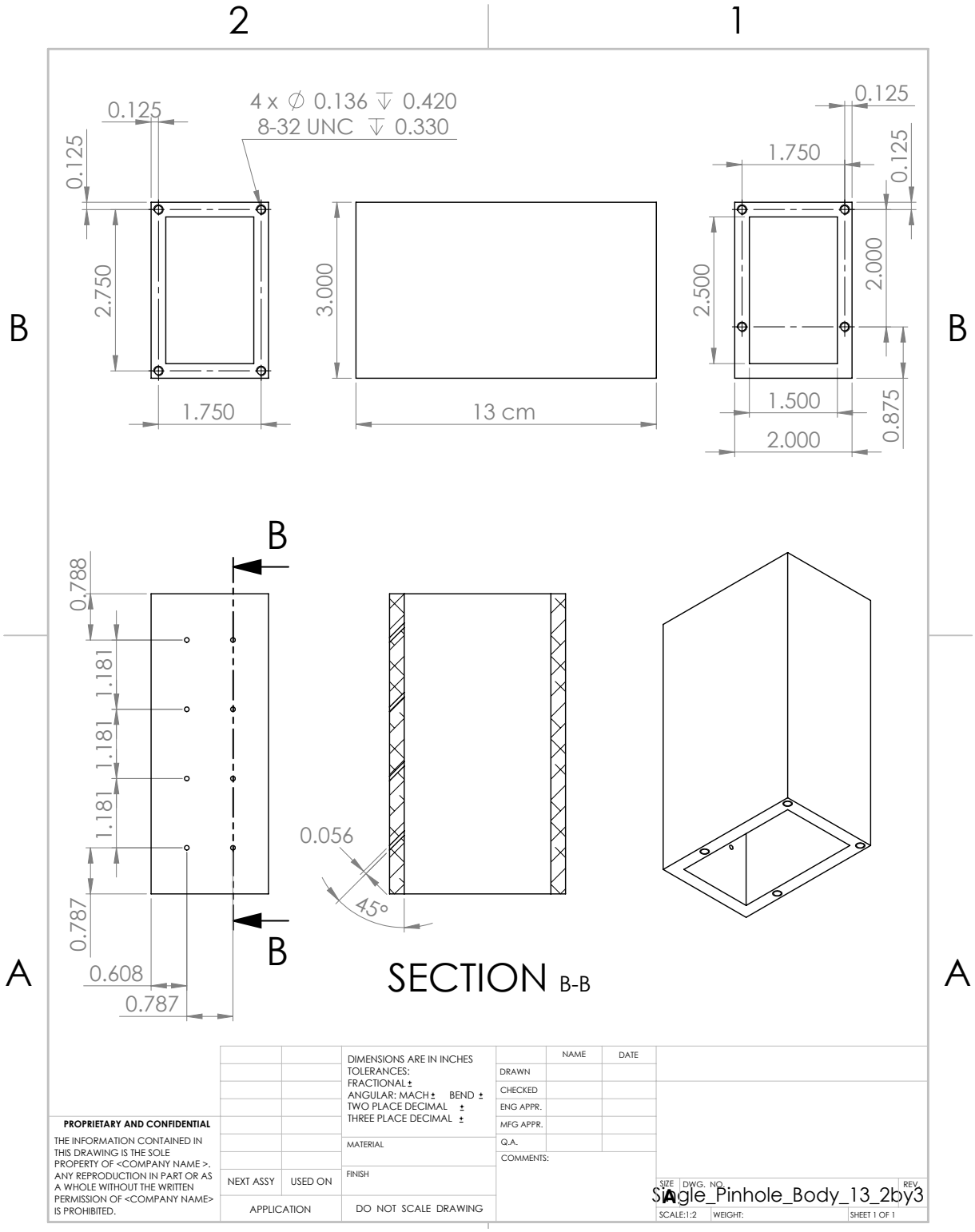

Figure B.3: Diagram of the 13 cm x-ray camera body.

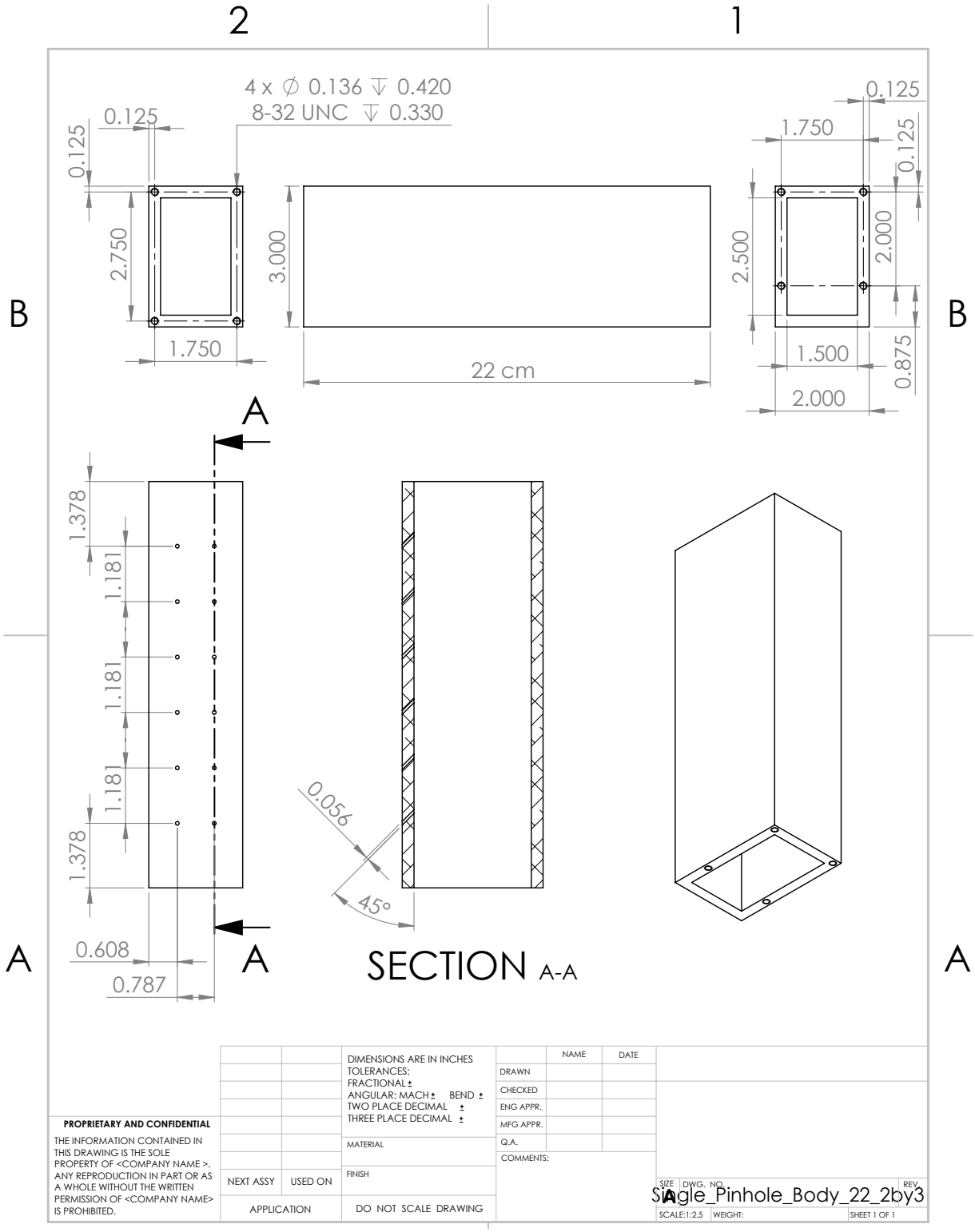

Figure B.4: Diagram of the 22 cm x-ray camera body.

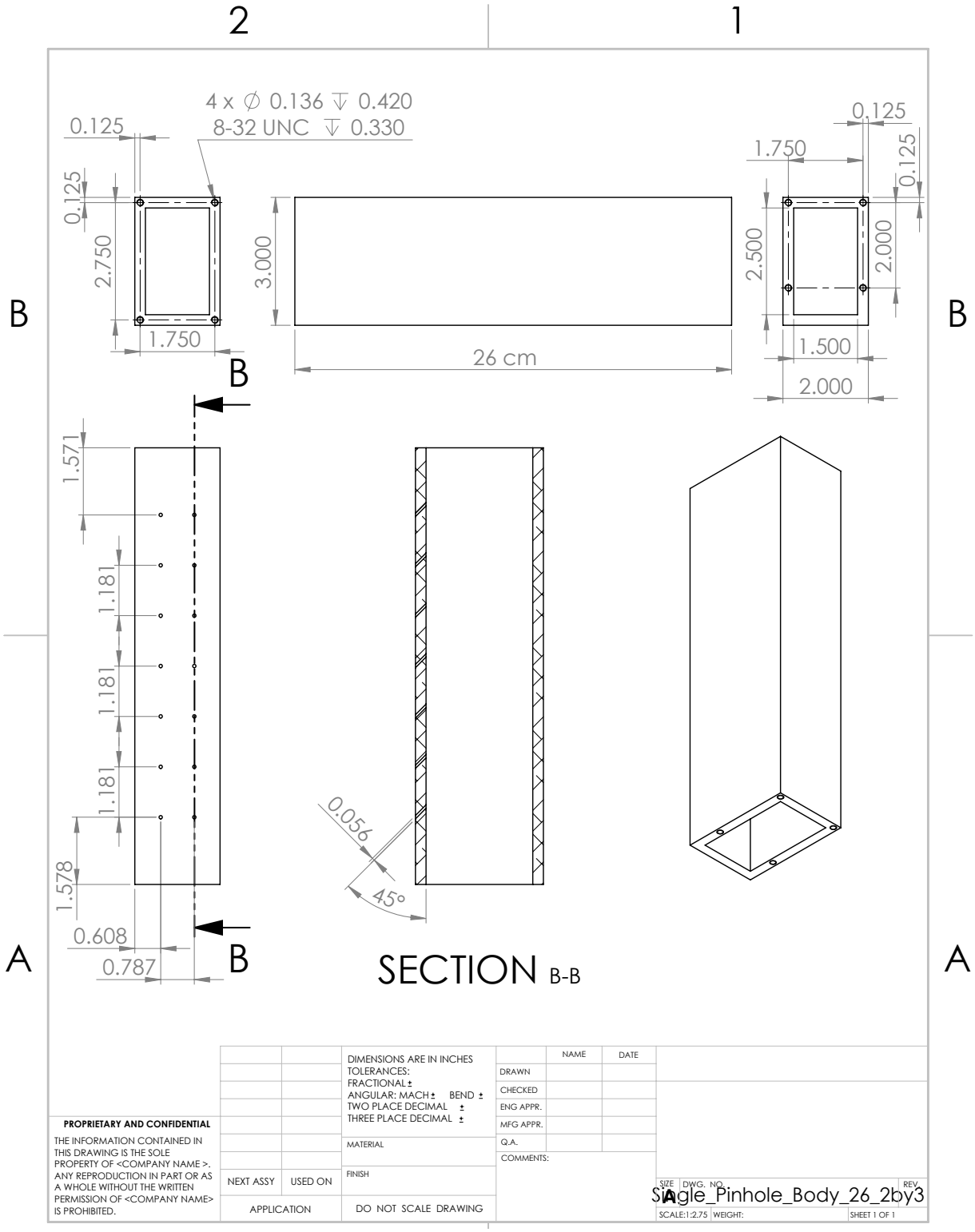

Figure B.5: Diagram of the 26 cm x-ray camera body.

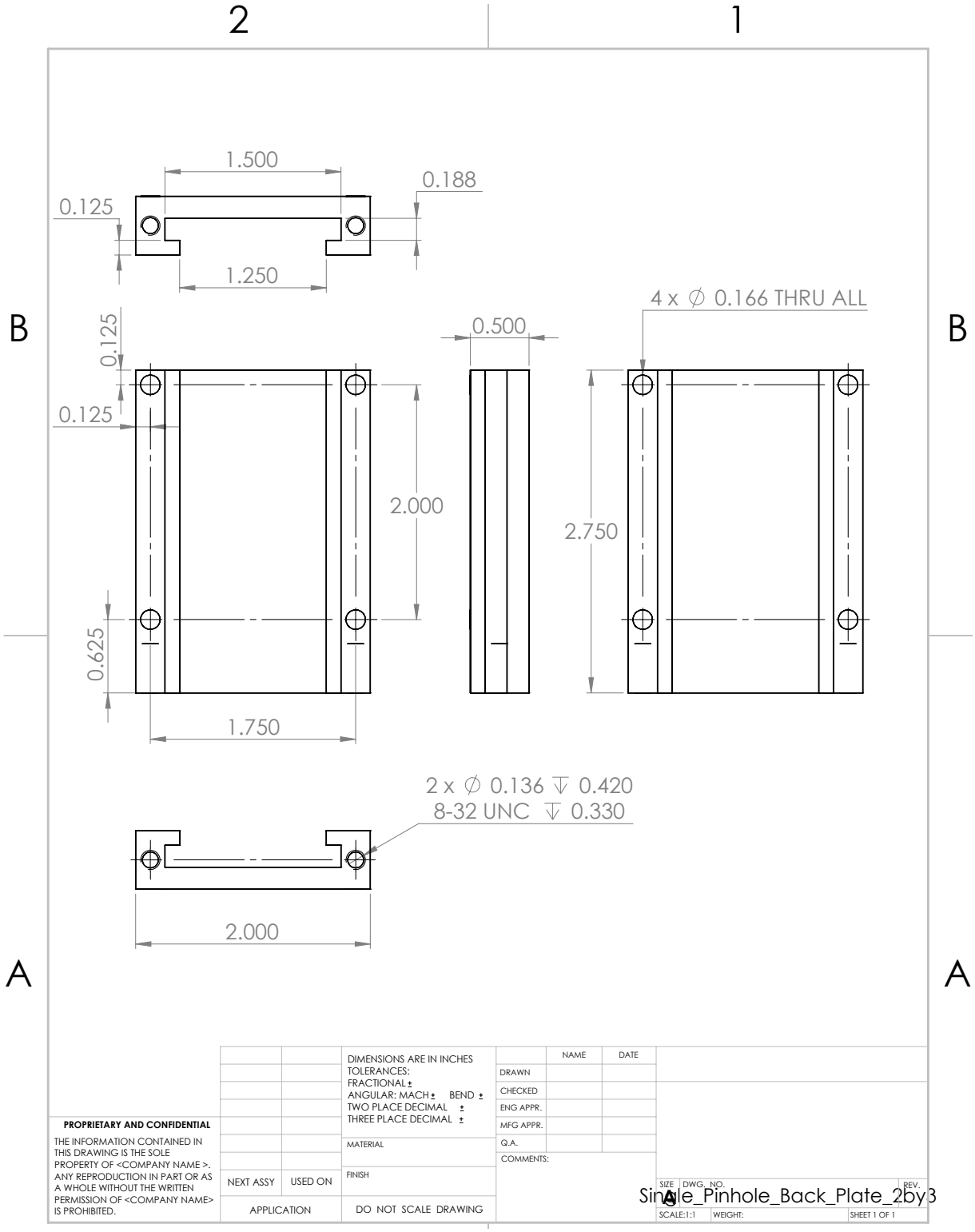

Figure B.6: Diagram of the top portion of the back panel. The back panel is in two pieces for easier machining of the film-holder slot.

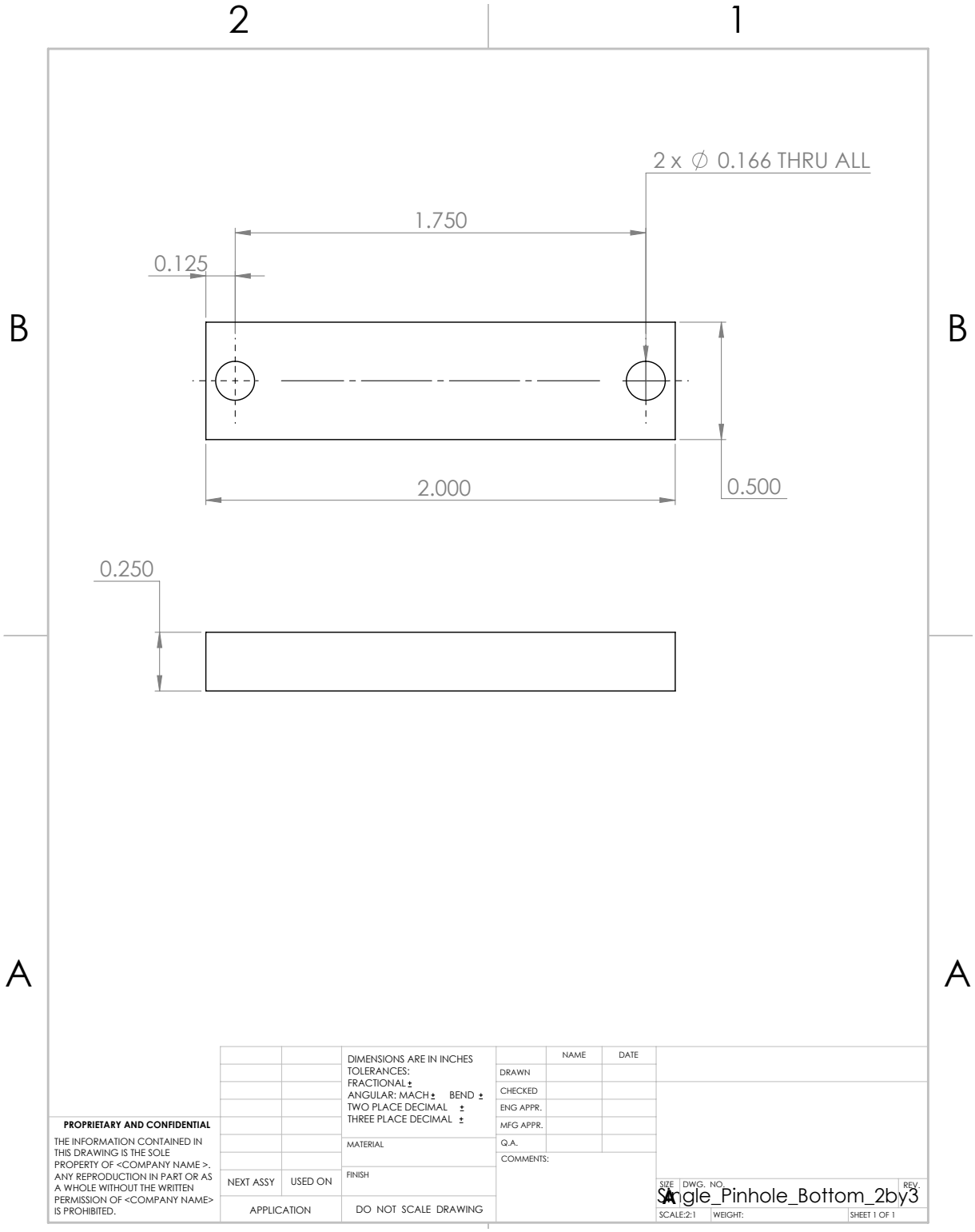

Figure B.7: Diagram of the bottom portion of the back panel. The back panel is in two pieces for easier machining of the film-holder slot.

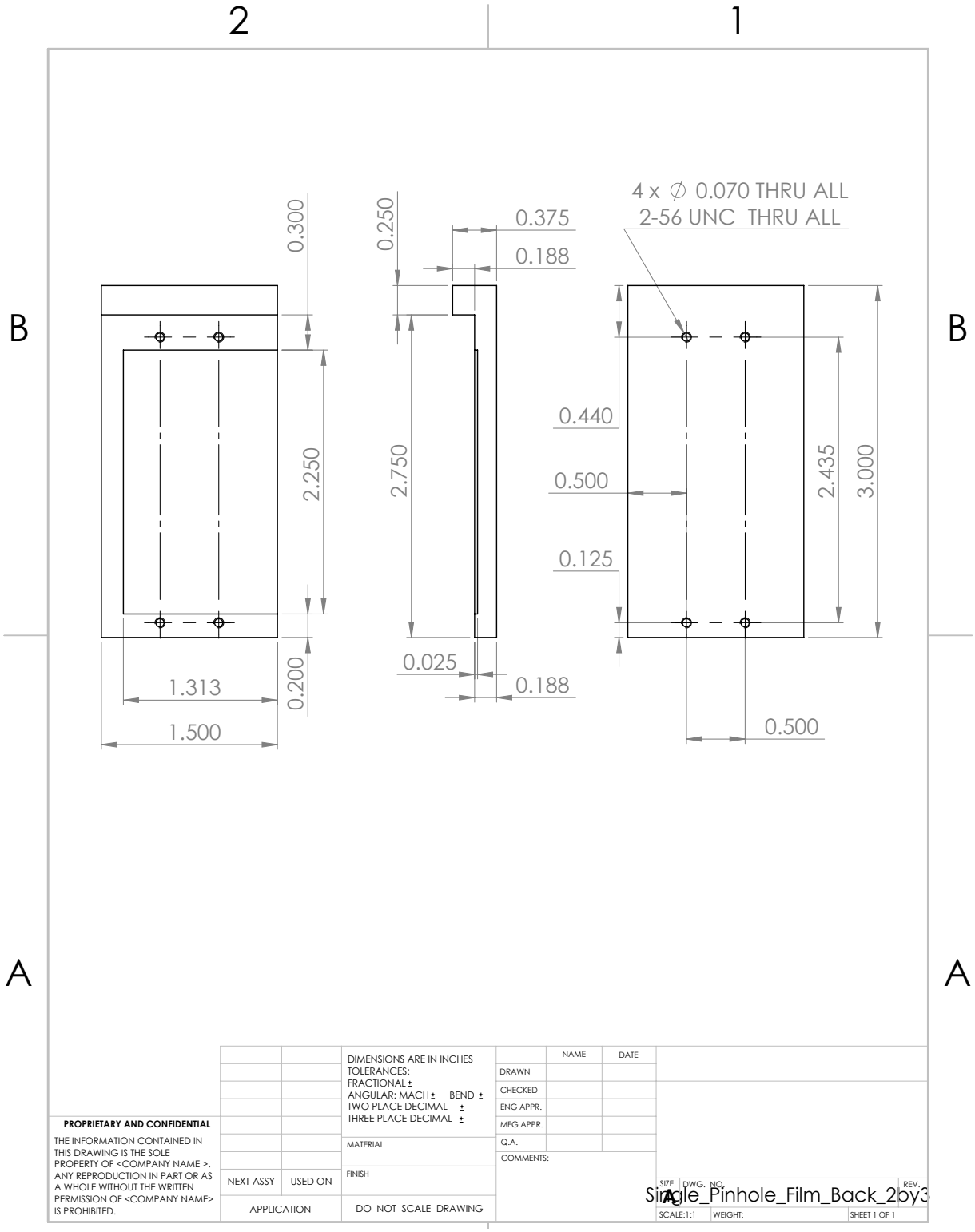

Figure B.8: Diagram of the back piece of the film-holder with film slot.

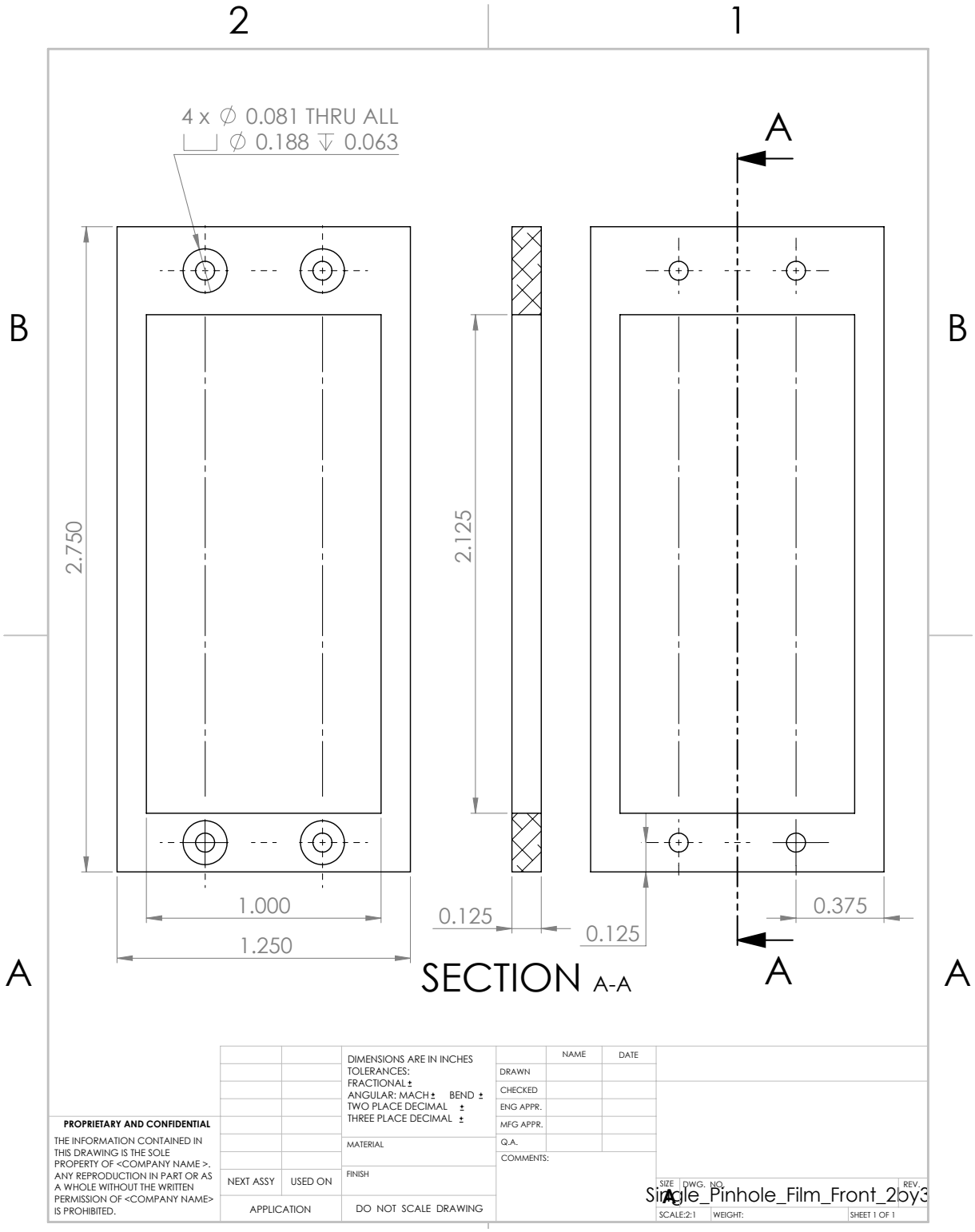

Figure B.9: Diagram of the front film retention piece of the film-holder.

APPENDIX C

Experimental Faraday Rotation Image Sets for Shots 2241, 2534, and 2933

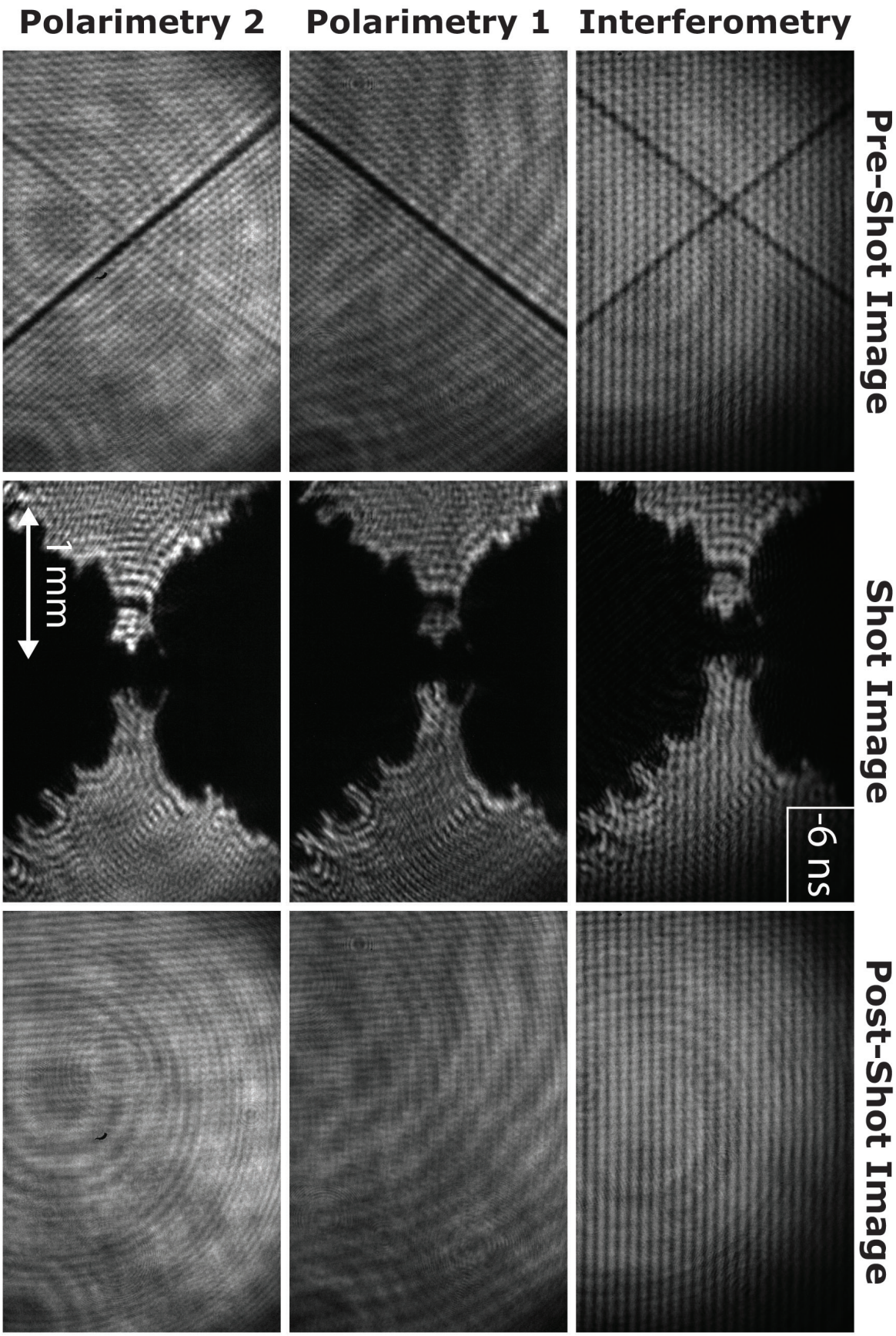

Figure C.1: Faraday rotation diagnostic images for Shot 2241. Image intensity scaled for visibility.

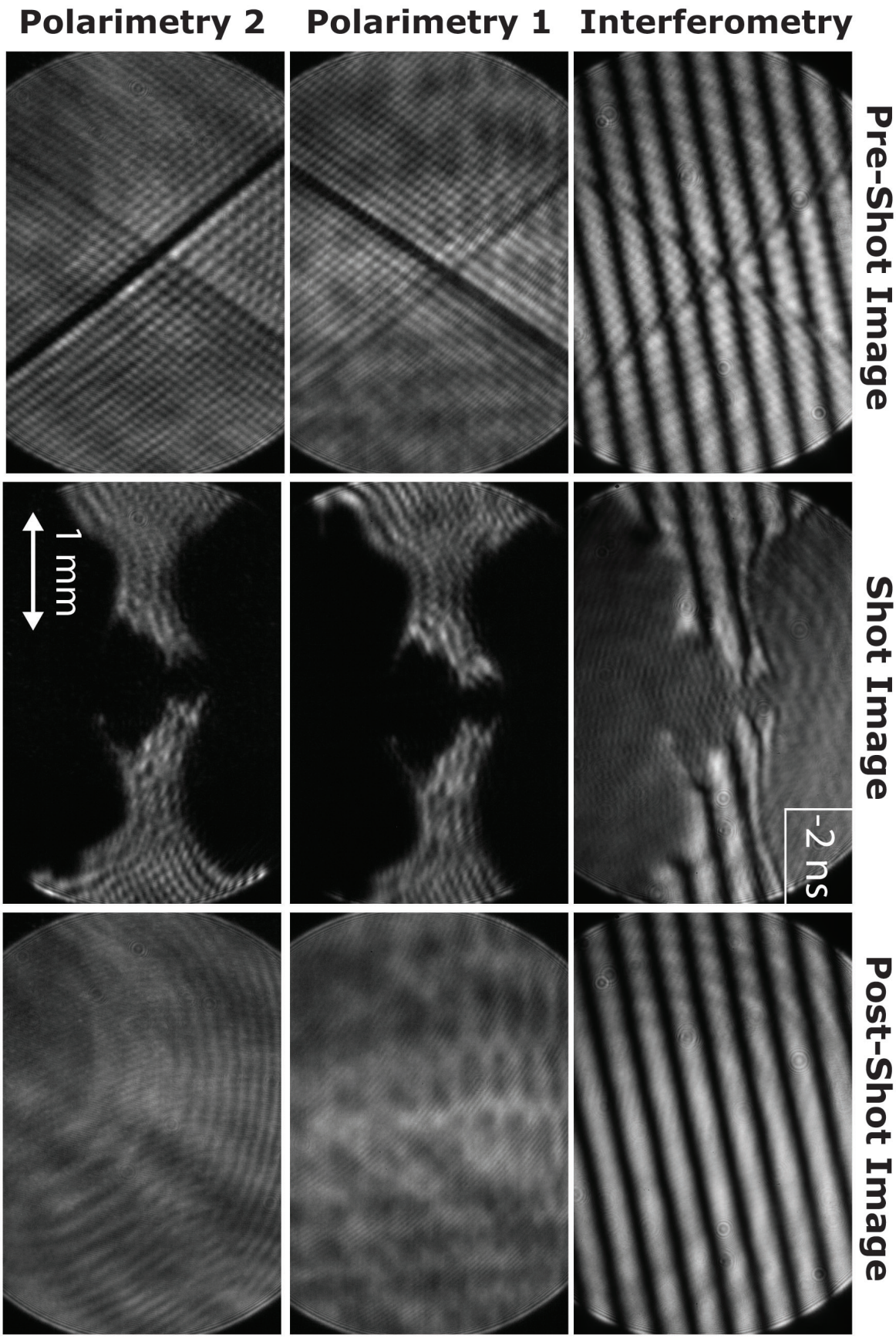

Figure C.2: Faraday rotation diagnostic images for Shot 2534. Image intensity scaled for visibility.

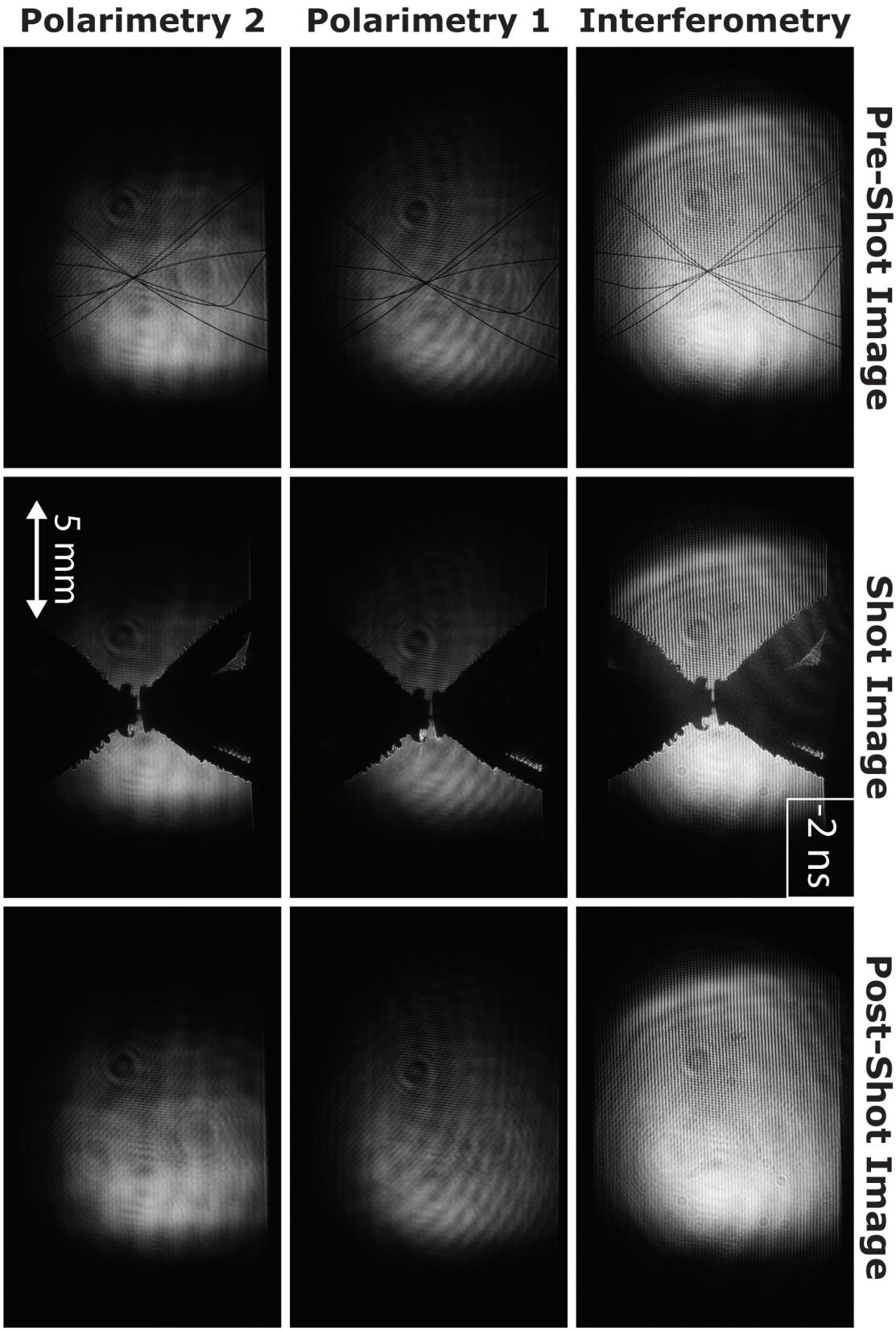

Figure C.3: Faraday rotation diagnostic images for Shot 2933. No additional intensity scaling.

APPENDIX D

Diagnostic Data from Deuterated Polyethylene Fiber Experiments

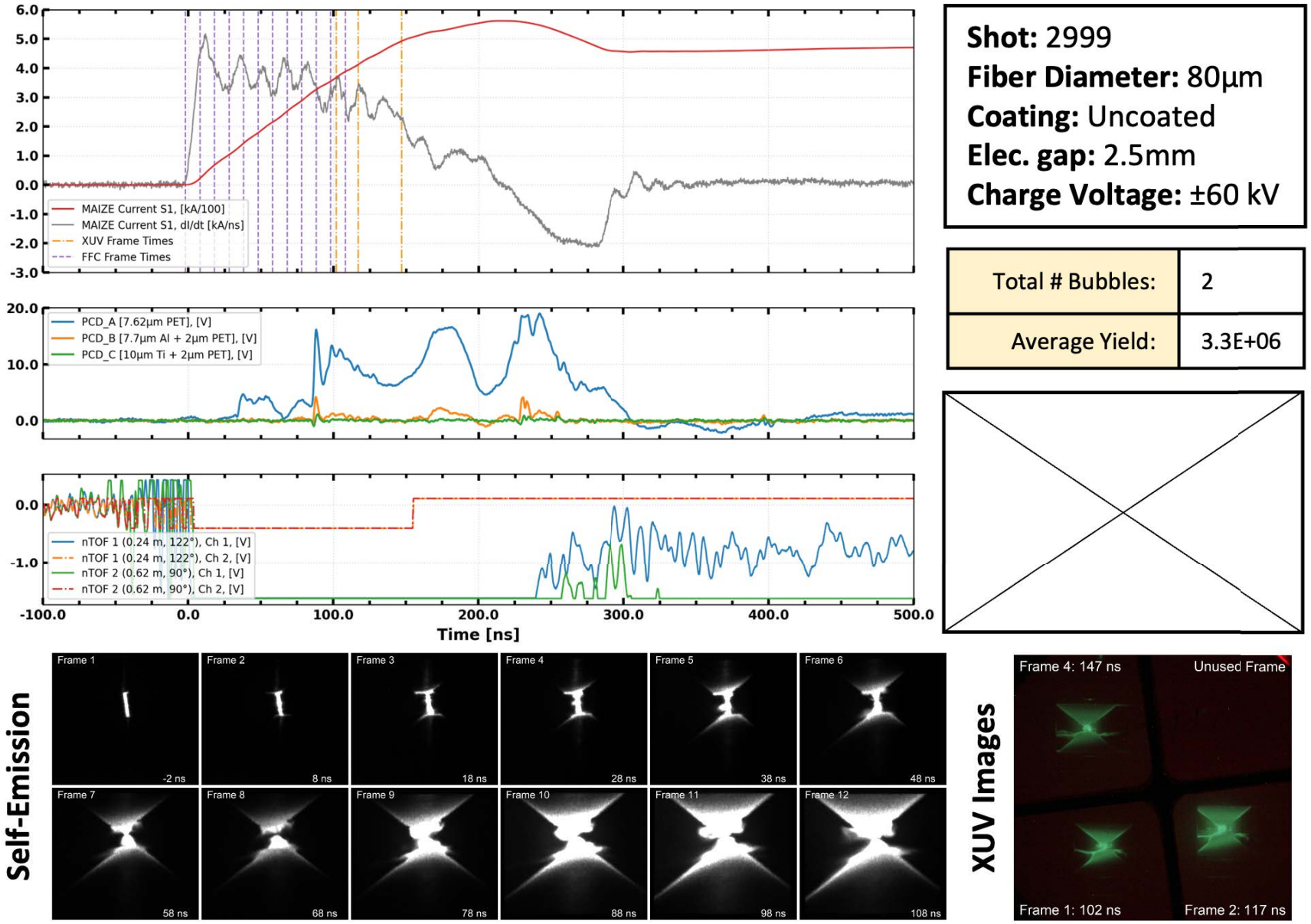

Figure D.1: Parameters and diagnostic data recorded for Shot 2999.

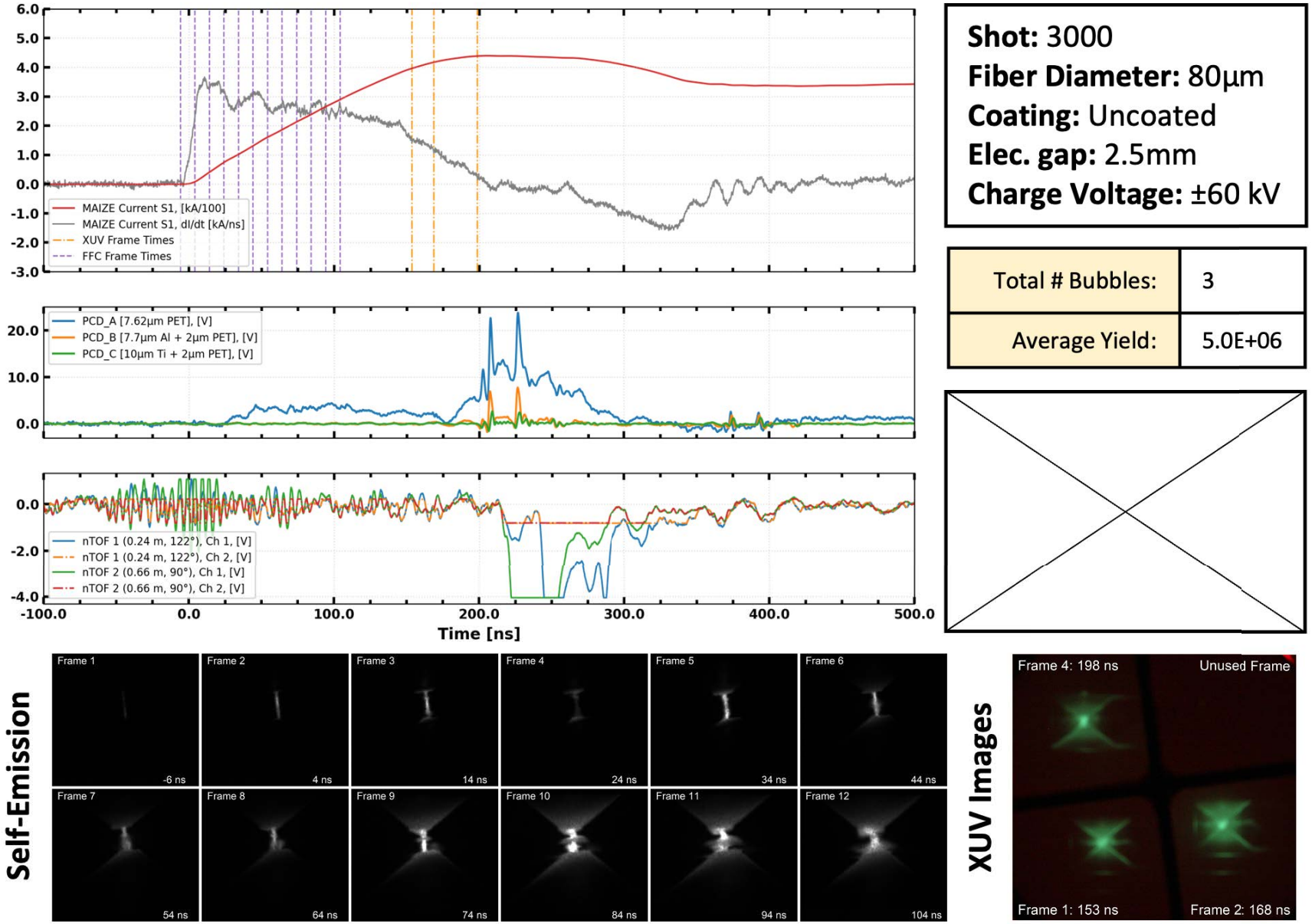

Figure D.2: Parameters and diagnostic data recorded for Shot 3000.

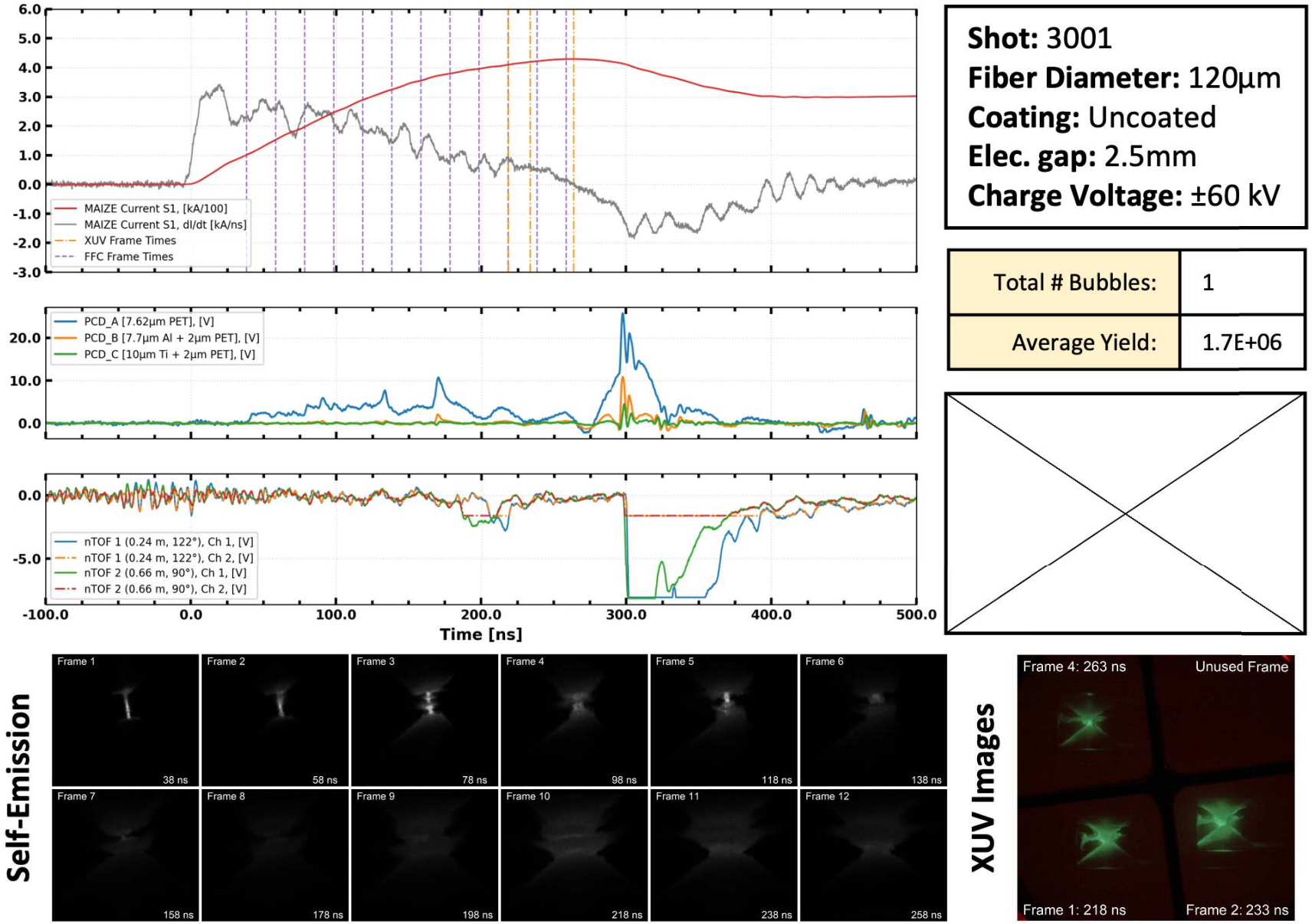

Figure D.3: Parameters and diagnostic data recorded for Shot 3001.

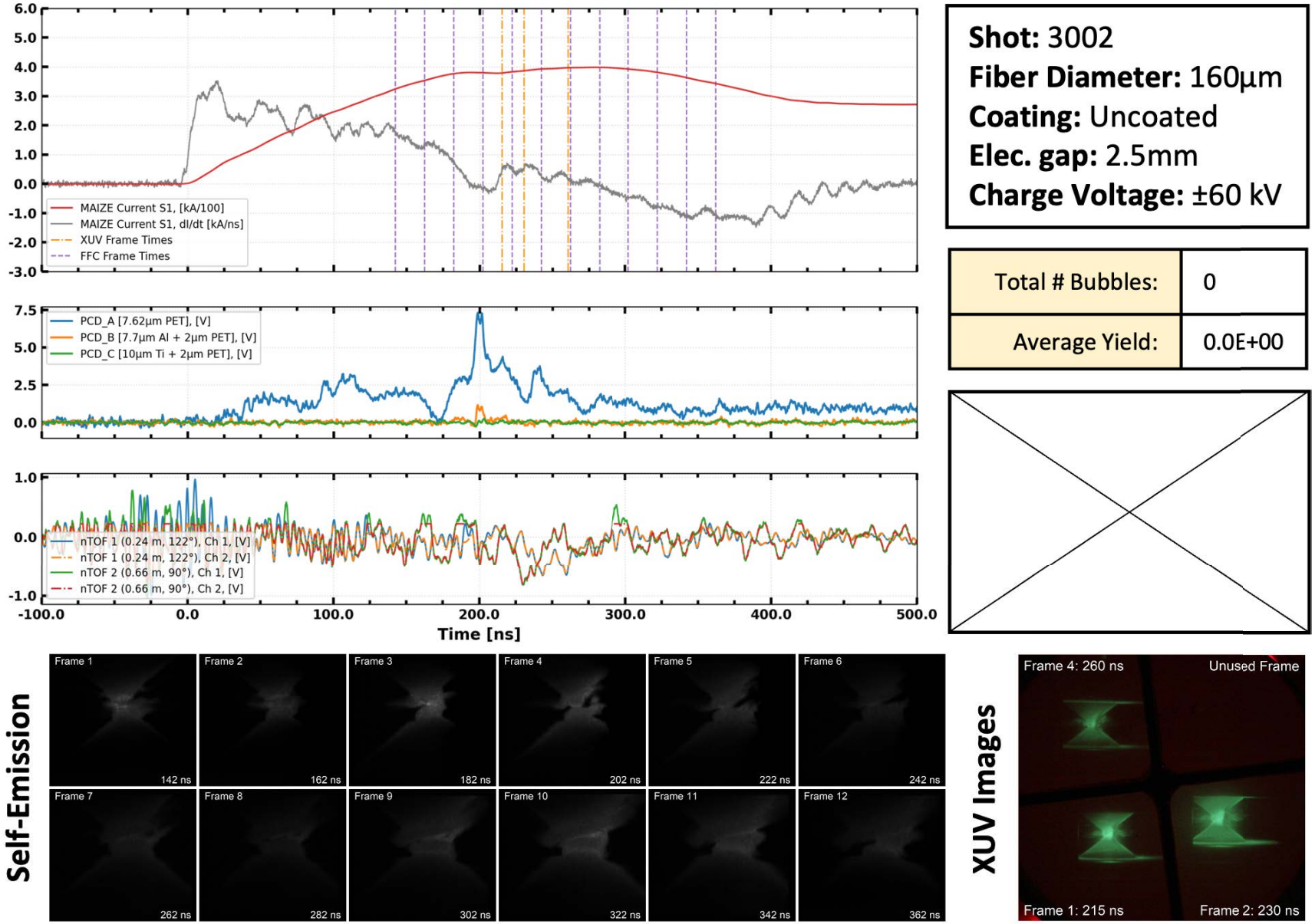

Figure D.4: Parameters and diagnostic data recorded for Shot 3002.

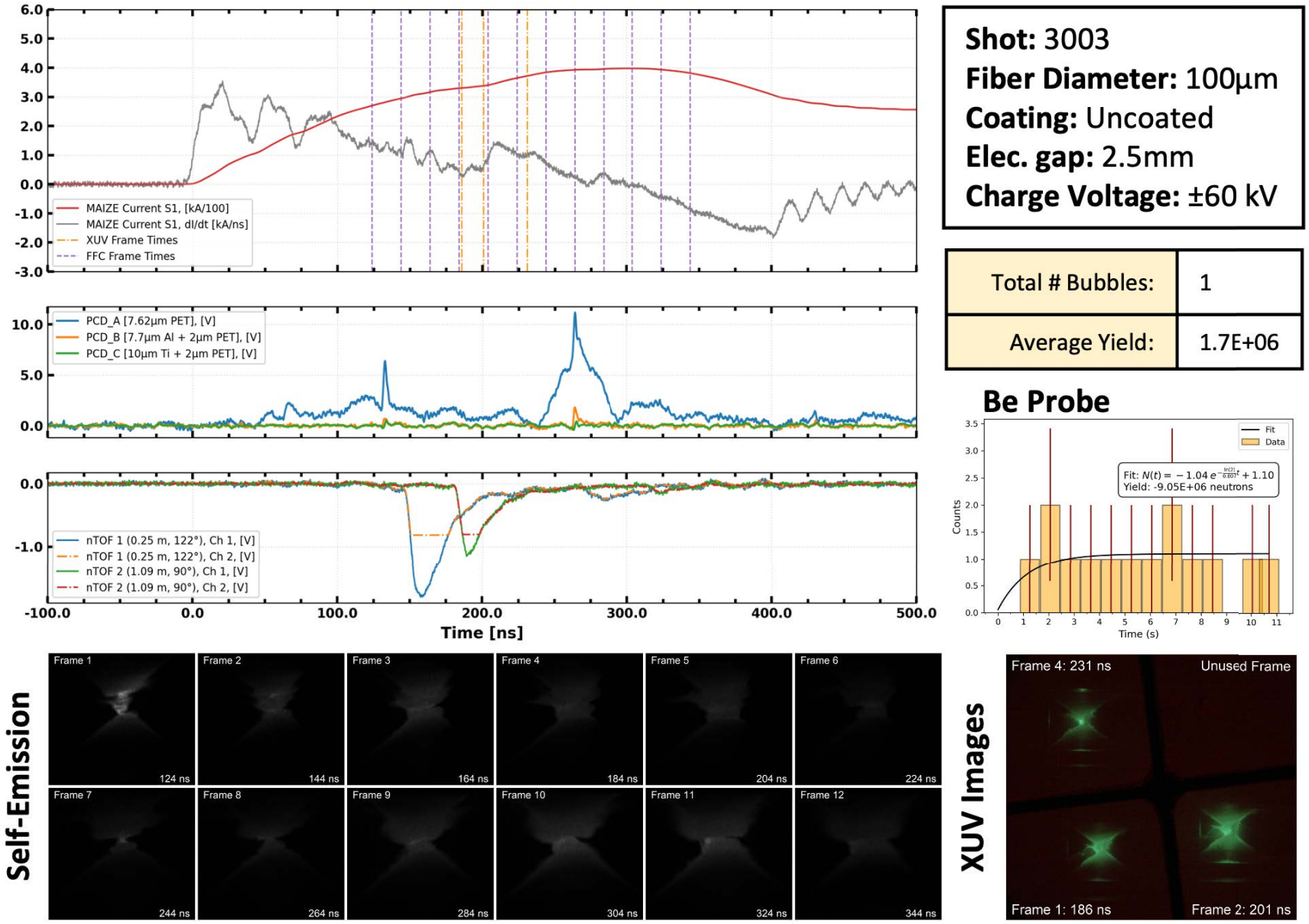

Figure D.5: Parameters and diagnostic data recorded for Shot 3003.

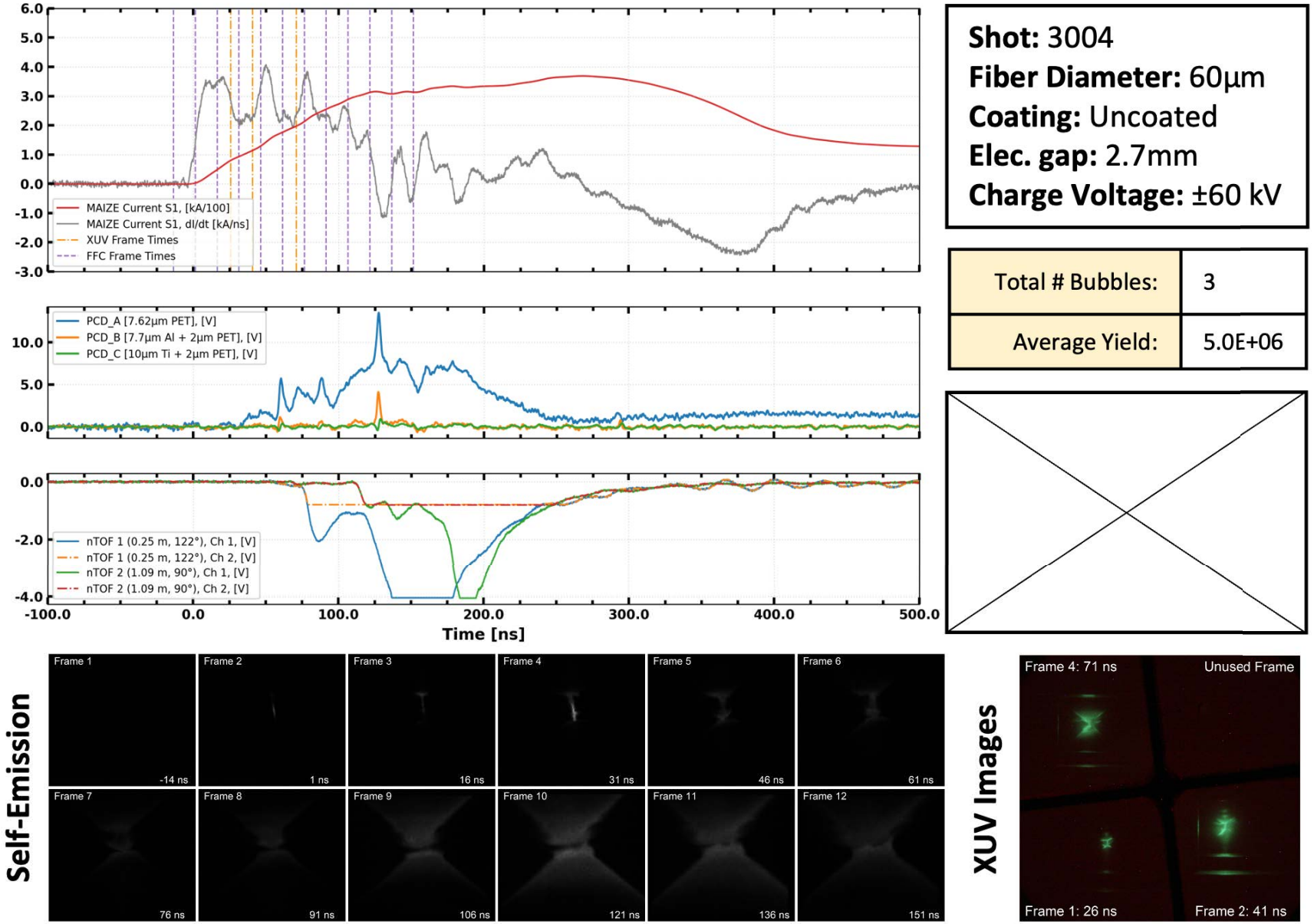

Figure D.6: Parameters and diagnostic data recorded for Shot 3004.

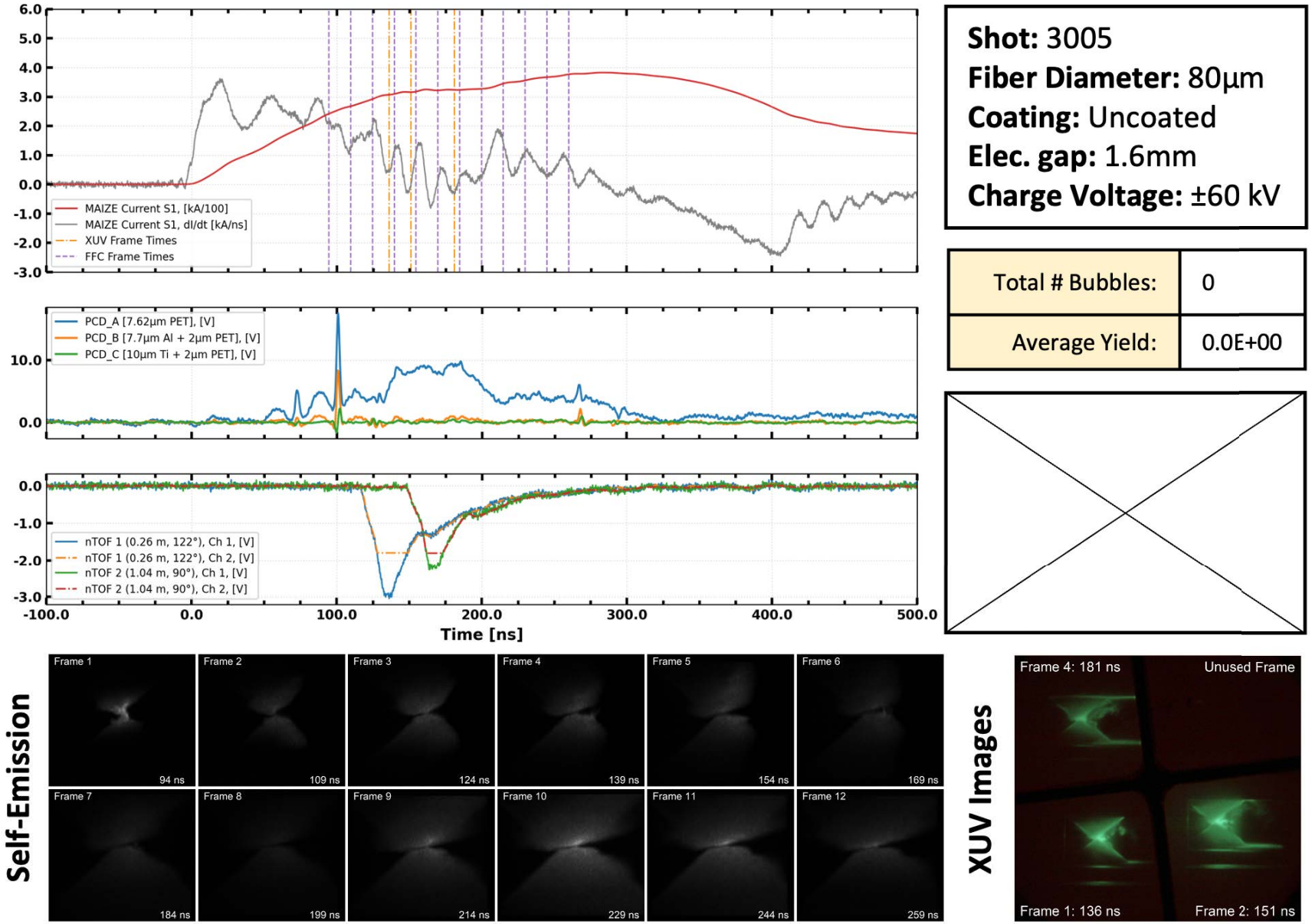

Figure D.7: Parameters and diagnostic data recorded for Shot 3005.

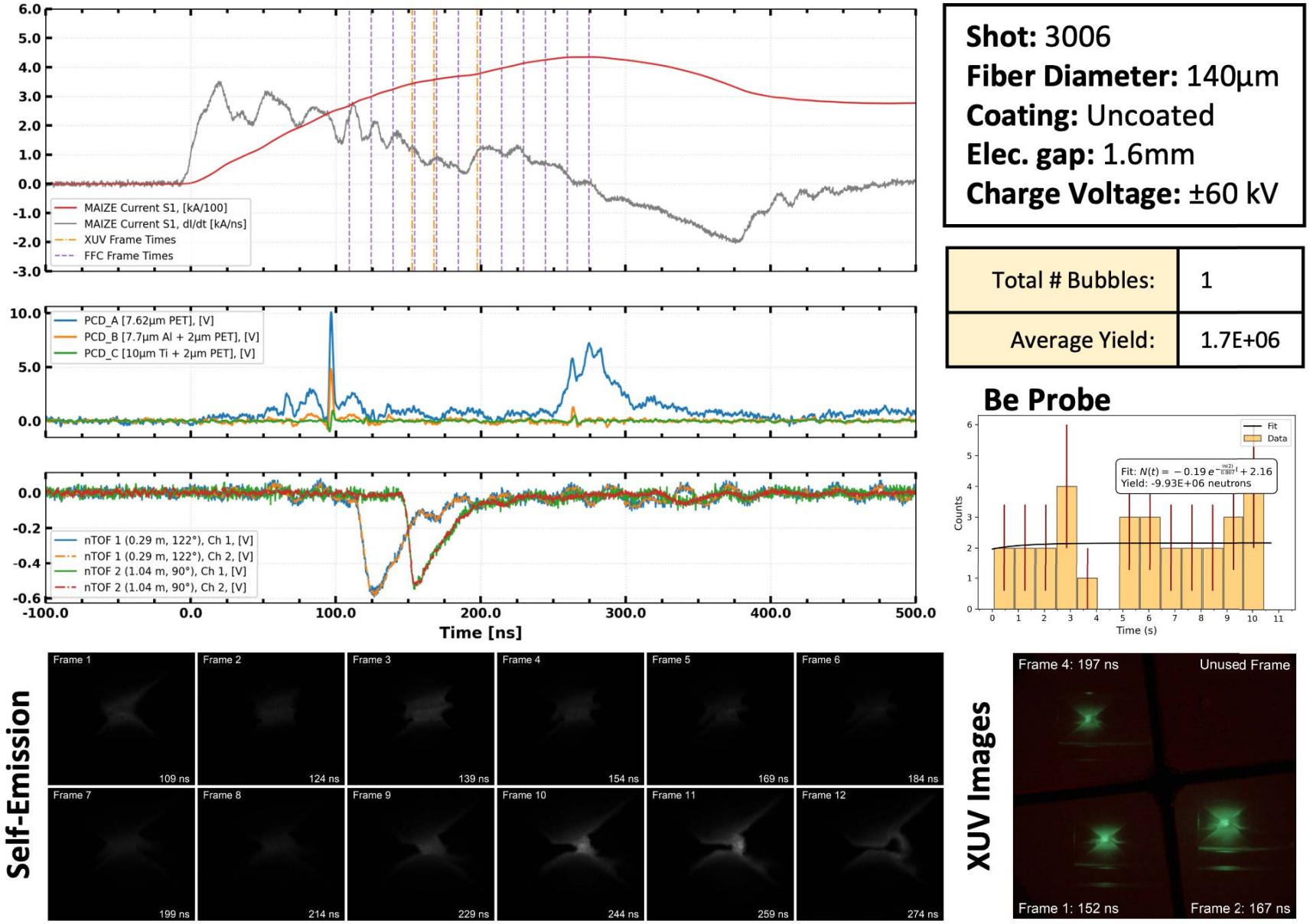

Figure D.8: Parameters and diagnostic data recorded for Shot 3006.

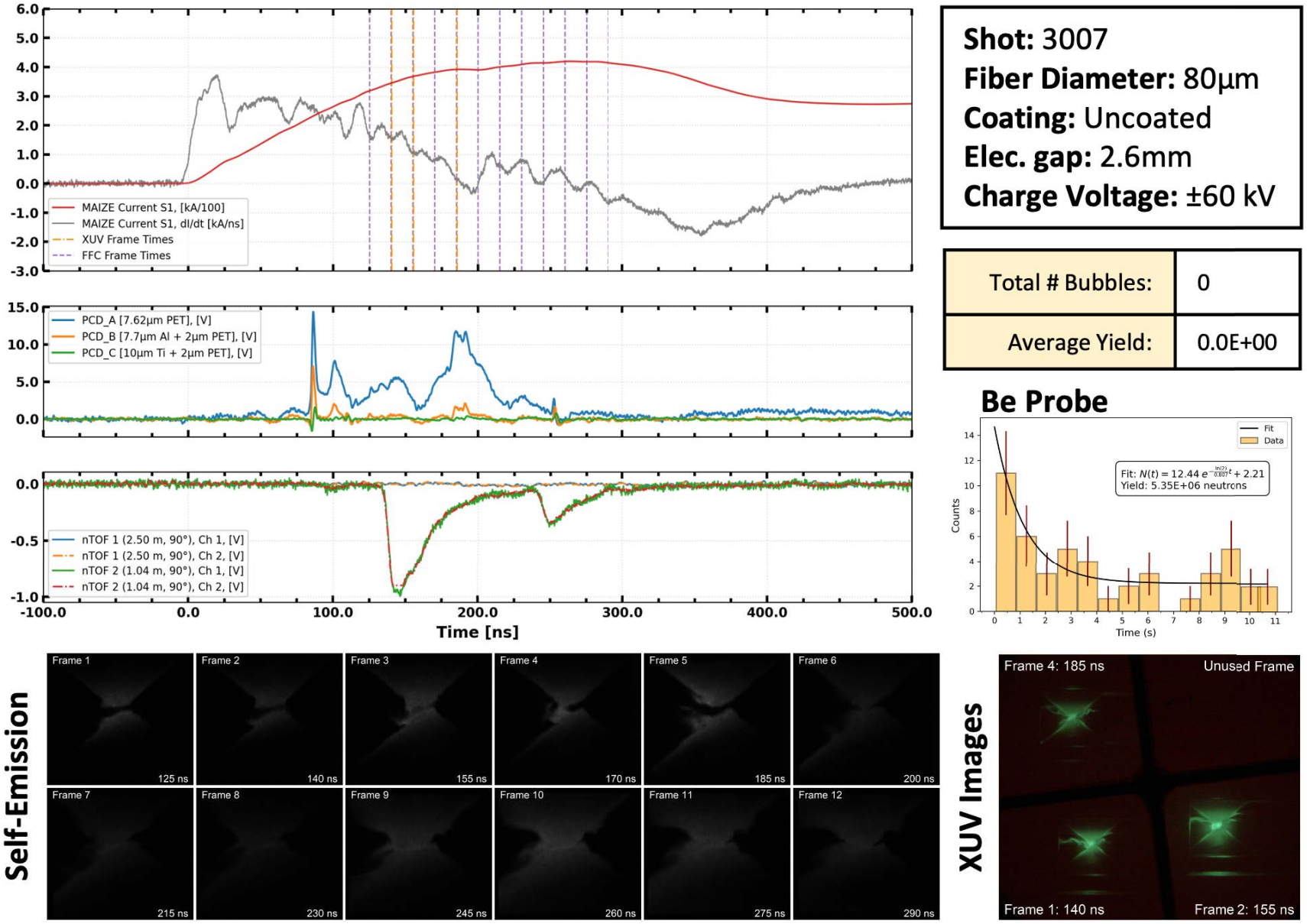

Figure D.9: Parameters and diagnostic data recorded for Shot 3007.

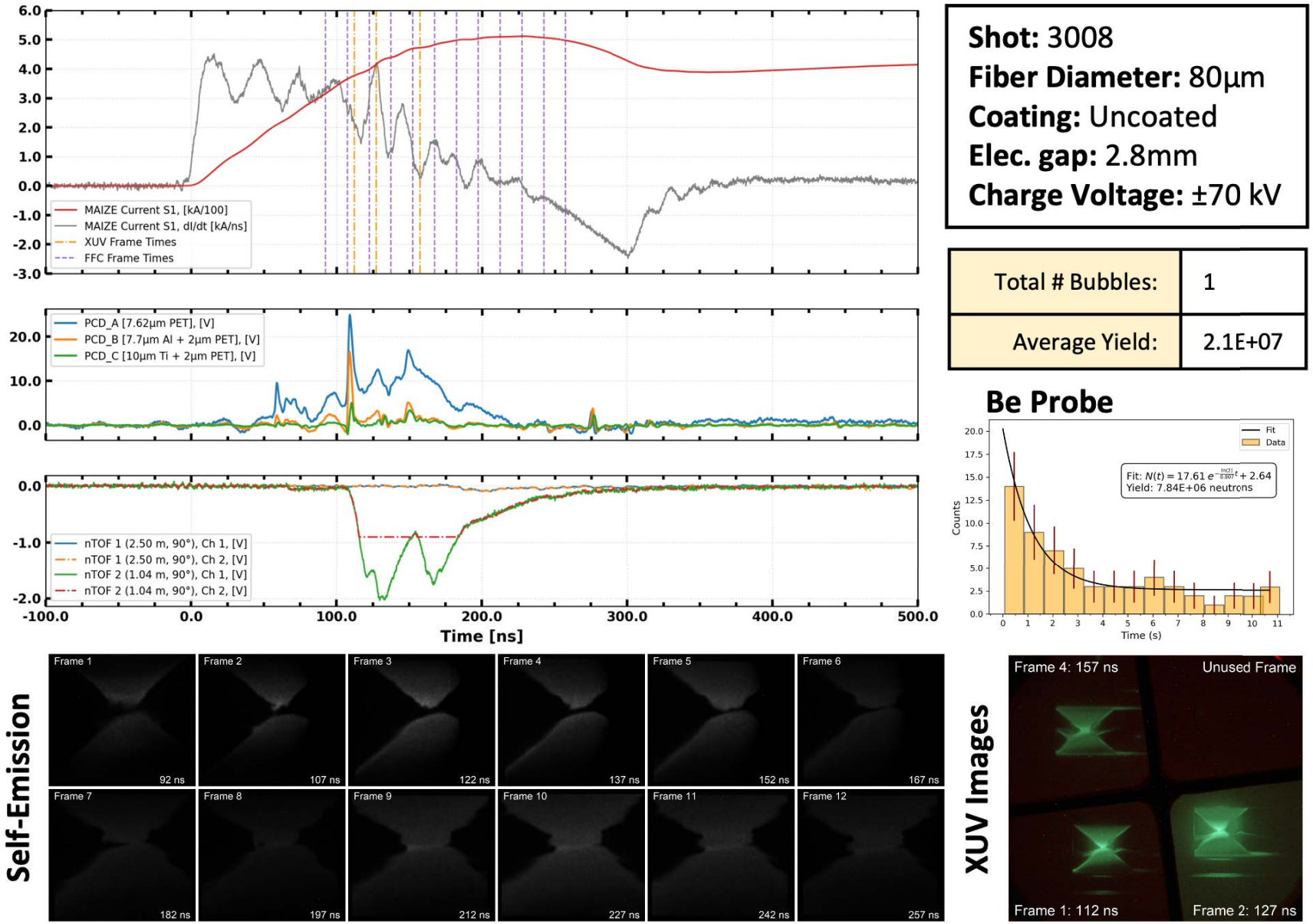

Figure D.10: Parameters and diagnostic data recorded for Shot 3008.

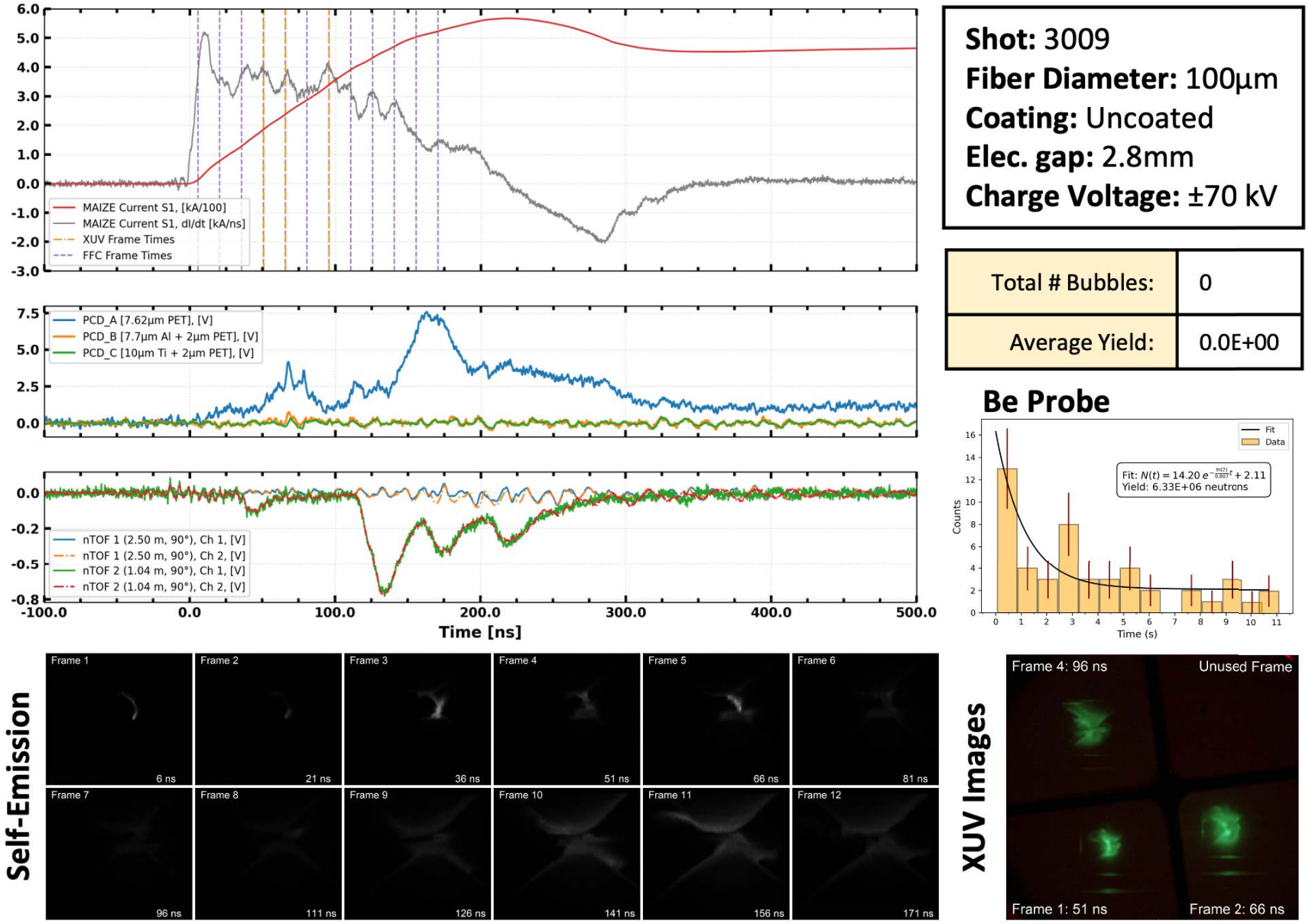

Figure D.11: Parameters and diagnostic data recorded for Shot 3009.

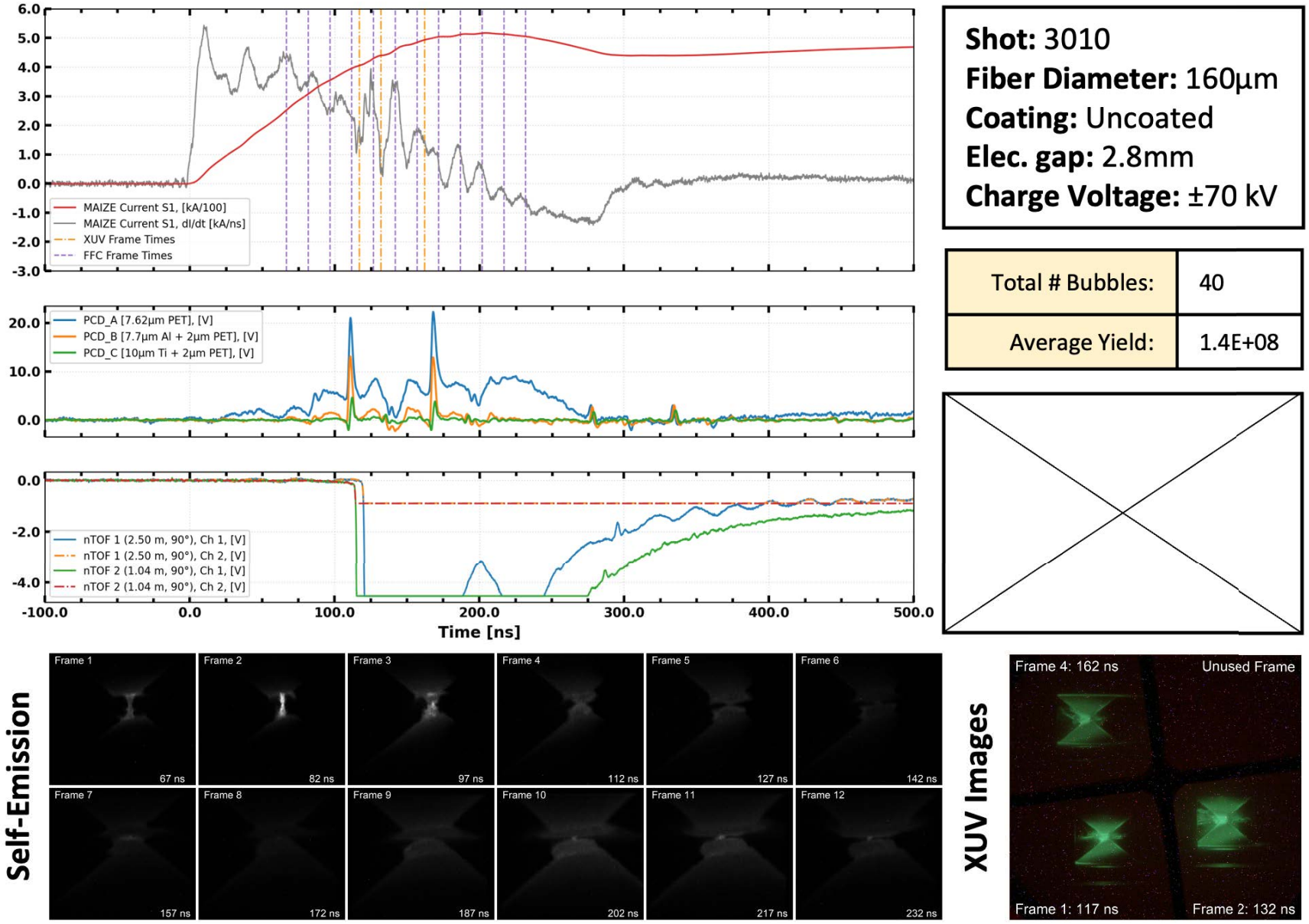

Figure D.12: Parameters and diagnostic data recorded for Shot 3010.

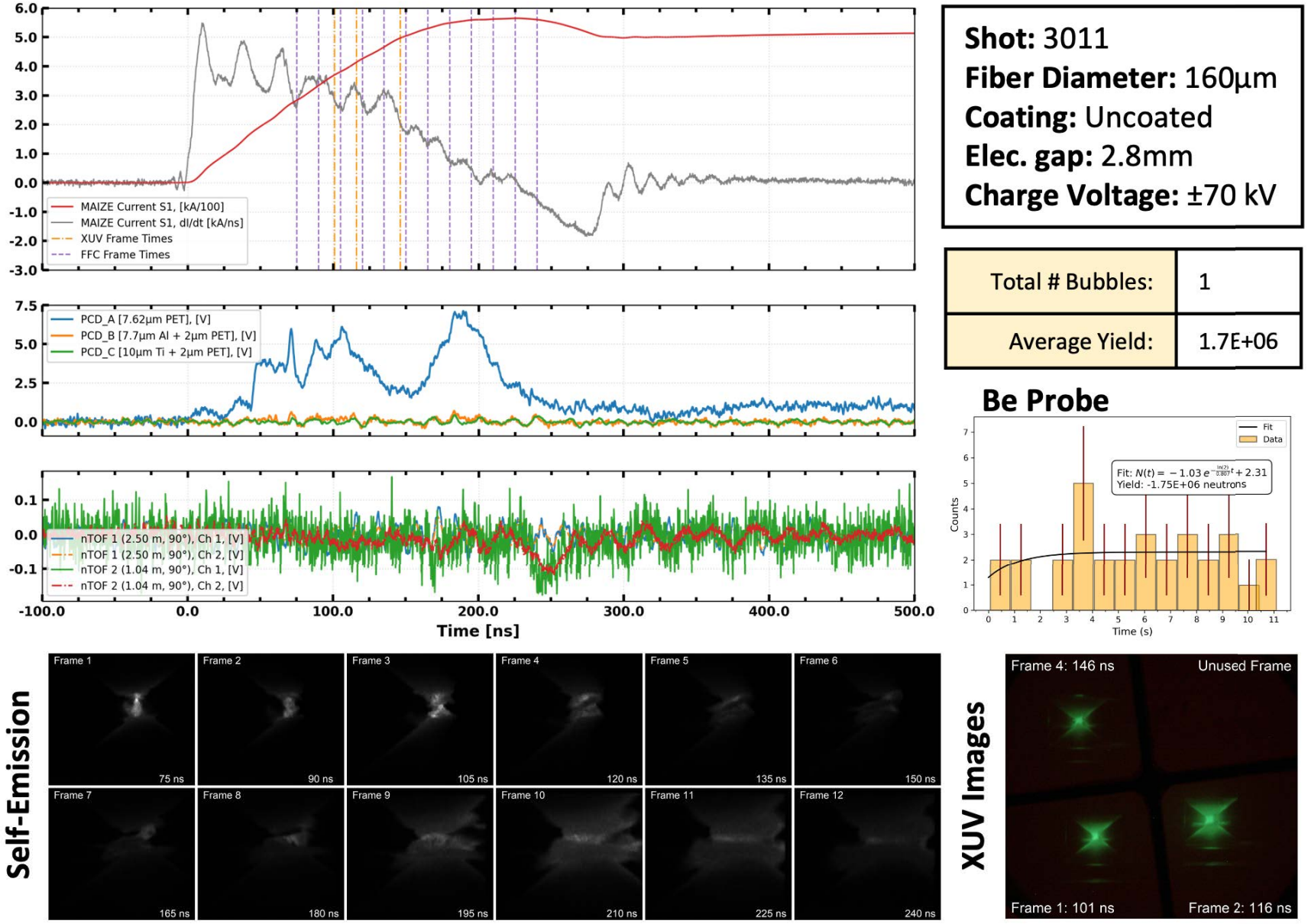

Figure D.13: Parameters and diagnostic data recorded for Shot 3011.

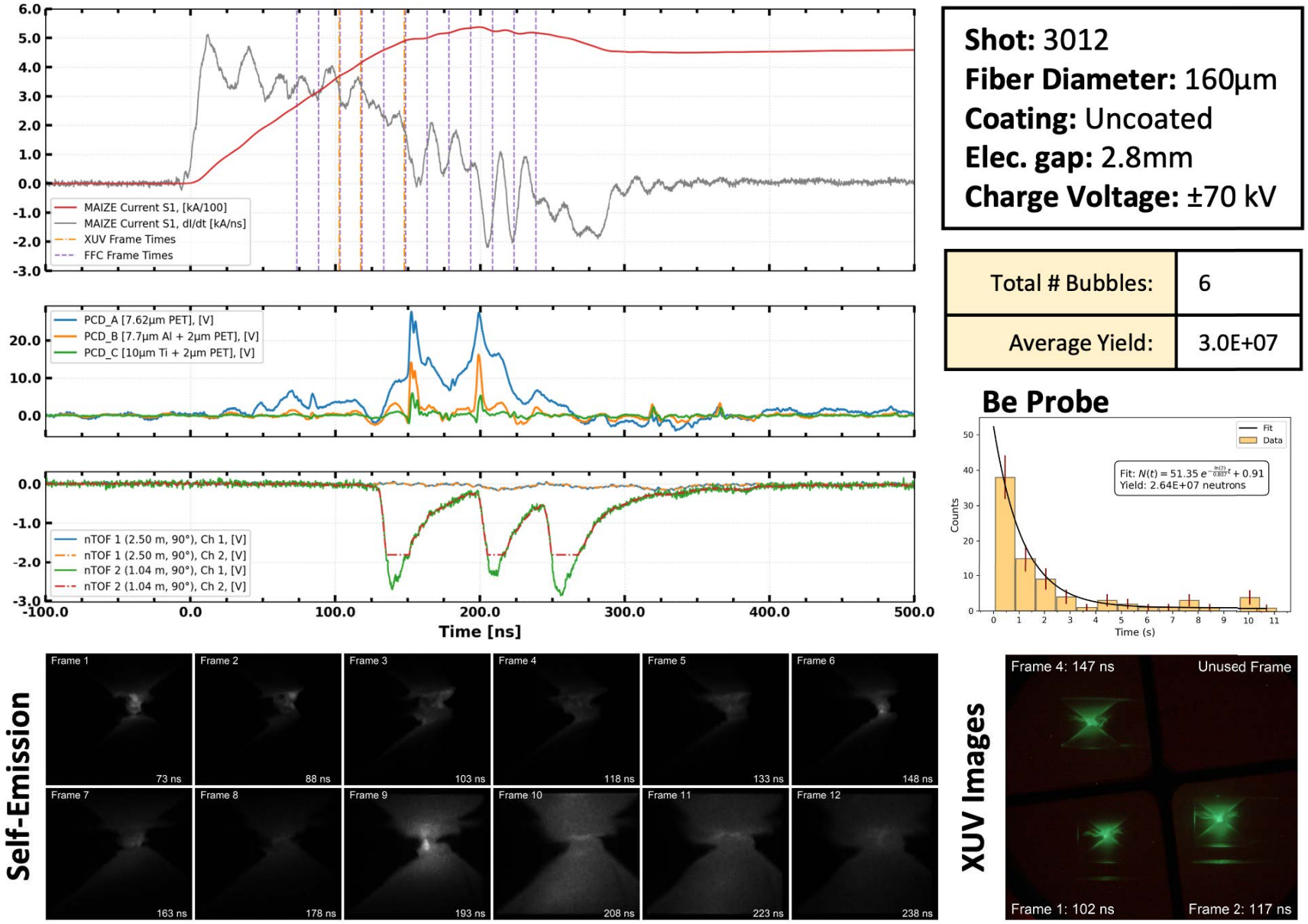

Figure D.14: Parameters and diagnostic data recorded for Shot 3012.

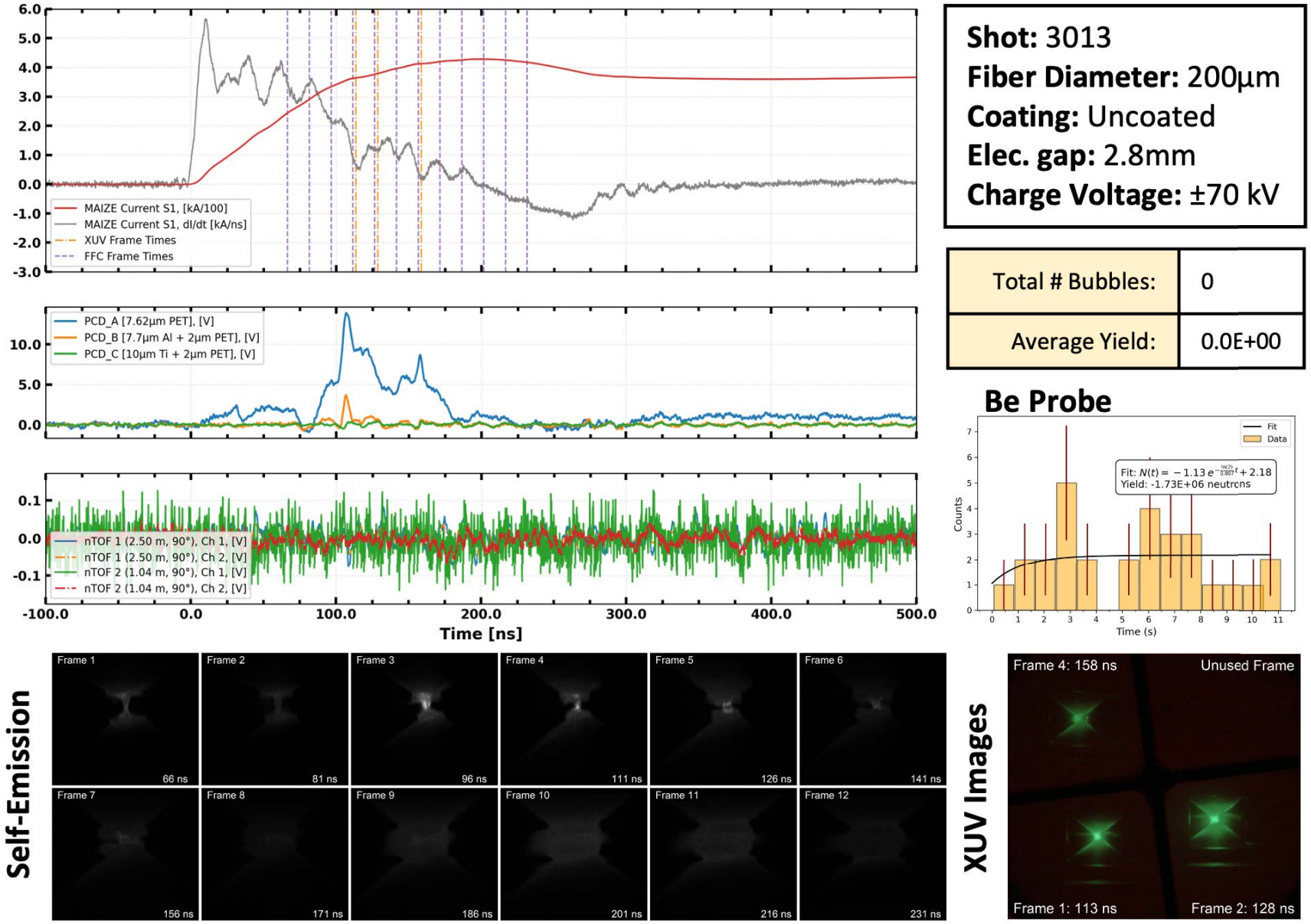

Figure D.15: Parameters and diagnostic data recorded for Shot 3013.

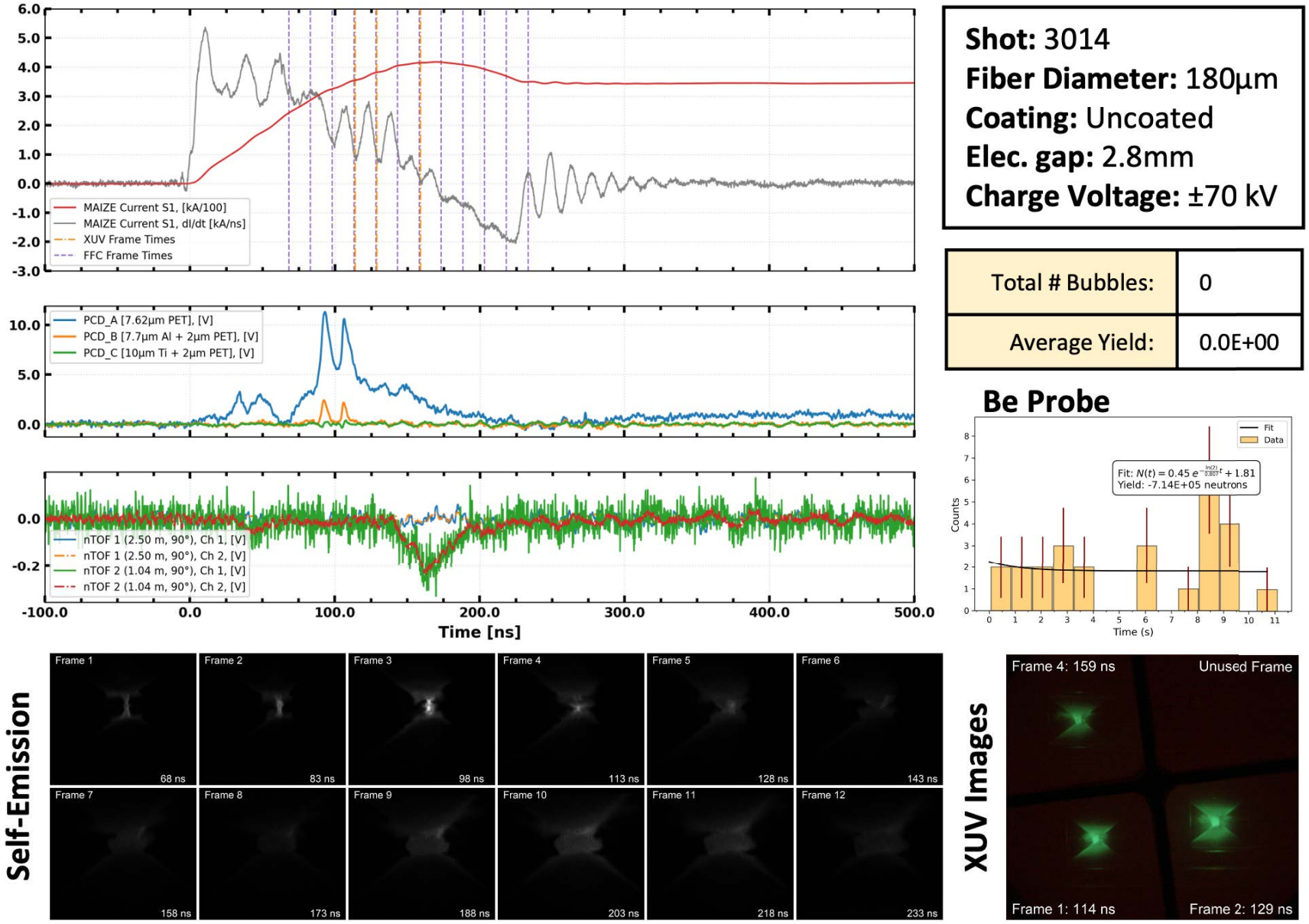

Figure D.16: Parameters and diagnostic data recorded for Shot 3014.

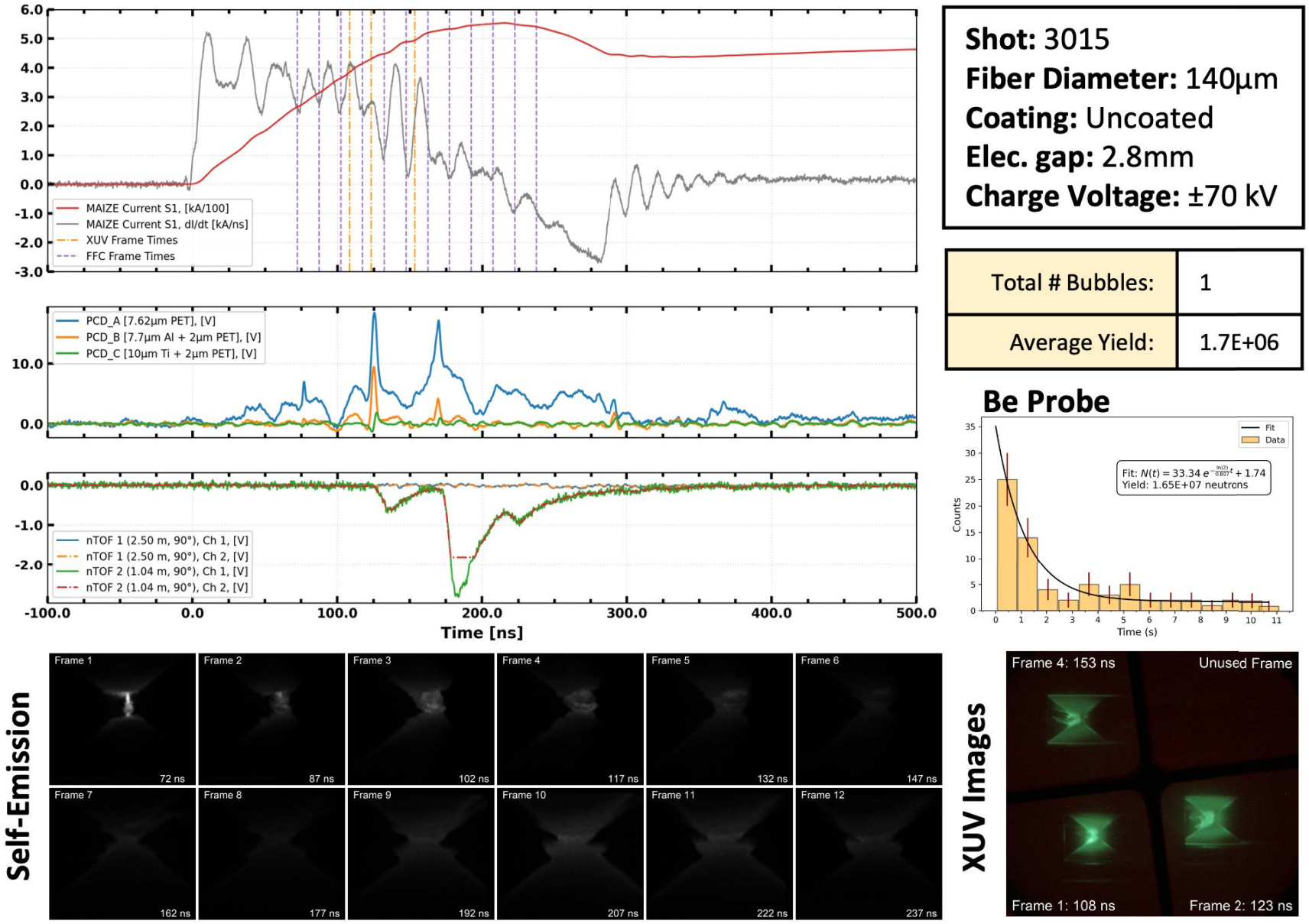

Figure D.17: Parameters and diagnostic data recorded for Shot 3015.

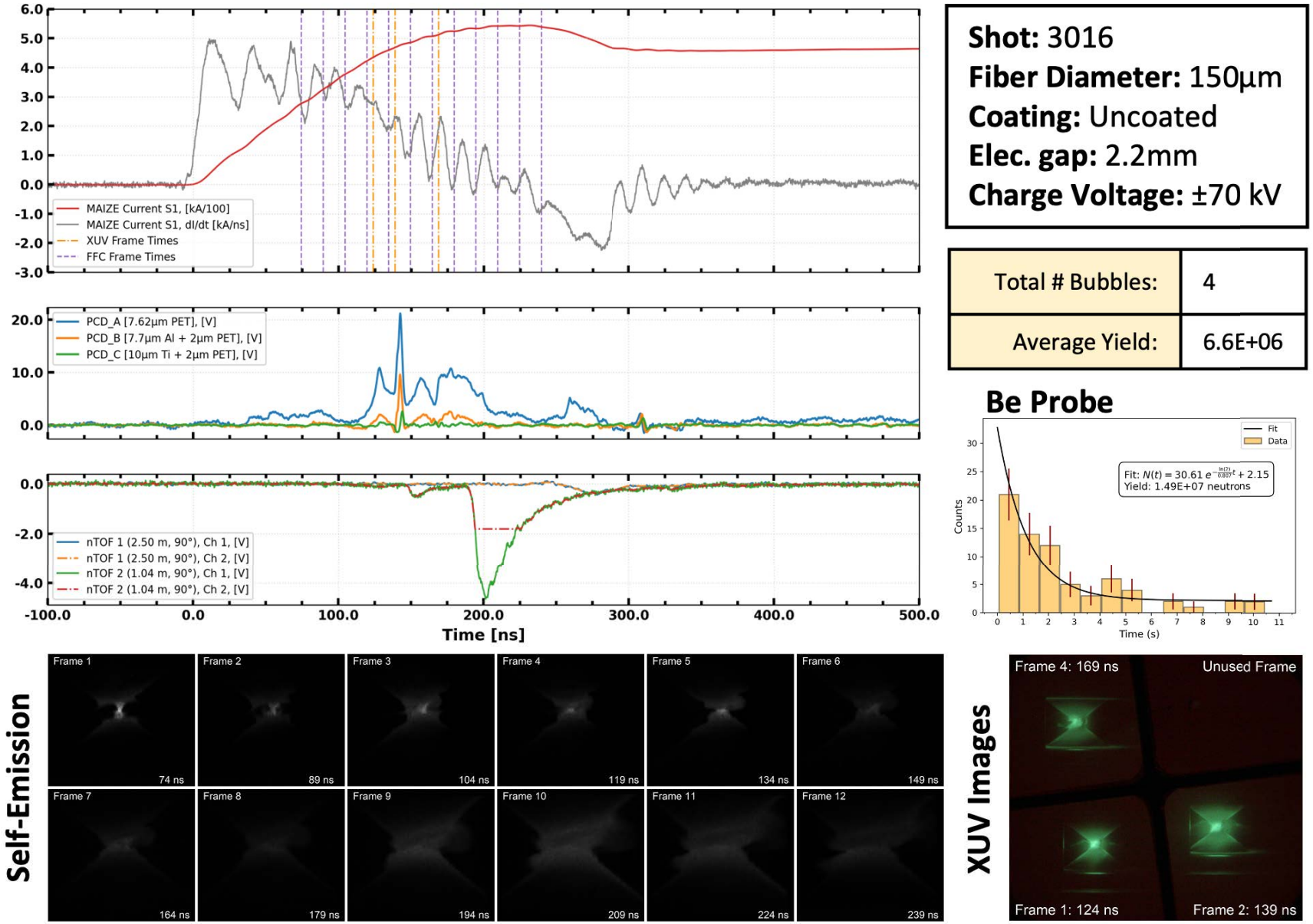

Figure D.18: Parameters and diagnostic data recorded for Shot 3016.

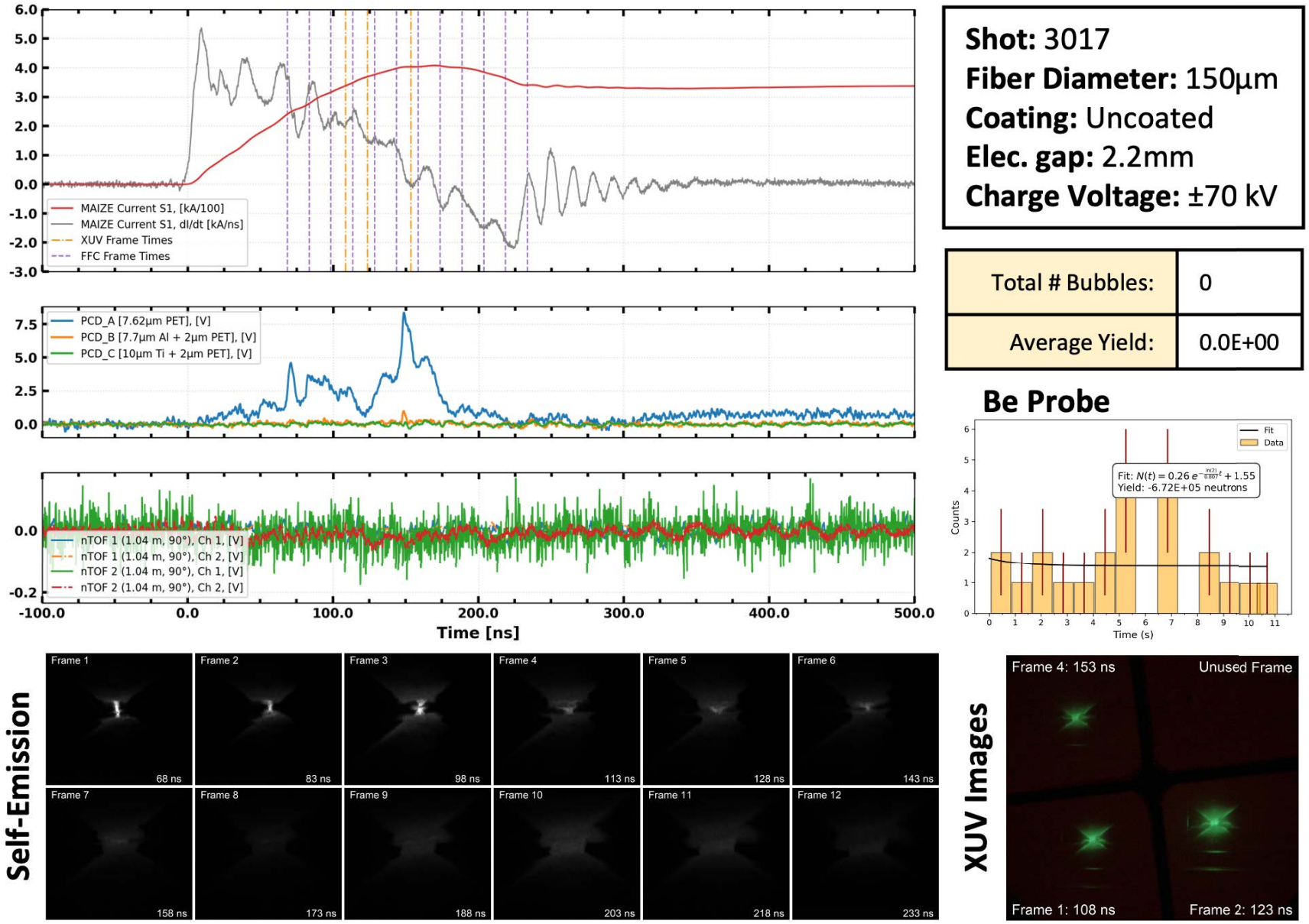

Figure D.19: Parameters and diagnostic data recorded for Shot 3017.

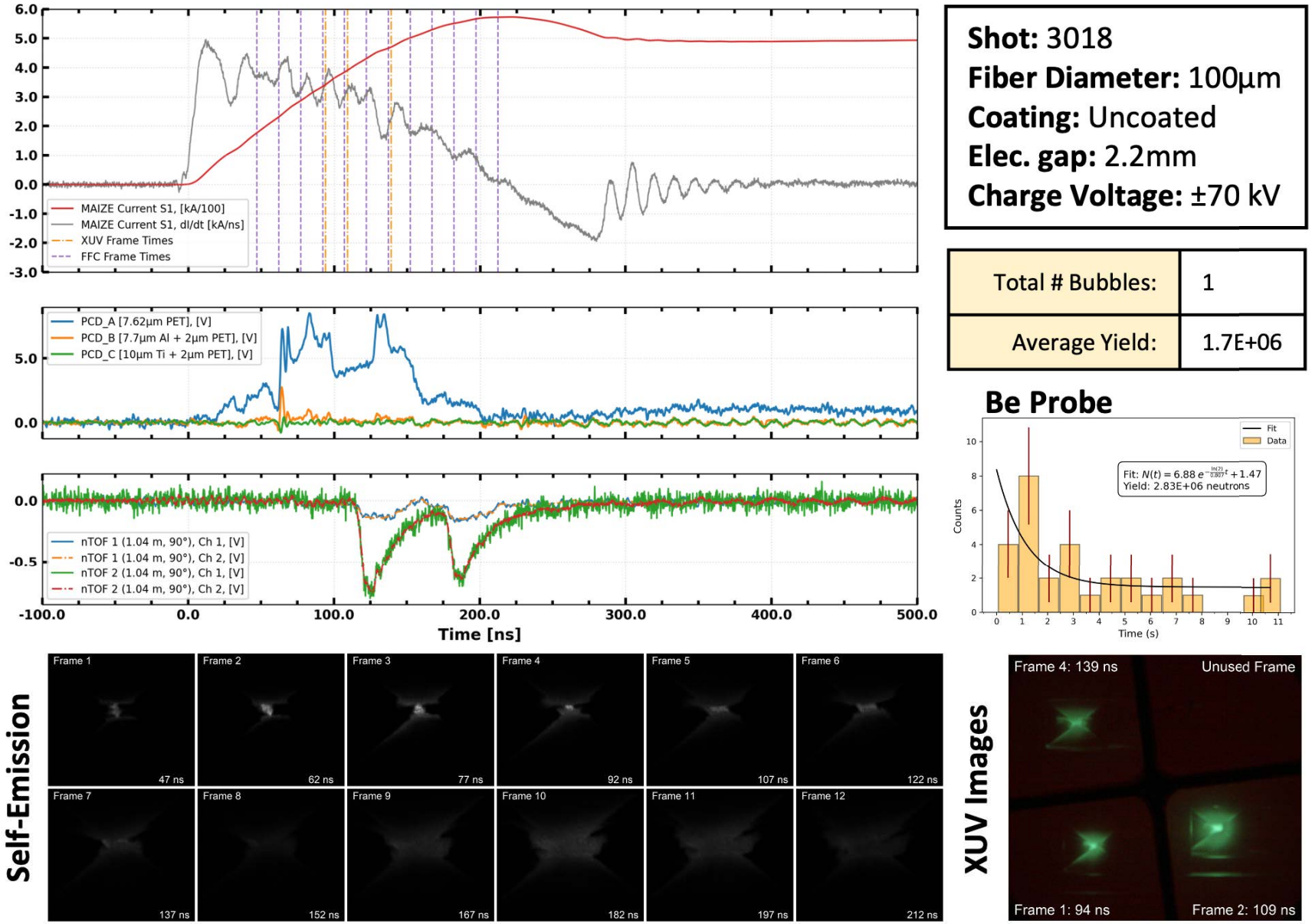

Figure D.20: Parameters and diagnostic data recorded for Shot 3018.

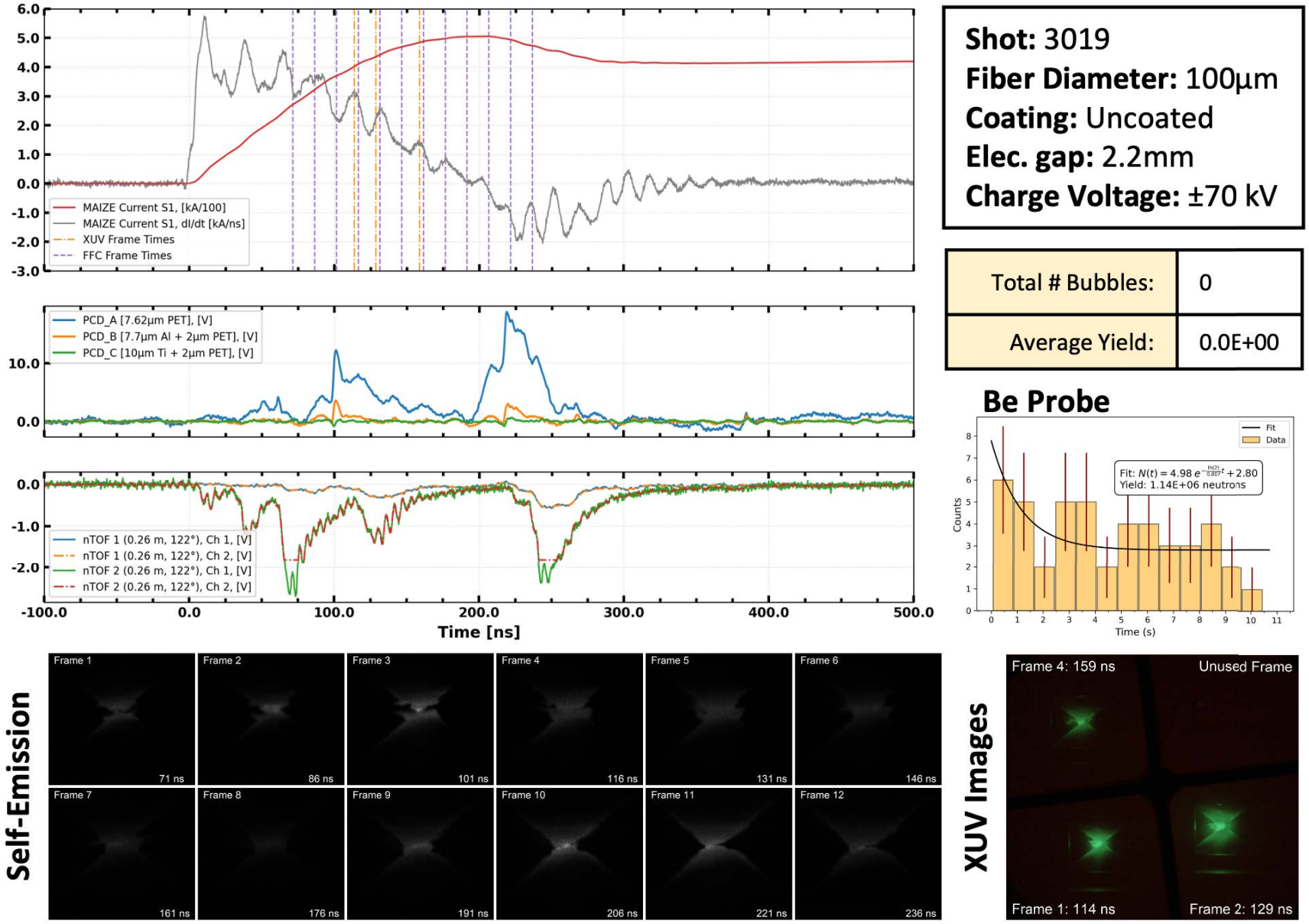

Figure D.21: Parameters and diagnostic data recorded for Shot 3019.

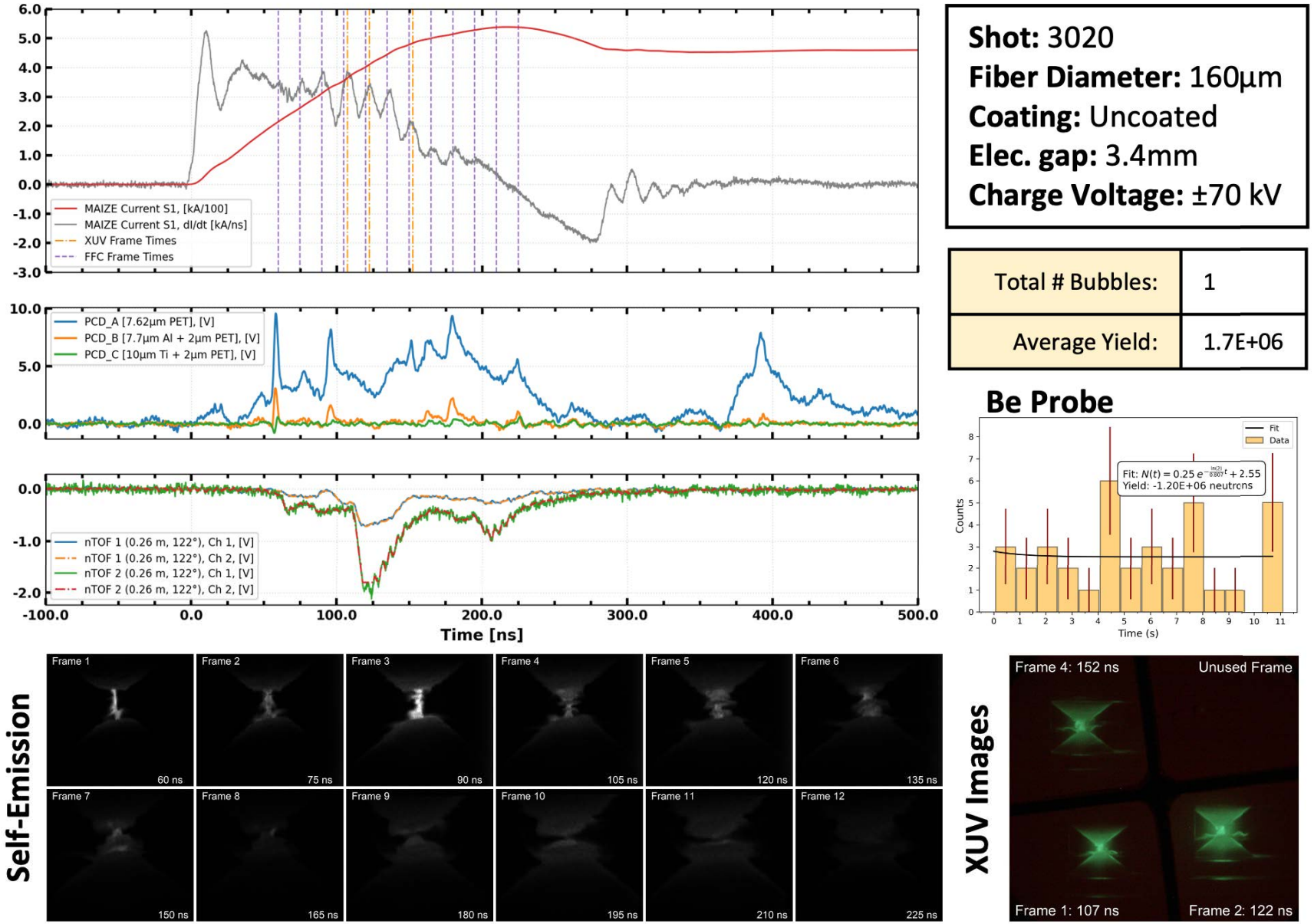

Figure D.22: Parameters and diagnostic data recorded for Shot 3020.

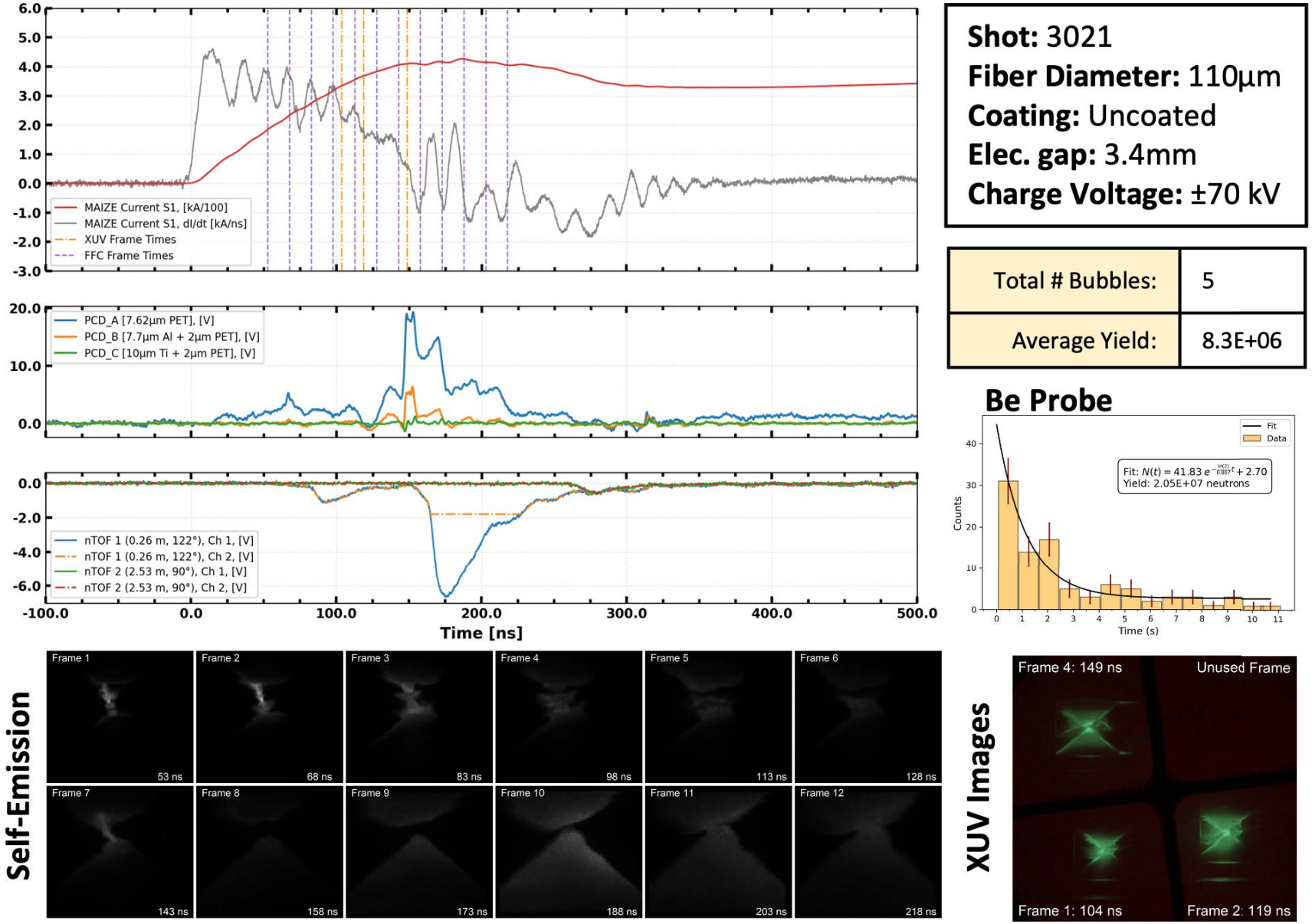

Figure D.23: Parameters and diagnostic data recorded for Shot 3021.

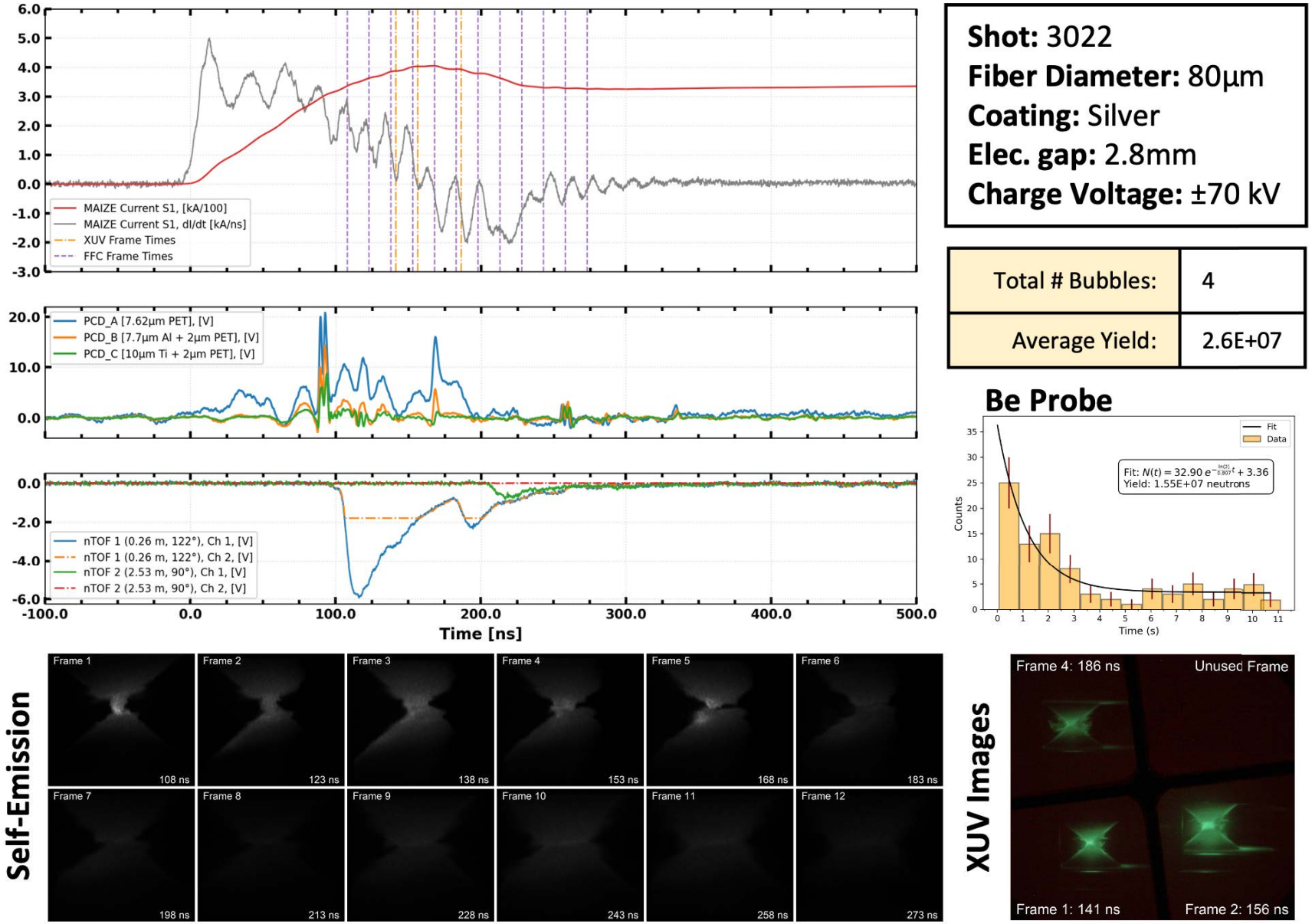

Figure D.24: Parameters and diagnostic data recorded for Shot 3022.

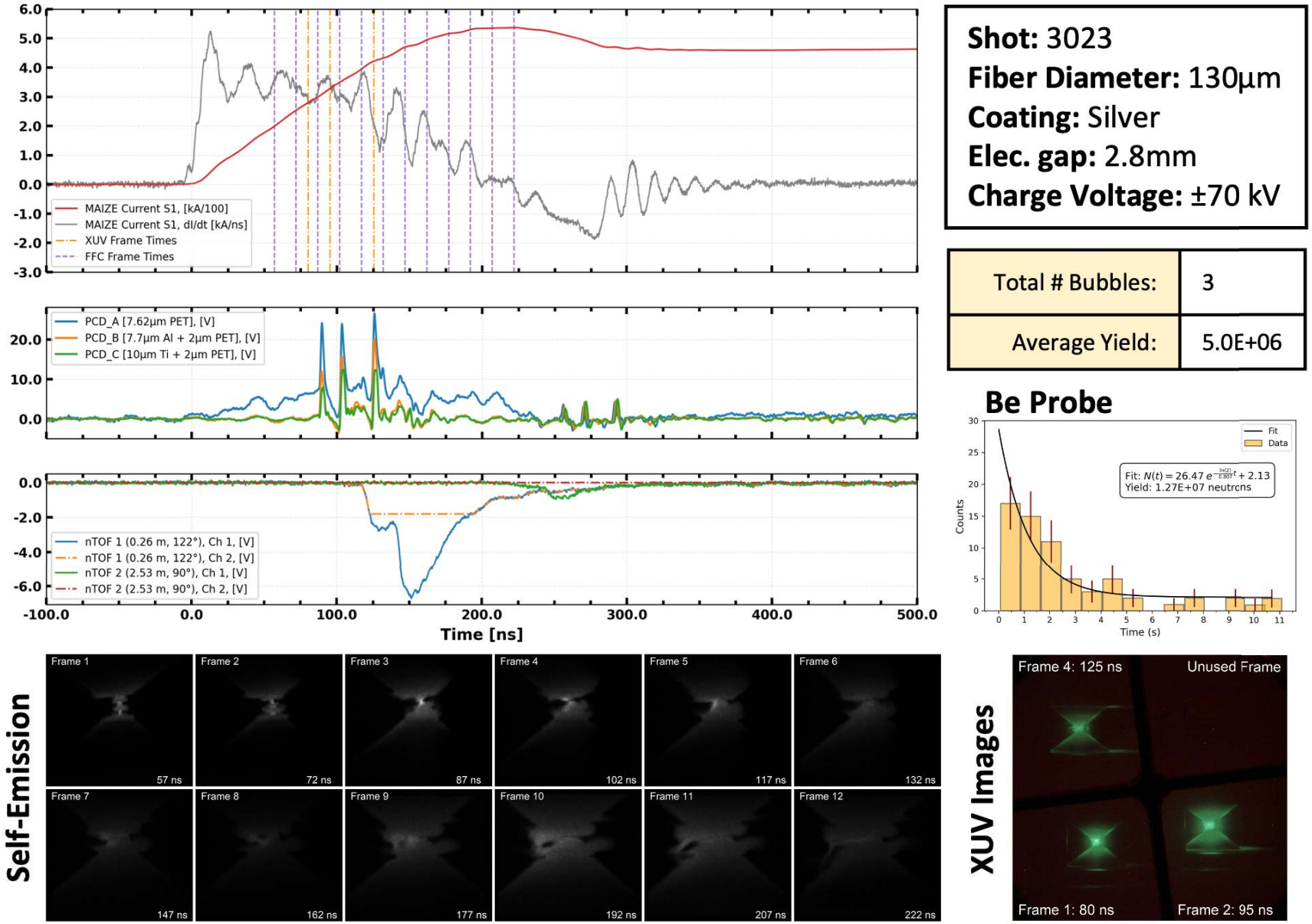

Figure D.25: Parameters and diagnostic data recorded for Shot 3023.

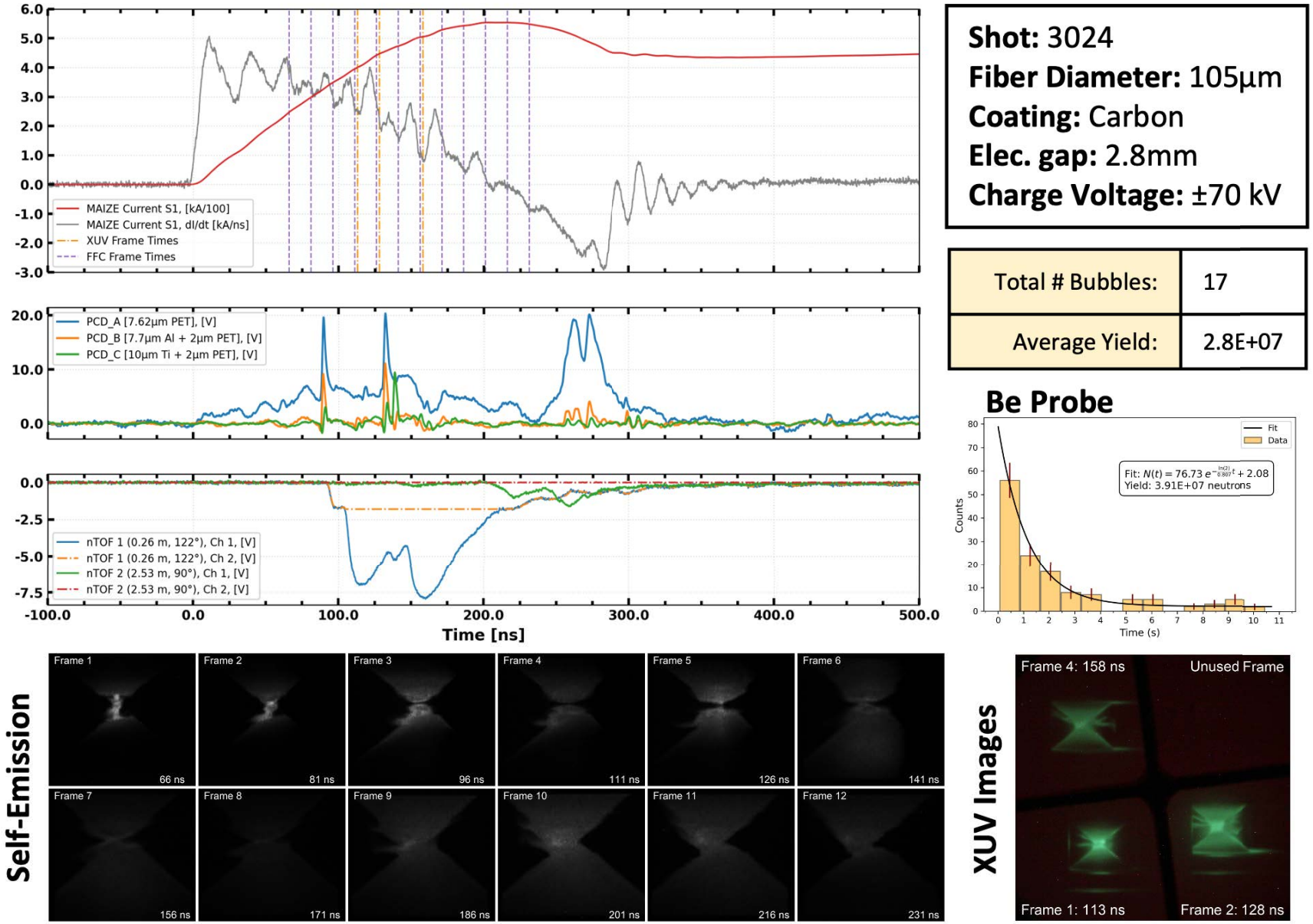

Figure D.26: Parameters and diagnostic data recorded for Shot 3024.

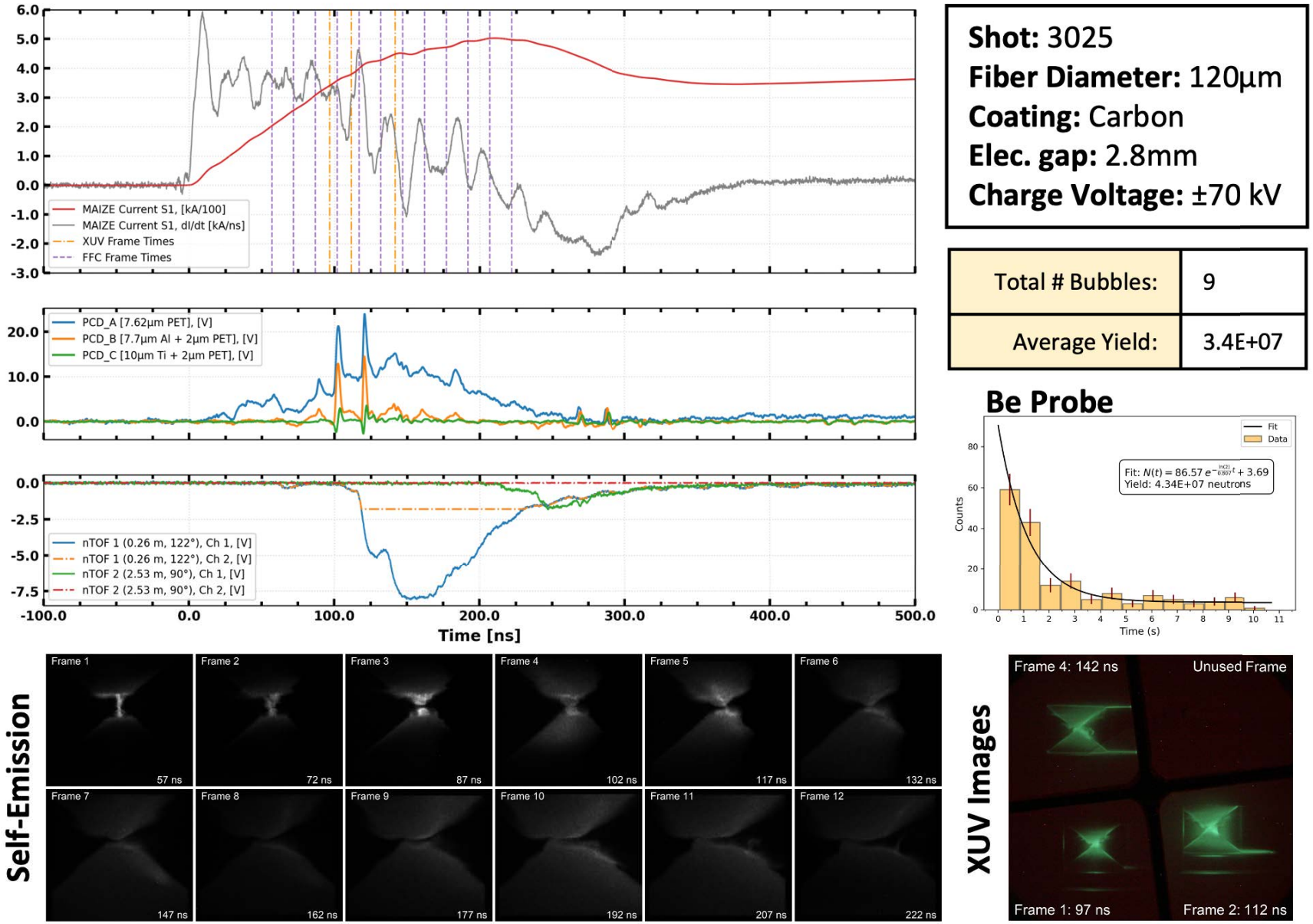

Figure D.27: Parameters and diagnostic data recorded for Shot 3025.

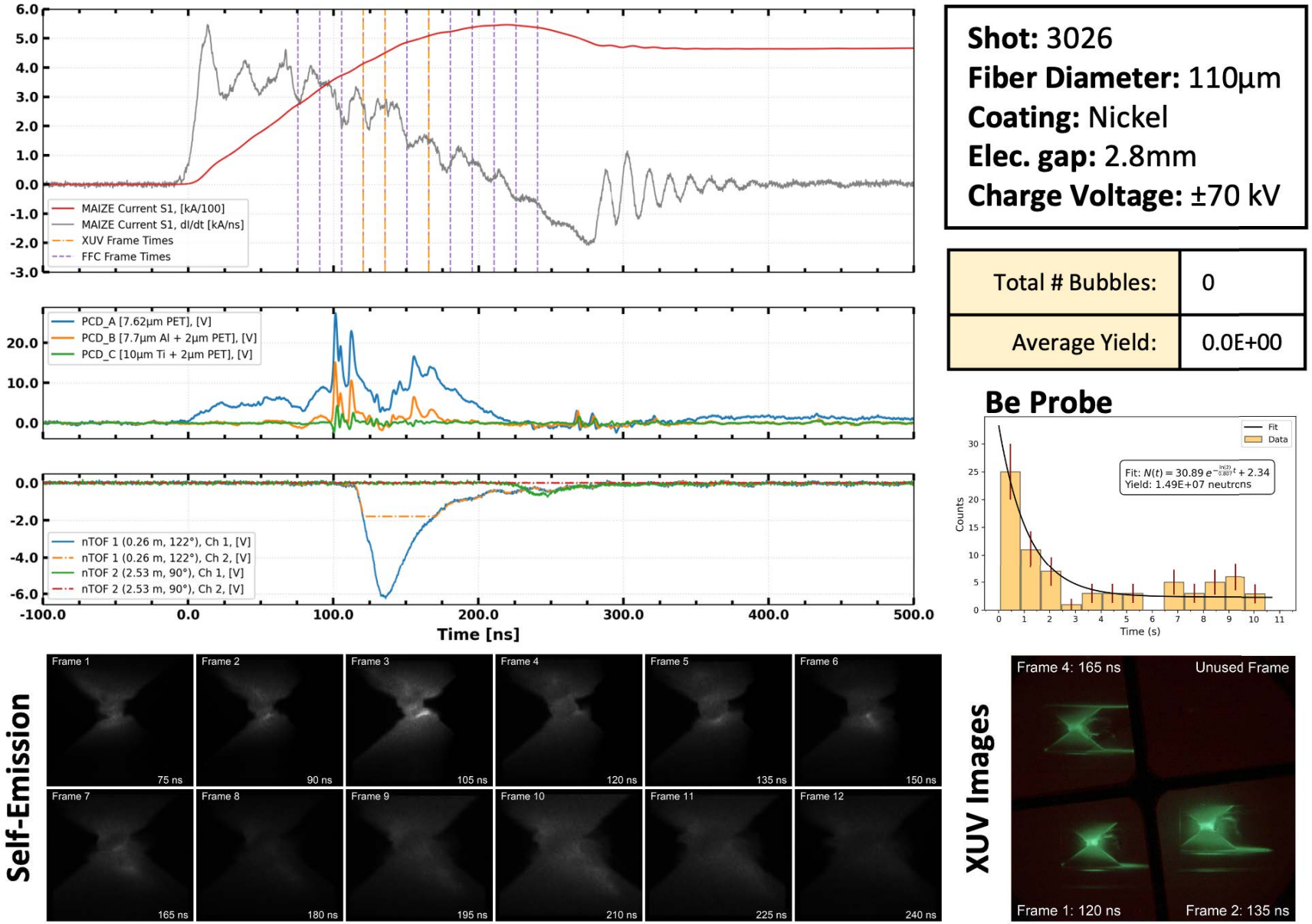

Figure D.28: Parameters and diagnostic data recorded for Shot 3026.

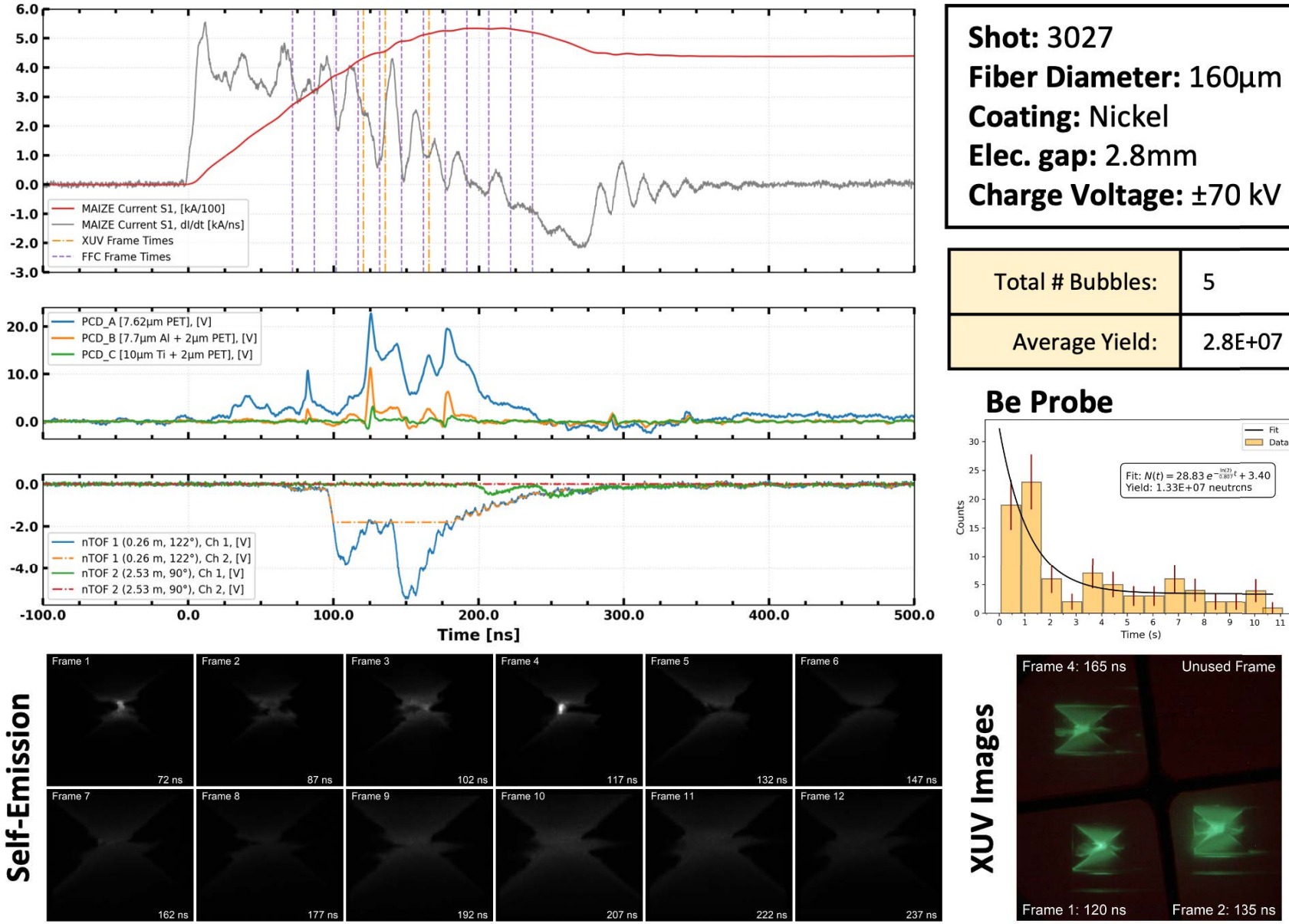

Figure D.29: Parameters and diagnostic data recorded for Shot 3027.

BIBLIOGRAPHY

[1] S. A. Slutz, M. C. Herrmann, R. A. Vesey, A. B. Sefkow, D. B. Sinars, D. C. Rovang, K. J. Peterson, and M. E. Cuneo, "Pulsed-power-driven cylindrical liner implosions of laser preheated fuel magnetized with an axial field," *Physics of Plasmas*, vol. 17, p. 056303, May 2010.

[2] S. A. Slutz and R. A. Vesey, "High-Gain Magnetized Inertial Fusion," *Phys. Rev. Lett.*, vol. 108, p. 025003, Jan. 2012.

[3] M. E. Cuneo, M. C. Herrmann, D. B. Sinars, S. A. Slutz, W. A. Stygar, R. A. Vesey, A. B. Sefkow, G. A. Rochau, G. A. Chandler, J. E. Bailey, J. L. Porter, R. D. McBride, D. C. Rovang, M. G. Mazarakis, E. P. Yu, D. C. Lamppa, K. J. Peterson, C. Nakhleh, S. B. Hansen, A. J. Lopez, M. E. Savage, C. A. Jennings, M. R. Martin, R. W. Lemke, B. W. Atherton, I. C. Smith, P. K. Rambo, M. Jones, M. R. Lopez, P. J. Christenson, M. A. Sweeney, B. Jones, L. A. McPherson, E. Harding, M. R. Gomez, P. F. Knapp, T. J. Awe, R. J. Leeper, C. L. Ruiz, G. W. Cooper, K. D. Hahn, J. McKenney, A. C. Owen, G. R. McKee, G. T. Leifeste, D. J. Ampleford, E. M. Waisman, A. Harvey-Thompson, R. J. Kaye, M. H. Hess, S. E. Rosenthal, and M. K. Matzen, "Magnetically Driven Implosions for Inertial Confinement Fusion at Sandia National Laboratories," *IEEE Trans. Plasma Sci.*, vol. 40, pp. 3222–3245, Dec. 2012.

[4] M. Gomez, S. Slutz, A. Sefkow, D. Sinars, K. Hahn, S. Hansen, E. Harding, P. Knapp, P. Schmit, C. Jennings, T. Awe, M. Geissel, D. Rovang, G. Chandler, G. Cooper, M. Cuneo, A. Harvey-Thompson, M. Herrmann, M. Hess, O. Johns, D. Lamppa, M. Martin, R. McBride, K. Peterson, J. Porter, G. Robertson, G. Rochau, C. Ruiz, M. Savage, I. Smith, W. Stygar, and R. Vesey, "Experimental Demonstration of Fusion-Relevant Conditions in Magnetized Liner Inertial Fusion," *Phys. Rev. Lett.*, vol. 113, p. 155003, Oct. 2014.

[5] G. A. Rochau, J. E. Bailey, Y. Maron, G. A. Chandler, G. S. Dunham, D. V. Fisher, V. I. Fisher, R. W. Lemke, J. J. MacFarlane, K. J. Peterson, D. G. Schroen, S. A. Slutz, and E. Stambulchik, "Radiating Shock Measurements in the Z -Pinch Dynamic Hohlraum," *Phys. Rev. Lett.*, vol. 100, p. 125004, Mar. 2008.

[6] D. B. Sinars, M. A. Sweeney, C. S. Alexander, D. J. Ampleford, T. Ao, J. P. Apruzese, C. Aragon, D. J. Armstrong, K. N. Austin, T. J. Awe, A. D. Baczewski, J. E. Bailey, K. L. Baker, C. R. Ball, H. T. Barclay, S. Beatty, K. Beckwith, K. S. Bell, J. F. Benage, N. L. Bennett, K. Blaha, D. E. Bliss, J. J. Boerner, C. J. Bourdon, B. A. Branch, J. L. Brown, E. M. Campbell, R. B. Campbell, D. G. Chacon, G. A. Chandler, K. Chandler, P. J. Christenson, M. D. Christison, E. B. Christner, R. C. Clay, K. R. Cochrane, A. P. Colombo, B. M. Cook,

C. A. Coverdale, M. E. Cuneo, J. S. Custer, A. Dasgupta, J.-P. Davis, M. P. Desjarlais, D. H. Dolan, J. D. Douglass, G. S. Dunham, S. Duwal, A. D. Edens, M. J. Edwards, E. G. Evstatiev, B. G. Farfan, J. R. Fein, E. S. Field, J. A. Fisher, T. M. Flanagan, D. G. Flicker, M. D. Furnish, B. R. Galloway, P. D. Gard, T. A. Gardiner, M. Geissel, J. L. Giuliani, M. E. Glinsky, M. R. Gomez, T. Gomez, G. P. Grim, K. D. Hahn, T. A. Haill, N. D. Hamlin, J. H. Hammer, S. B. Hansen, H. L. Hanshaw, E. C. Harding, A. J. Harvey-Thompson, D. Headley, M. C. Herrmann, M. H. Hess, C. Highstrete, O. A. Hurricane, B. T. Hutsel, C. A. Jennings, O. M. Johns, D. Johnson, M. D. Johnston, B. M. Jones, M. C. Jones, P. A. Jones, P. E. Kalita, R. J. Kamm, J. W. Kellogg, M. L. Kiefer, M. W. Kimmel, P. F. Knapp, M. D. Knudson, A. Kreft, G. R. Laity, P. W. Lake, D. C. Lamppa, W. L. Langston, J. S. Lash, K. R. LeChien, J. J. Leckbee, R. J. Leeper, G. T. Leifeste, R. W. Lemke, W. Lewis, S. A. Lewis, G. P. Loisel, Q. M. Looker, A. J. Lopez, D. J. Lucero, S. A. MacLaren, R. J. Magyar, M. A. Mangan, M. R. Martin, T. R. Mattsson, M. K. Matzen, A. J. Maurer, M. G. Mazarakis, R. D. McBride, H. S. McLean, C. A. McCoy, G. R. McKee, J. L. McKenney, A. R. Miles, J. A. Mills, M. D. Mitchell, N. W. Moore, C. E. Myers, T. Nagayama, G. Natoni, A. C. Owen, S. Patel, K. J. Peterson, T. D. Pointon, J. L. Porter, A. J. Porwitzky, S. Radovich, K. S. Raman, P. K. Rambo, W. D. Reinhart, G. K. Robertson, G. A. Rochau, S. Root, D. V. Rose, D. C. Rovang, C. L. Ruiz, D. E. Ruiz, D. Sandoval, M. E. Savage, M. E. Sceiford, M. A. Schaeuble, P. F. Schmit, M. S. Schollmeier, J. Schwarz, C. T. Seagle, A. B. Sefkow, D. B. Seidel, G. A. Shipley, J. Shores, L. Shulenburger, S. C. Simpson, S. A. Slutz, I. C. Smith, C. S. Speas, P. E. Specht, M. J. Speir, D. C. Spencer, P. T. Springer, A. M. Steiner, B. S. Stoltzfus, W. A. Stygar, J. Ward Thornhill, J. A. Torres, J. P. Townsend, C. Tyler, R. A. Vesey, P. E. Wakeland, T. J. Webb, E. A. Weinbrecht, M. R. Weis, D. R. Welch, J. L. Wise, M. Wu, D. A. Yager-Elorriaga, A. Yu, and E. P. Yu, "Review of pulsed power-driven high energy density physics research on Z at Sandia," *Physics of Plasmas*, vol. 27, p. 070501, July 2020.

[7] R. D. McBride, W. A. Stygar, M. E. Cuneo, D. B. Sinars, M. G. Mazarakis, J. J. Leckbee, M. E. Savage, B. T. Hutsel, J. D. Douglass, M. L. Kiefer, and et al., "A primer on pulsed power and linear transformer drivers for high energy density physics applications," *IEEE Transactions on Plasma Science*, vol. 46, p. 3928–3967, Nov 2018.

[8] N. R. Pereira and J. Davis, "X rays from z -pinches on relativistic electron-beam generators," *Journal of Applied Physics*, vol. 64, pp. R1–R27, Aug. 1988.

[9] D. D. Ryutov, M. S. Derzon, and M. K. Matzen, "The physics of fast Z pinches," *Rev. Mod. Phys.*, vol. 72, no. 1, p. 57, 2000.

[10] J. L. Giuliani and R. J. Commisso, "A Review of the Gas-Puff Z -Pinch as an X-Ray and Neutron Source," *IEEE Trans. Plasma Sci.*, vol. 43, pp. 2385–2453, Aug. 2015.

[11] S. N. Bland, S. V. Lebedev, J. P. Chittenden, G. N. Hall, F. Suzuki-Vidal, D. J. Ampleford, S. C. Bott, J. B. A. Palmer, S. A. Pikuz, and T. A. Shelkovenko, "Implosion and stagnation of wire array Z pinches," *Physics of Plasmas*, vol. 14, no. 5, p. 056315, 2007.

[12] R. D. McBride, T. A. Shelkovenko, S. A. Pikuz, D. A. Hammer, J. B. Greenly, B. R. Kusse, J. D. Douglass, P. F. Knapp, K. S. Bell, I. C. Blesener, and D. A. Chalenski, "Implosion

dynamics and radiation characteristics of wire-array Z pinches on the Cornell Beam Research Accelerator," *Physics of Plasmas*, vol. 16, p. 012706, Jan. 2009.

[13] M. Krishnan, "The Dense Plasma Focus: A Versatile Dense Pinch for Diverse Applications," *IEEE Transactions on Plasma Science*, vol. 40, no. 12, pp. 3189–3221, 2012.

[14] R. D. McBride, M. R. Martin, R. W. Lemke, J. B. Greenly, C. A. Jennings, D. C. Rovang, D. B. Sinars, M. E. Cuneo, M. C. Herrmann, S. A. Slutz, C. W. Nakhleh, D. D. Ryutov, J.-P. Davis, D. G. Flicker, B. E. Blue, K. Tomlinson, D. Schroen, R. M. Stamm, G. E. Smith, J. K. Moore, T. J. Rogers, G. K. Robertson, R. J. Kamm, I. C. Smith, M. Savage, W. A. Stygar, G. A. Rochau, M. Jones, M. R. Lopez, J. L. Porter, and M. K. Matzen, "Beryllium liner implosion experiments on the Z accelerator in preparation for magnetized liner inertial fusion," *Physics of Plasmas*, vol. 20, p. 056309, May 2013.

[15] R. D. McBride, S. A. Slutz, C. A. Jennings, D. B. Sinars, M. E. Cuneo, M. C. Herrmann, R. W. Lemke, M. R. Martin, R. A. Vesey, K. J. Peterson, A. B. Sefkow, C. Nakhleh, B. E. Blue, K. Killebrew, D. Schroen, T. J. Rogers, A. Laspe, M. R. Lopez, I. C. Smith, B. W. Atherton, M. Savage, W. A. Stygar, and J. L. Porter, "Penetrating Radiography of Imploding and Stagnating Beryllium Liners on the Z Accelerator," *Phys. Rev. Lett.*, vol. 109, p. 135004, Sept. 2012.

[16] D. B. Sinars, S. A. Slutz, M. C. Herrmann, R. D. McBride, M. E. Cuneo, K. J. Peterson, R. A. Vesey, C. Nakhleh, B. E. Blue, K. Killebrew, D. Schroen, K. Tomlinson, A. D. Edens, M. R. Lopez, I. C. Smith, J. Shores, V. Bigman, G. R. Bennett, B. W. Atherton, M. Savage, W. A. Stygar, G. T. Leifeste, and J. L. Porter, "Measurements of Magneto-Rayleigh-Taylor Instability Growth during the Implosion of Initially Solid Al Tubes Driven by the 20-MA, 100-ns Z Facility," *Phys. Rev. Lett.*, vol. 105, p. 185001, Oct. 2010.

[17] D. B. Sinars, S. A. Slutz, M. C. Herrmann, R. D. McBride, M. E. Cuneo, C. A. Jennings, J. P. Chittenden, A. L. Velikovich, K. J. Peterson, R. A. Vesey, C. Nakhleh, E. M. Waisman, B. E. Blue, K. Killebrew, D. Schroen, K. Tomlinson, A. D. Edens, M. R. Lopez, I. C. Smith, J. Shores, V. Bigman, G. R. Bennett, B. W. Atherton, M. Savage, W. A. Stygar, G. T. Leifeste, and J. L. Porter, "Measurements of magneto-Rayleigh–Taylor instability growth during the implosion of initially solid metal liners," *Physics of Plasmas*, vol. 18, p. 056301, May 2011.

[18] A. M. Steiner, P. C. Campbell, D. A. Yager-Elorriaga, K. R. Cochrane, T. R. Mattsson, N. M. Jordan, R. D. McBride, Y. Y. Lau, and R. M. Gilgenbach, "The electro-thermal stability of tantalum relative to aluminum and titanium in cylindrical liner ablation experiments at 550 kA," *Physics of Plasmas*, vol. 25, p. 032701, Mar. 2018.

[19] D. A. Yager-Elorriaga, Y. Y. Lau, P. Zhang, P. C. Campbell, A. M. Steiner, N. M. Jordan, R. D. McBride, and R. M. Gilgenbach, "Evolution of sausage and helical modes in magnetized thin-foil cylindrical liners driven by a Z-pinch," *Physics of Plasmas*, vol. 25, p. 056307, May 2018.

[20] S. B. Hansen, M. R. Gomez, A. B. Sefkow, S. A. Slutz, D. B. Sinars, K. D. Hahn, E. C. Harding, P. F. Knapp, P. F. Schmit, T. J. Awe, R. D. McBride, C. A. Jennings, M. Geissel,

A. J. Harvey-Thompson, K. J. Peterson, D. C. Rovang, G. A. Chandler, G. W. Cooper, M. E. Cuneo, M. C. Herrmann, M. H. Hess, O. Johns, D. C. Lamppa, M. R. Martin, J. L. Porter, G. K. Robertson, G. A. Rochau, C. L. Ruiz, M. E. Savage, I. C. Smith, W. A. Stygar, R. A. Vesey, B. E. Blue, D. Ryutov, D. G. Schroen, and K. Tomlinson, "Diagnosing magnetized liner inertial fusion experiments on Za)," *Phys. Plasmas*, vol. 22, p. 056313, May 2015.

[21] M. R. Gomez, S. A. Slutz, P. F. Knapp, K. D. Hahn, M. R. Weis, E. C. Harding, M. Geissel, J. R. Fein, M. E. Glinsky, S. B. Hansen, A. J. Harvey-Thompson, C. A. Jennings, I. C. Smith, D. Woodbury, D. J. Ampleford, T. J. Awe, G. A. Chandler, M. H. Hess, D. C. Lamppa, C. E. Myers, C. L. Ruiz, A. B. Sefkow, J. Schwarz, D. A. Yager-Elorriaga, B. Jones, J. L. Porter, K. J. Peterson, R. D. Mcbride, G. A. Rochau, and D. B. Sinars, "Assessing Stagnation Conditions and Identifying Trends in Magnetized Liner Inertial Fusion," *IEEE Trans. Plasma Sci.*, vol. 47, pp. 2081–2101, May 2019.

[22] S. A. Pikuz, T. A. Shelkovenko, and D. A. Hammer, "X-pinch. Part I," *Plasma Physics Reports*, vol. 41, pp. 291–342, Apr. 2015.

[23] S. A. Pikuz, T. A. Shelkovenko, and D. A. Hammer, "X-pinch. Part II," *Plasma Physics Reports*, vol. 41, pp. 445–491, June 2015.

[24] T. A. Shelkovenko, S. A. Pikuz, R. D. McBride, P. F. Knapp, H. Wilhelm, D. A. Hammer, and D. B. Sinars, "Nested multilayered X pinches for generators with mega-ampere current level," *Physics of Plasmas*, vol. 16, p. 050702, May 2009.

[25] D. B. Sinars, R. D. McBride, S. A. Pikuz, T. A. Shelkovenko, D. F. Wenger, M. E. Cuneo, E. P. Yu, J. P. Chittenden, E. C. Harding, S. B. Hansen, B. P. Peyton, D. J. Ampleford, and C. A. Jennings, "Investigation of High-Temperature Bright Plasma X-ray Sources Produced in 5-MA X-Pinch Experiments," *Phys. Rev. Lett.*, vol. 109, p. 155002, Oct. 2012.

[26] T. A. Shelkovenko, S. A. Pikuz, A. D. Cahill, P. F. Knapp, D. A. Hammer, D. B. Sinars, I. N. Tilikin, and S. N. Mishin, "Hybrid X-pinch with conical electrodes," *Physics of Plasmas*, vol. 17, p. 112707, Nov. 2010.

[27] T. A. Shelkovenko, S. A. Pikuz, C. L. Hoyt, A. D. Cahill, and D. A. Hammer, "Study of New Configurations of Hybrid X Pinches," *IEEE Trans. Plasma Sci.*, vol. 42, pp. 748–752, Mar. 2014.

[28] G. Sarkisov, S. Pikuz, T. Shelkovenko, and V. Romanova, "Laser probing experiments with X-pinches," in *IEEE Conference Record - Abstracts. 1997 IEEE International Conference on Plasma Science*, (San Diego, CA, USA), pp. 177–178, IEEE, 1997.

[29] M. Mitchell, *X-pinch plasma dynamics studied with high temporal resolution diagnostics*. Ph.D. thesis, Cornell University, 2007.

[30] S. Bott, D. Haas, Y. Eshaq, U. Ueda, S. Lebedev, J. Chittenden, J. Palmer, S. Bland, G. Hall, D. Ampleford, and F. Beg, "Quantitative Measurements of Wire Ablation in Tungsten X-pinches at 80 kA," *IEEE Trans. Plasma Sci.*, vol. 36, pp. 2759–2764, Oct. 2008.

[31] R. M. Gilgenbach, M. R. Gomez, J. C. Zier, W. W. Tang, D. M. French, Y. Y. Lau, M. G. Mazarakis, M. E. Cuneo, M. D. Johnston, B. V. Oliver, T. A. Mehlhorn, A. A. Kim, V. A. Sinebryukhov, B. R. Kusse, and D. A. Hammer, "MAIZE: a 1 MA LTD-Driven Z-Pinch at The University of Michigan," in *AIP Conference Proceedings*, (Alexandria, Virginia (USA)), pp. 259–262, AIP, 2009.

[32] J. L. Giuliani, F. N. Beg, R. M. Gilgenbach, V. L. Kantsyrev, B. R. Kusse, V. V. Ivanov, and R. Presura, "Plasma Pinch Research on University Pulsed-Power Generators in the United States," *IEEE Trans. Plasma Sci.*, vol. 40, pp. 3246–3264, Dec. 2012.

[33] S. C. Bott, D. M. Haas, R. E. Madden, U. Ueda, Y. Eshaq, G. Collins, K. Gunasekera, D. Mariscal, J. Peebles, F. N. Beg, M. Mazarakis, K. Struve, and R. Sharpe, "250 kA compact linear transformer driver for wire array z -pinch loads," *Phys. Rev. ST Accel. Beams*, vol. 14, p. 050401, May 2011.

[34] S. N. Bland, Y. E. Krasik, D. Yanuka, R. Gardner, J. MacDonald, A. Virozub, S. Efimov, S. Gleizer, and N. Chaturvedi, "Generation of highly symmetric, cylindrically convergent shockwaves in water," *Physics of Plasmas*, vol. 24, p. 082702, Aug. 2017.

[35] B. Sporer, A. Shah, G. Dowhan, R. Shapovalov, D. Packard, M. Wisher, J. Leckbee, K. Hendricks, B. Hoff, Y. Lau, R. Gilgenbach, N. Jordan, and R. McBride, "Multicavity linear transformer driver facility for Z -pinch and high-power microwave research," *Phys. Rev. Accel. Beams*, vol. 24, p. 100402, Oct. 2021.

[36] G. F. Swadling, S. V. Lebedev, G. N. Hall, S. Patankar, N. H. Stewart, R. A. Smith, A. J. Harvey-Thompson, G. C. Burdiak, P. de Grouchy, J. Skidmore, L. Suttle, F. Suzuki-Vidal, S. N. Bland, K. H. Kwek, L. Pickworth, M. Bennett, J. D. Hare, W. Rozmus, and J. Yuan, "Diagnosing collisions of magnetized, high energy density plasma flows using a combination of collective Thomson scattering, Faraday rotation, and interferometry (invited)," *Review of Scientific Instruments*, vol. 85, p. 11E502, Nov. 2014.

[37] P. M. Bellan, "Fundamentals of Plasma Physics," p. 298–325, 2008.

[38] K. N. Koshelev and N. R. Pereira, "Plasma points and radiative collapse in vacuum sparks," *Journal of Applied Physics*, vol. 69, pp. R21–R44, May 1991.

[39] J. W. Strutt, *The form of Standing Waves on the Surface of Running Water*, p. 69–78. 1883.

[40] M. R. Weis, *Magneto-Rayleigh-Taylor Instability: theory and simulation in planar and cylindrical pulsed power targets*. Ph.D. thesis, University of Michigan, 2015.

[41] M. Kruskal and M. Schwarzschild, "Some Instabilities of a Completely Ionized Plasma," *Proc. R. Soc. Lond. A*, vol. 223, no. 1154, pp. 348–360, 1954.

[42] J. W. Shearer, "Contraction of *Z* pinches actuated by radiation losses," *The Physics of Fluids*, vol. 19, pp. 1426–1428, Sept. 1976.

[43] J. P. Chittenden and M. G. Haines, "Processes terminating radiative collapse in a hydrogen fiber Z pinch," *Physics of Fluids B: Plasma Physics*, vol. 2, pp. 1889–1897, Aug. 1990.

[44] J. P. Chittenden, A. Ciardi, C. A. Jennings, S. V. Lebedev, D. A. Hammer, S. A. Pikuz, and T. A. Shelkovenko, "Structural Evolution and Formation of High-Pressure Plasmas in X Pinches," *Phys. Rev. Lett.*, vol. 98, p. 025003, Jan. 2007.

[45] J. P. Chittenden, S. V. Lebedev, C. A. Jennings, S. N. Bland, and A. Ciardi, "X-ray generation mechanisms in three-dimensional simulations of wire array Z-pinches," *Plasma Phys. Control. Fusion*, vol. 46, pp. B457–B476, Dec. 2004.

[46] N. Chaturvedi, J. Chittenden, and N. Niasse, "Modelling high energy density systems with strong radiative loss using static mesh refinement," in *APS Division of Plasma Physics Meeting Abstracts*, vol. 2021 of *APS Meeting Abstracts*, p. NP11.090, Jan. 2021.

[47] N. Chaturvedi, J. Chittenden, and A. Crilly, "Simulating radiative collapse in single fibre z-pinches," vol. 2023 of *DZP 2023*, 2023.

[48] A. T. Elshafiey, J. H. Musk, S. A. Pikuz, T. A. Shelkovenko, and D. A. Hammer, "Studies and optimization of hybrid X-pinches," *Plasma Res. Express*, vol. 3, p. 015004, Mar. 2021.

[49] A. Elshafiey, *Investigation of X-Pinch Plasma Dynamics Using a PS Time-Resolved X-Ray Streak Camera*. Ph.D. thesis, Cornell University, 2023.

[50] N. D. Hamlin and C. E. Seyler, "Relativistic Modeling Capabilities in PERSEUS Extended-MHD Simulation Code for HED Plasmas," *IEEE Trans. Plasma Sci.*, vol. 44, pp. 1112–1126, July 2016.

[51] S. Patel, D. Chalenski, R. Gilgenbach, A. Steiner, D. Yager-Elorriaga, and Y. Lau, "X-Pinch Experiments on UM Linear Transformer Drivers," in *APS Division of Plasma Physics Meeting Abstracts*, vol. 54 of *APS Meeting Abstracts*, p. TP8.134, Oct. 2012.

[52] S. Patel, D. Chalenski, R. Gilgenbach, A. Steiner, D. Yager-Elorriaga, and Y. Lau, "X-pinch experiments on the um 1-ma linear transformer driver," in *2012 Abstracts IEEE International Conference on Plasma Science*, pp. 2P–84–2P–84, 2012.

[53] S. G. Patel, D. A. Yager-Elorriaga, A. M. Steiner, R. M. Gilgenbach, N. M. Jordan, D. A. Chalenski, and Y. Y. Lau, "Hybrid X-pinch Experiments on a MA Linear Transformer Driver," in *APS Division of Plasma Physics Meeting Abstracts*, vol. 2013 of *APS Meeting Abstracts*, p. BP8.123, Oct. 2013.

[54] P. C. Campbell, J. M. Woolstrum, F. Antoulinakis, T. M. Jones, D. A. Yager-Elorriaga, S. M. Miller, N. M. Jordan, Y. Y. Lau, R. M. Gilgenbach, and R. D. Mcbride, "Diagnostic and Power Feed Upgrades to the MAIZE Facility," *IEEE Trans. Plasma Sci.*, vol. 46, pp. 3973–3981, Nov. 2018.

[55] D. Haas, S. C. Bott, V. Vikhrev, Y. Eshaq, U. Ueda, T. Zhang, E. Baranova, S. I. Krasheninnikov, and F. N. Beg, "Dynamics of low density coronal plasma in low current x-pinches," *Plasma Phys. Control. Fusion*, vol. 49, pp. 1151–1162, Aug. 2007.

[56] H. L. L. van Paassen, "A Time-Resolved Ross Filter System for Measuring X-Ray Spectra in Z-Pinch Plasma Focus Devices," *Review of Scientific Instruments*, vol. 42, no. 12, pp. 1823–1824, 1971.

[57] J. B. Greenly, J. D. Douglas, D. A. Hammer, B. R. Kusse, S. C. Glidden, and H. D. Sanders, "A 1MA, variable risetime pulse generator for high energy density plasma research," *Review of Scientific Instruments*, vol. 79, p. 073501, July 2008.

[58] D. B. Sinars, S. N. Bland, R. D. McBride, D. F. Wenger, J. P. Chittenden, S. A. Pikuz, E. Harding, C. A. Jennings, D. J. Ampleford, E. P. Yu, M. E. Cuneo, T. A. Shelkovenko, and S. B. Hansen, "Scaling of X pinches from 1 MA to 6 MA.," Tech. Rep. SAND2010-7318, 1011205, Sept. 2010. Issue: SAND2010-7318, 1011205.

[59] S. Dan'ko, S. Anan'ev, Y. Bakshaev, A. Bartov, P. Blinov, A. Chernenko, Y. Kalinin, E. Kazakov, A. Kingsep, V. Korolev, V. Mizhiritsky, V. Smirnov, A. Zelenin, T. Shelkovenko, S. Tkachenko, and S. Pikuz, "Plasma dynamics in different kinds of experiments at megaampere range on s-300 machine," in *2008 17th International Conference on High Power Particle Beams (BEAMS)*, pp. 1–4, 2008.

[60] Jian Wu, Ai'ci Qiu, Gang Wu, Min Lv, Liangping Wang, Tianshi Lei, Ning Guo, Juanjuan Han, Xinjun Zhang, Hailiang Yang, Peitian Cong, and Mengtong Qiu, "X-Pinch Experiments on 1-MA "QiangGuang-1" Facility," *IEEE Trans. Plasma Sci.*, vol. 38, pp. 639–645, Apr. 2010.

[61] D. B. Sinars, "1 MA x-pinch experiments at cornell university," No. sand2007-1965c, United States. National Nuclear Security Administration; distributed by the Office of Scientific and Technical Information, U.S. Dept. of Energy, Mar. 2007.

[62] D. B. Sinars, R. D. McBride, E. P. Yu, S. B. Hansen, D. J. Ampleford, C. A. Jennings, M. E. Cuneo, D. F. Wenger, S. A. Pikuz, T. A. Shelkovenko, J. P. Chittenden, and S. N. Bland, "6 MA x-pinch scaling experiments.,"

[63] T. Pisarczyk, A. A. Rupasov, G. S. Sarkisov, and A. S. Shikanov, "Faraday-rotation method for magnetic-field diagnostics in a laser plasma," *Journal of Soviet Laser Research*, vol. 11, pp. 1–32, Jan. 1990.

[64] S. N. Bland, D. J. Ampleford, S. C. Bott, A. Guite, G. N. Hall, S. M. Hardy, S. V. Lebedev, P. Shardlow, A. Harvey-Thompson, F. Suzuki, and K. H. Kwek, "Use of Faraday probing to estimate current distribution in wire array z pinches," *Review of Scientific Instruments*, vol. 77, p. 10E315, Oct. 2006.

[65] V. V. Ivanov, A. A. Anderson, D. Papp, B. R. Talbot, J. P. Chittenden, N. Niasse, and I. A. Begishev, "UV Laser-Probing Diagnostics for the Dense Z Pinch," *IEEE Trans. Plasma Sci.*, vol. 42, pp. 1153–1162, May 2014.

[66] V. V. Ivanov, A. A. Anderson, and D. Papp, "Investigation of wire-array Z-pinches by laser probing diagnostics," *Matter and Radiation at Extremes*, vol. 4, p. 017401, Jan. 2019.

[67] W. Syed, *Development of novel techniques to study the magnetic field evolution in wire-array Z-pinches and X-pinches*. Ph.D. thesis, Cornell University, 2010.

[68] W. Syed, R. B. van Dover, J. R. Petrie, M. D. Mitchell, and D. A. Hammer, "Technique to measure sub-microsecond magnetic field pulses using magnetic (CoPt) thin films," *Appl. Phys. Lett.*, vol. 87, p. 182505, Oct. 2005.

[69] W. Syed, "Magnetic Field Measurements in Wire-Array Z-Pinches and X Pinches," in *AIP Conference Proceedings*, vol. 808, (Oxford (United Kingdom)), pp. 315–318, AIP, 2006.

[70] V. Ivanov, G. Sarkisov, P. Laca, V. Sotnikov, V. Kantsyrev, B. Jones, C. Coverdale, P. Lepell, C. Deeney, K. Struve, A. Astanovitskiy, D. Fedin, B. Le Galloudec, V. Nalajala, I. Shrestha, and T. Cowan, "Investigation of Magnetic Fields in 1-MA Wire Arrays and X-Pinches," *IEEE Trans. Plasma Sci.*, vol. 34, pp. 2247–2255, Oct. 2006.

[71] A. Anderson, V. Ivanov, and D. Papp, "Visualization of the magnetic field and current path in Z-pinch and X-pinch plasmas," *High Energy Density Physics*, vol. 15, pp. 1–3, June 2015.

[72] M. Gomez, *Experimental Examination of Plasma Formation and Current Loss in Post-Hole Convolutes*. Ph.D. thesis, University of Michigan, 2010.

[73] I. H. Hutchinson, *Principles of plasma diagnostics*. Cambridge ; New York: Cambridge University Press, 2nd ed ed., 2002.

[74] T. A. Shelkovenko, D. B. Sinars, S. A. Pikuz, and D. A. Hammer, "Radiographic and spectroscopic studies of X-pinch plasma implosion dynamics and x-ray burst emission characteristics," *Physics of Plasmas*, vol. 8, no. 4, p. 1305, 2001.

[75] I. H. Mitchell, J. M. Bayley, J. P. Chittenden, J. F. Worley, A. E. Dangor, M. G. Haines, and P. Choi, "A high impedance mega-ampere generator for fiber z -pinch experiments," *Review of Scientific Instruments*, vol. 67, pp. 1533–1541, Apr. 1996.

[76] Z. Jiang, J. Wu, Z. Chen, Z. Wang, H. Shi, and X. Li, "Improved measurement method for the Faraday rotation distribution using beam splitting," *Opt. Express*, vol. 30, p. 8917, Mar. 2022.

[77] Z. Jiang, J. Wu, Z. Chen, W. Wang, Z. Wang, Y. Lu, H. Shi, X. Li, and A. Qiu, "Improvement of Faraday Rotation and Its Application in Preconditioned Single-Wire Z-Pinch Plasma," *IEEE Trans. Plasma Sci.*, vol. 51, pp. 944–952, Apr. 2023.

[78] S. Zakharov, G. Ivanenkov, A. Kolomenskij, S. Pikuz, A. Samokhin, and I. Ulshmid, "Wire X-pinch in a high-current diode," *Pis'ma v Zhurnal Tekhnicheskoj Fiziki*, vol. 8, pp. 1060–1063, Sept. 1982.

[79] G. F. Swadling, S. V. Lebedev, N. Niasse, J. P. Chittenden, G. N. Hall, F. Suzuki-Vidal, G. Burdiak, A. J. Harvey-Thompson, S. N. Bland, P. De Grouchy, E. Khoory, L. Pickworth, J. Skidmore, and L. Suttle, "Oblique shock structures formed during the ablation phase of aluminium wire array z-pinches," *Physics of Plasmas*, vol. 20, p. 022705, Feb. 2013.

[80] G. Swadling, *An experimental investigation of the azimuthal structures formed during the ablation phase of wire array z-pinches*. Ph.D. thesis, Imperial College London, 2011.

[81] J. D. Hare, J. MacDonald, S. N. Bland, J. Dranczewski, J. W. D. Halliday, S. V. Lebedev, L. G. Suttle, E. R. Tubman, and W. Rozmus, "Two-colour interferometry and Thomson scattering measurements of a plasma gun," *Plasma Phys. Control. Fusion*, vol. 61, p. 085012, Aug. 2019.

[82] R. Spielman, G. Baldwin, and G. Cooper, "Dd fusion experiments using fast z pinches," tech. rep., Sandia National Lab.(SNL-NM), Albuquerque, NM (United States), 1998.

[83] R. Aliaga-Rossel, I. H. Mitchell, and H. Schmidt, "Neutron production in the MAGPIE generator using," in *The fourth international conference on dense z-pinches*, (Vancouver, BC, Canada), pp. 61–65, ASCE, 1997.

[84] K. A. Gerber and J. D. Sethian, "Neutron measurements on ZFX," *Review of Scientific Instruments*, vol. 61, pp. 3169–3171, Oct. 1990.

[85] J. D. Sethian, A. E. Robson, K. A. Gerber, and A. W. DeSilva, "Enhanced stability and neutron production in a dense Z -pinch plasma formed from a frozen deuterium fiber," *Phys. Rev. Lett.*, vol. 59, pp. 892–895, Aug. 1987.

[86] K. D. Hahn, G. A. Chandler, C. L. Ruiz, G. W. Cooper, M. R. Gomez, S. Slutz, A. B. Sefkow, D. B. Sinars, S. B. Hansen, P. F. Knapp, P. F. Schmit, E. Harding, C. A. Jennings, T. J. Awe, M. Geissel, D. C. Rovang, J. A. Torres, J. A. Bur, M. E. Cuneo, V. Y. Glebov, A. J. Harvey-Thompson, M. C. Herrman, M. H. Hess, O. Johns, B. Jones, D. C. Lamppa, J. S. Lash, M. R. Martin, R. D. McBride, K. J. Peterson, J. L. Porter, J. Reneker, G. K. Robertson, G. A. Rochau, M. E. Savage, I. C. Smith, J. D. Styron, and R. A. Vesey, "Fusion-neutron measurements for magnetized liner inertial fusion experiments on the Z accelerator," *J. Phys.: Conf. Ser.*, vol. 717, p. 012020, May 2016.

[87] W. Kies, G. Decker, M. Mälzig, C. van Calker, J. Westheide, G. Ziethen, H. Bachmann, K. Baumung, H. Bluhm, D. Rusch, W. Ratajczak, O. Stoltz, and J. M. Bayley, "Terawatt fiber pinch experiments," *Journal of Applied Physics*, vol. 70, pp. 7261–7272, Dec. 1991.

[88] D. Klir, J. Kravarik, P. Kubes, Y. L. Bakshaev, P. I. Blinov, A. S. Chernenko, S. A. Danko, V. D. Korolev, G. I. Ustroev, M. I. Ivanov, and C. Hongchun, "Deuterated fibre Z-pinch on the S-300 generator," *Phys. Scr.*, vol. T123, pp. 116–119, Apr. 2006.

[89] A. P. Shah, *Effects of Pre-Ionization on the Gas-Puff Z-pinch*. Ph.D. thesis, University of Michigan, 2022.

[90] E. S. McKee, *Neutron Production from Z-pinch Plasmas at the 1 MA Zebra Generator*. Ph.D. thesis, University of Nevada, Reno, 2016.

[91] S. S. Anan'ev, Y. L. Bakshaev, P. I. Blinov, V. A. Bryzgunov, V. V. Vikhrev, S. A. Dan'ko, A. A. Zelenin, E. D. Kazakov, Y. G. Kalinin, A. S. Kingsep, V. D. Korolev, E. A. Smirnova, G. I. Ustroev, A. S. Chernenko, and V. A. Shchagin, "X-pinch-based neutron source," *Plasma Phys. Rep.*, vol. 36, pp. 601–608, July 2010.

[92] K. C. Mittal, D. H. Kalantar, N. Qi, D. A. Hammer, K. A. Gerber, and J. D. Sethian, "Neutron production in dense *x* -pinch plasmas produced from deuterated polyethylene fibers," *Journal of Applied Physics*, vol. 70, pp. 6712–6717, Dec. 1991.

[93] A. Shyam and R. Rout, "Observation of neutrons from palladium deuteride X pinches using a simple low energy capacitor bank," *IEEE Trans. Plasma Sci.*, vol. 27, pp. 1210–1213, Aug. 1999.

[94] J. Maenchen, H. T. Sheldon, G. D. Rondeau, J. B. Greenly, and D. A. Hammer, "Voltage and current measurements on high power self-magnetically insulated vacuum transmission lines," *Review of Scientific Instruments*, vol. 55, pp. 1931–1940, Dec. 1984.

[95] A. L. Velikovich, R. W. Clark, J. Davis, Y. K. Chong, C. Deeney, C. A. Coverdale, C. L. Ruiz, G. W. Cooper, A. J. Nelson, J. Franklin, and L. I. Rudakov, "Z-pinch plasma neutron sources," *Physics of Plasmas*, vol. 14, p. 022701, Feb. 2007.

[96] D. T. Offermann, D. R. Welch, D. V. Rose, C. Thoma, R. E. Clark, C. B. Mostrom, A. E. Schmidt, and A. J. Link, "Transition from Beam-Target to Thermonuclear Fusion in High-Current Deuterium Z -Pinch Simulations," *Phys. Rev. Lett.*, vol. 116, p. 195001, May 2016.

[97] J. G. Linhart, "Beam-target fusion in a dense Z-pinch," *Plasma Phys. Control. Fusion*, vol. 30, pp. 1641–1657, Nov. 1988.

[98] B. Viswanathan, "Nuclear Fusion," in *Energy Sources*, pp. 127–137, Elsevier, 2017.

[99] S. Glasstone and R. H. Lovberg, *Controlled thermonuclear reactions: an introduction to theory and experiment*. van Nostrand Princeton, 1960.

[100] C. Ruiz, J. Styron, D. Fehl, K. Hahn, B. McWatters, M. Mangan, G. Cooper, J. Vaughan, G. Chandler, B. Jones, J. Torres, S. Slutz, D. Ampleford, M. Gomez, E. Harding, A. Harvey-Thompson, and P. Knapp, "Novel beryllium-scintillator, neutron-fluence detector for magnetized liner inertial fusion experiments," *Phys. Rev. Accel. Beams*, vol. 22, p. 042901, Apr. 2019.

[101] H. Ing and H. Birnboim, "A bubble-damage polymer detector for neutrons," *Nuclear Tracks and Radiation Measurements (1982)*, vol. 8, pp. 285–288, Jan. 1984.

[102] C.-Q. Tu, S.-L. Guo, Y.-L. Wang, X.-H. Hao, C.-M. Chen, and J.-L. Su, "Study of bubble damage detectors for neutron detection," *Radiation Measurements*, vol. 28, no. 1, pp. 159–162, 1997. International Conference on Nuclear Tracks in Solids.

[103] L. Li, J. Jakowski, C. Do, and K. Hong, "Deuteration and Polymers: Rich History with Great Potential," *Macromolecules*, vol. 54, pp. 3555–3584, Apr. 2021.

[104] B. M. Habersberger, K. E. Hart, D. Gillespie, and T. Huang, "Molecular Weight Dependence of Deuterium Exchange on Polyethylene: Direct Measurement and SANS Model," *Macromolecules*, vol. 48, pp. 5951–5958, Aug. 2015.

[105] D. Ress, R. A. Lerche, R. J. Ellis, S. M. Lane, and K. A. Nugent, "Neutron imaging of inertial confinement fusion targets at Nova," *Review of Scientific Instruments*, vol. 59, pp. 1694–1696, Aug. 1988.